

Institute of Physics and Astronomy

Theoretical Physics

Patterns of synchrony and disorder in networks of coupled oscillators

Habilitation

In partial fulfillment of the requirements for the academic degree

Doctor rerum naturalium habilitatus

(Dr. rer. nat. habil.)

Submitted to

Faculty of Science, University of Potsdam

Dr. Oleh Omelchenko

Potsdam, May 2021

Dean: Prof. habil. Helmut Elsenbeer, PhD

Reviewers: Prof. Dr. Arkady Pikovsky
Prof. Dr. Ulrike Feudel
Prof. Dr. Uwe Thiele

Published online on the
Publication Server of the University of Potsdam:
<https://doi.org/10.25932/publishup-53596>
<https://nbn-resolving.org/urn:nbn:de:kobv:517-opus4-535961>

Abstract

Synchronization of coupled oscillators manifests itself in many natural and man-made systems, including circadian clocks, central pattern generators, laser arrays, power grids, chemical and electrochemical oscillators, only to name a few. The mathematical description of this phenomenon is often based on the paradigmatic Kuramoto model, which represents each oscillator by one scalar variable, its phase. When coupled, phase oscillators constitute a high-dimensional dynamical system, which exhibits complex behaviour, ranging from synchronized uniform oscillation to quasiperiodicity and chaos. The corresponding collective rhythms can be useful or harmful to the normal operation of various systems, therefore they have been the subject of much research.

Initially, synchronization phenomena have been studied in systems with all-to-all (global) and nearest-neighbour (local) coupling, or on random networks. However, in recent decades there has been a lot of interest in more complicated coupling structures, which take into account the spatially distributed nature of real-world oscillator systems and the distance-dependent nature of the interaction between their components. Examples of such systems are abundant in biology and neuroscience. They include spatially distributed cell populations, cilia carpets and neural networks relevant to working memory. In many cases, these systems support a rich variety of patterns of synchrony and disorder with remarkable properties that have not been observed in other continuous media. Such patterns are usually referred to as the coherence-incoherence patterns, but in symmetrically coupled oscillator systems they are also known by the name chimera states.

The main goal of this work is to give an overview of different types of collective behaviour in large networks of spatially distributed phase oscillators and to develop mathematical methods for their analysis. We focus on the Kuramoto models for one-, two- and three-dimensional oscillator arrays with nonlocal coupling, where the coupling extends over a range wider than nearest neighbour coupling and depends on separation. We use the fact that, for a special (but still quite general) phase interaction function, the long-term coarse-grained dynamics of the above systems can be described by a certain integro-differential equation that follows from the mathematical approach called the Ott-Antonsen theory. We show that this equation adequately represents all relevant patterns of synchrony and disorder, including stationary, periodically breathing and moving coherence-incoherence patterns. Moreover, we show that this equation can be used to completely solve the existence and stability problem for each of these patterns and to reliably predict their main properties in many application relevant situations.

The habilitation thesis is a compilation of the author's papers [79, 81, 84, 85, 86, 87] with improved notations and suitably organized exposition of results. Several new results are also included in the text and are accompanied by their proofs.

Contents

1	Introduction	7
1.1	Self-sustained oscillators and synchronization phenomena	7
1.2	Phase models	8
1.3	Spatially extended oscillator systems and nonlocal coupling	12
1.4	Phenomenology of spatially extended oscillatory systems	15
1.5	Extensive chaos in coupled oscillator systems	25
2	Continuum limit formalism	27
2.1	Ott-Antonsen manifold	28
2.2	Dynamics in the Ott-Antonsen manifold	30
2.3	Ott-Antonsen equations for spatially extended oscillatory systems	33
3	Completely incoherent state	36
4	Relative equilibria of the Ott-Antonsen equation	37
4.1	Riccati equation with constant coefficients	39
4.2	Self-consistency equation	40
4.3	Modified self-consistency equation	42
4.4	Stability analysis	43
4.5	Computation of the discrete spectrum	46
5	Nonlocal coupling of the convolution type	48
5.1	Twisted states	48
5.2	Primary branches of spatially modulated partially coherent states	51
5.3	The uniform partially coherent state and secondary branches of spatially modulated partially coherent states	54
6	Stationary chimera states in oscillator arrays of different dimensionality	58
6.1	The Ott-Antonsen equation method	63
6.2	Antiphase chimeras in $1D$, $2D$ and $3D$	64
6.3	Twisted chimeras ($2D$) and twisted planes ($3D$)	67
6.4	Spiral chimera ($2D$) and spiral rolls ($3D$)	70
6.5	Classical chimera ($1D$), coherent stripe ($2D$) and coherent plane ($3D$)	73
6.6	Coherent spot ($2D$) and coherent tube ($3D$)	76
6.7	Coherent ball ($3D$)	78
6.8	Other coupling functions	81
6.9	Open problems	83

7	Breathing chimera states	86
7.1	Periodic complex Riccati equation	88
7.2	Solution operator \mathcal{U} for periodic complex Riccati equation	92
7.3	Derivatives of the solution operator \mathcal{U}	94
7.4	Self-consistency equation	95
7.5	Modified self-consistency equation	96
7.6	Modified self-consistency equation for cosine coupling function	97
7.7	Stability analysis of relative periodic orbits	99
7.8	Computation of the discrete spectrum	104
7.9	Example of a breathing chimera state	106
8	Nonstationary coherence-incoherence patterns	109
8.1	Poincaré section method	110
8.2	Stability diagram of nonstationary coherence-incoherence patterns	111
8.3	Remarks	115
9	Travelling chimera states	116
9.1	Continuation algorithm for travelling chimera states	121
9.2	Stability of travelling chimera states	129
10	Conclusion and outlook	136
	Appendix	137
	Acknowledgements	141
	References	143

1 Introduction

1.1 Self-sustained oscillators and synchronization phenomena

Many physical, chemical and biological systems can behave as self-sustained oscillators. Spiking neurons, mammalian hearts, pendulum clocks, lasers, and pulsating variable stars are just a few examples of this kind. The main characteristic feature of a self-sustained oscillator is that in isolation it exhibits rhythmic activity, which is due to the inherent properties of the oscillator only and does not depend on the initial conditions [41]. This activity can be measured as the output signal of the system. Then, in general, the period and shape of the signal will remain almost unchanged, even if the oscillator is placed in a certain environment. This property, obviously, implies that a self-sustained oscillator can neither be a conservative nor a linear system. In contrast, it is typically a nonlinear dissipative system with a steady intrinsic source of power. For example, a pendulum clock contains a weight on a chain that turns a sprocket and thus compensates for the effect of friction in this mechanical system. Similarly, a typical semiconductor laser needs to be pumped by an external light source or electric current in order to compensate for dissipation losses in the cavity. Finally, cellular oscillations [6] are usually driven by the chemical energy liberated during adenosine triphosphate (ATP) hydrolysis.

The dynamics of a self-sustained oscillator is usually described by a nonlinear autonomous system of differential equations, which has a stable limit cycle solution. If one slightly disturbs such an oscillator, then after a relatively short transient it restores the form of its oscillation, but with some shift in time. For a single oscillator this time shift plays no role. However, if one considers two or more similar self-sustained oscillators, then the relative time shift between their outputs becomes a meaningful quantity. For example, the sum of two oscillations with no time shift between them has twice bigger amplitude than the amplitude of a single oscillator. In this case, the corresponding oscillators are called *synchronized*. In contrast, if the time shift between two oscillations is close to the half-period, then these oscillations tend to cancel each other and therefore the corresponding oscillators are called *asynchronous*.

In nature and in man-made systems, self-sustained oscillators often occur not individually but in groups. In this case, they interact with each other so that their rhythms tend to adjust in a certain order. In general, their oscillations may remain mutually asynchronous or may become partially or completely synchronized. This interaction of rhythms is commonly referred to as *synchronization phenomenon* [133, 96, 3]. Synchronization has been observed in different real-world systems and laboratory experiments, including populations of fireflies [14] and yeast cells [23], chemical [123] and electrochemical oscillators [48]. Moreover, it has been shown that this phenomenon underlies many physiological processes in living organisms such as generation of circadian rhythms, heart beating and locomotion [31, 139]. On the other hand, it can be associated with certain brain disorders, such as schizophrenia, epilepsy, Alzheimer's and Parkinson's diseases [127, 63].

The general interest in synchronization phenomena has led to the development of mathematical models that provide a rigorous description of the synchronized and asynchronous oscillations in terms of phase oscillators. Roughly speaking, if one considers several nearly identical, weakly interacting self-sustained oscillators, then their dynamics can be approximately described by a specific model, called the *phase model*. In such a model, the state of each oscillator is represented by a single scalar quantity, the oscillator's phase. The phase is qualitatively similar to the time shift of oscillation and usually is normalized so that it increases by 2π after every complete oscillation.

First phase models were proposed about 50 years ago by Arthur Winfree [133] and Yoshiki Kuramoto [53]. In particular, the model suggested by Kuramoto became very popular because of its simplicity and rigorous mathematical justification. Initially, phase models were used to explain synchronization transitions in populations of all-to-all coupled oscillators [118, 2], but later their field of application was extended to complex oscillator networks [3]. In this work, we focus on a specific class of oscillator networks where the interaction between individual oscillators is determined by the distance between their positions in real physical space, therefore we call such networks spatially extended. We show that these networks constitute a new type of pattern forming systems with extremely rich dynamical behaviour, including complex spatiotemporal patterns of synchrony and disorder which, in some cases, are called *chimera states*. Note that our main goal is not only to demonstrate these bizarre patterns, but also to reveal the dynamical mechanisms responsible for their emergence, as well as to describe effective mathematical tools that can be used to study their properties.

1.2 Phase models

Mathematical description of self-sustained oscillators usually relies on ordinary differential equations of the form

$$\frac{dX}{dt} = F_0(X), \tag{1.1}$$

where $X(t) \in \mathbb{R}^n$ is the state vector of the oscillator and $F_0 : \mathbb{R}^n \rightarrow \mathbb{R}^n$ is a nonlinear function describing the oscillator dynamics. This representation is valid for many textbook examples such as Stuart-Landau oscillator, Van der Pol oscillator and Duffing oscillator [117]. Moreover, different neuron models, including FitzHugh-Nagumo, Morris-Lecar and Hindmarsh-Rose models, can also be written in this form [27].

To be a self-sustained oscillator, Eq. (1.1) must have an asymptotically stable periodic solution $X_0(t)$ with a minimal period T_0 . Then, for varying time t the point $X_0(t)$ moves along a closed curve C_0 in \mathbb{R}^n , called *limit cycle*. Selecting an arbitrary point $X_* \in C_0$ one can characterize all other points on the limit cycle by the time $\Phi(X_0(t)) \in [0, T_0)$ since the last passing of X_* . The obtained scalar quantity $\Phi(X_0(t))$ is called phase of oscillations. Using the mathematical concept of isochrones [34, 53], the definition of phase $\Phi(X)$ can also be extended

outside the limit cycle C_0 . Then it can be shown that for any system of weakly interacting oscillators of the form (1.1) their dynamics reduces to the dynamics of the oscillator phases only. In mathematical literature, this fact is known as Malkin theorem, which for the purposes of the present work we formulate as follows (the proof of the theorem can be found in [39]).

Theorem 1.1 *Let the dynamical system (1.1) behave as a self-sustained oscillator, i.e. it has an asymptotically stable periodic solution $X_0(t)$ with a minimal period T_0 . Consider a system of N nearly identical weakly connected oscillators of the form*

$$\frac{dX_k}{dt} = F_0(X_k) + \varepsilon F_k(X_k) + \varepsilon \sum_{j=1}^N G_{kj}(X_k, X_j), \quad k = 1, \dots, N, \quad (1.2)$$

where $\varepsilon \in \mathbb{R}$ is a small parameter, $F_k : \mathbb{R}^n \rightarrow \mathbb{R}^n$ and $G_{kj} : \mathbb{R}^n \times \mathbb{R}^n \rightarrow \mathbb{R}^n$. Then there exists $\varepsilon_0 > 0$ such that for every $\varepsilon \in (0, \varepsilon_0)$ the long-term dynamics of system (1.2) is given by

$$X_k(t) = X_0(t + \varphi_k(\varepsilon t)) + O(\varepsilon), \quad (1.3)$$

where the vector of phase deviations $\varphi_k(\tau)$ is a solution to

$$\frac{d\varphi_k}{d\tau} = \nu_k + \sum_{j=1}^N H_{kj}(\varphi_j - \varphi_k), \quad k = 1, \dots, N, \quad (1.4)$$

and

$$\begin{aligned} \nu_k &= \frac{1}{T_0} \int_0^{T_0} Q(t)^\top F_k(X_0(t)) dt, \\ H_{kj}(\psi) &= \frac{1}{T_0} \int_0^{T_0} Q(t)^\top G_{kj}(X_0(t), X_0(t + \psi)) dt, \end{aligned}$$

where $Q(t) \in \mathbb{R}^n$ is the unique nontrivial T_0 -periodic solution to the linear system

$$\frac{dQ}{dt} = -[\nabla_X F_0(X_0(t))]^\top Q$$

satisfying the normalization condition

$$Q(t)^\top F(X_0(t)) = 1$$

for some (and hence all) t .

Theorem 1.1 is very useful for studying synchronization phenomena in model (1.2). Indeed, it allows to replace the $(N \times n)$ -dimensional model (1.2) with a simpler N -dimensional phase model (1.4). Notice that all ingredients of Eq. (1.4) are defined explicitly. To compute ν_k and $H_{kj}(\psi)$, apart from the functions $F_k(X)$ and $G_{kj}(X, Y)$ one needs to know only the periodic solution $X_0(t)$ and the Jacobian $\nabla_X F_0(X_0(t))$ of nonlinear system (1.1).

Importantly, system (1.4) describes the dynamics of phase deviations $\varphi_k(\tau)$, while the oscillator phases are given by $t + \varphi_k(\varepsilon t)$, see formula (1.3). In practice it is more convenient to rescale these phases in the following way

$$\theta_k(t) = \omega_0(t + \varphi_k(\varepsilon t)) \quad \text{where} \quad \omega_0 = \frac{2\pi}{T_0}.$$

Then, the new phases $\theta_k(t)$ vary from 0 to 2π (not from 0 to T_0). Moreover, it follows from Eq. (1.4) that $\theta_k(t)$ evolve according to

$$\frac{d\theta_k}{dt} = \omega_k + \varepsilon \sum_{j=1}^N \Gamma_{kj}(\theta_k(t) - \theta_j(t)), \quad k = 1, \dots, N, \quad (1.5)$$

where $\omega_k = \omega_0 + \varepsilon\omega_0\nu_k$ and $\Gamma_{kj}(\psi) = \omega_0 H_{kj}(-\psi/\omega_0)$ are 2π -periodic functions of ψ .

Remark 1.2 *A mathematical approach concerned with the derivation of phase models approximating the behaviour of general networks of self-sustained oscillators is called phase reduction. More details about this approach can be found in recent review papers [4, 95, 56].*

The most studied version of the phase model (1.5) involves a factorization

$$\Gamma_{kj}(\psi) = -w_{kj} \sin(\psi + \alpha),$$

where w_{kj} are real weights and α is a phase lag parameter. This form of the phase coupling function $\Gamma_{kj}(\psi)$ can be justified for system (1.2) if oscillator (1.1) is near a Hopf bifurcation and the interaction term reads $G_{kj}(X, Y) = w_{kj}G_0(X, Y)$, see [39, 5]. Then, different choices of weights w_{kj} lead to qualitatively different models (1.5), which can be classified as follows.

Globally coupled phase oscillators. This is a system of all-to-all coupled phase oscillators

$$\frac{d\theta_k}{dt} = \omega_k - \frac{\kappa}{N} \sum_{j=1}^N \sin(\theta_k(t) - \theta_j(t) + \alpha), \quad k = 1, \dots, N, \quad (1.6)$$

where ω_k denotes the natural frequency of oscillator k , and κ is the coupling constant. The frequencies ω_k are drawn randomly and independently from a distribution $h(\omega)$, therefore in the absence of coupling all phases $\theta_k(t)$ drift with respect to each other and remain disordered.

For increasing coupling strength κ , the phases show a tendency to synchronize following a specific bifurcation scenario called synchronization transition. The properties of synchronization transition depend on the type of distribution $h(\omega)$ and on the value of phase lag parameter α .

The model (1.6) with $\alpha = 0$ was first suggested and analyzed by Kuramoto in 1975 [53]. Later Sakaguchi and Kuramoto reconsidered it for nonvanishing phase lag α [107]. Synchronization transitions predicted in these works were observed in experiments with electrochemical oscillators [48] and BZ oscillatory catalytic particles [123]. Moreover, Wiesenfeld, Colet and Strogatz showed [130] that model (1.6) describes also synchronization transitions in Josephson junction arrays. A large number of other theoretical results concerned with model (1.6) can be found in reviews [118, 2, 98].

Locally coupled phase oscillators. These are one-, two- and three-dimensional arrays of nearest-neighbour coupled phase oscillators. In the simplest case of a one-dimensional array, the corresponding model reads

$$\frac{d\theta_k}{dt} = \omega_k - \kappa \sin(\theta_k(t) - \theta_{k+1}(t) + \alpha) - \kappa \sin(\theta_k(t) - \theta_{k-1}(t) + \alpha), \quad k = 1, \dots, N. \quad (1.7)$$

If natural frequencies ω_k vary slowly along the array, more precisely if $|\omega_{k+1} - \omega_k| < 1/N$, then typical solutions of Eq. (1.7) are phase-locked states. In the limit $N \rightarrow \infty$, their asymptotic behaviour can be described using a continuum limit equation derived by Kopell and Ermentrout in [49, 50]. Further results about the phase-locked solutions in one- and two-dimensional systems of locally coupled oscillators can be found in [101] and [93].

Modular oscillator networks. These are generalizations of the above Kuramoto-Sakaguchi model (1.6), where instead of a single population of globally coupled phase oscillators one considers several copies of them. In the case of two populations with sizes N_1 and N_2 , such model can be written in the form

$$\frac{d\theta_k^{(m)}}{dt} = \omega_k^{(m)} - \sum_{n=1}^2 \frac{\kappa_{mn}}{N_n} \sum_{j=1}^{N_n} \sin(\theta_k^{(m)}(t) - \theta_j^{(n)}(t) + \alpha_{mn}), \quad k = 1, \dots, N_m.$$

Note that the coupling constants κ_{mn} and the phase lags α_{mn} depend on the population indices only, hence the name modular network. An overview of the most interesting dynamical regimes observed in modular oscillator networks and the mathematical methods used to analyze their behaviour can be found in [9].

Random oscillator networks. If the connectivity between phase oscillators is described by a random graph (directed or undirected) with an adjacency matrix A_{kj} , then one can define a random network of oscillators

$$\frac{d\theta_k}{dt} = \omega_k - \kappa \sum_{j=1}^N A_{kj} \sin(\theta_k(t) - \theta_j(t) + \alpha), \quad k = 1, \dots, N. \quad (1.8)$$

For model (1.8) one usually studies the existence and stability of synchronized and clustered states as well as synchronization transitions for varying κ [10, 3, 25, 105].

Spatially extended oscillator systems. These are spatially weighted networks where the connectivity between oscillators depends on their distance from each other. Such models are the main subject of this work and are explained in the next section.

1.3 Spatially extended oscillator systems and nonlocal coupling

A realistic coupled oscillator system is always spatially distributed, because different oscillators have different positions in space. On the other hand, all physical interactions depend on the distance between interacting agents, therefore the phase coupling functions $\Gamma_{kj}(\psi)$ in (1.5) must be distance dependent too. To take this fact into account, Eq. (1.5) is usually modified as follows. One denotes the oscillator positions as points x_k , $k = 1, \dots, N$, in a certain domain D with volume $|D|$. This domain can be one-, two- or perhaps three-dimensional. Then, one chooses a relevant interaction function $G(x, y)$ and assumes that the coupling strength between the k th and j th oscillators is proportional to $G(x_k, x_j)$. This yields a model

$$\frac{d\theta_k}{dt} = \omega_k + \frac{|D|}{N} \sum_{j=1}^N G(x_k, x_j) f(\theta_k(t) - \theta_j(t)), \quad k = 1, \dots, N, \quad (1.9)$$

where $f(\psi)$ is a phase coupling function independent of the indices k and j . Obviously, for a constant function $G(x, y)$, model (1.9) coincides with a globally coupled system. On the other hand, if $G(x, y)$ has nonvanishing values around the diagonal $x = y$ only, then model (1.9) is qualitatively similar to a locally coupled system. This means that the coupling structure in (1.9) is in between of the global and local coupling, therefore it is usually called *nonlocal coupling*.

In many cases, a more specific form of nonlocal coupling is considered in (1.9). For instance, the interaction function $G(x, y)$ may depend only on the difference of x and y ,

$$G(x, y) = G_0(x - y),$$

resulting in the *convolution type* interaction between oscillators. Another example is function $G(x, y)$ depending on the distance between x and y ,

$$G(x, y) = G_0(|x - y|),$$

which represents the *isotropic* oscillator interaction. In the following we discuss the origin of nonlocal coupling in applications.

Nonlocal coupling in reaction-diffusion systems. First, we consider a model suggested by Kuramoto in [54]. This is a reaction-diffusion system of the form

$$\frac{\partial}{\partial t}A(x, t) = F(A(x, t)) + KS(x, t), \quad x \in D, \quad (1.10)$$

$$\tau \frac{\partial}{\partial t}S(x, t) = -S + d\Delta S + Q(A(x, t)), \quad x \in D, \quad (1.11)$$

where D is a spatial domain, $A(x, t) \in \mathbb{R}^n$ and $S(x, t) \in \mathbb{R}$ are concentration variables of some chemicals, $F : \mathbb{R}^n \rightarrow \mathbb{R}^n$ and $Q : \mathbb{R}^n \rightarrow \mathbb{R}$ are functions describing their interaction, $K \in \mathbb{R}^{n \times n}$ is a constant coupling matrix, d is a diffusion coefficient and τ is a time scale coefficient. Suppose that for $K = 0$ equation (1.10) has an attracting limit cycle, then for nonvanishing K system (1.10), (1.11) describes a continuum of coupled oscillators, which interact with each other not directly, but through the diffusive chemical S . If the time scale τ in Eq. (1.11) is very small, we can perform an adiabatic elimination of S . For this, using the Green's function $g(x, y)$ associated with the differential operator $\mathcal{I} - d\Delta$, we solve Eq. (1.11)

$$S(x, t) = \int_D g(x, y)Q(A(y, t))dy.$$

Then, inserting the result into Eq. (1.10) we obtain

$$\frac{\partial}{\partial t}A(x, t) = F(A(x, t)) + K \int_D g(x, y)Q(A(y, t))dy. \quad (1.12)$$

Although Eq. (1.12) was derived for a continuum of oscillators, it remains valid approximately for a large discrete set of positions x_k , $k = 1, \dots, N$, distributed uniformly in D . Indeed, for every x_k we have a Monte Carlo integral approximation

$$\int_D g(x_k, y)Q(A(y, t))dy \approx \frac{|D|}{N} \sum_{j=1}^N g(x_k, x_j)Q(A(x_j, t)),$$

where $|D|$ is the volume of the domain D . Hence for large enough N equation (1.12) implies

$$\frac{\partial}{\partial t}A(x_k, t) = F(A(x_k, t)) + \frac{K|D|}{N} \sum_{j=1}^N g(x_k, x_j)Q(A(x_j, t)), \quad k = 1, \dots, N.$$

If all entries of the coupling matrix K are small, we can also perform a phase reduction of the latter system. Thus, we obtain a phase oscillator model of the form (1.9). For example, a detailed description of the phase reduction step, for nonlinearities $F(A)$ that correspond to Stuart-Landau and FitzHugh-Nagumo oscillators, can be found in [55] and [114], respectively.

Remark 1.3 Note that the Green's function $g(x, y)$, which determines nonlocal coupling in (1.12), depends on the boundary conditions used in Eq. (1.11), therefore, in general, it is not of the convolution type. However, for periodic domains D (e.g., a ring or a flat torus) this function depends only on the distance between x and y , therefore in this case, it produces an isotropic, and hence a convolution type, nonlocal coupling.

The most relevant implementation of system (1.10), (1.11) in the experiment was reported in [122], where synchronization and pattern formation were studied on a chip of 15 artificial cells with gene expression cellular reactions and diffusion-based communication. Other experimental setups that directly impose a nonlocal coupling scheme in the form of Eq. (1.12) on a system of chemical or electrochemical oscillators were described in [124, 125, 129].

Nonlocal coupling in neuroscience. In [39], Hoppensteadt and Izhikevich developed a general theory of weakly connected neural networks. Supposing that each neuron is a system near a Hopf bifurcation, they showed that the dynamics of such a network is described by equations of the form

$$\frac{dz_k}{dt} = (a_k - b_k |z_k|^2) z_k + \sum_{j=1}^N w_{kj} z_j, \quad k = 1, \dots, N, \quad (1.13)$$

where $z_k(t)$ are complex functions representing neurons and a_k , b_k and w_{kj} are complex constants. If the neurons are similar and all weights w_{kj} are real, then applying Theorem 1.1 one can reduce system (1.13) to a phase model (1.5) with $\Gamma_{kj}(\psi) = w_{kj} \Gamma(\psi)$ and $\Gamma(\psi) \sim \sin(\psi + \alpha)$. In this model, weights w_{kj} encode the spatial structure of neural network. Typically, one chooses them in the form $w_{kj} = G(x_k, x_j)$ where x_k is the spatial position of the k th neuron and $G(x, y)$ is an interaction function. The most common choice of $G(x, y)$ is an isotropic function that depends on the distance between x and y only. Then, $G(x, y) = G_0(|x - y|)$ may be a Gaussian, exponential, 'Mexican hat', or with finite support, see [26, Sec. 6]. In some situations, however, $G(x, y)$ has to be chosen as a function of two variables. This holds, for example, in the case of a homogenized interaction function

$$G(x, y) = G_0(|x - y|) \left(\int_D G_0(|x - y|) dy \right)^{-1},$$

in the case of a non-uniform distribution $\rho(x)$ of neurons

$$G(x, y) = G_0(|x - y|) \rho(x) \rho(y),$$

or in the case of a Hebbian type connectivity

$$G(x, y) = \sum_{k=1}^K p_k(x) q_k(y)$$

determined by $2K$ functions $p_k(x)$ and $q_k(y)$.

Cilia arrays with hydrodynamic interaction. Cilia are slender, hair-like organelles that protrude from many types of cells. They are capable to generate a regular, beating waveform and thus behave as self-sustained oscillators [73]. In animal systems, ciliated cells are often found in the form of multicellular ensembles such as colonial protozoans, ciliary bands or epithelial surfaces. Typical functions of such ensembles include generation of feeding currents, pumping bodily fluids or enabling complex locomotion, so they require collective synchronization of cilia movement [29]. From the physical perspective, cilia operate in the low Reynolds number regime where hydrodynamics is dominated by viscous forces [32], therefore their interaction is mainly determined by a long-ranged hydrodynamic coupling. This fact was used in [126] to derive a mathematical model describing synchronization phenomena in cilia carpets. To this end, the ciliated surface was represented as a two-dimensional array of rotors on a substrate. In the case when the distance between the nearest cilia was much larger than their sizes, the hydrodynamic coupling between them was weak, and phase reduction was possible. Thus, a phase oscillator model (1.9) was obtained [126] with an isotropic power-law nonlocal coupling

$$G(x, y) = |x - y|^{-3/2}$$

and $f(\psi) = -\sin(\psi + \alpha)$ where α was determined by the beating waveform.

1.4 Phenomenology of spatially extended oscillatory systems

Let us consider a one-dimensional phase oscillator system

$$\frac{d\theta_k}{dt} = \omega_k - \frac{2\pi}{N} \sum_{j=1}^N G\left(\frac{2\pi}{N}(k-j)\right) \sin(\theta_k(t) - \theta_j(t) + \alpha), \quad k = 1, \dots, N, \quad (1.14)$$

where $G(x)$ is a non-constant 2π -periodic function. System (1.14) is a particular case of model (1.9), where $f(\psi) = -\sin(\psi + \alpha)$, the coupling is of the convolution type and the oscillator positions x_k are evenly distributed in the interval $[-\pi, \pi]$. The periodicity of $G(x)$ implies that system (1.14) is equipped with periodic boundary condition and thus describes a ring of nonlocally coupled oscillators.

In the following we give an overview of typical dynamical regimes observed in system (1.14). For this we consider two coupling functions:

1) a *top-hat coupling* defined as a 2π -periodic extension of the function

$$G(x) = \begin{cases} (2\pi\sigma)^{-1} & \text{for } |x| \leq \pi\sigma, \\ 0 & \text{for } \pi\sigma < |x| \leq \pi, \end{cases} \quad (1.15)$$

where $\sigma \in (0, 1)$ is the relative coupling radius;

2) and a *trigonometric coupling*

$$G(x) = \frac{1}{2\pi}(1 + A \cos x + B \sin x), \quad (1.16)$$

where A and B are real parameters.

Note that the top-hat coupling (1.15) is non-negative and reflection symmetric, i.e. it satisfies $G(-x) = G(x) \geq 0$. In contrast, the trigonometric coupling (1.16) is reflection symmetric only for $B = 0$. Moreover, it can be sign-changing for large values of A and B (for example for $A > 1$ and $B = 0$).

We also consider two representative cases of natural frequencies ω_k : *identical* oscillators and *heterogeneous* oscillators. In the former case, we choose $\omega_k = 0$, while in the latter case, we suppose that the frequencies are chosen randomly and independently from a Lorentzian distribution

$$h(\omega) = \frac{\gamma}{\pi} \frac{1}{\omega^2 + \gamma^2} \quad (1.17)$$

with width $\gamma > 0$. Note that the case of identical oscillators can formally be considered as the limiting case $\gamma \rightarrow 0$ of the Lorentzian distribution.

Complete coherence and q -twisted states. The most common solutions of the system (1.14) with identical oscillators are q -twisted states [132]

$$\theta_k(t) = \frac{2\pi qk}{N} + \Omega_q t, \quad k = 1, \dots, N,$$

where integer q counts the number of twists along the array and $\Omega_q \in \mathbb{R}$ is the angular speed of the oscillators, Fig. 1(a). In q -twisted states all oscillators rotate rigidly keeping their phase differences with respect to each other constant, therefore we call them phase-locked or *coherent*

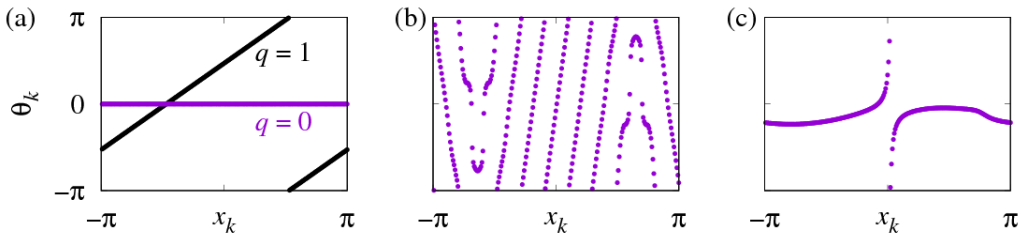


Figure 1: Coherent states in a system of $N = 256$ identical nonlocally coupled phase oscillators (1.14). (a) Completely coherent and 1-twisted states for the top-hat coupling (1.15) with $\sigma = 0.5$ and $\alpha = 0$. (b) Multi-twisted state for the top-hat coupling (1.15) with $\sigma = 0.14$ and $\alpha = \pi$. (c) Coherent traveling wave for the symmetric trigonometric coupling (1.16) with $A = 0.9$, $B = 0$ and $\alpha = \pi/2 - 0.1$.

states. Moreover, since the state with $q = 0$ consists of fully synchronized oscillators, we call it *complete coherence*.

Other coherent states. Apart from the q -twisted states, there are also other coherent states, which can be found in the system of identical oscillators (1.14). These are, for example, *multi-twisted* [30] and *rippled* [37] states, which have several spatial regions where oscillators are close to one or other twisted state, Fig. 1(b), or transient travelling waves, where rigidly rotating phase patterns drift simultaneously along the array, Fig. 1(c).

Chimera states. Coherent dynamics is not the only oscillator behaviour in system (1.14). In 2002 Kuramoto and Battogtokh discovered [55] that system (1.14) can also exhibit complex spatiotemporal patterns composed of coherent and incoherent regions. Here, the term *coherent* region applies to a group of oscillators which are phase-locked, i.e. their velocities $\dot{\theta}_k(t)$ are almost identical for sufficiently long time and the corresponding phases $\theta_k(t)$ evolve synchronously, whereas the term *incoherent* region refers to the rest of the oscillators which drift with respect to each other and with respect to all coherent regions. The coexistence of coherent and incoherent dynamics in the system of symmetrically connected identical oscillators (1.14) seems to be counterintuitive, therefore Abrams and Strogatz suggested to call it *chimera state* [1]. Two examples of such chimera states are shown in Fig. 2. These are a chimera state with a single coherent region, Fig. 2(a), and a chimera state with two anti-phase coherent regions, Fig. 2(e). Note that the coherent and incoherent regions can be recognized as clustered and sparsely distributed phases $\theta_k(t)$ respectively. Another way to distinguish between coherent

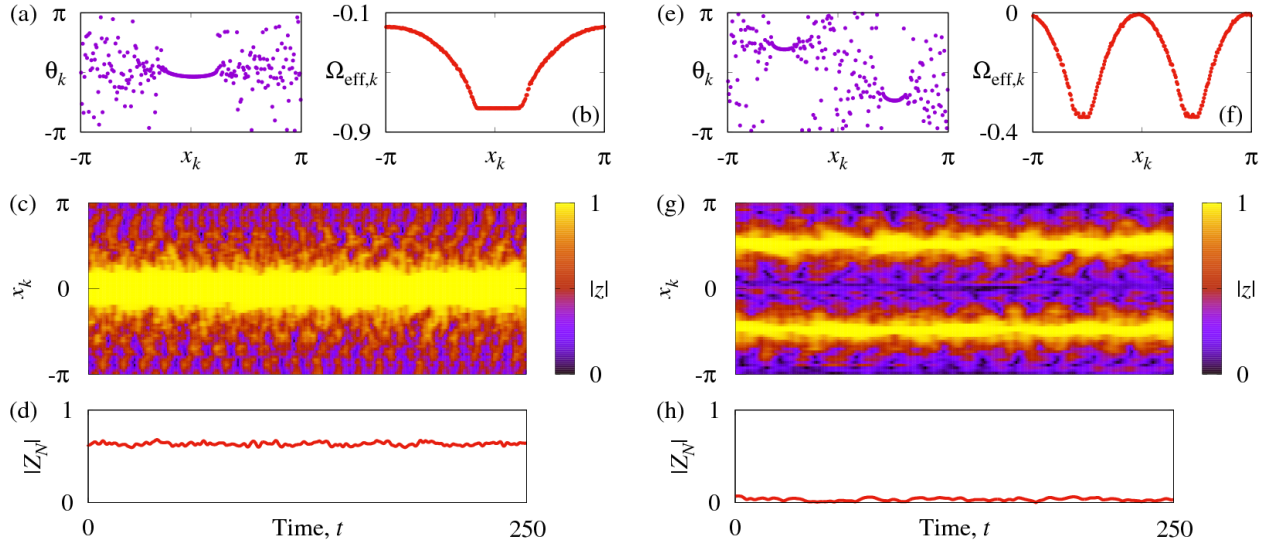


Figure 2: Two coexisting chimera states in a system of $N = 256$ identical phase oscillators (1.14). Parameters: Symmetric trigonometric coupling (1.16) with $A = 0.9$, $B = 0$ and $\alpha = \pi/2 - 0.1$.

and incoherent oscillators is to calculate their effective frequencies

$$\Omega_{\text{eff},k} = \frac{1}{\tau} \int_0^\tau \frac{d\theta_k}{dt} dt, \quad (1.18)$$

where the averaging must be carried out over sufficiently many oscillator rotations. A group of oscillators with equal $\Omega_{\text{eff},k}$ is identified as coherent (note that, in general, there can be several such groups with different common frequencies), whereas the remaining oscillators with different $\Omega_{\text{eff},k}$ are considered to be incoherent, see Fig. 2(b),(f).

For a more detailed characterization of chimera states one also uses two other quantities: global and local order parameters. The global order parameter is defined as an average

$$Z_N(t) = \frac{1}{N} \sum_{k=1}^N e^{i\theta_k(t)}. \quad (1.19)$$

Its modulus $|Z_N(t)|$ measures the collective synchrony of oscillators $\theta_k(t)$ such that the identity $|Z_N(t)| = 1$ holds for perfectly synchronized state only, while small values $|Z_N(t)| \approx 0$ usually indicate sparse phase distributions. If $|Z_N(t)| \neq 0$ the argument of $Z_N(t)$ yields the most likely value of $\theta_k(t)$. Moreover, if the inequality $|Z_N(t)| \neq 0$ holds for all t , then the average argument speed

$$\Omega = \frac{1}{\tau} \int_0^\tau d \arg Z_N(t) = \frac{1}{\tau} \int_0^\tau \text{Im} \left(\frac{\overline{Z_N(t)}}{|Z_N(t)|^2} \frac{dZ_N}{dt} \right) dt \quad (1.20)$$

is well-defined and is called global order parameter frequency.

In contrast to the global order parameter $Z_N(t)$, the local order parameter is defined as a position dependent function

$$z_{N,\varepsilon}(x, t) = \frac{1}{\#\{k : |x_k - x| < \varepsilon\}} \sum_{k : |x_k - x| < \varepsilon} e^{i\theta_k(t)}. \quad (1.21)$$

We assume that the k th oscillator position is $x_k = -\pi + 2\pi k/N$ and the averaging in (1.21) takes place over all oscillators lying in the ε -vicinity of $x \in [-\pi, \pi]$. For a good spatial resolution, the radius ε has to be small enough. On the other hand, it cannot be too small, because in the ε -vicinity of every point x there must be sufficiently many oscillators for averaging. Thus, the optimal strategy, in the case of a one-dimensional array (1.14), is to choose $\varepsilon = \pi/\sqrt{N}$.

The middle and bottom panels in Fig. 2 show the local $z(x, t)$ and the global $Z_N(t)$ order parameters of the chimera states described above. Their coherent and incoherent regions are determined by the conditions $|z(x, t)| \approx 1$ and $|z(x, t)| < 1$, respectively. A nearly constant behaviour of $|Z_N(t)|$ indicates that both chimera states are statistically stationary dynamical regimes.

Breathing chimera states. Figure 3 shows a more complicated type of chimera states for identical oscillators, called breathing chimera state. Its characteristic features are:

- (i) multiple coherent and incoherent regions in the θ_k -snapshot,
- (ii) multiple equidistant plateaus in the graph of effective frequencies $\Omega_{\text{eff},k}$,
- (iii) periodically varying (breathing) oscillator dynamics,
- (iv) oscillating modulus of the global order parameter $Z_N(t)$.

The equidistant effective frequency plateaus indicate that the macroscopic dynamics of breathing chimera states is quasiperiodic with two frequencies. For chimera states shown in Fig. 3, these frequencies can be found in the following way. Using formula (1.20) one calculates the primary frequency Ω_1 , while the secondary frequency Ω_2 can be extracted from the oscillations of global order parameter $Z_N(t)$. To this end, one first determines the minimal R_{\min} and the maximal R_{\max} values of $|Z_N(t)|$ and then seeks for the consecutive time moments t_k where the graph $|Z_N(t)|$ crosses the mean level $R_{\text{mean}} = (R_{\min} + R_{\max})/2$ from above, see circles in Fig. 3(d) and (h). Averaging the differences $t_k - t_{k-1}$ over k one obtains the period T_2 corresponding to the secondary frequency Ω_2 . The latter, obviously, equals $\Omega_2 = 2\pi/T_2$.

Remark 1.4 *Note that the above method for determining the breathing period T_2 relies on the assumption that the $|Z_N(t)$ -graph crosses the mid-level $(R_{\min} + R_{\max})/2$ only twice on the period (once from below and the other from above). If this is not the case, then one needs to select*

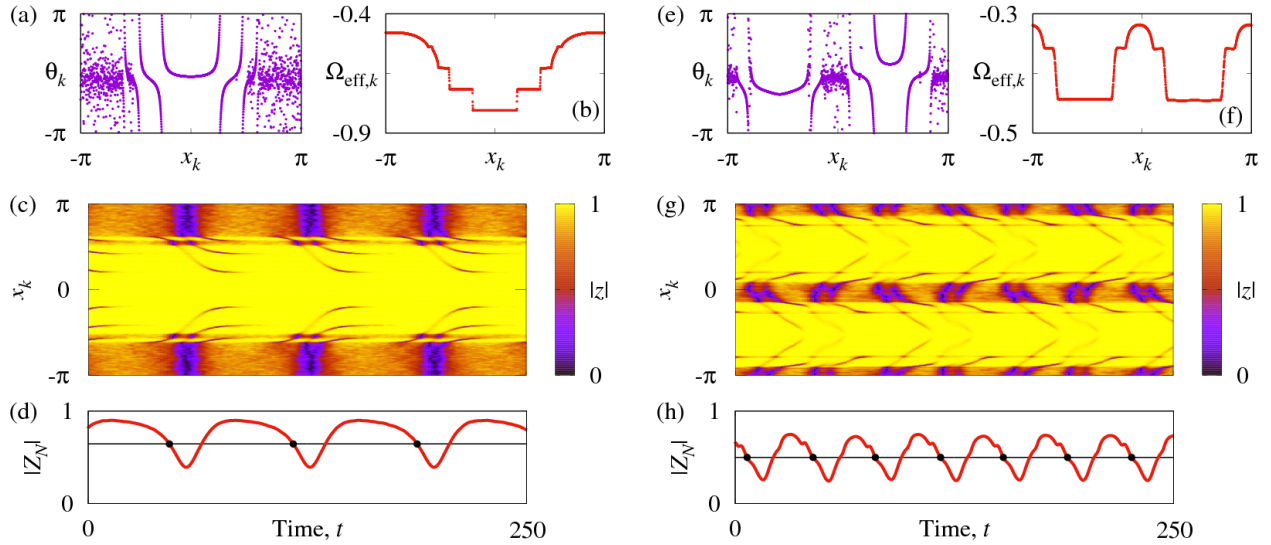


Figure 3: Breathing chimera states in a system of $N = 16384$ identical phase oscillators (1.14). Parameters: Symmetric trigonometric coupling (1.16) with (a)–(d) $A = 1.05$ and (e)–(h) $A = 1.19$, $B = 0$ and $\alpha = \pi/2 - 0.15$.

another mid-level value in the interval (R_{\min}, R_{\max}) , which guarantees the two intersections condition.

Complete incoherence and partially coherent twisted states. Now we consider a version of system (1.14) with heterogeneous phase oscillators, i.e. oscillators with non-identical natural frequencies ω_k . Without coupling $G(x) = 0$ such oscillators drift with respect to each other, therefore after some transient their phases become randomly distributed, see Fig. 4(a). This state usually is referred to as *complete incoherence*.

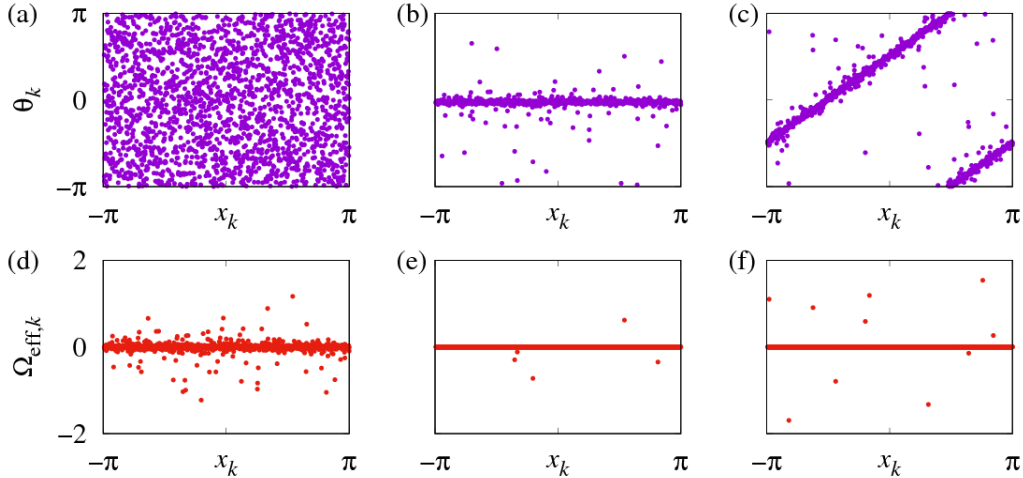


Figure 4: (a) Completely incoherent state and (b), (c) partially coherent twisted states in a system of $N = 16384$ heterogeneous phase oscillators (1.14). (d)–(f) Effective frequencies (1.18) of the states (a)–(c). Parameters: The natural frequencies ω_k are Lorentzian distributed with $\gamma = 0.01$. Figures (a), (d) were obtained for uncoupled oscillators $G(x) = 0$. Figures (b), (c), (e), (f) were obtained for the top-hat coupling (1.15) with $\sigma = 0.5$ and $\alpha = 0$.

When the nonlocal coupling between oscillators is switched on $G(x) \neq 0$, their dynamics often approaches one of partially coherent states [80]: a uniform partially coherent state, Fig. 4(b), or a partially coherent twisted state, Fig. 4(c). At first glance these states look similar to the completely coherent and 1-twisted states shown in Fig. 1(a). However, they have several important differences. Each snapshot in Fig. 4(b), (c) appears as a swarm of points distributed around a central line that is close to an exact completely coherent or 1-twisted state. Moreover, if we look at the corresponding plots of effective frequencies, see Fig. 4(e), (f), then close to any point x we find not only frequency-locked but also drifting oscillators. This fact explains the name ‘partially coherent’ for denoting these states.

Chimera states for heterogeneous phase oscillators. In 2009 Carlo Laing showed [57] that stationary and breathing chimera states persist for slightly heterogeneous phase oscillators.

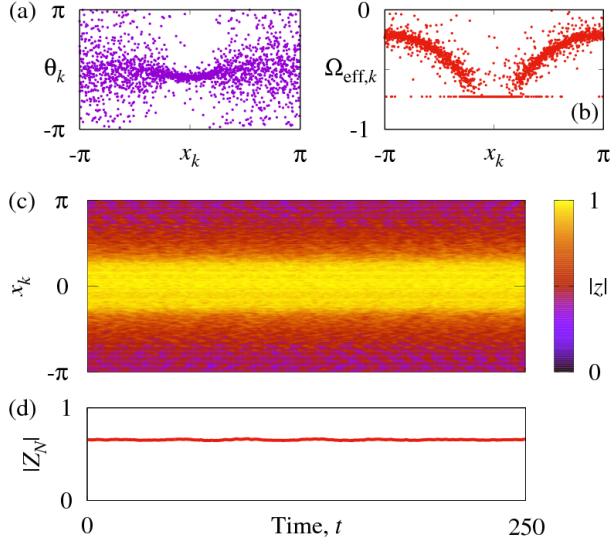


Figure 5: Chimera state in a system of $N = 16384$ heterogeneous phase oscillators (1.14). Parameters: Symmetric trigonometric coupling (1.16) with $A = 0.9$, $B = 0$ and $\alpha = \pi/2 - 0.1$. The natural frequencies ω_k are Lorentzian distributed with $\gamma = 0.01$.

However, in this case, their appearance changes. In particular, if one compares a chimera state for identical oscillators, Fig. 2(a)–(d), with the corresponding chimera state in a heterogeneous oscillator system, Fig. 5, one finds that in the latter case the difference between coherent and incoherent regions becomes blurred. Strictly speaking, in the heterogeneous oscillators case, every chimera state has no clear coherent region. Therefore, to recognize it one needs to distinguish between high coherence and low coherence regions corresponding to large and small values of the modulus of local order parameter $z(x, t)$, see Fig. 5(c).

A more interesting dynamical behaviour can be found if one considers an analog of breathing chimera states in systems of heterogeneous oscillators [86]. The interplay of the nonlocal coupling and the distributed natural frequencies leads to the emergence of pulsing and alternating chimera states, Fig. 6. A *pulsing chimera state* looks most of the time as a spatially modulated partially coherent state, Fig. 6(b). However, at certain moments it transforms into a short-living chimera state, Fig. 6(a), which eventually collapses to the modulated partial coherence again. This transformation process repeats nearly periodically as can be seen from the behaviour of local and global order parameters in Fig. 6(c), (d).

An *alternating chimera state* behaves similarly to pulsing chimera state, but in addition, its high coherence and low coherence regions regularly exchange their positions, Fig. 6(g). Roughly speaking, if one chooses a point in the middle of the high coherence region, then after a certain period of time it will become a center of the low coherence region, see Fig. 6(e), (f). Then,

after the same period of time the point will return in the middle of the high coherence region and so on. This cyclic process motivates the name of this state.

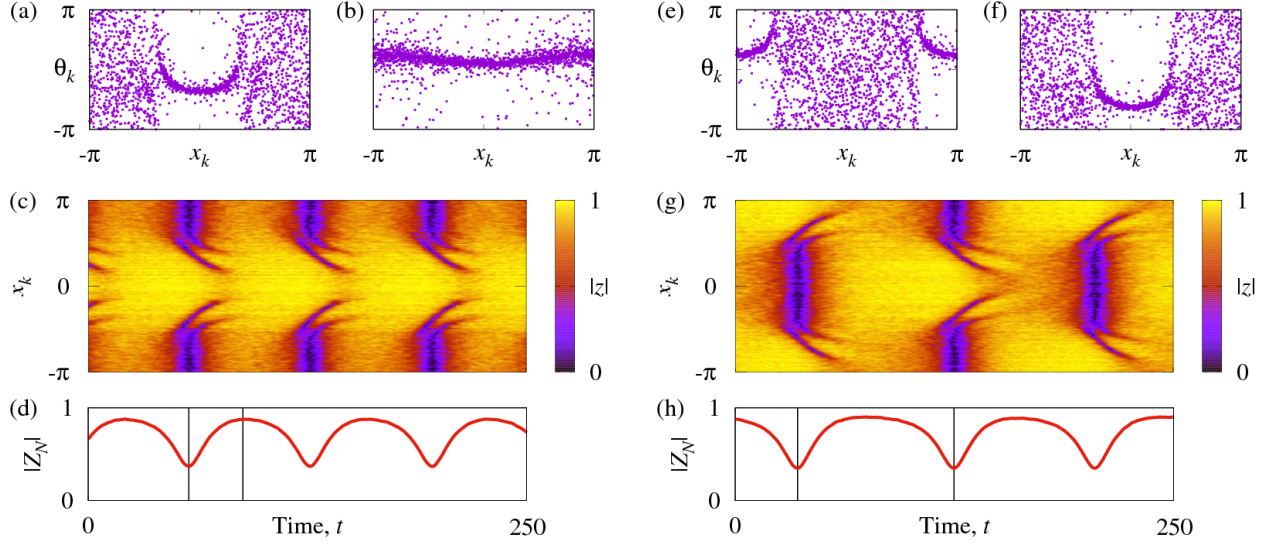


Figure 6: Pulsing and alternating chimera states in a system of $N = 16384$ heterogeneous phase oscillators (1.14). Parameters: Symmetric trigonometric coupling (1.16) with $A = 1.115$ (for pulsing chimera) and $A = 1.135$ (for alternating chimera), $B = 0$ and $\alpha = \pi/2 - 0.15$. The natural frequencies ω_k are Lorentzian distributed with $\gamma = 0.01$.

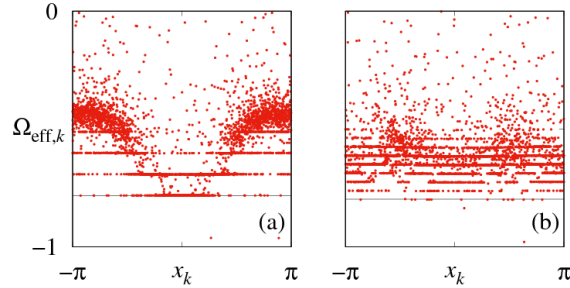


Figure 7: The effective frequencies (1.18) of the pulsing and alternating chimera states in Fig. 6. A thin horizontal line indicates the value of the global order parameter frequency (1.20).

Note that in pulsing or alternating chimera states, frequency-locked oscillators can be found not only in their high coherence regions but also around any position x , see Fig. 7. This is in

contrast to the breathing chimera states for identical phase oscillators, Fig. 3(b).

Travelling chimera states. So far, we have considered chimera states in systems with reflection symmetric coupling, i.e. in the case when the coupling function $G(x)$ satisfies condition $G(-x) = G(x)$. In this case, chimera states usually look like motionless patterns with fixed positions of their coherent and incoherent regions. More precisely, for finite system size N , the positions of the coherent and incoherent regions may show an irregular motion similar to the Brownian motion on the ring. But this motion is a finite size effect, which completely disappears in the large N limit [77]. The situation changes if coupling function $G(x)$ is asymmetric. Then every chimera state starts to drift in a preferred direction corresponding to the asymmetry of $G(x)$. This effect gives rise to travelling chimera states shown in Fig. 8.

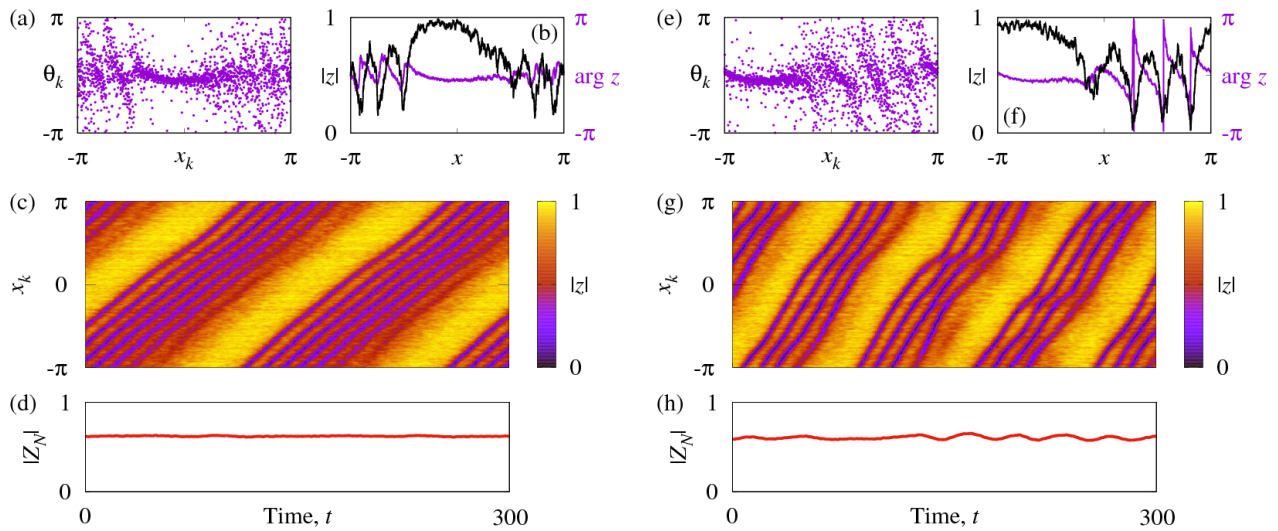


Figure 8: Travelling chimera states in a system of $N = 16384$ heterogeneous phase oscillators (1.14). Parameters: Asymmetric trigonometric coupling (1.16) with $A = 0.9$, $B = 0.09$ (left column) and $B = 0.13$ (right column), and $\alpha = \pi/2 - 0.1$. The natural frequencies ω_k are Lorentzian distributed with $\gamma = 0.01$.

To characterize the motion of a chimera state one needs to be able to determine its instantaneous position. This can be done in the following way. For each time moment t one computes Fourier coefficients

$$a_1(t) = \frac{2}{N} \sum_{k=1}^N |W_k(t)| \cos x_k, \quad b_1(t) = \frac{2}{N} \sum_{k=1}^N |W_k(t)| \sin x_k,$$

where x_k is the k th oscillator position and

$$W_k(t) = \frac{2\pi}{N} \sum_{j=1}^N G\left(\frac{2\pi(k-j)}{N}\right) e^{i\theta_j(t)}, \quad k = 1, \dots, N.$$

If the system size N is large, then all points $(x_k, |W_k(t)|)$ tend to align along a curve with a non-constant leading Fourier mode

$$|W_k(t)| \sim a_1(t) \cos x_k + b_1(t) \sin x_k = \sqrt{a_1^2(t) + b_1^2(t)} \cos(x_k - \xi(t)).$$

The value $\xi(t)$ in the above expression can be identified with the position of the chimera state at time t . Using this approach, one also can compute the mean lateral speed

$$s = \frac{1}{\tau} \int_0^\tau \frac{d\xi}{dt} dt \quad (1.22)$$

averaged over sufficiently large time τ .

A detailed study of travelling chimera states in the system (1.14) with trigonometric coupling (1.16) was carried out in [85]. For fixed $A = 0.9$ and varying asymmetry parameter B , the following results were obtained:

(i) *Pinning* of the chimera's position for small values B : There exists a critical value $B_{\text{cr}} > 0$ depending on N such that chimera state does not move for $B \leq B_{\text{cr}}$, but has a nonzero lateral speed s for $B > B_{\text{cr}}$, see Fig. 9.

(ii) For small values of the asymmetry parameter B , the lateral speed s is a monotonic function of B . In contrast, for $B > 0.08$ the combination of the forward and backward B -sweeps reveals a hysteretic behaviour, which indicates the coexistence of several travelling chimera states for certain ranges of B , see Fig. 9.

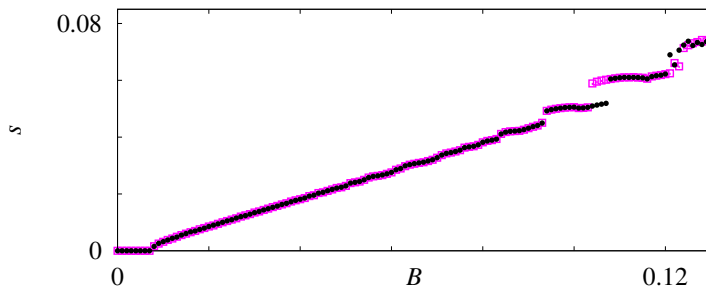


Figure 9: The mean lateral speed of the travelling chimera state in system (1.14) versus the asymmetry parameter B of the coupling function (1.16). Circles and squares denote the values from the forward and backward scans, respectively. All parameters as in Fig. 8.

(iii) For small B the spatial profile of travelling chimera state looks as a slightly deformed profile of the corresponding stationary ($B = 0$) chimera state. In contrast, for large B a new spatial structure appears on top of the stationary chimera state, compare Fig. 5 and Fig. 8. In particular, the tail of the travelling chimera state breaks into a number of alternating high coherence and low coherence regions, Fig. 8(a)–(d). Moreover, the argument of the corresponding local order parameter $z(x, t)$ computed by (1.21) becomes more and more “twisted”, see the snapshots in Fig. 8(b) and (f).

(iv) When the asymmetry parameter B grows above a certain threshold, there appear *modulated travelling chimera states*. Their spatial profiles and hence their instantaneous lateral speeds and global order parameters change nearly periodically in time, Fig. 8(e)–(h).

Remark 1.5 *Note that asymmetric coupling is not necessary for the observation of travelling chimera states. Similar states can be found in systems with symmetric coupling too [136]. In this case, their occurrence is concerned with a spontaneous symmetry breaking.*

Remark 1.6 *Travelling chimera states have been found numerically not only for heterogeneous but also for identical phase oscillators, both with symmetric [136] and asymmetric [7] coupling functions $G(x)$. However, their rigorous mathematical description can be provided for heterogeneous oscillator systems only [83, 85].*

1.5 Extensive chaos in coupled oscillator systems

Regarding their microscopic dynamics, all states observed in system (1.14) can be divided into two main groups. The first group includes states associated with a low-dimensional behaviour of the system such as equilibria, periodic and quasiperiodic orbits and low-dimensional chaotic attractors. For example, all coherent states described in Section 1.4 belong to this group. A complementary group includes more complicated dynamical regimes referred to as extensive chaos. This term is explained in Fig. 10 where we show Lyapunov spectra computed along chimera trajectories in the system (1.14) with a top-hat coupling (1.15). Each spectrum has a number of positive Lyapunov exponents, which is approximately proportional to the system size N . The latter is a characteristic feature of extensive chaos [97]. Apart from chimera states [134, 13], similar Lyapunov spectra were found for completely incoherent and partially coherent states in all-to-all coupled oscillator systems [100]. Moreover, there are no doubts that extensive chaos also underlies the dynamics of all partially coherent states and coherence-incoherence patterns mentioned in Section 1.4.

Note that the chaotic nature of chimera states includes also many other aspects reported in [77, 134, 135]. In particular, for increasing system size the largest Lyapunov exponent tends to zero and hence chimera states can be identified as weakly chaotic attractors. The Lyapunov dimension N_L of this attractor is approximately proportional to the system size N . Moreover,

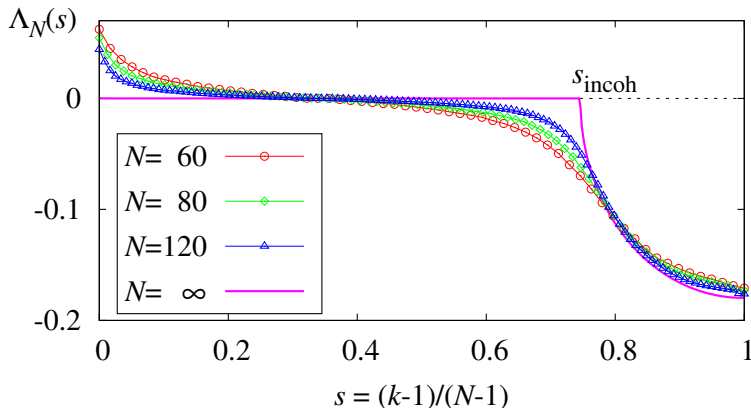


Figure 10: Lyapunov spectra $\Lambda_N(s)$ computed for chimera trajectories in the system (1.14) with identical oscillators ($\omega_k = 0$) and different system sizes $N = 60$ (red circles), $N = 90$ (green diamonds), $N = 120$ (blue triangles). Parameters: $\alpha = 1.5$ and top-hat coupling (1.15) with $\sigma = 0.7$.

from the numerical simulations it follows that there exists a limiting value

$$s_{\text{incoh}} = \lim_{N \rightarrow \infty} \frac{N_L}{N}$$

that coincides with the relative number of incoherent oscillators as $N \rightarrow \infty$. In fact, there are reasons to believe that as $N \rightarrow \infty$ the Lyapunov spectrum $\Lambda_N(s)$ converges to a curve representing a suitably scaled spectral density of real parts $\text{Re}\Sigma(\mathcal{L})$, where $\Sigma(\mathcal{L})$ is the spectrum of the operator \mathcal{L} describing the linear stability of this chimera state in the continuum limit, see Chapter 4 for more detail.

Other remarkable features of the chimera states in system (1.14) are irregular wandering of position [77] and a finite lifetime [135]. These properties play an important role if one considers chimera states in small size systems (1.14) or if one monitors their behaviour on a large time-scale. Fig. 11 illustrates both phenomena in a system (1.14) with $N = 40$ oscillators. Note that the macroscopic shapes of the coherent and incoherent regions do not vary in time, while the chimera state moves erratically as a rigid body. The trajectory of this movement can be determined by the method explained at the end of Section 1.4. Its statistical analysis shows [77] that chimera state wanders as a Brownian particle on the ring. Moreover, the corresponding diffusion coefficient scales inversely with some power of the system size N , so that the movement stops for infinitely large N .

Fig. 11 also shows that small size chimera states can collapse to the completely synchronized state. Typically, the chimera's lifetime τ is extremely sensitive to initial data and behaves as a

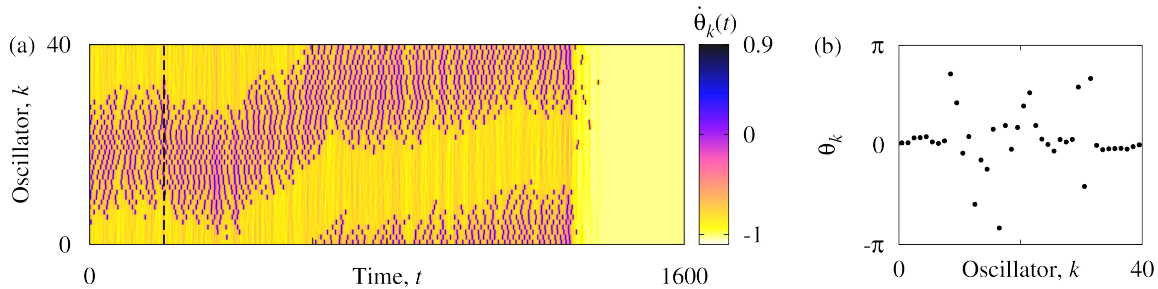


Figure 11: (a) Irregular position wandering and collapse of a chimera state in Eq. (1.14) with identical oscillators ($\omega_k = 0$). (b) Snapshot of the chimera state at $t = 200$. Parameters: $N = 40$, $\alpha = 1.46$, top-hat coupling (1.15) with $\sigma = 0.7$.

random variable with an exponential distribution

$$E(\tau) = \frac{1}{\tau_m} e^{-\tau/\tau_m},$$

where τ_m is the mean lifetime. Numerical simulations reveal [135] an exponential growth of τ_m for increasing system size N such that

$$\log \tau_m \sim N.$$

Thus, for system sizes $N > 60$ it is very unlikely that one observes even a single collapse event within the time span that is amenable to numerical simulation. Nevertheless, it seems more correct to consider the chimera states from Section 1.4 as chaotic transients rather than as chaotic attractors.

Note that the above scenario of the chimera collapse is not universal. For example, a chimera state with two coherent regions can collapse to a chimera state with a single coherent region, as shown in [81, Fig. 2]. On the other hand, there are situations when chimera states become true attractors and do not collapse at all. Such situations can be found in modified versions of system (1.14) when one applies a specific control scheme [115] or when one uses a non-sinusoidal phase interaction function $f(\theta)$, see [119].

2 Continuum limit formalism

For small numbers N , spatially extended oscillator system (1.9) is a low dimensional dynamical system, therefore its behaviour can be analyzed using the qualitative theory of ordinary differential equations. This approach, however, becomes inefficient for large N . Then, one needs to

look for more suitable statistical physics methods. A naive way is to consider system (1.9) as an oscillatory medium with a continuously varying phase $\theta(x, t)$ that evolves according to an integro-differential equation

$$\frac{\partial \theta}{\partial t} = \omega(x) + \int_D G(x, y) f(\theta(x, t) - \theta(y, t)), \quad x \in D,$$

where $\omega(x)$ is an appropriately chosen function. In [51, 102] it was shown that such approach does help to describe all coherent states in a large size system (1.9) consisting of identical oscillators. But it cannot be applied to partially coherent states and coherence-incoherence patterns, because in this case two arbitrarily close oscillators may drift with respect to each other and therefore their dynamics cannot be represented by a continuous function $\theta(x, t)$.

This difficulty can be overcome if one employs statistical description of system (1.9). Then, its state at time t is represented by a distribution $\rho(\theta, \omega, x, t)$ yielding the probability to find an oscillator $\theta_k(t) \approx \theta$ with the natural frequency $\omega_k \approx \omega$ at the position $x_k \approx x$. From Eq. (1.9) it follows, see for example [12] or [20, Appendix B], that in the continuum limit $N \rightarrow \infty$ the probability density ρ evolves according to the integro-differential equation

$$\frac{\partial \rho}{\partial t} + \frac{\partial}{\partial \theta} \left(\rho \left[\omega + \int_D dx' \int_{-\infty}^{\infty} d\omega' \int_0^{2\pi} G(x, x') f(\theta - \theta') \rho(\theta', \omega', x', t) d\theta' \right] \right) = 0. \quad (2.1)$$

This equation is universal in the sense that it describes not only coherent states but also partially coherent states, coherence-incoherence patterns and other types of dynamics in system (1.9). However, the analysis of Eq. (2.1) usually is extremely complicated, because one needs to consider its measure-valued solutions ρ . A particular case of Eq. (2.1) allowing to avoid this complication is explained in the next section.

2.1 Ott-Antonsen manifold

The standard way of constructing solutions to Eq. (2.1) is based on their representation as a Fourier series

$$\rho(\theta, \omega, x, t) = \frac{h(\omega)}{2\pi} \left(1 + \sum_{n=1}^{\infty} \left[\bar{u}_n(\omega, x, t) e^{in\theta} + u_n(\omega, x, t) e^{-in\theta} \right] \right), \quad (2.2)$$

where $u_n : \mathbb{R} \times D \times \mathbb{R} \rightarrow \mathbb{C}$ is the n -th Fourier coefficient, \bar{u}_n denotes the complex conjugate of u_n , and where one factorizes explicitly the time-independent term $h(\omega)$.

Inserting (2.2) into Eq. (2.1) and expanding the resulting equation in a Fourier series with respect to θ , one obtains an infinite chain of coupled integro-differential equations for the Fourier coefficients

$$u_n(\omega, x, t) = \int_0^{2\pi} \frac{\rho(\theta, \omega, x, t)}{h(\omega)} e^{in\theta} d\theta. \quad (2.3)$$

The infinite-dimensional system for $\{u_n\}$ is extremely complicated and so far has been considered in the case of global coupling [17, 20, 21, 24, 116] or several globally coupled populations [59] only. However, for a specific choice of the phase coupling function f , its analysis can be significantly simplified via the invariant manifold reduction discovered by Ott and Antonsen in [88, 89]. Roughly speaking, their observation can be formulated as follows. In the case $f(\psi) = -\sin(\psi + \alpha)$, almost all solutions ρ of Eq. (2.1) converge asymptotically in time to the manifold consisting of all distributions ρ given by the formula (2.2) with $u_n(\omega, x, t) = u^n(\omega, x, t)$ and $|u(\omega, x, t)| \leq 1$. The next proposition shows that this manifold, called usually *Ott-Antonsen manifold*, is invariant with respect to Eq. (2.1).

Proposition 2.1 *Let*

$$f(\psi) = -\sin(\psi + \alpha), \quad \alpha \in \mathbb{R}.$$

Suppose that $u : \mathbb{R} \times D \times \mathbb{R} \rightarrow \mathbb{C}$ is a solution to the equation

$$\frac{du}{dt} = i\omega u(\omega, x, t) + \frac{1}{2}e^{-i\alpha}\mathcal{F}u - \frac{1}{2}e^{i\alpha}u^2(\omega, x, t)\mathcal{F}\bar{u}, \quad (2.4)$$

where

$$(\mathcal{F}u)(x, t) := \int_{-\infty}^{\infty} d\omega' \int_D h(\omega')G(x, x')u(\omega', x', t)dx'. \quad (2.5)$$

Moreover, suppose that $|u(\omega, x, t)| \leq 1$.

Then, formula (2.2) with $u_n(\omega, x, t) = u^n(\omega, x, t)$ yields a solution to equation (2.1).

The benefits provided by Proposition 2.1 can be described as follows. If one is not interested in the transient dynamics of Eq. (2.1) and looks for established dynamical regimes only, then Eq. (2.1) can be replaced with Eq. (2.4). Although Eq. (2.4) is still an infinite-dimensional integro-differential equation, its phase space is spanned by the single function u instead of an infinite sequence $\{u_n\}$. Its analysis is therefore much simpler than the analysis of the initial equation (2.1). Moreover, the function u parameterizing Ott-Antonsen manifold turns out to have a simple interpretation for the corresponding coupled oscillator system

$$\frac{d\theta_k}{dt} = \omega_k - \frac{|D|}{N} \sum_{j=1}^N G(x_k, x_j) \sin(\theta_k(t) - \theta_j(t) + \alpha), \quad k = 1, \dots, N. \quad (2.6)$$

Recall that for a large system (2.6) the conditional probability density $\rho(\theta, \omega, x, t)/h(\omega)$ yields, by definition, the distribution of phases $\theta_k(t)$ for oscillators with $\omega_k \approx \omega$ and $x_k \approx x$. On the other hand, if $u_n(\omega, x, t) = u^n(\omega, x, t)$ and $|u(\omega, x, t)| < 1$ the summation in (2.2) can be carried out explicitly and we obtain

$$\rho(\theta, \omega, x, t) = h(\omega)P_u(\theta), \quad \text{where} \quad P_u(\theta) := \frac{1}{2\pi} \frac{1 - |u|^2}{1 - 2|u| \cos(\theta - \arg u) + |u|^2} \quad (2.7)$$

is a Poisson distribution (see Fig. 12).

For $|u(\omega, x, t)| = 0$ formula (2.7) yields a uniform distribution

$$\frac{\rho(\theta, \omega, x, t)}{h(\omega)} = \frac{1}{2\pi}$$

corresponding to the *complete incoherence* of phases $\theta_k(t)$. For an intermediate value $0 < |u| < 1$ distribution $P_u(\theta)$ has a bell shaped profile centered at $\theta = \arg u$, and $|u|$ characterizes the distribution width. This means the oscillators $\theta_k(t)$ with $\omega_k \approx \omega$ and $x_k \approx x$ are drifting with respect to each other although their phases are more likely to be found at the value $\theta_k(t) = \arg u$. Such local behaviour in the following will be referred to as *incoherence*. Finally, considering the distribution $P_u(\theta)$ in the limit $|u(\omega, x, t)| \rightarrow 1$ we find that it degenerates into a delta function,

$$P_u(\theta) = \delta(\theta - \arg u),$$

representing a phase-locked state $\theta_k(t) = \arg u$ for the oscillators with $\omega_k \approx \omega$ and $x_k \approx x$. Therefore identity $|u(\omega, x, t)| = 1$ implies *coherence* at the point (ω, x) .

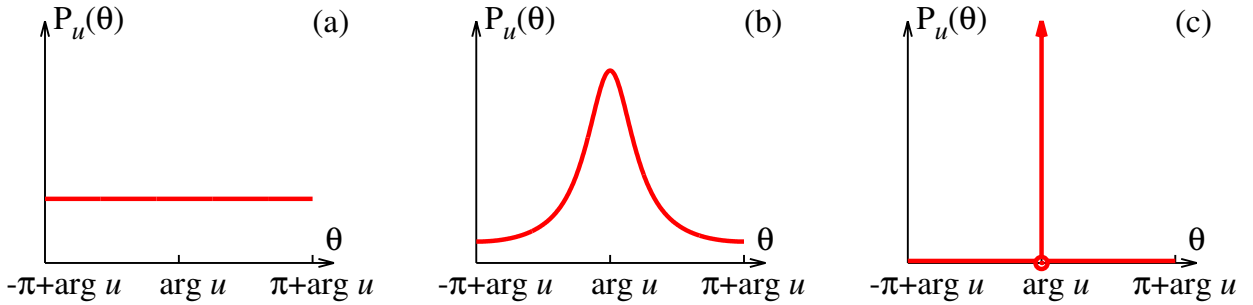


Figure 12: The Poisson distribution $P_u(\theta)$ for (a) $|u| = 0$, (b) $0 < |u| < 1$ and (c) $|u| = 1$.

2.2 Dynamics in the Ott-Antonsen manifold

In this section we consider Eq. (2.4) describing the dynamics in the Ott-Antonsen manifold. We reveal its symmetries and invariant sets, and give an overview of its typical solutions. We also derive continuum limit analogs of the formulas for global order parameter, local order parameter and effective frequencies.

1. The definition of the Ott-Antonsen manifold requires $|u(\omega, x, t)| \leq 1$. Otherwise the series (2.2) with $u_n(\omega, x, t) = u^n(\omega, x, t)$ does not converge even in the sense of weak convergence of measures. This motivates us to define the set of *admissible solutions* of Eq. (2.4)

$$V = \{v(\omega, x) : |v(\omega, x)| \leq 1 \text{ for all } (\omega, x) \in \mathbb{R} \times D\}.$$

It turns out, see [79, Lemma 2], that the set of admissible solutions V is flow-invariant with respect to Eq. (2.4). In other words, if at the instant $t = 0$ one has $u(\cdot, 0) \in V$ then $u(\cdot, t) \in V$ for all $t > 0$.

Similarly, if for a given admissible solution $u(\omega, x, t)$ of Eq. (2.4) we define its *coherent region*

$$S_{\text{coh}}(u, t) = \{(\omega, x) \in \mathbb{R} \times D : |u(\omega, x, t)| = 1\}$$

and its *incoherent region*

$$S_{\text{incoh}}(u, t) = \{(\omega, x) \in \mathbb{R} \times D : |u(\omega, x, t)| < 1\},$$

then they are also flow-invariant, i.e.

$$S_{\text{coh}}(u, t) = S_{\text{coh}}(u, 0) \quad \text{and} \quad S_{\text{incoh}}(u, t) = S_{\text{incoh}}(u, 0) \quad \text{for all } t > 0.$$

This implies that coherent phase oscillators never can become incoherent phase oscillators and vice versa.

2. Since the integral operator \mathcal{F} is linear, see (2.5), equation (2.4) always has a trivial solution $u(\omega, x, t) = 0$ corresponding to the completely incoherent state.

3. Eq. (2.4) has a complex phase shift symmetry: The set of its solutions is invariant with respect to the transformation

$$u(\omega, x, t) \mapsto u(\omega, x, t)e^{i\phi} \quad \text{for } \phi \in \mathbb{R}.$$

Because of this symmetry typical nontrivial solutions of Eq. (2.4) are *relative equilibria*

$$u(\omega, x, t) = a(\omega, x)e^{i\Omega t} \quad \text{where } \Omega \in \mathbb{R} \quad \text{and } a(\omega, x) \text{ is independent of } t, \quad (2.8)$$

and *relative periodic orbits*

$$u(\omega, x, t) = a(\omega, x, t)e^{i\Omega t} \quad \text{where } \Omega \in \mathbb{R} \quad \text{and } a(\omega, x, t) \text{ is a periodic function of } t. \quad (2.9)$$

The word 'relative' refers here to the fact that every solution (2.8) becomes an equilibrium and every solution (2.9) becomes a periodic orbit in an appropriate corotating frame only.

4. In some cases, for example when the kernel $G(x, y)$ in (2.5) is a function of the difference $x - y$ only and the domain D is periodic (e.g. a ring or a flat torus), Eq. (2.4) has also a translation symmetry: The set of its solutions is invariant with respect to the spatial translations

$$u(\omega, x, t) \mapsto u(\omega, x + c, t) \quad \text{for } c \in \mathbb{R}^n \quad \text{where } n \text{ is the dimension of } x.$$

Then along with relative equilibria (2.8) and relative periodic orbits (2.9) typical solutions of Eq. (2.4) include also *travelling solutions*

$$u(\omega, x, t) = a(\omega, x - st)e^{i\Omega t} \quad (2.10)$$

where $\Omega \in \mathbb{R}$, $s \in \mathbb{R}^n$ and $a(\omega, x)$ is a periodic function of x , as well as *modulated travelling solutions*

$$u(\omega, x, t) = a(\omega, x - st, t)e^{i\Omega t} \quad (2.11)$$

where $\Omega \in \mathbb{R}$, $s \in \mathbb{R}^n$ and $a(\omega, x, t)$ is a periodic function of x and t .

5. Every solution $u(\omega, x, t)$ of Eq. (2.4) can be associated with some established dynamics in the corresponding oscillator system (2.6). This fact can be used to compute continuum limit analogs of the effective frequencies, global order parameter and local order parameter defined in Section 1.4.

For a system (2.6) global order parameter $Z_N(t)$ is defined by averaging the complex exponent $e^{i\theta_k(t)}$ over all oscillator indices k , see (1.19). In the continuum limit this average reads

$$Z(t) = \frac{1}{|D|} \int_D dx \int_{-\infty}^{\infty} d\omega \int_0^{2\pi} \rho(\theta, \omega, x, t) e^{i\theta} d\theta = \frac{1}{|D|} \int_D dx \int_{-\infty}^{\infty} h(\omega) u(\omega, x, t) d\omega, \quad (2.12)$$

where we took into account that due to (2.3) it holds

$$u(\omega, x, t) = \int_0^{2\pi} \frac{\rho(\theta, \omega, x, t)}{h(\omega)} e^{i\theta} d\theta. \quad (2.13)$$

The local order parameter $z_{N,\varepsilon}(x, t)$ is defined as the average of $e^{i\theta_k(t)}$ over all oscillators with $x_k \approx x$ only, see (1.21). Therefore the continuum limit analog of $z_{N,\varepsilon}(x, t)$ is obtained by canceling the spatial averaging in (2.12) what yields

$$z(x, t) = \int_{-\infty}^{\infty} h(\omega) u(\omega, x, t) d\omega. \quad (2.14)$$

For computing the effective frequencies $\Omega_{\text{eff},k}$ it is convenient to rewrite Eq. (2.6) in the form

$$\frac{d\theta_k}{dt} = \omega_k - \text{Im} \left(e^{i\alpha} \overline{W}_k(t) e^{i\theta_k(t)} \right) \quad \text{where} \quad W_k(t) = \frac{|D|}{N} \sum_{j=1}^N G(x_k, x_j) e^{i\theta_j(t)}.$$

Since for infinitely large N points x_k densely fill the domain D , we assume that there exists a function $W(x, t)$ such that $W_k(t) = W(x_k, t)$. Then $\Omega_{\text{eff},k}$ equals the time average of the expression $\omega_k - \text{Im} \left(e^{i\alpha} \overline{W}(x_k, t) e^{i\theta_k(t)} \right)$. Obviously, the definition of $W_k(t)$ and formulas (2.5) and (2.13) imply $W(x, t) = (\mathcal{F}u)(x, t)$. On the other hand, if system (2.6) is ergodic, then the time average of $e^{i\theta_k(t)}$ can be replaced with the distribution average (2.13). Thus we conclude $\Omega_{\text{eff},k} = \Omega_{\text{eff}}(\omega_k, x_k)$ where

$$\Omega_{\text{eff}}(\omega, x) = \omega - \text{Im} \left(e^{i\alpha} \lim_{\tau \rightarrow \infty} \frac{1}{\tau} \int_0^\tau u(\omega, x, t) (\mathcal{F}\overline{u})(x, t) dt \right). \quad (2.15)$$

2.3 Ott-Antonsen equations for spatially extended oscillatory systems

Let us consider two specific cases of system (2.6):

(i) the case of identical oscillators $\omega_k = 0$,

(ii) and the case of heterogeneous oscillators with the natural frequencies ω_k chosen randomly and independently from a Lorentzian distribution (1.17) with width $\gamma > 0$.

For each of these cases we write a simplified version of Eq. (2.4) relevant to the dynamics in the Ott-Antonsen manifold. We start with the case of Lorentzian distributed ω_k and use a special mathematical trick suggested by Ott and Antonsen in [88] to simplify the integral operator (2.5). Suppose that solution $u(\omega, x, t)$ of Eq. (2.4) has an analytic extension in the complex half-plane $\text{Im } \omega \geq 0$, then using the residue theorem we can compute explicitly the integral in the definition of local order parameter (2.14)

$$z(x, t) = \int_{-\infty}^{\infty} h(\omega)u(\omega, x, t)d\omega = \int_{-\infty}^{\infty} \frac{\gamma}{\pi} \frac{u(\omega, x, t)d\omega}{\omega^2 + \gamma^2} = u(i\gamma, x, t). \quad (2.16)$$

This fact allows us to restrict Eq. (2.4) to a single point $\omega = i\gamma$. Indeed, using (2.16) we obtain a closed integro-differential equation

$$\frac{\partial z}{\partial t} = -\gamma z + \frac{1}{2}e^{-i\alpha}\mathcal{G}z - \frac{1}{2}e^{i\alpha}z^2\mathcal{G}\bar{z} \quad (2.17)$$

where the integral operator \mathcal{G} is defined by

$$(\mathcal{G}z)(x, t) = \int_D G(x, y)z(y, t)dy. \quad (2.18)$$

In the following we call Eq. (2.17) *the Ott-Antonsen equation for heterogeneous oscillators*.

Remark 2.2 *Note that in the original paper of Ott and Antonsen [88] they considered a complex conjugate version of Eq. (2.4). Its solution $\bar{u}(\omega, x, t)$ has an analytic extension in the lower (not upper!) complex half-plane $\text{Im } \omega \leq 0$. Therefore applying the residue theorem, instead of identity (2.16) one obtains*

$$\bar{z}(x, t) = \int_{-\infty}^{\infty} \frac{\gamma}{\pi} \frac{\bar{u}(\omega, x, t)d\omega}{\omega^2 + \gamma^2} = \bar{u}(-i\gamma, x, t).$$

Then restricting the complex conjugate of Eq. (2.4) to a single point $\omega = -i\gamma$ one obtains the complex conjugate of Eq. (2.17). Such derivation of Eq. (2.17) can be found, for example, in [57].

The *Ott-Antonsen equation for identical oscillators* can be obtained from Eq. (2.17) in the limit of vanishing Lorentzian width $\gamma \rightarrow 0$. This yields

$$\frac{\partial z}{\partial t} = \frac{1}{2}e^{-i\alpha}\mathcal{G}z - \frac{1}{2}e^{i\alpha}z^2\mathcal{G}\bar{z}. \quad (2.19)$$

The phase interaction function in (2.6) is sinusoidal, therefore due to Proposition 2.1 we may expect that all dynamical regimes observed in this coupled oscillator system can be described by Eq. (2.17) for heterogeneous oscillators and by Eq. (2.19) for identical oscillators. This is indeed the case. For example, Table 1 shows how different coherent and partially coherent states as well as stationary and nonstationary coherence-incoherence patterns described in Section 1.4 can be represented by specific solutions of Eqs. (2.17) and (2.19) in the case of one-dimensional domain D . Moreover, the same relation usually holds for Eqs. (2.17) and (2.19) and the corresponding systems (2.6) where D is a two-, three- or hyper-dimensional domain.

Importantly, for the observation of twisted states and moving coherence-incoherence patterns Eqs. (2.17) and (2.19) have to be translationally symmetric, in other words the coupling function $G(x, y)$ has to depend on the difference of x and y only and the domain D has to be periodic (e.g. a ring or a flat torus). In contrast, all other patterns and states listed in Table 1 in general can be found for any coupling function $G(x, y)$.

The main advantage of Eqs. (2.17) and (2.19) is concerned with the fact that they provide a mathematical framework for rigorous theoretical analysis of partially coherent states and coherence-incoherence patterns, which otherwise can be studied only numerically. Indeed, in a coupled oscillator system (2.6) these patterns and states appear as complex chaotic trajectories, whereas in Eqs. (2.17) and (2.19) they correspond to relative equilibria, relative periodic orbits or other explicit solutions. This simplifies significantly their analysis and makes possible the prediction of their properties.

For example, let $z = z(x, t)$ be a solution of Eq. (2.17) or Eq. (2.19), then the solution itself describes approximately the dynamics of the local order parameter $z_{N,\varepsilon}(x, t)$, see (1.21), in the corresponding finite size system (2.6). Using formula (2.12) we also find that

$$Z(t) = \frac{1}{|D|} \int_D z(x, t) dx \quad (2.20)$$

yields an approximate value of the global order parameter $Z_N(t)$, see (1.19). Moreover, if all oscillators in (2.6) are identical and hence $z(x, t)$ is a solution of Eq. (2.19), then using (2.15) we can compute the approximate values of the effective frequencies $\Omega_{\text{eff},k} = \Omega_{\text{eff}}(x_k)$, where

$$\Omega_{\text{eff}}(x) = -\text{Im} \left(e^{i\alpha} \lim_{\tau \rightarrow \infty} \frac{1}{\tau} \int_0^\tau z(x, t)(\mathcal{G}\bar{z})(x, t) dt \right). \quad (2.21)$$

Other results concerned with the long-term dynamics of system (2.6) will be obtained using Eqs. (2.17) and (2.19) in the next sections of this work.

Coherent states	
Complete coherence	$z = e^{i\Omega t}$
Twisted states	$z = e^{i(qx + \Omega t)}$
Coherent states, in general	$z = e^{i\varphi(x,t)}$
Incoherent and partially coherent states	
Complete incoherence	$z = 0$
Uniform partial coherence	$z = ae^{i\Omega t}$ with $0 < a < 1$
Partially coherent twisted states	$z = ae^{i(qx + \Omega t)}$ with $0 < a < 1$
Coherence-incoherence patterns (CIPs)	
Stationary CIPs, incl. chimera states	$z = a(x)e^{i\Omega t}$ with $0 \leq a(x) \leq 1$
Nonstationary CIPs, incl. breathing, pulsing and alternating chimera states	$z = a(x,t)e^{i\Omega t}$ with $0 \leq a(x,t) \leq 1$
Moving coherence-incoherence patterns	
Travelling chimera states	$z = a(x - st)e^{i\Omega t}$ with $0 \leq a(x) \leq 1$
Modulated travelling chimera states	$z = a(x - st, t)e^{i\Omega t}$ with $0 \leq a(x, t) \leq 1$

Table 1: Different types of solutions of the Ott-Antonsen equations (2.19) and (2.17).

Remark 2.3 Let $z = z_0(x, t)$ be a solution of Eq. (2.19) for $\alpha = \alpha_0$, then the complex conjugate of Eq. (2.19) reads

$$\frac{\partial \bar{z}_0}{\partial t} = \frac{1}{2} e^{i\alpha_0} \mathcal{G} \bar{z}_0 - \frac{1}{2} e^{-i\alpha_0} \bar{z}_0^2 \mathcal{G} z_0.$$

This means $z = \bar{z}_0(x, t)$ is a solution of Eq. (2.19) for $\alpha = -\alpha_0$. If we denote by $\Omega_{\text{eff}}^{(1)}(x)$ and $\Omega_{\text{eff}}^{(2)}(x)$ the effective frequency profiles corresponding to the solutions $z = z_0(x, t)$ and $z = \bar{z}_0(x, t)$, then from (2.21) we obtain $\Omega_{\text{eff}}^{(2)}(x) = -\Omega_{\text{eff}}^{(1)}(x)$.

Thus we conclude that every solution of Eq. (2.19) has its conjugate counterpart. Moreover, the effective frequency profiles of the conjugated solutions are mirror images of each other with respect to the axis $\Omega_{\text{eff}} = 0$.

Remark 2.4 Ott-Antonsen equation (2.17) looks similar to the well-known complex Ginzburg-Landau equation (CGLE)

$$\frac{\partial z}{\partial t} = z + (1 + ic_1) \Delta z - (1 + ic_2) |z|^2 z.$$

In particular, they both have the same cubic nonlinearities and the same complex phase shift and translation symmetries. However, in contrast to CGLE, Ott-Antonsen equation does not contain any spatial derivatives, therefore its solutions, in general, should not be smooth. Moreover, while the coefficients c_1 and c_2 in CGLE do not depend on each other, the coefficients at $\mathcal{G}z$ and $z^2 \mathcal{G} \bar{z}$ in Eq. (2.17) are complex conjugate. This property ensures the existence of the trapping region $|z| \leq 1$ for solutions of Eq. (2.19), as was explained in Section 2.2.

3 Completely incoherent state

The completely incoherent state

$$z(x, t) = 0$$

always satisfies Eq. (2.19). However, for different system parameters it can be stable or unstable solution. In order to check its stability we linearize Eq. (2.19) around zero. Thus we obtain a linear integro-differential equation

$$\frac{\partial v}{\partial t} = \frac{1}{2} e^{-i\alpha} \mathcal{G} v, \tag{3.1}$$

which describes evolution of small perturbations $v(x, t)$. The stability of incoherent state is determined by the spectrum of the integral operator on the right-hand side of Eq. (3.1). To compute this spectrum we insert ansatz

$$v(x, t) = v_1(x) e^{\lambda t} + \bar{v}_2(x) e^{\bar{\lambda} t}$$

into Eq. (3.1) and equate separately the terms at $e^{\lambda t}$ and the terms at $e^{\bar{\lambda}t}$. This yields a system of two uncoupled equations

$$\lambda v_1 = \frac{1}{2}e^{-i\alpha}\mathcal{G}v_1, \quad \lambda v_2 = \frac{1}{2}e^{i\alpha}\mathcal{G}v_2. \quad (3.2)$$

Obviously, if some pair $(\lambda, v_1(x)) = (\lambda_*, v_*(x))$ satisfies the former equation then the pair $(\lambda, v_2(x)) = (\bar{\lambda}_*, \bar{v}_*(x))$ satisfies the latter equation and vice versa. Therefore the spectrum determined by the whole system (3.2) comprises all eigenvalues of the operator $\frac{1}{2}e^{-i\alpha}\mathcal{G}$ as well as their complex conjugates. Using this fact we can formulate the following stability criterion.

Proposition 3.1 *Let $\text{Re}(e^{-i\alpha}\lambda) \leq 0$ for all $\lambda \in \text{spec } \mathcal{G}$, then the incoherent state $z(x, t) = 0$ is neutrally stable. Conversely, if $\text{Re}(e^{-i\alpha}\lambda) > 0$ at least for one value $\lambda \in \text{spec } \mathcal{G}$, then the incoherent state is unstable.*

4 Relative equilibria of the Ott-Antonsen equation

In this chapter we consider relative equilibria of Eq. (2.19). These are its solutions of the form

$$z = a(x)e^{i\Omega t}, \quad (4.1)$$

where $a(x)$ is a complex function satisfying $|a(x)| \leq 1$ and Ω is a real number. In the case of constant $|a(x)|$ such solutions represent coherent (if $|a(x)| = 1$) and partially coherent (if $0 < |a(x)| < 1$) states. Otherwise they describe stationary coherence-incoherence patterns.

This chapter is organized as follows. In Section 4.1 we consider a complex Riccati equation related to Eq. (2.19). We calculate its fixed points and analyze their stability. Using these results, in Section 4.2 we show that the amplitude $a(x)$ and the frequency Ω of every admissible stable relative equilibrium (4.1) satisfy a self-consistency equation

$$\mu w = \mathcal{G}(H(|w|^2)w), \quad (4.2)$$

where

$$\mu = i\Omega e^{i\alpha}, \quad w(x) = -\frac{i}{\Omega}e^{-i\alpha}\mathcal{G}a(x),$$

and

$$H(|w|^2) = \begin{cases} \frac{1 - i\sqrt{|w|^2 - 1}}{|w|^2} & \text{for } |w| \geq 1, \\ \frac{1 - \sqrt{1 - |w|^2}}{|w|^2} & \text{for } |w| < 1 \end{cases} \quad (4.3)$$

is a universal function independent of any parameters. Conversely, we obtain that every solution $(\mu_*, w_*(x))$ of Eq. (4.2) determines two admissible relative equilibria of Eq. (2.19) for two

If $(\mu_*, w_*(x))$ satisfies Eq. (4.2), then $z = a(x)e^{i\Omega t}$ is a solution of Eq. (2.19) for $\alpha = \alpha_*$

$a(x) = H(w_*(x) ^2)w_*(x)$	$a(x) = \overline{H(w_*(x) ^2)w_*(x)}$
$\Omega = - \mu_* $	$\Omega = \mu_* $
$e^{i\alpha_*} = i\frac{\mu_*}{ \mu_* }$ or $\alpha_* = \frac{\pi}{2} + \arg \mu_*$	$e^{i\alpha_*} = -i\frac{\bar{\mu}_*}{ \mu_* }$ or $\alpha_* = -\frac{\pi}{2} - \arg \mu_*$

Table 2: The correspondence between the solutions $(\mu_*, w_*(x))$ of problem (4.2) and the relative equilibria (4.1) of the Ott-Antonsen equation (2.19).

specific values of phase lag α , see Table 2. However, these equilibria are not necessarily stable. It follows from the above observations that all admissible stable relative equilibria of Eq. (2.19) can be found if one solves Eq. (4.2) and carry out the stability analysis of the corresponding solutions in Table 2.

A method for solving Eq. (4.2) numerically is suggested in Section 4.3, while the stability issue is clarified in Section 4.4. There we study a linear operator concerned with the linearization of Eq. (2.19) around the relative equilibrium in the left column of Table 2 (the relative equilibrium in the right column can be analyzed similarly). We show that the essential spectrum of this operator reads

$$\Sigma_{\text{ess}} = \{|\mu_*|\eta(|w_*(x)|^2) : x \in D\} \cup \{|\mu_*|\eta(|w_*(x)|^2) : x \in D\} \quad (4.4)$$

where

$$\eta(|w|^2) = \begin{cases} -\sqrt{|w|^2 - 1} & \text{for } |w| \geq 1, \\ i\sqrt{1 - |w|^2} & \text{for } |w| < 1. \end{cases} \quad (4.5)$$

For the discrete spectrum Σ_{disc} of the operator we derive a nonlocal eigenvalue problem

$$\begin{pmatrix} v_1 \\ v_2 \end{pmatrix} = \frac{i}{2|\mu_*|} \begin{pmatrix} -\frac{\bar{\mu}_*}{\lambda - |\mu_*|\eta(|w_*|^2)} & -\frac{\mu_* H^2(|w_*|^2)w_*^2}{\lambda - |\mu_*|\eta(|w_*|^2)} \\ \frac{\mu_* H^2(|w_*|^2)w_*^2}{\lambda - |\mu_*|\eta(|w_*|^2)} & \frac{\mu_*}{\lambda - |\mu_*|\eta(|w_*|^2)} \end{pmatrix} \begin{pmatrix} \mathcal{G}v_1 \\ \mathcal{G}v_2 \end{pmatrix} \quad (4.6)$$

such that for every $\lambda \in \Sigma_{\text{disc}}$ there exists a bounded nontrivial solution $(v_1(x), v_2(x))$ of Eq (4.6).

A relative equilibrium (4.1) is unstable if the corresponding spectrum $\Sigma_{\text{ess}} \cup \Sigma_{\text{disc}}$ has a nonempty intersection with the right half-plane $\text{Re } \lambda > 0$. In the opposite case we call it

neutrally stable. Formula (4.4) ensures that the essential spectrum Σ_{ess} is always neutrally stable and lies on the imaginary axis and on the stable part of the real axis, therefore all instabilities of a relative equilibrium (4.1) can be concerned with the discrete spectrum Σ_{disc} only. The latter spectrum is symmetric with respect to the real axis and comprises at most a finite number of isolated eigenvalues, which can be computed approximately using a method described in Section 4.5.

4.1 Riccati equation with constant coefficients

Let $\mathbb{D} = \{v \in \mathbb{C} : |v| < 1\}$ denote the open unit disc of the complex plane and $\overline{\mathbb{D}} = \mathbb{D} \cup \partial\mathbb{D}$ be its closure. In this section we consider a complex Riccati equation of the form

$$\frac{du}{dt} = W - isu(t) - \overline{W}u^2(t) \quad (4.7)$$

where s is a real coefficient and W is a complex coefficient, and search for all its stable fixed points in the disc $\overline{\mathbb{D}}$.

Proposition 4.1 *For every nonzero $s \in \mathbb{R}$ and every nonzero $W \in \mathbb{C}$, Eq. (4.7) has a unique (neutrally) stable fixed point in the unit disc $\overline{\mathbb{D}}$, which is given by the formula*

$$u = H_s(|W|^2)W, \quad (4.8)$$

where

$$H_s(|W|^2) = \begin{cases} \frac{-is + \sqrt{4|W|^2 - s^2}}{2|W|^2} & \text{for } 4|W|^2 - s^2 \geq 0, \\ \frac{-is + i \operatorname{sgn}(s)\sqrt{s^2 - 4|W|^2}}{2|W|^2} & \text{for } 4|W|^2 - s^2 < 0. \end{cases}$$

Proof: Fixed points of Eq. (4.7) are roots of the equation

$$\overline{W}u^2 + isu - W = 0.$$

For $W \neq 0$ this quadratic equation can be solved explicitly. Thus, for $4|W|^2 - s^2 > 0$ we obtain two roots

$$u_{\pm} = \frac{-is \pm \sqrt{4|W|^2 - s^2}}{2\overline{W}} = \frac{-is \pm \sqrt{4|W|^2 - s^2}}{2|W|^2}W, \quad (4.9)$$

while for $4|W|^2 - s^2 < 0$ we obtain two roots

$$u_{\pm} = \frac{-is \pm i\sqrt{s^2 - 4|W|^2}}{2\overline{W}} = \frac{-is \pm i\sqrt{s^2 - 4|W|^2}}{2|W|^2}W. \quad (4.10)$$

Simple calculations show that in the former case the identity $|u_+| = |u_-| = 1$ holds, whereas in the latter case we have $|u_+| < 1 < |u_-|$ if $s > 0$, or $|u_-| < 1 < |u_+|$ if $s < 0$.

To analyze the stability of a fixed point u_* of Eq. (4.7) one needs to consider the corresponding linearized equation

$$\frac{dv}{dt} = -(is + 2\overline{W}u_*)v(t),$$

which describes evolution of small perturbations $v(t)$. If $\text{Re}(is + 2\overline{W}u_*) > 0$, then all perturbations decay in time and hence u_* is a stable fixed point. In contrast, if $\text{Re}(is + 2\overline{W}u_*) < 0$, then the modulus $|v(t)|$ grows exponentially and therefore u_* is an unstable fixed point. The case $\text{Re}(is + 2\overline{W}u_*) = 0$ will be referred to as the neutrally stable case.

Using formula (4.9) we calculate $\text{Re}(is + 2\overline{W}u_{\pm}) = \pm\sqrt{4|W|^2 - s^2}$, therefore for $4|W|^2 - s^2 > 0$ the root u_+ is stable while the other root u_- is unstable. On the other hand, using formula (4.10) we obtain $\text{Re}(is + 2\overline{W}u_{\pm}) = 0$, therefore for $4|W|^2 - s^2 < 0$ the both roots u_+ and u_- are neutrally stable.

Summarizing the above results we see that among two fixed points of Eq. (4.7) only one is (neutrally) stable and simultaneously satisfies the inequality $|u| \leq 1$. This fixed point is given by formula (4.8). Importantly, for $4|W|^2 - s^2 = 0$ both expressions (4.9) and (4.10) coincide and yield $u_+ = u_-$, therefore in this case Eq. (4.7) has a single degenerate fixed point, which obviously is neutrally stable. ■

4.2 Self-consistency equation

Using a substitution

$$z(x, t) = u(x, t)e^{i\Omega t}$$

we write Eq. (2.19) in the form

$$\frac{\partial u}{\partial t} = \frac{1}{2}e^{-i\alpha}\mathcal{G}u - i\Omega u - \frac{1}{2}e^{i\alpha}u^2\mathcal{G}\bar{u}. \quad (4.11)$$

Obviously, every relative equilibrium $z = a(x)e^{i\Omega t}$ of Eq. (2.19) corresponds to a fixed point $u = a(x)$ of Eq. (4.11) and vice versa. On the other hand, for every x equation (4.11) is a particular case of the complex Riccati equation (4.7) for $s = \Omega$ and

$$W(x) = \frac{1}{2}e^{-i\alpha}\mathcal{G}a. \quad (4.12)$$

We are interested only in such fixed points $u = a(x)$, which satisfy the inequality $|a(x)| \leq 1$ and are locally stable for every x . Due to Proposition 4.1 these requirements yield

$$a(x) = H_{\Omega}(|W(x)|^2)W(x). \quad (4.13)$$

Introducing a new complex function

$$w(x) = -2iW(x)/\Omega, \quad (4.14)$$

we replace identity (4.12) with

$$i\Omega e^{i\alpha} w(x) = \mathcal{G}a. \quad (4.15)$$

Moreover, inserting $W(x) = i\Omega w(x)/2$ into (4.13) we obtain

$$a(x) = H(|w(x)|^2)w(x) \quad \text{for } \Omega < 0, \quad \text{and} \quad a(x) = \overline{H(|w(x)|^2)}w(x) \quad \text{for } \Omega > 0, \quad (4.16)$$

where $H(|w|^2)$ is the function defined by (4.3). Obviously, formulas (4.15) and (4.16) agree with each other if and only if the following self-consistency equation is satisfied

$$i\Omega e^{i\alpha} w = \mathcal{G}(H(|w|^2)w) \quad \text{for } \Omega < 0, \quad \text{and} \quad i\Omega e^{i\alpha} w = \mathcal{G}(\overline{H(|w|^2)}w) \quad \text{for } \Omega > 0. \quad (4.17)$$

Abbreviating $\mu = i\Omega e^{i\alpha}$ we write (4.17) in the form

$$\mu w = \mathcal{G}(H(|w|^2)w) \quad \text{for } \Omega < 0, \quad \text{and} \quad \mu w = \mathcal{G}(\overline{H(|w|^2)}w) \quad \text{for } \Omega > 0. \quad (4.18)$$

Suppose that $(\mu_*, w_*(x))$ is a solution of the first equation in (4.18), then it is easy to verify that $(\bar{\mu}_*, \bar{w}_*(x))$ is a solution of the second equation in (4.18). These results are interpreted as follows. In the former case $\mu_* = i\Omega e^{i\alpha}$ and $\Omega < 0$, therefore using the first formula in (4.16) we obtain that

$$a(x) = H(|w_*(x)|^2)w_*(x) \quad (4.19)$$

is a fixed point of Eq. (4.11) for $\Omega = -|\mu_*|$ and $\alpha = \pi/2 + \arg \mu_*$. In contrast, in the latter case we have $\bar{\mu}_* = i\Omega e^{i\alpha}$ and $\Omega > 0$, therefore using the second formula in (4.16) we obtain that

$$a(x) = \overline{H(|w_*(x)|^2)w_*(x)} \quad (4.20)$$

is a fixed point of Eq. (4.11) for $\Omega = |\mu_*|$ and $\alpha = -\pi/2 - \arg \mu_*$. Recalling the relation between the fixed points of Eq. (4.11) and the relative equilibria of the Ott-Antonsen equation (2.19) we summarize the obtained results in Table 2.

Remark 4.2 *If parameters α , Ω and functions $a(x)$, $w(x)$ satisfy relations (4.16) and (4.17), then formula (4.15) implies $e^{-i\alpha}\mathcal{G}a = i\Omega w$.*

Proposition 4.3 *Let $(\mu_*, w_*(x))$ be a solution of Eq. (4.2) and let $z = a(x)e^{i\Omega t}$ be the corresponding relative equilibrium of Eq. (2.19), see Table 2. Then the continuum limit analog of the global order parameter can be computed by*

$$|Z(t)| = \frac{1}{|D|} \left| \int_D a(x) dx \right| = \frac{1}{|D|} \left| \int_D H(|w_*(x)|^2)w_*(x) dx \right|,$$

while the effective frequency profile is given by

$$\Omega_{\text{eff}}(x) = -\text{Im} \left(e^{i\alpha} a(x) (\mathcal{G}\bar{a})(x) \right) = \Omega \text{Re} \left(H(|w_*(x)|^2) |w_*(x)|^2 \right).$$

Proof: The first formula for $|Z(t)|$ follows directly from (2.20), (4.19) and (4.20). In order to obtain the second formula for $\Omega_{\text{eff}}(x)$ we insert the ansatz $z = a(x)e^{i\Omega t}$ into (2.21) and use Remark 4.2. Then in the resulting expression we replace $a(x)$ by (4.19) or (4.20) in accordance with the choice $w(x) = w_*(x)$ or $w(x) = \bar{w}_*(x)$. Note that in both cases we obtain identical formulas for $\Omega_{\text{eff}}(x)$. ■

4.3 Modified self-consistency equation

Suppose that the integral operator \mathcal{G} has a degenerate kernel, i.e. there exist two sets of linearly independent functions $\phi_k(x)$, $k = 1, \dots, K$, and $\psi_k(x)$, $k = 1, \dots, K$, such that

$$(\mathcal{G}u)(x) = \sum_{k=1}^K \langle \phi_k, u \rangle \psi_k(x), \quad (4.21)$$

where $\langle \cdot, \cdot \rangle$ is a scalar product on the corresponding functional space. Then Eq. (4.2) can be written in the following form

$$\mu w = \sum_{k=1}^K \langle \phi_k, H(|w|^2)w \rangle \psi_k. \quad (4.22)$$

This implies

$$w(x) = \sum_{k=1}^K \hat{w}_k \psi_k(x) \quad \text{for some } \hat{w}_k \in \mathbb{C}. \quad (4.23)$$

Inserting (4.23) into Eq. (4.22) and applying the scalar product operation $\langle \psi_m, \cdot \rangle$ to both sides of the resulting equation we obtain

$$\mu \sum_{k=1}^K \hat{w}_k \langle \psi_m, \psi_k \rangle = \sum_{k=1}^K \langle \phi_k, H(|w|^2)w \rangle \langle \psi_m, \psi_k \rangle, \quad m = 1, \dots, K. \quad (4.24)$$

Because of the complex phase shift symmetry of Eq. (4.2) we can assume that one of the unknown coefficients \hat{w}_k in (4.23), say \hat{w}_K , is real and positive. If we denote $p = \hat{w}_K$ then we can express the parameter μ from the equation (4.24) for $m = K$

$$\mu = \left(\sum_{k=1}^K \langle \phi_k, H(|w|^2)w \rangle \langle \psi_K, \psi_k \rangle \right) / \left(p \langle \psi_K, \psi_K \rangle + \sum_{k=1}^{K-1} \hat{w}_k \langle \psi_K, \psi_k \rangle \right). \quad (4.25)$$

Inserting this expression into the other equations (4.24) for $m = 1, \dots, K - 1$ we obtain a system

$$\begin{aligned} & \left(\sum_{k=1}^K \langle \phi_k, H(|w|^2)w \rangle \langle \psi_K, \psi_k \rangle \right) \left(p \langle \psi_m, \psi_K \rangle + \sum_{k=1}^{K-1} \hat{w}_k \langle \psi_m, \psi_k \rangle \right) \\ &= \left(p \langle \psi_K, \psi_K \rangle + \sum_{k=1}^{K-1} \hat{w}_k \langle \psi_K, \psi_k \rangle \right) \left(\sum_{k=1}^K \langle \phi_k, H(|w|^2)w \rangle \langle \psi_m, \psi_k \rangle \right), \end{aligned} \quad (4.26)$$

where

$$w(x) = p\psi_K(x) + \sum_{k=1}^{K-1} \hat{w}_k \psi_k(x). \quad (4.27)$$

Note that the system (4.26), (4.27) has no complex phase shift symmetry, therefore for different values of parameter p it typically has a locally unique solution \hat{w}_m , $m = 1, \dots, K - 1$, which can be found, for example, by means of a standard Newton method. Thus one obtains a one-parameter family of functions $w(x)$ in the form (4.27). The corresponding values μ can be computed explicitly using formula (4.25).

Remark 4.4 *The system (4.26) simplifies significantly if the functions $\psi_k(x)$ satisfy the orthonormality condition*

$$\langle \psi_k, \psi_m \rangle = \delta_{km}.$$

Then it reads

$$\langle \phi_K, H(|w|^2)w \rangle \hat{w}_m = p \langle \phi_m, H(|w|^2)w \rangle, \quad m = 1, \dots, K - 1. \quad (4.28)$$

Respectively, instead of the formula (4.25) we obtain

$$\mu = \frac{1}{p} \langle \phi_K, H(|w|^2)w \rangle, \quad (4.29)$$

while the ansatz (4.27) remains unchanged.

4.4 Stability analysis

Let $(\mu_*, w_*(x))$ be a solution to the nonlinear eigenvalue problem (4.2), then

$$z = a_*(x) e^{i\Omega_* t} \quad \text{where} \quad a_*(x) = H(|w_*(x)|^2)w_*(x) \quad \text{and} \quad \Omega_* = -|\mu_*| \quad (4.30)$$

is a stationary solution to Eq. (2.19) for $\alpha = \alpha_* = \pi/2 + \arg \mu_*$. The stability of the solution (4.30) can be analyzed in the following way. We insert the ansatz

$$z = (a_*(x) + v(x, t)) e^{i\Omega_* t}$$

into the Ott–Antonsen equation (2.19) and linearize it with respect to the small perturbation $v(x, t)$, obtaining

$$\frac{\partial v}{\partial t} = - (i\Omega_* + e^{i\alpha_*} a_*(x) \mathcal{G} \bar{a}_*) v + \frac{1}{2} e^{-i\alpha_*} \mathcal{G} v - \frac{1}{2} e^{i\alpha_*} a_*^2(x) \mathcal{G} \bar{v}. \quad (4.31)$$

Using Remark 4.2 to calculate $e^{i\alpha_*} \mathcal{G} \bar{a}_*$ we get $e^{i\alpha_*} a_*(x) \mathcal{G} \bar{a}_* = -i\Omega_* H(|w_*(x)|^2) |w_*(x)|^2$. This identity along with the formula (4.3) yields

$$i\Omega_* + e^{i\alpha_*} a_*(x) \mathcal{G} \bar{a}_* = \Omega_* \eta(|w_*(x)|^2)$$

where $\eta(|w|^2)$ is the function defined by (4.5). Hence Eq. (4.31) is equivalent to

$$\frac{\partial v}{\partial t} = -\Omega_* \eta(|w_*(x)|^2) v + \frac{1}{2} e^{-i\alpha_*} \mathcal{G} v - \frac{1}{2} e^{i\alpha_*} a_*^2(x) \mathcal{G} \bar{v}. \quad (4.32)$$

Remark 4.5 *Because of the complex phase shift symmetry of Eq. (2.19) its linearization can be carried out using any ansatz of the form*

$$z = (a_*(x) e^{i\varphi} + v(x, t)) e^{i\Omega_* t} \quad \text{where } \varphi \in \mathbb{R}.$$

The resulting linearized equation may have coefficients differing from those in Eq. (4.32) (see, for example, equation (20) in [84, Sec. 2.3]), but the stability properties of the zero solution in this equation and Eq. (4.31) will be the same.

According to the linear stability principle, the stability / instability of the solution (4.30) is determined by the stability / instability of the zero solution to Eq. (4.32), which in its turn is determined by the spectrum of the operator on the right-hand side of Eq. (4.32). To find the latter we use the ansatz

$$v(x, t) = v_1(x) e^{\lambda t} + \bar{v}_2(x) e^{\bar{\lambda} t}, \quad (4.33)$$

where $\lambda \in \mathbb{C}$ and $v_1(x)$ and $v_2(x)$ are complex functions. Inserting (4.33) into Eq. (4.32) and equating separately the terms at $e^{\lambda t}$ and the terms at $e^{\bar{\lambda} t}$ we obtain a system of two equations

$$\begin{aligned} \lambda v_1 &= -\Omega_* \eta(|w_*|^2) v_1 + \frac{1}{2} (e^{-i\alpha_*} \mathcal{G} v_1 - e^{i\alpha_*} a_*^2 \mathcal{G} v_2), \\ \lambda v_2 &= -\Omega_* \overline{\eta(|w_*|^2)} v_2 + \frac{1}{2} (e^{i\alpha_*} \mathcal{G} v_2 - e^{-i\alpha_*} \bar{a}_*^2 \mathcal{G} v_1), \end{aligned}$$

which can be written in a matrix form

$$\lambda \begin{pmatrix} v_1 \\ v_2 \end{pmatrix} = \mathcal{L}_m \begin{pmatrix} v_1 \\ v_2 \end{pmatrix} + \mathcal{L}_i \begin{pmatrix} v_1 \\ v_2 \end{pmatrix} \quad (4.34)$$

with a multiplication operator

$$\mathcal{L}_m \begin{pmatrix} v_1 \\ v_2 \end{pmatrix} = \begin{pmatrix} -\Omega_*\eta(|w_*|^2) & 0 \\ 0 & -\Omega_*\overline{\eta(|w_*|^2)} \end{pmatrix} \begin{pmatrix} v_1 \\ v_2 \end{pmatrix}$$

and an integral operator

$$\mathcal{L}_i \begin{pmatrix} v_1 \\ v_2 \end{pmatrix} = \frac{1}{2} \begin{pmatrix} e^{-i\alpha_*} & -e^{i\alpha_*}a_*^2 \\ -e^{-i\alpha_*}\bar{a}_*^2 & e^{i\alpha_*} \end{pmatrix} \begin{pmatrix} \mathcal{G}v_1 \\ \mathcal{G}v_2 \end{pmatrix}.$$

In the following we focus on the spectrum of the operator $\mathcal{L}_m + \mathcal{L}_i$. If this spectrum lies in the left half-plane $\operatorname{Re} \lambda \leq 0$, then the zero solution to Eq. (4.32) is (neutrally) stable. In contrast, if some part of the spectrum lies in the right half-plane $\operatorname{Re} \lambda > 0$, then the zero solution is unstable.

First, we consider the spectrum of the multiplication operator \mathcal{L}_m . It is purely essential and consists of all $\lambda \in \mathbb{C}$ such that the matrix

$$\begin{pmatrix} -\Omega_*\eta(|w_*|^2) - \lambda & 0 \\ 0 & -\Omega_*\overline{\eta(|w_*|^2)} - \lambda \end{pmatrix}$$

is not invertible, i.e. one of its diagonal elements vanishes. Since $w_*(x)$ depends on $x \in D$ this condition yields

$$\Sigma_{\text{ess}}(\mathcal{L}_m) = \left\{ -\Omega_*\eta(|w_*(x)|^2) : x \in D \right\} \cup \left\{ -\Omega_*\overline{\eta(|w_*(x)|^2)} : x \in D \right\}.$$

Note that because of the inequality $\Omega_* < 0$ and because of the definition (4.5) every $\lambda \in \Sigma_{\text{ess}}(\mathcal{L}_m)$ satisfies $\operatorname{Re} \lambda \leq 0$, hence the spectrum $\Sigma_{\text{ess}}(\mathcal{L}_m)$ is always (neutrally) stable.

Taking into account that the integral operator \mathcal{G} is a compact operator and hence \mathcal{L}_i is a compact operator too, we conclude that the essential spectra of the operators $\mathcal{L}_m + \mathcal{L}_i$ and \mathcal{L}_m coincide with each other. Therefore the spectrum of the operator $\mathcal{L}_m + \mathcal{L}_i$ has a nonempty intersection with the unstable half-plane $\operatorname{Re} \lambda > 0$ if and only if there is a part of the discrete spectrum $\Sigma_{\text{disc}}(\mathcal{L}_m + \mathcal{L}_i)$ lying there. To determine the discrete spectrum $\Sigma_{\text{disc}}(\mathcal{L}_m + \mathcal{L}_i)$ we consider the eigenvalue problem (4.34) for $\lambda \notin \Sigma_{\text{ess}}(\mathcal{L}_m + \mathcal{L}_i) = \Sigma_{\text{ess}}(\mathcal{L}_m)$. In this case we have

$$(\lambda\mathcal{I} - \mathcal{L}_m)^{-1} = \begin{pmatrix} \left(\lambda + \Omega_*\eta(|w_*|^2) \right)^{-1} & 0 \\ 0 & \left(\lambda + \Omega_*\overline{\eta(|w_*|^2)} \right)^{-1} \end{pmatrix},$$

therefore Eq. (4.34) is equivalent to

$$\begin{aligned} \begin{pmatrix} v_1 \\ v_2 \end{pmatrix} &= (\lambda \mathcal{I} - \mathcal{L}_m)^{-1} \mathcal{L}_i \begin{pmatrix} v_1 \\ v_2 \end{pmatrix} \\ &= \frac{1}{2} \begin{pmatrix} e^{-i\alpha_*} (\lambda + \Omega_* \eta(|w_*|^2))^{-1} & -e^{i\alpha_*} (\lambda + \Omega_* \eta(|w_*|^2))^{-1} a_*^2 \\ -e^{-i\alpha_*} (\lambda + \Omega_* \overline{\eta(|w_*|^2)})^{-1} \bar{a}_*^2 & e^{i\alpha_*} (\lambda + \Omega_* \overline{\eta(|w_*|^2)})^{-1} \end{pmatrix} \begin{pmatrix} \mathcal{G}v_1 \\ \mathcal{G}v_2 \end{pmatrix}. \end{aligned} \quad (4.35)$$

Inserting here instead of $a_*(x)$ and Ω_* their expressions from (4.30) and replacing $e^{i\alpha_*}$ with $i\mu_*/|\mu_*|$ we rewrite Eq. (4.35) in the form (4.6). The discrete spectrum $\Sigma_{\text{disc}}(\mathcal{L}_m + \mathcal{L}_i)$ consists of all complex values λ such that the system of integral equations (4.35) has a bounded nontrivial solution $(v_1(x), v_2(x))$. In this case, the function pair $(v_1(x), v_2(x))$ is called the eigenmode corresponding to the eigenvalue λ . Note that if $(\lambda, v_1(x), v_2(x))$ is a solution of the problem (4.35) so is $(\bar{\lambda}, \bar{v}_2(x), \bar{v}_1(x))$. It follows that the eigenvalues λ are either real or occur in complex-conjugate pairs.

Remark 4.6 *If $|w_*(x)| \geq 1$ for all $x \in D$, then the matrix in the definition of the multiplication operator \mathcal{L}_m is Hermitian, and therefore this operator is self-adjoint. On the other hand, if $e^{i\alpha_*}$ is real, i.e. $\alpha_* = 0$ or $\alpha_* = \pi$, and the integral operator \mathcal{G} is self-adjoint, for example it is a convolution type operator with a real symmetric kernel $G(x)$, then the operator \mathcal{L}_m and the operator $\mathcal{L}_m + \mathcal{L}_i$ are self-adjoint too. In this case, the spectrum of the composed operator $\mathcal{L}_m + \mathcal{L}_i$ lies on the real axis only.*

In Section 4.2 we showed that every solution $(\mu_*, w_*(x))$ of the nonlinear eigenvalue problem (4.2) determine two relative equilibria. One of them was considered above. The other one

$$z = a_{**}(x) e^{i\Omega_{**}t} \quad \text{where} \quad a_{**}(x) = \overline{H(|w_*(x)|^2)w_*(x)} \quad \text{and} \quad \Omega_{**} = |\mu_*| \quad (4.36)$$

is a solution of Eq. (2.19) for $\alpha = \alpha_{**} = -\pi/2 - \arg \mu_*$. Repeating the same arguments as above we can show that the relative equilibrium (4.36) has the same stability properties as the relative equilibrium (4.30).

4.5 Computation of the discrete spectrum

Suppose the operator \mathcal{G} has a degenerate kernel and can be written in the form (4.21). Then there exists a more explicit description of the discrete spectrum Σ_{disc} relevant to the stability of a relative equilibrium (4.30). Indeed, in this case every solution $(v_1(x), v_2(x))$ to the eigenvalue problem (4.35) satisfy

$$\begin{pmatrix} \mathcal{G}v_1 \\ \mathcal{G}v_2 \end{pmatrix} = \sum_{k=1}^K \begin{pmatrix} \langle \phi_k, v_1 \rangle \\ \langle \phi_k, v_2 \rangle \end{pmatrix} \psi_k = \sum_{k=1}^K \hat{V}_k \psi_k \quad \text{for some} \quad \hat{V}_k \in \mathbb{C}^2.$$

Inserting this ansatz into Eq. (4.35) and applying the scalar product operation $\langle \phi_m, \cdot \rangle$ to both sides of the resulting equation, we obtain a self-consistency system for the K pairs of complex coefficients \hat{V}_m , $m = 1, \dots, K$

$$\hat{V}_m = \frac{1}{2} \sum_{n=1}^K B_{mn}(\lambda) \hat{V}_n, \quad (4.37)$$

where

$$B_{mn}(\lambda) = \begin{pmatrix} \left\langle \phi_m, \frac{e^{-i\alpha_*} \psi_n}{\lambda + \Omega_* \eta(|w_*|^2)} \right\rangle & - \left\langle \phi_m, \frac{e^{i\alpha_*} a_*^2 \psi_n}{\lambda + \Omega_* \eta(|w_*|^2)} \right\rangle \\ - \left\langle \phi_m, \frac{e^{-i\alpha_*} \bar{a}_*^2 \psi_n}{\lambda + \Omega_* \eta(|w_*|^2)} \right\rangle & \left\langle \phi_m, \frac{e^{i\alpha_*} \psi_n}{\lambda + \Omega_* \eta(|w_*|^2)} \right\rangle \end{pmatrix}. \quad (4.38)$$

Collecting the coefficients \hat{V}_m into a single vector $\hat{V} \in \mathbb{C}^{2K}$, we can rewrite equations (4.37) as an equivalent matrix equation

$$\hat{V} = \frac{1}{2} B(\lambda) \hat{V}, \quad (4.39)$$

where we solve for the eigenvalue λ and the corresponding kernel vector $\hat{V} \in \mathbb{C}^{2K}$. The matrix $B(\lambda)$ has the structure

$$B(\lambda) = \begin{pmatrix} B_{11}(\lambda) & B_{12}(\lambda) & \cdots & B_{1K}(\lambda) \\ B_{21}(\lambda) & B_{22}(\lambda) & \cdots & B_{2K}(\lambda) \\ \vdots & \vdots & \ddots & \vdots \\ B_{K1}(\lambda) & B_{K2}(\lambda) & \cdots & B_{KK}(\lambda) \end{pmatrix}$$

and consists of 2×2 blocks $B_{nm}(\lambda)$ defined above.

The eigenvalues λ can be found as solutions of the characteristic equation

$$\det \left[I_{2K} - \frac{1}{2} B(\lambda) \right] = 0, \quad (4.40)$$

where I_n denotes the $n \times n$ identity matrix. If all solutions $\lambda \neq 0$ to Eq. (4.40) lie in the left half-plane, $\text{Re } \lambda < 0$, then the corresponding relative equilibrium (4.30) is stable. In contrast, if Eq. (4.40) has at least one solution $\lambda = \lambda_*$ such that $\text{Re } \lambda_* > 0$, then the relative equilibrium is unstable.

5 Nonlocal coupling of the convolution type

In this chapter we consider a one-dimensional Ott-Antonsen equation (2.19) with a nonlocal coupling of the convolution type. For this we assume that x is a one-dimensional real variable and $G(x)$ is a piecewise continuous 2π -periodic function. Respectively, the integral operator \mathcal{G} is defined as follows

$$(\mathcal{G}u)(x) = \int_{-\pi}^{\pi} G(x-y)u(y)dy. \quad (5.1)$$

Function $G(x)$ has a Fourier series representation of the form

$$G(x) = \sum_{n=-\infty}^{\infty} g_n e^{inx}, \quad \text{where} \quad g_n = \frac{1}{2\pi} \int_{-\pi}^{\pi} G(x) e^{-inx}. \quad (5.2)$$

Note that for an arbitrary real function $G(x)$ we obtain complex Fourier coefficients g_n , which satisfy $g_{-n} = \bar{g}_n$. However, if $G(x)$ is symmetric (in the sense that $G(-x) = G(x)$), then its coefficients g_n are real and satisfy $g_{-n} = g_n$. Using (5.2), one can easily verify that every complex exponent e^{int} with integer n is an eigenfunction of the operator \mathcal{G} such that

$$\mathcal{G}e^{inx} = 2\pi g_n e^{inx}. \quad (5.3)$$

This property of operator \mathcal{G} allows us to obtain two important results:

(1) For every $g_n \neq 0$ the Ott-Antonsen equation (2.19) has two branches of relative equilibria corresponding to partially coherent and coherent n -twisted states (see Section 5.1).

(2) If $G(x)$ is symmetric, then for every $g_n \neq 0$ satisfying some additional conditions the Ott-Antonsen equation (2.19) has also four branches of relative equilibria corresponding to spatially modulated partially coherent states. Two of them (see Section 5.2) bifurcate from the zero solution of Eq. (2.19) and therefore are called *primary branches*. The other two branches (see Section 5.3) bifurcate from spatially uniform relative equilibria of Eq. (2.19) and therefore are called *secondary branches*. The branches of spatially modulated solutions are important, because their extensions computed with the method of Section 4.3 can be relevant to different types of chimera states, see [79, Figs. 5 and 6] and [81, Fig. 10].

5.1 Twisted states

Some of the relative equilibria of Eq. (2.19) can be found explicitly. For example, these are twisted solutions of the form

$$z = ae^{i(nx+\Omega t)}, \quad (5.4)$$

where n is an integer indicating the number of twists and their direction, a is a positive real number and $\Omega \in \mathbb{R}$. Inserting ansatz (5.4) into Eq. (2.19), using (5.3) and cancelling identical

non-zero terms from both sides of the resulting equation we obtain

$$i\Omega = \pi g_n e^{-i\alpha} - \pi g_{-n} e^{i\alpha} a^2 = \pi g_n e^{-i\alpha} - \pi \bar{g}_n e^{i\alpha} a^2. \quad (5.5)$$

For every integer n and $g_n \neq 0$ equation (5.5) has two types of solutions:

- (i) $\text{Re}(g_n e^{-i\alpha}) = 0$, $a > 0$ and $\Omega = \pi(1 + a^2)\text{Im}(g_n e^{-i\alpha})$,
- (ii) $\text{Re}(g_n e^{-i\alpha}) \neq 0$, $a = 1$ and $\Omega = 2\pi\text{Im}(g_n e^{-i\alpha})$.

These solutions are shown in Fig. 13. An interesting feature of these graphs are two points,

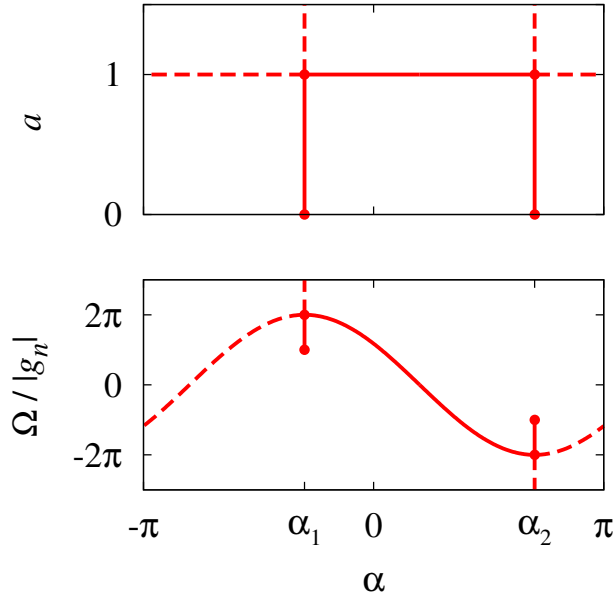


Figure 13: Parameters a and Ω of the twisted solution (5.4). Dashed curves show spurious solutions (see detail in the text). Frequency Ω is normalized by the n th Fourier coefficient g_n . Values α_1 and α_2 are determined from the equation $\text{Re}(g_n e^{-i\alpha}) = 0$.

where horizontal and vertical lines meet together. The points correspond to a complex fold bifurcation, which is a bifurcation with normal form

$$u^2 = p, \quad \text{where } u \in \mathbb{C} \quad \text{and} \quad p \in \mathbb{R},$$

see Fig. 14. Indeed, in the vicinity of every point where $\text{Re}(g_n e^{-i\alpha}) = 0$, $\Omega = 2\pi\text{Im}(g_n e^{-i\alpha})$ and $a = 1$, equation (5.5) can be transformed to this form using the non-degenerate coordinate transformation

$$p = 1 - \left| \frac{2\pi g_n}{\Omega} \right|^2 a^2, \quad u = 1 + \frac{2\pi g_n i e^{-i\alpha}}{\Omega}.$$

Importantly, complex fold bifurcations are typical for the Ott-Antonsen equation (2.19). In fact, they appear in all cases when a partially coherent relative equilibrium (4.1) with $|a(x)| < 1$ transforms into a coherent state with $|a(x)| = 1$ or into a coherence-incoherence pattern (e.g. a chimera state).

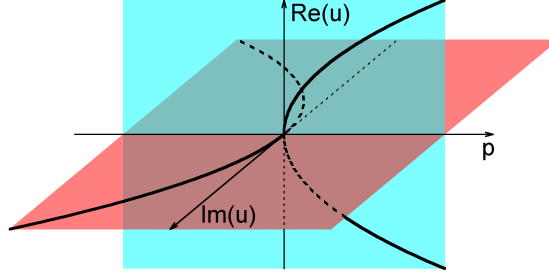


Figure 14: Complex fold bifurcation in the algebraic equation $u^2 = p$ with a complex unknown u and real parameter p .

Let us consider four solution branches coming together at a complex fold point in Fig. 13. It turns out that only two of them (solid curves) are relevant to the dynamics of the corresponding coupled oscillator system (2.6). Two other branches (dashed curves) are spurious, because one of them represents twisted solutions which don't satisfy the inequality $|z| \leq 1$, while the other branch represents twisted solutions with unstable essential spectra (the stability analysis of this solution can be carried out following the line of Section 4.4). If we discard the spurious branches, then the remaining two branches constitute a continuous (but not smooth) curve in the vicinity of a complex fold point. This solution curve can be automatically identified using the self-consistency equation (4.2), which by construction yields only admissible ($|z| \leq 1$) solutions of Eq. (2.19) with stable essential spectra. For this we insert the ansatz

$$w(x) = pe^{inx}, \quad \text{where } p \in (0, \infty), \quad (5.6)$$

into Eq. (4.2) and obtain

$$\mu = 2\pi g_n H(p^2).$$

Using the left column of Table 2 we find

$$z = H(p^2)pe^{i(nx+\Omega t)} \quad \text{with } \Omega = -|2\pi g_n H(p^2)| \quad (5.7)$$

is a solution of Eq. (2.19) for $\alpha = \pi/2 + \arg(g_n H(p^2))$. Similarly, using the right column of Table 2 we find

$$z = \overline{H}(p^2)pe^{i(-nx+\Omega t)} \quad \text{with } \Omega = |2\pi g_n H(p^2)| \quad (5.8)$$

is a solution of Eq. (2.19) for $\alpha = -\pi/2 - \arg(g_n H(p^2))$. The formula (5.8) can be written differently, if we replace index n by $-n$. Then taking into account that $g_{-n} = \bar{g}_n$ we obtain

$$z = \bar{H}(p^2) p e^{i(n x + \Omega t)} \quad \text{with} \quad \Omega = |2\pi g_n H(p^2)| \quad (5.9)$$

is a solution of Eq. (2.19) for $\alpha = -\pi/2 + \arg(g_n \bar{H}(p^2))$. Now, increasing p from 0 to ∞ and plotting the parameters of the relative equilibria (5.7) and (5.9) we obtain all points on the solid curves in Fig. 13. Notice that according to the definition (4.3), for $0 < p < 1$ the expression $H(p^2)p$ is real and satisfies the inequality $0 < H(p^2)p < 1$, while for $p \geq 1$ this expression is complex and satisfies $|H(p^2)p| = 1$.

Remark 5.1 *Let us consider a twisted solution (5.7), then for every $p < 1$ we have*

$$e^{i\alpha} = \frac{i\mu}{|\mu|} = \frac{i g_n H(p^2)}{|g_n H(p^2)|} = \frac{i g_n}{|g_n|}.$$

On the other hand, for every $p > 1$ we have

$$e^{i\alpha} = \frac{i\mu}{|\mu|} = \frac{i g_n H(p^2)}{|g_n H(p^2)|} = \frac{i g_n H(p^2) p}{|g_n|} = \frac{g_n}{|g_n|} \frac{i + \sqrt{p^2 - 1}}{p},$$

therefore

$$\cos \alpha = \frac{g_n}{|g_n|} \frac{\sqrt{p^2 - 1}}{p}.$$

Moreover, in this case also holds

$$|\mu| = 2\pi |g_n H(p^2)| = \frac{2\pi |g_n|}{p}.$$

5.2 Primary branches of spatially modulated partially coherent states

Let the coupling function $G(x)$ be symmetric, then its Fourier coefficients g_n are real and satisfy $g_{-n} = g_n$. Moreover, for every positive integer n we have

$$\langle \cos(nx), \mathcal{G}u \rangle = 2\pi g_n \langle \cos(nx), u \rangle \quad \text{and} \quad \langle \sin(nx), \mathcal{G}u \rangle = 2\pi g_n \langle \sin(nx), u \rangle,$$

where the scalar product $\langle \cdot, \cdot \rangle$ is defined as follows

$$\langle \phi, \psi \rangle = \frac{1}{2\pi} \int_{-\pi}^{\pi} \overline{\phi(x)} \psi(x) dx. \quad (5.10)$$

The above property allows us to conclude that the operator \mathcal{G} is invariant on the following functional spaces:

- (i) the space \mathbb{O}_n of all real odd $2\pi/n$ -periodic functions with a fixed $n \geq 1$,
- (ii) the space \mathbb{E}_n of all real even $2\pi/n$ -periodic functions with a fixed $n \geq 1$.

In the following we show that for every nonvanishing Fourier coefficient g_n with $n \geq 1$ the self-consistency equation (4.2) has, in general, a branch of spatially modulated solutions $w(x) \in \mathbb{O}_n$ bifurcating from zero. In accordance with Table 2 this ensures the existence of two branches of spatially modulated solutions of Eq. (2.19): a branch for $\alpha = \pi/2$ and a branch for $\alpha = -\pi/2$.

Proposition 5.2 *Let $g_n \neq 0$, $n \geq 1$, be a Fourier coefficient of the coupling function $G(x)$ and $g_n \neq g_{(j+1)n}$ for all $j \in \mathbb{N}$. Then there exists $\varepsilon_* > 0$ such that for all $\varepsilon \in (0, \varepsilon_*)$ the self-consistency equation (4.2) has a solution*

$$\begin{aligned}\mu &= \pi g_n + \frac{3\pi g_n}{16} \varepsilon^2 + O(\varepsilon^4), \\ w(x) &= \varepsilon \sin(nx) - \frac{g_{3n}}{16(g_n - g_{3n})} \varepsilon^3 \sin(3n) + O(\varepsilon^5).\end{aligned}$$

Moreover, μ is real and $w(x) \in \mathbb{O}_n$.

Proof: Let us consider the restriction of Eq. (4.2) on the subspace $(\mu, w(x)) \in \mathbb{R} \times \mathbb{O}_n$. It is well-defined because of the definition (4.3) and the invariance properties of the operator \mathcal{G} . Next, we define a projection operator

$$\mathcal{P}_s u = 2 \langle \sin(nx), u \rangle \sin(nx),$$

then Eq. (4.2) is equivalent to a system

$$\mu \langle \sin(nx), w \rangle = \langle \sin(nx), \mathcal{G}(H(|w|^2)w) \rangle, \quad (5.11)$$

$$\mu(\mathcal{I} - \mathcal{P}_s)w = (\mathcal{I} - \mathcal{P}_s)\mathcal{G}(H(|w|^2)w), \quad (5.12)$$

where \mathcal{I} denotes the identity operator. We are going to show that the system (5.11), (5.12) has a solution of the form

$$w(x) = \varepsilon \sin(nx) + \varepsilon^3 v(x, \varepsilon), \quad (5.13)$$

where $\varepsilon > 0$ is a small real number and $v(x, \varepsilon) \in \mathbb{O}_n$ is a bounded function satisfying the orthogonality condition $\langle \sin(nx), v \rangle = 0$. Inserting the ansatz (5.13) into Eqs. (5.11) and (5.12) we obtain

$$\mu\varepsilon/2 = 2\pi g_n \langle \sin(nx), H((\varepsilon \sin(nx) + \varepsilon^3 v)^2)(\varepsilon \sin(nx) + \varepsilon^3 v) \rangle, \quad (5.14)$$

$$\mu\varepsilon^3 v = (\mathcal{I} - \mathcal{P}_s)\mathcal{G}(H((\varepsilon \sin(nx) + \varepsilon^3 v)^2)(\varepsilon \sin(nx) + \varepsilon^3 v)). \quad (5.15)$$

Then expressing μ from Eq. (5.14) and inserting the result into Eq. (5.15) we obtain a single equation

$$v = \frac{(\mathcal{I} - \mathcal{P}_s)\mathcal{G} \left(H((\varepsilon \sin(nx) + \varepsilon^3 v)^2)(\varepsilon \sin(nx) + \varepsilon^3 v) \right)}{4\pi g_n \varepsilon^2 \langle \sin(nx), H((\varepsilon \sin(nx) + \varepsilon^3 v)^2)(\varepsilon \sin(nx) + \varepsilon^3 v) \rangle}. \quad (5.16)$$

Using the definition (4.3) we can write an asymptotic formula

$$H(q) = \frac{1}{2} + \frac{1}{8}q + O(q^2) \quad \text{for } q \rightarrow 0, \quad (5.17)$$

therefore

$$H((\varepsilon \sin(nx) + \varepsilon^3 v)^2)(\varepsilon \sin(nx) + \varepsilon^3 v) = \frac{1}{2}(\varepsilon \sin(nx) + \varepsilon^3 v) + \frac{1}{8}\varepsilon^3 \sin^3(nx) + O(\varepsilon^5).$$

Next, taking into account the identity $\sin^3(nx) = (3\sin(nx) - \sin(3nx))/4$ we compute

$$(\mathcal{I} - \mathcal{P}_s)\mathcal{G} \left(H((\varepsilon \sin(nx) + \varepsilon^3 v)^2)(\varepsilon \sin(nx) + \varepsilon^3 v) \right) = \frac{1}{8}\varepsilon^3 \left(4\mathcal{G}v - \frac{\pi g_{3n}}{2} \sin(3nx) \right) + O(\varepsilon^5)$$

and

$$4\pi g_n \varepsilon^2 \langle \sin(nx), H((\varepsilon \sin(nx) + \varepsilon^3 v)^2)(\varepsilon \sin(nx) + \varepsilon^3 v) \rangle = \pi g_n \varepsilon^3 + \frac{3\pi g_n}{16} \varepsilon^5 + O(\varepsilon^7).$$

This allows us to write Eq. (5.16) in the form

$$v = \frac{\mathcal{G}v}{2\pi g_n} - \frac{g_{3n}}{16g_n} \sin(3nx) + O(\varepsilon^2). \quad (5.18)$$

It is easy to verify that

$$v(x) = -\frac{g_{3n}}{16(g_n - g_{3n})} \sin(3nx)$$

is a solution to Eq. (5.18) for $\varepsilon = 0$. Hence, the Implicit function theorem yields the required result. \blacksquare

The results of Proposition 5.2 can be interpreted using Table 2. Inserting the obtained solution $(\mu, w(x))$ into the left column of the table and using the asymptotics (5.17) we conclude

$$z = a(x)e^{i\Omega t} \quad \text{with} \quad a(x) = \frac{\varepsilon}{2} \sin(nx) + O(\varepsilon^3) \quad \text{and} \quad \Omega = -\pi|g_n| \left(1 + \frac{3}{16}\varepsilon^2 \right) + O(\varepsilon^4)$$

is a solution of Eq. (2.19) for $\alpha = \pi/2 + \arg g_n$. Since the parameter ε is small, this relative equilibrium corresponds to a spatially modulated partially coherent state. Similarly, using the right column of Table 2 we obtain

$$z = a(x)e^{i\Omega t} \quad \text{with} \quad a(x) = \frac{\varepsilon}{2} \sin(nx) + O(\varepsilon^3) \quad \text{and} \quad \Omega = \pi|g_n| \left(1 + \frac{3}{16}\varepsilon^2 \right) + O(\varepsilon^4)$$

is a solution of Eq. (2.19) for $\alpha = -\pi/2 - \arg g_n$. Importantly, the above formulas hold for both $g_n > 0$ and $g_n < 0$, therefore we kept the term $\arg g_n$ in the expression of α .

5.3 The uniform partially coherent state and secondary branches of spatially modulated partially coherent states

In this section we continue to assume that $G(x)$ is a symmetric coupling function. We consider a family of constant solutions of the self-consistency equation (4.2)

$$(\mu_*, w_*(x)) = (2\pi g_0 H(p^2), p) \quad \text{where } p \in (0, \infty) \quad (5.19)$$

and the corresponding relative equilibria

$$z = a_* e^{i\Omega_* t}, \quad \text{where } a_* = H(p^2)p \quad \text{and} \quad \Omega_* = -2\pi |g_0 H(p^2)|, \quad (5.20)$$

which solve the Ott-Antonsen equation (2.19) for $\alpha = \alpha_* = \pi/2 + \arg \mu_*$. According to the formula (4.3) we have $0 < |a_*| < 1$ for $0 < p < 1$ and $|a_*| = 1$ for $p \geq 1$. Respectively, the solution (5.20) corresponds to a uniform partially coherent state for $0 < p < 1$ and to the completely coherent state for $p \geq 1$. In the following we carry out the stability analysis of the solution (5.20) and show that in some cases a spatially modulated relative equilibrium can bifurcate from it.

Proposition 5.3 *The linear stability of the solution (5.20) is determined by the essential Σ_{ess} and discrete Σ_{disc} spectra of the corresponding linearized equation.*

The essential spectrum Σ_{ess} comprises a pair of imaginary numbers $\pm 2\pi i |g_0 H(p^2)| \sqrt{1-p^2}$ for $p < 1$ and a negative real number $-2\pi |g_0 H(p^2)| \sqrt{p^2-1}$ for $p > 1$.

The discrete spectrum Σ_{disc} comprises all roots λ of the equations

$$\det \left[I_2 - \frac{1}{2} B_{nn}(\lambda) \right] = 0, \quad (5.21)$$

where

$$B_{nn}(\lambda) = 2\pi g_n \begin{pmatrix} \frac{e^{-i\alpha_*}}{\lambda + \Omega_* \eta(p^2)} & -\frac{e^{i\alpha_*} a_*^2}{\lambda + \Omega_* \eta(p^2)} \\ -\frac{e^{-i\alpha_*} \bar{a}_*^2}{\lambda + \Omega_* \bar{\eta}(p^2)} & \frac{e^{i\alpha_*}}{\lambda + \Omega_* \bar{\eta}(p^2)} \end{pmatrix}. \quad (5.22)$$

Proof: The general stability analysis of the relative equilibria (4.1) was carried out in Sections 4.4 and 4.5, therefore we can use formulas obtained there. In particular, inserting (5.19) into (4.4) and using (4.5) we find the essential spectrum Σ_{ess} .

To determine the discrete spectrum Σ_{disc} we approximate $G(x)$ with its finite Fourier sum

$$G(x) = \sum_{n=-K}^K g_n e^{inx},$$

then the corresponding integral operator \mathcal{G} can be written in the form

$$(\mathcal{G}u)(x) = \sum_{n=-K}^K \langle \phi_n, u \rangle \psi_n(x),$$

where $\phi_n(x) = 2\pi g_n e^{inx}$, $\psi_n(x) = e^{inx}$ and the scalar product $\langle \cdot, \cdot \rangle$ is defined by (5.10). Now we use the results of Section 4.5. We compute the matrices $B_{mn}(\lambda)$ defined by (4.38) and find that they are nonzero only for $n = m$. Therefore the composed matrix $B(\lambda)$ is block diagonal and hence the determinant of the characteristic equation (4.40) factorizes as follows

$$\det \left[I_{4K+2} - \frac{1}{2} B(\lambda) \right] = \prod_{n=-K}^K \det \left[I_2 - \frac{1}{2} B_{nn}(\lambda) \right].$$

This implies that Eq. (4.40) is equivalent to a set of equations (5.21) for all possible n . \blacksquare

Proposition 5.4 *Every Eq. (5.21) with $g_n \neq 0$ has either a pair of real roots or a pair of complex-conjugate imaginary roots. Depending on the value g_n/g_0 one of the following scenarios can be observed for increasing parameter p .*

(i) *If $g_n/g_0 < 0$, then the roots of Eq. (5.21) are purely imaginary for $0 < p < 1$ and real negative for $p > 1$.*

(ii) *If $0 < g_n/g_0 < 1$, then there exists $p_0 = \sqrt{1 - g_n^2/g_0^2} \in (0, 1)$ such that the roots of Eq. (5.21) are purely imaginary for $0 < p < p_0$ and real for $p > p_0$. Moreover, the real roots have opposite signs for $p_0 < p < 1$ and are both negative for $p > 1$.*

(iii) *If $g_n/g_0 > 1$, then the roots of Eq. (5.21) are purely imaginary for $0 < p < 1$ and real with opposite signs for $p > 1$.*

Proof: Inserting (5.22) into Eq. (5.21) we obtain

$$\det \left[I_2 - \frac{1}{2} B_{nn}(\lambda) \right] = \frac{(\lambda + \Omega_* \eta(p^2) - \pi g_n e^{-i\alpha_*})(\lambda + \Omega_* \overline{\eta(p^2)} - \pi g_n e^{i\alpha_*}) - \pi^2 g_n^2 |a_*|^4}{(\lambda + \Omega_* \eta(p^2)) (\lambda + \Omega_* \overline{\eta(p^2)})}.$$

The numerator of this fraction is a quadratic equation

$$\lambda^2 + 2C_1 \lambda + C_2 = 0, \tag{5.23}$$

where

$$C_1 = \operatorname{Re} C_0, \quad C_2 = |C_0|^2 - \pi^2 g_n^2 |a_*|^4 \quad \text{and} \quad C_0 = \Omega_* \eta(p^2) - \pi g_n e^{-i\alpha_*}.$$

Since the coefficients C_1 and C_2 are real, Eq. (5.23) has either a pair of real roots or a pair of complex-conjugate roots, depending on the discriminant value

$$4C_1^2 - 4C_2 = 4 \left(\pi^2 g_n^2 |a_*|^4 - (\text{Im } C_0)^2 \right).$$

For $p > 1$ we have $|a_*| = |H(p^2)|_{p=1}$ and $\text{Im } \eta(p^2) = 0$, this yields $\text{Im } C_0 = \pi g_n \sin \alpha$ and $4C_1^2 - 4C_2 = 4\pi^2 g_n^2 \cos^2 \alpha$. Hence the roots of Eq. (5.23) are real

$$\lambda_{\pm} = -C_1 \pm \sqrt{C_1^2 - C_2} = \pi g_n \cos \alpha - \Omega_* \sqrt{p^2 - 1} \pm \pi |g_n \cos \alpha|.$$

Using Remark 5.1 and formula (5.20) the latter expression can be written in the form

$$\lambda_{\pm} = \pi g_n \frac{g_0}{|g_0|} \frac{\sqrt{p^2 - 1}}{p} - 2\pi |g_0| \frac{\sqrt{p^2 - 1}}{p} \pm \pi |g_n| \frac{\sqrt{p^2 - 1}}{p} = \pi |g_0| \frac{\sqrt{p^2 - 1}}{p} \left(\frac{g_n}{g_0} - 2 \pm \frac{|g_n|}{|g_0|} \right).$$

Clearly, $\lambda_- < \lambda_+$. Moreover, if $g_n/g_0 < 1$, then $\lambda_+ < 0$. In contrast, if $g_n/g_0 > 1$, then $\lambda_+ > 0$.

Now we consider the case $p < 1$. Using Remark 5.1 to replace $e^{-i\alpha_*}$ and the formula (5.20) to replace Ω_* we find

$$C_0 = -2\pi i |g_0 H(p^2)| \sqrt{1 - p^2} + \pi i |g_n|.$$

This yields $C_1 = \text{Re } C_0 = 0$. Moreover, using the identities

$$|H(p^2)|^2 p^2 + 1 = 2|H(p^2)| \quad \text{and} \quad |H(p^2)|^2 p^2 - 1 = -2\sqrt{1 - p^2} |H(p^2)| \quad \text{for } p < 1,$$

we obtain

$$C_2 = 4\pi^2 g_n^2 |H(p^2)|^2 \sqrt{1 - p^2} \left(1 - \frac{g_0}{g_n} \right) \left(1 - \frac{g_0}{g_n} \sqrt{1 - p^2} \right).$$

If $g_0/g_n < 1$, then $C_2 > 0$, and therefore Eq. (5.23) has a pair of imaginary roots $\lambda_{\pm} = \pm i\sqrt{C_2}$. On the other hand, if $g_0/g_n > 1$, then there exists a point $p_0 \in (0, 1)$ at which the expression C_2 changes its sign from positive to negative. In other words, for $p < p_0$ equation (5.23) has purely imaginary roots $\lambda_{\pm} = \pm i\sqrt{C_2}$, while for $p > p_0$ it has two real roots with opposite signs $\lambda_{\pm} = \pm\sqrt{-C_2}$. ■

Proposition 5.4 allows us to conclude about the stability of the completely coherent state and the uniform partially coherent states. In particular, the completely coherent state is unstable if there exists at least one Fourier coefficient g_n such that $g_n/g_0 > 1$. Otherwise it is neutrally stable. Regarding the uniform partially coherent states, they are unstable only in one case: if there exists g_n such that $0 < g_n/g_0 < 1$ and $\sqrt{1 - g_n^2/g_0^2} < p < 1$. Otherwise they are neutrally stable too.

It turns out that all Fourier coefficients g_n satisfying the inequality $0 < g_n/g_0 < 1$, in general, give rise to spatially modulated partially coherent solutions of Eq. (2.19).

Proposition 5.5 *Let $g_0 \neq 0$ and $g_n \neq 0$, $n \geq 1$, be a Fourier coefficient of the coupling function $G(x)$ such that $0 < g_n/g_0 < 1$ and $g_n \neq g_{(j+1)n}$ for all $j \in \mathbb{N}$. Then there exists $\varepsilon_* > 0$ such that for all $\varepsilon \in (0, \varepsilon_*)$ the self-consistency equation (4.2) has a solution*

$$\begin{aligned}\mu &= \frac{2\pi g_0^2}{g_0 + g_n} + O(\varepsilon^2), \\ w(x) &= \sqrt{1 - g_n^2/g_0^2} + \varepsilon \cos(nx) + O(\varepsilon^2).\end{aligned}$$

Moreover, μ is real and $w(x) \in \mathbb{E}_n$.

Proof: The proof is similar to the proof of Proposition 5.2. We consider the restriction of Eq. (4.2) on the subspace $(\mu, w(x)) \in \mathbb{R} \times \mathbb{E}_n$. Defining a projection operator

$$\mathcal{P}_c u = 2\langle \cos(nx), u \rangle \cos(nx),$$

we transform Eq. (4.2) into an equivalent system

$$\mu \langle \cos(nx), w \rangle = \langle \cos(nx), \mathcal{G}(H(w^2)w) \rangle, \quad (5.24)$$

$$\mu(\mathcal{I} - \mathcal{P}_c)w = (\mathcal{I} - \mathcal{P}_c)\mathcal{G}(H(w^2)w), \quad (5.25)$$

where \mathcal{I} denotes the identity operator.

We recall that the relative equilibrium (5.20) becomes unstable for $p = p_0 = \sqrt{1 - g_n^2/g_0^2}$. Therefore we look for spatially modulated solutions of the system (5.24), (5.25) in the vicinity of its constant solution $(\mu, w(x)) = (\mu_0, p_0)$, where $\mu_0 = 2\pi g_0 H(p_0^2) = 2\pi g_0^2/(g_0 + g_n)$. For this we use the ansatz

$$w(x) = p_0 + \varepsilon \cos(nx) + \varepsilon^2 v(x, \varepsilon),$$

where $\varepsilon > 0$ is a small real number and $v(x, \varepsilon) \in \mathbb{E}_n$ is a bounded function satisfying the orthogonality condition $\langle \cos(nx), v \rangle = 0$. It is easy to verify, see (4.3), that

$$\begin{aligned}H((p_0 + q)^2)(p_0 + q) &= H(p_0^2)p_0 + (H(p_0^2) + 2H'(p_0^2)p_0^2)q + O(q^2) \\ &= \sqrt{\frac{g_0 - g_n}{g_0 + g_n}} + \frac{g_0^2}{g_n(g_0 + g_n)}q + O(q^2) \quad \text{for } q \rightarrow 0.\end{aligned} \quad (5.26)$$

Using this asymptotics we expand Eqs. (5.24) and (5.25) in the Taylor series with respect to ε . Moreover, because of the property $g_n \neq g_{n(j+1)}$, $j \in \mathbb{N}$, we conclude that the linear operator

$$\mu_0 \mathcal{I} - \mathcal{G}(H(p_0^2) + 2H'(p_0^2)p_0^2) = \mu_0 \mathcal{I} - \frac{g_0^2}{g_n(g_0 + g_n)} \mathcal{G}$$

has a one dimensional kernel in \mathbb{E}_n spanned by the function $\cos(nx)$. This allows us to apply the Implicit function theorem and obtain the required result. \blacksquare

In accordance with Table 2 every solution $(\mu, w(x))$ obtained in the Proposition 5.5 determines two relative equilibria of Eq. (2.19) representing spatially modulated partially coherent states. Indeed, for $\epsilon \rightarrow 0$ the equation (2.19) with $\alpha = \pi/2 + \arg g_n$ has a branch of relative equilibria

$$z = a(x)e^{i\Omega t} \quad \text{where} \quad a(x) = \sqrt{\frac{g_0 - g_n}{g_0 + g_n}} + \epsilon \cos(nx) + O(\epsilon^2) \quad \text{and} \quad \Omega = -\frac{2\pi g_0^2}{g_0 + g_n} + O(\epsilon^2).$$

Similarly, the equation (2.19) with $\alpha = -\pi/2 - \arg g_n$ has a branch of relative equilibria

$$z = a(x)e^{i\Omega t} \quad \text{where} \quad a(x) = \sqrt{\frac{g_0 - g_n}{g_0 + g_n}} + \epsilon \cos(nx) + O(\epsilon^2) \quad \text{and} \quad \Omega = \frac{2\pi g_0^2}{g_0 + g_n} + O(\epsilon^2).$$

Note the small parameter in the above formulas is denoted by ϵ , because it abbreviates the product $\epsilon = \varepsilon g_0^2 / (g_n(g_0 + g_n))$, see (5.26). Moreover, the term $\arg g_n$ remains in the expressions of α , because they can be considered for both $g_n > 0$ and $g_n < 0$.

6 Stationary chimera states in oscillator arrays of different dimensionality

In this chapter we show how theoretical framework developed in Chapter 4 can be applied for the analysis of stationary chimera states. The results presented below are adapted from [84]. We consider three systems of identical nonlocally coupled phase oscillators of increasing complexity, oscillators on a ring, on a two-dimensional torus and on a three-dimensional torus. In the first of these cases we look at the dynamics of phase oscillators $\{\theta_k(t)\}_{k=1}^N$ evolving according to the equations

$$\frac{d\theta_k}{dt} = -\frac{2\pi}{N} \sum_{k'=1}^N G\left(\frac{2\pi}{N}(k - k')\right) \sin(\theta_k - \theta_{k'} + \alpha), \quad (6.1)$$

where $\alpha \in (-\pi/2, \pi/2)$ is the *phase lag parameter* and

$$G(x) = \frac{1}{2\pi} \left(1 + A \cos x\right), \quad A \in \mathbb{R}, \quad (6.2)$$

is a *1D cosine function* determining a specific index-dependent coupling between oscillators. Since $G(x)$ is 2π -periodic the connections between oscillators have circular symmetry and the resulting system (6.1)–(6.2) is in fact a ring of coupled oscillators.

If instead of the one-dimensional oscillator array we consider a square lattice of phase oscillators $\{\theta_{kl}(t)\}_{k,l=1}^N$, we can write a two-dimensional analog of system (6.1)

$$\frac{d\theta_{kl}}{dt} = - \left(\frac{2\pi}{N} \right)^2 \sum_{k',l'=1}^N G \left(\frac{2\pi}{N}(k - k'), \frac{2\pi}{N}(l - l') \right) \sin(\theta_{kl} - \theta_{k'l'} + \alpha) \quad (6.3)$$

with the *2D cosine function*

$$G(x, y) = \frac{1}{(2\pi)^2} \left(1 + A \cos x + A \cos y \right), \quad A \in \mathbb{R}. \quad (6.4)$$

The most complicated model considered in this chapter is a cubic lattice of coupled phase oscillators $\{\theta_{klm}(t)\}_{k,l,m=1}^N$ described by the equations

$$\frac{d\theta_{klm}}{dt} = - \left(\frac{2\pi}{N} \right)^3 \sum_{k',l',m'=1}^N G \left(\frac{2\pi}{N}(k - k'), \frac{2\pi}{N}(l - l'), \frac{2\pi}{N}(m - m') \right) \sin(\theta_{klm} - \theta_{k'l'm'} + \alpha) \quad (6.5)$$

with the *3D cosine function*

$$G(x, y, z) = \frac{1}{(2\pi)^3} \left(1 + A \cos x + A \cos y + A \cos z \right), \quad A \in \mathbb{R}. \quad (6.6)$$

Note that in all formulas of this chapter we assume x , y and z to be scalars. They should not be confused with the function $z(x, t)$ in Chapter 2 or with the general vector x in Chapter 4.

The choice of the cosine functions (6.2), (6.4) and (6.6) is motivated by the fact that this is one of the rare cases where a stability analysis of the observed chimera states becomes feasible. Moreover, varying the kernel parameter A we can sweep over several qualitatively different coupling topologies. For example, when $A = 0$ the kernel (6.2) determines a global (all-to-all) coupling in model (6.1). In contrast, when $A \in (0, 1)$ the connectivity matrix $G(2\pi(k - k')/N)$ describes nonidentical but positive coupling strengths which decay with growing distance between pairs of oscillators. This type of coupling is usually called nonlocal. A different type of nonlocal coupling is obtained for $A \in (1, \infty)$. In this case, the short-range coupling between oscillators remains positive, while the long-range coupling between them becomes negative. Finally, in the limit $A \rightarrow \infty$ model (6.1)–(6.2) is equivalent (after a suitable time rescaling) to the system (6.1) with the balanced coupling function $G(x) = \cos x$ considered in [136]. Here the terms *balanced* and *non-balanced* refer to the sum total coupling strengths

$$\int_{-\pi}^{\pi} G(x) dx = 0 \quad \text{and} \quad \int_{-\pi}^{\pi} G(x) dx \neq 0, \quad \text{respectively.}$$

The role of the parameter A in the higher-dimensional functions (6.4) and (6.6) is qualitatively the same: Varying A from zero to infinity one passes in succession from global, to positive non-local, sign-changing nonlocal and balanced coupling topologies similar to the one-dimensional case.

Performing numerical simulations of models (6.1)–(6.2), (6.3)–(6.4) and (6.5)–(6.6) we found eleven different types of chimera states, see Tables 3 and 4, which are naturally grouped together based on the value of the global order parameter and the inheritance principle formulated below. Note that in all snapshots of the chimera states we use the scaled oscillator positions $x_k = -\pi + 2\pi k/N$, $y_l = -\pi + 2\pi l/N$ and $z_m = -\pi + 2\pi m/N$ instead of the integer indices k , l and m . This convention will help us later to compare the reported coherence-incoherence patterns with their continuum limit counterparts.

The primary difference between the chimera states shown in Tables 3 and 4 comes from the fact that they have different degrees of global synchrony. More precisely, for every chimera pattern from Table 3 the corresponding global order parameter

$$R(t) = \frac{1}{N} \left| \sum_{k=1}^N e^{i\theta_k(t)} \right|, \quad R(t) = \frac{1}{N^2} \left| \sum_{k,l=1}^N e^{i\theta_{kl}(t)} \right|, \quad \text{or} \quad R(t) = \frac{1}{N^3} \left| \sum_{k,l,m=1}^N e^{i\theta_{klm}(t)} \right|$$

stays close to zero for all time, while for every pattern from Table 4 the value of $R(t)$ is well-separated from zero and fluctuates around some positive constant level. Notice that according to the theoretical results of Sections 6.2–6.7 chimera states with vanishing order parameter can be found for both balanced and non-balanced cosine functions. In contrast, chimera states with positive global order parameter exist in systems with non-balanced coupling functions only.

In general, every chimera state found in the one-dimensional model (6.1)–(6.2) can be trivially extended to become a solution of the two-dimensional model (6.3)–(6.4) and of the three-dimensional model (6.5)–(6.6). Similarly, every two-dimensional chimera pattern can be lifted into a solution of the three-dimensional model (6.5)–(6.6). We call this simple observation the *inheritance principle* and use it to group the chimera states in different columns of Tables 3 and 4. Each of these columns is named after the symmetry group relevant to the topmost pattern in the column (details regarding this classification are presented in Sections 6.2–6.7). In Sections 6.2–6.7 we also show that the stability region of every inherited chimera state is a subset of the stability region of the corresponding lower-dimensional parent chimera state. In particular, an inherited chimera state can be everywhere unstable (left column in Table 3), have the same stability region as the parent chimera (middle and right columns in Table 3), or its stability region can be a proper subset of the stability region of the parent chimera state (left and middle columns in Table 4).

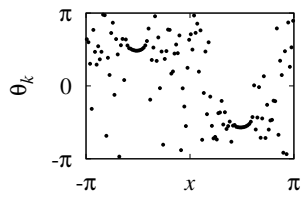
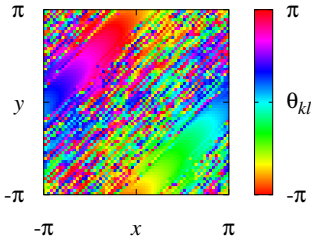
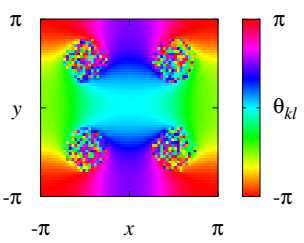
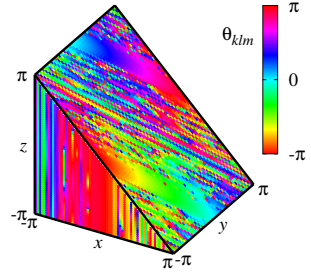
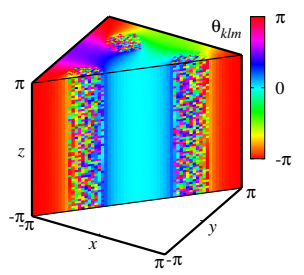
	D_2	$Z_2 \times O(2)$	$\text{Dih}(C_4)$
$1D$	antiphase chimera 		
$2D$	unstable	twisted chimera 	spiral chimera 
$3D$	unstable	twisted plane 	spiral rolls 

Table 3: Chimera states with vanishing global order parameter in models (6.1)–(6.2), (6.3)–(6.4) and (6.5)–(6.6).

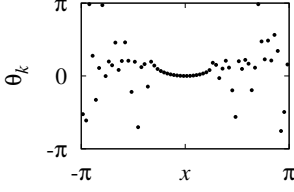
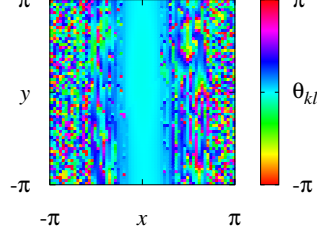
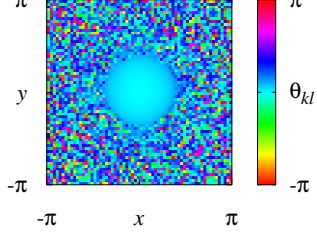
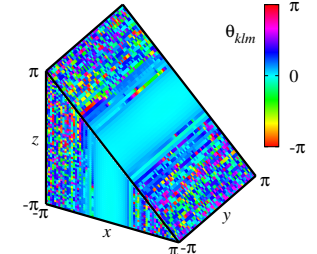
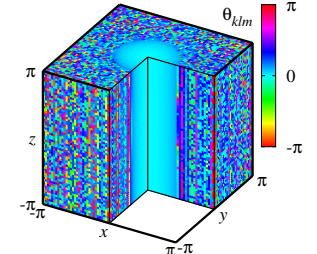
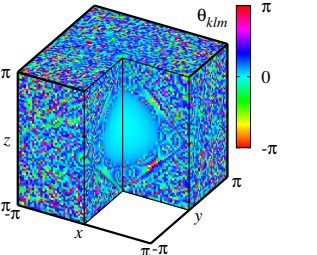
	Z_2	D_4	O_h
1D	classical chimera 		
2D	coherent stripe 	coherent spot 	
3D	coherent plane 	coherent tube 	coherent ball 

Table 4: Chimera states with non-vanishing global order parameter in the models (6.1)–(6.2), (6.3)–(6.4) and (6.5)–(6.6).

6.1 The Ott-Antonsen equation method

If the number of oscillators N in the model (6.1), (6.3) or (6.5) tends to infinity, then stationary chimera states in this model can be described by relative equilibria of the corresponding Ott-Antonsen equation (2.19). In Chapter 4 we showed that such equilibria can be found using the self-consistency equation (4.2) and their stability can be analyzed using the characteristic equation (4.40).

Depending on the dimensionality of the model ($1D$ for model (6.1), $2D$ for model (6.3) and $3D$ for model (6.5)) one has to consider different versions of Eq. (4.2). More precisely, one has to assume that the unknown function in this equation is

$$\begin{aligned} w(x) &\in C_{\text{per}}([-\pi, \pi]; \mathbb{C}), \\ w(x, y) &\in C_{\text{per}}([-\pi, \pi]^2; \mathbb{C}), \\ w(x, y, z) &\in C_{\text{per}}([-\pi, \pi]^3; \mathbb{C}). \end{aligned}$$

Then the symbol \mathcal{G} in Eq. (4.2) denotes respectively the integral operators

$$(\mathcal{G}u)(x) = \int_{-\pi}^{\pi} G(x - x')u(x')dx', \quad (6.7)$$

$$(\mathcal{G}u)(x, y) = \int_{-\pi}^{\pi} dx' \int_{-\pi}^{\pi} G(x - x', y - y', z - z')u(x', y')dy', \quad (6.8)$$

$$(\mathcal{G}u)(x, y, z) = \int_{-\pi}^{\pi} dx' \int_{-\pi}^{\pi} dy' \int_{-\pi}^{\pi} G(x - x', y - y', z - z')u(x', y', z')dz'. \quad (6.9)$$

It turns out that all chimera states in Tables 3 and 4 are represented by solutions $w(x)$, $w(x, y)$ and $w(x, y, z)$ that are invariant with respect to a nontrivial subgroup of the symmetry group of the corresponding coupling function G , therefore we call these chimera states the *symmetric chimeras*.

In the following we concentrate in greatest detail on the three-dimensional case of Eq. (4.2) with the corresponding integral operator (6.9). For the cosine function (6.6), the range of the operator (6.9) obviously is spanned by seven basis functions

$$(\psi_1(x, y, z), \dots, \psi_7(x, y, z))^T = (1, \cos x, \cos y, \cos z, \sin x, \sin y, \sin z)^T. \quad (6.10)$$

Moreover, if we define seven co-basis functions

$$(\phi_1(x, y, z), \dots, \phi_7(x, y, z))^T = (1, A \cos x, A \cos y, A \cos z, A \sin x, A \sin y, A \sin z)^T, \quad (6.11)$$

then this operator can be written in the form (4.21), where the scalar product $\langle \cdot, \cdot \rangle$ is calculated by the formula

$$\langle \phi(x, y, z), \psi(x, y, z) \rangle = \frac{1}{(2\pi)^3} \int_{-\pi}^{\pi} dx \int_{-\pi}^{\pi} dy \int_{-\pi}^{\pi} \bar{\phi}(x, y, z)\psi(x, y, z)dz. \quad (6.12)$$

The representation (4.21) allows us to simplify the self-consistency equation (4.2) following the method of Section 4.3. Indeed, in this case all solutions to Eq. (4.2) can be written in the form

$$w(x, y, z) = \sum_{k=1}^7 \hat{w}_k \psi_k(x, y, z) \quad \text{where} \quad \hat{w}_k \in \mathbb{C}. \quad (6.13)$$

Since the basis (6.10) is orthonormal with respect to the scalar product (6.12), it is easy to verify that expression (6.13) yields a solution to Eq. (4.2) if and only if the coefficients \hat{w}_k solve the system

$$\mu \hat{w}_k = \langle \phi_k, H(|w|^2)w \rangle, \quad k = 1, \dots, 7, \quad (6.14)$$

where $H(|w|^2)$ is defined by (4.3). In a similar way, following the method of Section 4.5 we can show that for every solution $w(x, y, z)$ to Eq. (4.2) all eigenvalues λ determining the stability of the corresponding relative equilibrium to Eq. (2.19) satisfy a 14-dimensional characteristic equation (4.40). The stability matrix $B(\lambda)$ in Eq. (4.40) is composed of 49 blocks $B_{mn}(\lambda)$ given by the formula (4.38), where ϕ_m and ψ_n are basis and co-basis functions (6.10) and (6.11). Note that for the cosine function (6.6) the reduction to finite dimension implied by formula (4.21) is exact. It is this fact that makes the computations that follow tractable.

In the next sections we give an overview of the results concerned with the impact of the coupling function in models (6.1), (6.3) and (6.5) on the types of observed chimera states. For every chimera state in Tables 3 and 4 we write the corresponding solution to the self-consistency equation (4.2) and analyze its symmetries. Moreover, we describe the stability regions of these chimera states in the two-dimensional parameter space (A, α) .

6.2 Antiphase chimeras in 1D, 2D and 3D

The chimera state shown in the top-left panel of Table 3 comprises two equidistant coherent regions of equal size, which are in antiphase to each other. In the following we call this state the antiphase chimera.

Self-consistency equation. Antiphase chimeras correspond to solutions of the self-consistency equation (4.2) given by the formula

$$w(x, y, z) = p \cos x, \quad \text{where} \quad p \in (1, \infty). \quad (6.15)$$

The minimal dimension needed for chimera states of this type is 1D, but they are also inherited in 2D and 3D cases. Substituting ansatz (6.15) into (6.14) shows that all but one of the equations are automatically satisfied and that the only non-trivial equation reads

$$\mu = A \langle \cos x, H(p^2 \cos^2 x) \cos x \rangle. \quad (6.16)$$

For different $p \in (1, \infty)$ expression (6.16) delivers the corresponding values of Ω and α , see Table 2. Thus, we obtain an explicit parametric representation of antiphase chimera states.

Note that the absence of a constant term in expression (6.15) analogous to \hat{w}_1 in (6.13) implies the global order parameter of every antiphase chimera state vanishes.

Symmetries. The function (6.15) is invariant under the following discrete symmetry operations:

$$\begin{aligned}\kappa_1 &: w(x, \cdot) \rightarrow w(-x, \cdot), \\ \kappa_2 &: w(x, \cdot) \rightarrow -w(\pi - x, \cdot).\end{aligned}$$

Both these operations are elements of order two ($\kappa_1^2 = 1$, $\kappa_2^2 = 1$), and therefore generate the Klein four-group D_2 . The symmetry group of antiphase chimeras is therefore D_2 . In this statement we omit the translation and reflection invariance of w with respect to the variables y and z .

Stability. In view of expressions (4.38) and (6.15) the matrix $B(\lambda)$ has the following structure:

$$B(\lambda) = \begin{pmatrix} B_{11}(\lambda) & 0 & 0 & 0 & 0 & 0 & 0 \\ 0 & B_{22}(\lambda) & 0 & 0 & 0 & 0 & 0 \\ 0 & 0 & B_{33}(\lambda) & 0 & 0 & 0 & 0 \\ 0 & 0 & 0 & B_{33}(\lambda) & 0 & 0 & 0 \\ 0 & 0 & 0 & 0 & B_{55}(\lambda) & 0 & 0 \\ 0 & 0 & 0 & 0 & 0 & B_{33}(\lambda) & 0 \\ 0 & 0 & 0 & 0 & 0 & 0 & B_{33}(\lambda) \end{pmatrix}.$$

The characteristic equation (4.40) therefore decouples into four independent equations:

$$\det \left[I_2 - \frac{1}{2} B_{11}(\lambda) \right] = 0, \quad (6.17)$$

$$\det \left[I_2 - \frac{1}{2} B_{22}(\lambda) \right] = 0, \quad (6.18)$$

$$\det \left[I_2 - \frac{1}{2} B_{33}(\lambda) \right] = 0, \quad (6.19)$$

$$\det \left[I_2 - \frac{1}{2} B_{55}(\lambda) \right] = 0. \quad (6.20)$$

Recall that antiphase chimeras are $1D$ geometric patterns that are inherited by the $2D$ and $3D$ coupled oscillator models. As a result these states may have two types of instabilities: longitudinal instabilities relevant to the main pattern direction (in the case of expression (6.15)

this is the x -direction), and transverse instabilities appearing for inherited patterns in higher-dimensional models. In order to distinguish these instabilities, the blocks of the matrix $B(\lambda)$ corresponding to the y - and z -directions are colored in blue. The longitudinal instabilities are described by Eqs. (6.17), (6.18) and (6.20), while the transverse instabilities appearing in the $2D$ and $3D$ cases are determined by Eq. (6.19). Because the blocks of the matrix $B(\lambda)$ corresponding to the y -instabilities and those corresponding to the z -instabilities coincide, the $2D$ inherited antiphase chimera and the $3D$ inherited antiphase chimera are stable or unstable simultaneously.

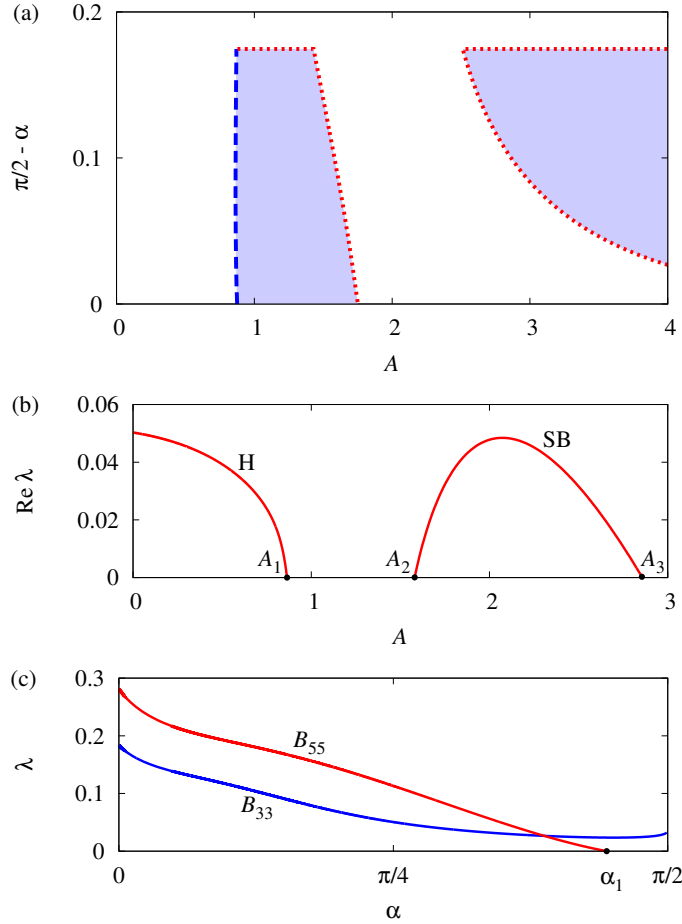


Figure 15: (a) Stability region of antiphase chimera states in the $1D$ case. Dashed and dotted lines indicate Hopf and symmetry-breaking bifurcations, respectively. (b) Complex eigenvalues (H) and real eigenvalues (SB) obtained as solution of Eq. (6.17) with $p = 1.043$ ($\alpha \approx 1.47$). (c) Real eigenvalues obtained as solutions of Eqs. (6.19) and (6.20) with $A = 1$.

Eq. (6.17) has two types of unstable eigenvalues, complex eigenvalues corresponding to Hopf modes (H) and real eigenvalues corresponding to symmetry-breaking modes (SB). These modes are present for small and large values of the parameter A , respectively, as shown in Figure 15(b). Figure 15(a) shows the corresponding stability region in the $(A, \pi/2 - \alpha)$ parameter plane. This region is bounded by curves of Hopf (dashed) and symmetry-breaking (dotted) bifurcations and represents the stability region for antiphase chimera states in $1D$. In fact, in the present case the complex conjugate eigenvalues emerge from the essential spectrum on the imaginary axis, i.e., from the edge of the essential spectrum, in a manner that is reminiscent of the eigenvalue behavior in the so-called edge bifurcation [43]. For larger values of A the characteristic equation (6.17) has instead a real unstable point eigenvalue. This eigenvalue also emerges from the essential spectrum as A increases, although it is subsequently reabsorbed by it. Thus the stability region of antiphase chimeras turns out to consist of two disjoint domains.

In contrast the blocks $B_{nn}(\lambda)$ with $n > 1$ can only produce A -independent instabilities. Indeed, the expression $\mu = i\Omega e^{i\alpha}$ together with Eq. (6.16) imply that the ratio Ω/A does not depend on A . Consequently, if we consider the matrix $B_{nn}(A\lambda')$, we easily verify that it depends on λ' and p but not on A . In other words, if a block $B_{nn}(\lambda)$ with $n > 1$ determines an unstable eigenvalue for some A then this fact remains true for any other $A \neq 0$. As a consequence for $n > 1$ it is enough to analyze instabilities produced by blocks $B_{nn}(\lambda)$ with $A = 1$. In particular we find that Eq. (6.18) yields no unstable eigenvalues, although it always determines one zero eigenvalue. Another zero eigenvalue always appears as a solution of Eq. (6.20). Moreover, Eq. (6.20) has a real unstable eigenvalue for $\alpha < \alpha_1$ where $\alpha_1 \approx 1.396$, see Figure 15(c). This fact accounts for the horizontal line of symmetry-breaking bifurcations in Figure 15(a). Figure 15(c) also shows that Eq. (6.19) has a real unstable eigenvalue for all $\alpha \in (0, \pi/2)$. This means that antiphase chimeras are always unstable in $2D$ and $3D$ and so can only be observed as stable patterns in the $1D$ case.

6.3 Twisted chimeras ($2D$) and twisted planes ($3D$)

Self-consistency equation. The twisted plane chimera, Figure 16, corresponds to the solution of the self-consistency equation (4.2) given by the expression

$$w(x, y, z) = p(e^{ix} + e^{iy}), \quad \text{where } p \in (1/2, \infty). \quad (6.21)$$

It has a $2D$ counterpart, namely the twisted chimera, but no $1D$ counterpart. Substituting ansatz (6.21) into (6.14) shows that some of these equations are satisfied automatically, while the remaining ones are all equivalent to a single equation of the form

$$\mu = A \langle \cos x, H(p^2 |e^{ix} + e^{iy}|^2)(e^{ix} + e^{iy}) \rangle. \quad (6.22)$$

Expression (6.22) provides an explicit parametric representation of twisted plane chimeras, determining Ω and α as functions of $p \in (1/2, \infty)$, see Table 2. As for antiphase chimeras, the global order parameter of every twisted plane chimera vanishes.

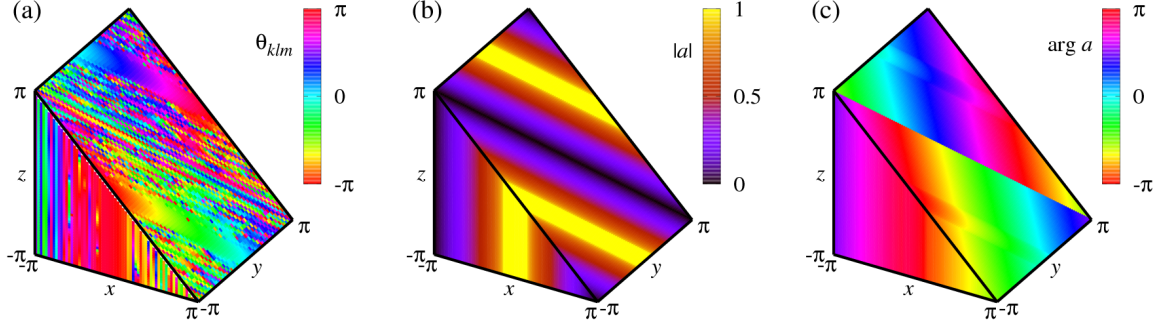


Figure 16: Twisted plane chimera state. (a) Phase snapshot from Eqs. (6.5)–(6.6) for $A = 1.5$ and $\alpha = 1.5$. (b) Modulus $|a(x, y, z)|$ and (c) argument $\arg a(x, y, z)$ of the corresponding relative equilibrium (4.1).

Symmetries. The function (6.21) is invariant under the symmetry operations

$$\begin{aligned}\kappa_1 &: w(x, y, \cdot) \rightarrow w(y, x, \cdot), \\ \kappa_2 &: w(x, y, \cdot) \rightarrow \bar{w}(-x, -y, \cdot),\end{aligned}$$

as well as the continuous transformation

$$\kappa_3 : w(x, y, \cdot) \rightarrow e^{-i\phi} w(x + \phi, y + \phi, \cdot) \quad \text{for all } \phi \in \mathbb{R}.$$

The first two operations are elements of order two ($\kappa_1^2 = 1$, $\kappa_2^2 = 1$). Moreover κ_2 and κ_3 do not commute. The symmetry group of twisted plane chimera state is therefore the group $Z_2 \times O(2)$. In this statement we omit the translation and reflection symmetries associated with the z -direction.

Stability. In view of (4.38) and (6.21) the matrix $B(\lambda)$ has the following structure:

$$B(\lambda) = \begin{pmatrix} B_{11}(\lambda) & 0 & 0 & 0 & 0 & 0 & 0 \\ 0 & B_{22}(\lambda) & B_{23}(\lambda) & 0 & B_{25}(\lambda) & B_{26}(\lambda) & 0 \\ 0 & B_{23}(\lambda) & B_{22}(\lambda) & 0 & B_{26}(\lambda) & B_{25}(\lambda) & 0 \\ 0 & 0 & 0 & B_{44}(\lambda) & 0 & 0 & 0 \\ 0 & B_{25}(\lambda) & B_{26}(\lambda) & 0 & B_{55}(\lambda) & B_{56}(\lambda) & 0 \\ 0 & B_{26}(\lambda) & B_{25}(\lambda) & 0 & B_{56}(\lambda) & B_{55}(\lambda) & 0 \\ 0 & 0 & 0 & 0 & 0 & 0 & B_{44}(\lambda) \end{pmatrix}.$$

The characteristic equation (4.40) therefore decouples into the three independent equations:

$$\det \left[I_2 - \frac{1}{2} B_{11}(\lambda) \right] = 0, \quad (6.23)$$

$$\det \left[I_8 - \frac{1}{2} \begin{pmatrix} B_{22}(\lambda) & B_{23}(\lambda) & B_{25}(\lambda) & B_{26}(\lambda) \\ B_{23}(\lambda) & B_{22}(\lambda) & B_{26}(\lambda) & B_{25}(\lambda) \\ B_{25}(\lambda) & B_{26}(\lambda) & B_{55}(\lambda) & B_{56}(\lambda) \\ B_{26}(\lambda) & B_{25}(\lambda) & B_{56}(\lambda) & B_{55}(\lambda) \end{pmatrix} \right] = 0, \quad (6.24)$$

$$\det \left[I_2 - \frac{1}{2} B_{44}(\lambda) \right] = 0. \quad (6.25)$$

Notice that Eq. (6.24) can be further simplified. Using the column/row interchange property of a determinant we rewrite Eq. (6.24) in the form

$$\det \left[I_8 - \frac{1}{2} \begin{pmatrix} B_{22}(\lambda) & B_{25}(\lambda) & B_{23}(\lambda) & B_{26}(\lambda) \\ B_{25}(\lambda) & B_{55}(\lambda) & B_{26}(\lambda) & B_{56}(\lambda) \\ B_{23}(\lambda) & B_{26}(\lambda) & B_{22}(\lambda) & B_{25}(\lambda) \\ B_{26}(\lambda) & B_{56}(\lambda) & B_{25}(\lambda) & B_{55}(\lambda) \end{pmatrix} \right] = 0. \quad (6.26)$$

The block symmetry of the latter determinant allows us to represent it as a product of two half-size determinants and to show that every solution of Eq. (6.26) solves simultaneously one of the following equations

$$\det \left[I_4 - \frac{1}{2} \begin{pmatrix} B_{22}(\lambda) - B_{23}(\lambda) & B_{25}(\lambda) - B_{26}(\lambda) \\ B_{25}(\lambda) - B_{26}(\lambda) & B_{55}(\lambda) - B_{56}(\lambda) \end{pmatrix} \right] = 0, \quad (6.27)$$

$$\det \left[I_4 - \frac{1}{2} \begin{pmatrix} B_{22}(\lambda) + B_{23}(\lambda) & B_{25}(\lambda) + B_{26}(\lambda) \\ B_{25}(\lambda) + B_{26}(\lambda) & B_{55}(\lambda) + B_{56}(\lambda) \end{pmatrix} \right] = 0. \quad (6.28)$$

Thus, Eq. (6.24) is equivalent to the two independent equations (6.27) and (6.28).

In contrast to the case of antiphase chimeras, none of equations (6.23), (6.24) and (6.25) have zero roots. However, Eq. (6.23) determines a pair of unstable complex conjugate eigenvalues for small values A , while Eq. (6.24) yields another pair of complex eigenvalues (this time of double multiplicity) for $\alpha \leq 1.45$. The resulting stability region of twisted chimera states is shown in Figure 17. It is bounded by two Hopf bifurcation curves and extends to arbitrarily large values A . The latter observation agrees with previously reported results from [137].

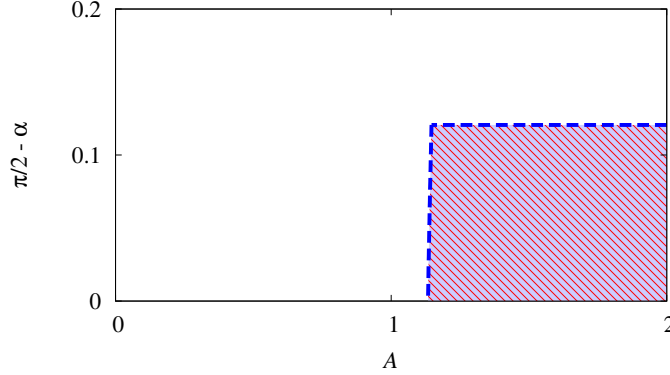


Figure 17: Stability regions of the twisted chimera state in $2D$ (shaded) and of the twisted plane chimera in $3D$ (hatched) coincide. Dashed lines indicate Hopf bifurcations. Note that the horizontal line $\alpha \approx 1.45$ corresponds to a Hopf bifurcation of double multiplicity.

6.4 Spiral chimera ($2D$) and spiral rolls ($3D$)

Self-consistency equation. The spiral roll chimera, Figure 18, corresponds to a solution of the self-consistency equation (4.2) given by the expression

$$w(x, y, z) = p(\cos x + i \cos y), \quad \text{where } p \in (1/\sqrt{2}, \infty). \quad (6.29)$$

This chimera state has a $2D$ counterpart, namely the spiral chimera, but no $1D$ counterpart. Substituting the ansatz (6.29) into (6.14) shows that some of these equations are again satisfied automatically, while the remaining ones are all equivalent to a single equation of the form

$$\mu = A \langle \cos x, H(p^2(\cos^2 x + \cos^2 y))(\cos x + i \cos y) \rangle = A \langle \cos x, H(p^2(\cos^2 x + \cos^2 y)) \cos x \rangle. \quad (6.30)$$

Expression (6.30) provides an explicit parametric representation of spiral roll chimeras, determining Ω and α as functions of $p \in (1/\sqrt{2}, \infty)$, see Table 2. As for antiphase chimeras, the global order parameter of every spiral roll chimera vanishes.

Symmetries. Symmetries of the function (6.29) were analyzed in [82] in the context of a study of $2D$ spiral chimeras where it was shown that (6.29) is invariant under the following symmetry operations:

$$\begin{aligned} \kappa_1 &: w(x, y, \cdot) \rightarrow w(x, -y, \cdot) \\ \kappa_2 &: w(x, y, \cdot) \rightarrow w(-x, y, \cdot) \\ \kappa_3 &: w(x, y, \cdot) \rightarrow e^{-i\pi/2} w(\pi - y, x, \cdot). \end{aligned}$$

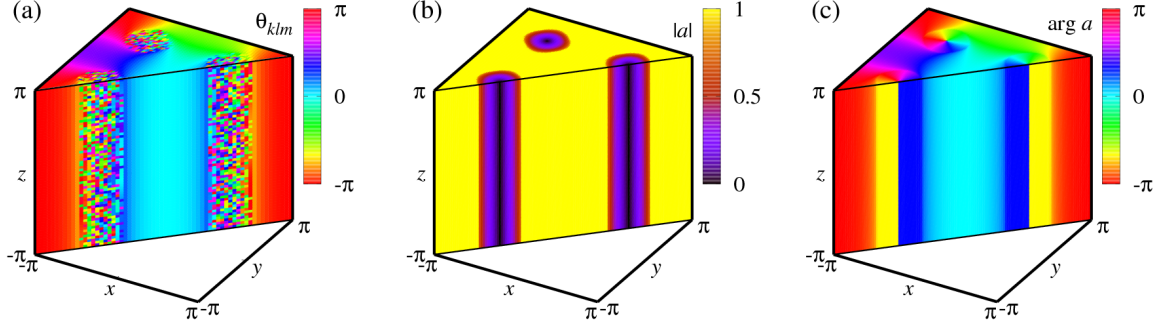


Figure 18: Spiral roll chimera state. (a) Phase snapshot from Eqs. (6.5)–(6.6) for $A = 1.5$ and $\alpha = 0.8$. (b) Modulus $|a(x, y, z)|$ and (c) argument $\arg a(x, y, z)$ of the corresponding relative equilibrium (4.1).

The reflections κ_1 and κ_2 are elements of order two ($\kappa_1^2 = 1, \kappa_2^2 = 1$), while κ_3 is an element of order four ($\kappa_3^4 = 1$). Moreover, $\kappa_2 = \kappa_3 \kappa_1 \kappa_3^{-1}$. Therefore the spatial symmetries of the spiral roll chimera constitute the generalized dihedral group of the cyclic group C_4 , i.e. $\text{Dih}(C_4)$.

Stability. In view of (4.38) and (6.29) the matrix $B(\lambda)$ has the following structure:

$$B(\lambda) = \begin{pmatrix} B_{11}(\lambda) & 0 & 0 & 0 & 0 & 0 & 0 \\ 0 & B_{22}(\lambda) & B_{23}(\lambda) & 0 & 0 & 0 & 0 \\ 0 & B_{23}(\lambda) & B_{33}(\lambda) & 0 & 0 & 0 & 0 \\ 0 & 0 & 0 & B_{44}(\lambda) & 0 & 0 & 0 \\ 0 & 0 & 0 & 0 & B_{55}(\lambda) & 0 & 0 \\ 0 & 0 & 0 & 0 & 0 & B_{66}(\lambda) & 0 \\ 0 & 0 & 0 & 0 & 0 & 0 & B_{44}(\lambda) \end{pmatrix}.$$

The characteristic equation (4.40) therefore decouples into five independent equations:

$$\det \left[I_2 - \frac{1}{2} B_{11}(\lambda) \right] = 0, \quad (6.31)$$

$$\det \left[I_4 - \frac{1}{2} \begin{pmatrix} B_{22}(\lambda) & B_{23}(\lambda) \\ B_{23}(\lambda) & B_{33}(\lambda) \end{pmatrix} \right] = 0, \quad (6.32)$$

$$\det \left[I_2 - \frac{1}{2} B_{44}(\lambda) \right] = 0, \quad (6.33)$$

$$\det \left[I_2 - \frac{1}{2} B_{55}(\lambda) \right] = 0, \quad (6.34)$$

$$\det \left[I_2 - \frac{1}{2} B_{66}(\lambda) \right] = 0. \quad (6.35)$$

Numerical analysis of Eqs. (6.31)–(6.35) reveals [84] the stability region of spiral roll chimeras, see Figure 19. We find that Eqs. (6.32), (6.34) and (6.35) have simple zero roots for all A and α . Moreover, for small values of A equation (6.31) determines a pair of unstable complex conjugate eigenvalues. For fixed α and increasing A these eigenvalues move to the imaginary axis where they are absorbed by the essential spectrum indicating a Hopf bifurcation.

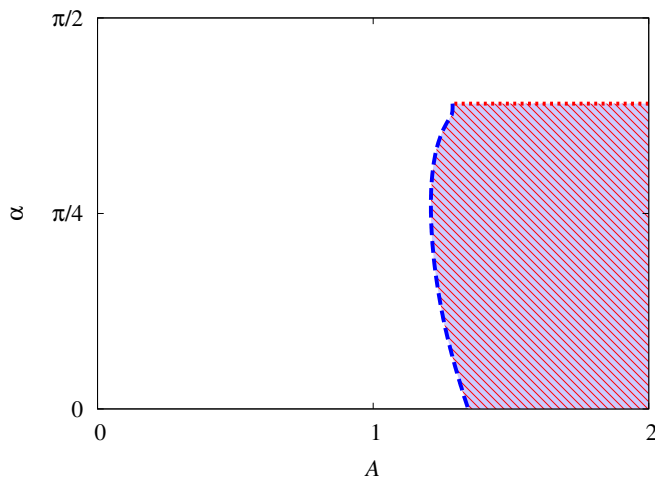


Figure 19: Stability regions of spiral chimeras in $2D$ (shaded) and of spiral roll chimeras in $3D$ (hatched). As in Figure 17 these stability regions are identical. Dashed and dotted lines indicate Hopf and symmetry-breaking bifurcations, respectively.

As for Eq. (6.20) it can be shown that all instabilities determined by Eq. (6.34) are A -independent. Our analysis reveals that for $\alpha > \alpha_2 \approx 1.23$ this equation has a real positive eigenvalue. Hence, the line $\alpha = \alpha_2$ corresponds to symmetry-breaking bifurcations.

Our extensive search did not reveal any other unstable eigenvalues, including those potentially determined by Eqs. (6.32) and (6.33). This indicates that $3D$ spiral roll chimeras are stable/unstable for the same parameters (A, α) as their $2D$ counterparts, i.e. spiral chimeras. Moreover, the stability region from Figure 19 apparently extends to arbitrarily large values A , a result that agrees with that reported in [137], where stable $2D$ spiral chimeras were observed in the case of a balanced cosine coupling function.

6.5 Classical chimera (1D), coherent stripe (2D) and coherent plane (3D)

Self-consistency equation. The coherent plane chimera, Figure 20, corresponds to a solution of the self-consistency equation (4.2) given by the expression

$$w(x, y, z) = \hat{w}_0 + p \cos x, \quad \text{where } \hat{w}_0 \in \mathbb{C} \quad \text{and} \quad p \in (0, \infty). \quad (6.36)$$

This state has both 1D and 2D counterparts, namely the classical chimera state and the coherent stripe chimera, respectively. Substituting ansatz (6.36) into (6.14) shows that this system is equivalent to the two equations

$$\begin{aligned} \mu \hat{w}_0 &= \langle 1, H(|\hat{w}_0 + p \cos x|^2)(\hat{w}_0 + p \cos x) \rangle, \\ \mu p &= A \langle \cos x, H(|\hat{w}_0 + p \cos x|^2)(\hat{w}_0 + p \cos x) \rangle, \end{aligned}$$

which can be rewritten in the form

$$\hat{w}_0 = \frac{p \langle 1, H(|\hat{w}_0 + p \cos x|^2)(\hat{w}_0 + p \cos x) \rangle}{A \langle \cos x, H(|\hat{w}_0 + p \cos x|^2)(\hat{w}_0 + p \cos x) \rangle}, \quad (6.37)$$

$$\mu = \frac{A}{p} \langle \cos x, H(|\hat{w}_0 + p \cos x|^2)(\hat{w}_0 + p \cos x) \rangle. \quad (6.38)$$

These equations can be understood as follows: We first solve Eq. (6.37) for \hat{w}_0 as a function of p . We then substitute $(p, \hat{w}_0(p))$ into Eq. (6.38) and determine the corresponding values Ω and α according to Table 2. Note that for the coherent plane chimeras we always have $\hat{w}_0 \neq 0$, implying that for these states the global order parameter is strictly positive, see Figure 21.

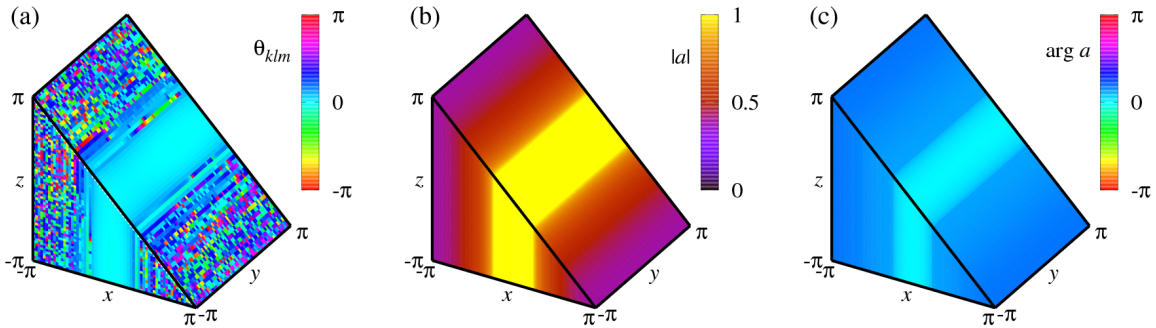


Figure 20: Coherent plane chimera state. (a) Phase snapshot from Eqs. (6.5)–(6.6) for $A = 0.9$ and $\alpha = 1.46$. (b) Modulus $|a(x, y, z)|$ and (c) argument $\arg a(x, y, z)$ of the corresponding relative equilibrium (4.1).

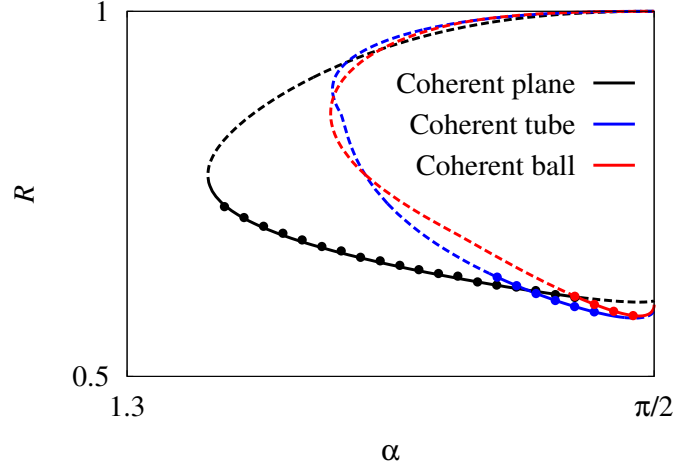


Figure 21: Global order parameter R versus the phase lag α for the three chimera states computed from Eqs. (6.37)–(6.38), (6.43)–(6.44) and (6.49)–(6.50) with $A = 0.9$. Solid and dashed curves indicate stable and unstable branches, respectively. Bullets of different colors correspond to chimera states observed in numerical simulations of the model (6.5)–(6.6) with $N = 128$.

Symmetries. The function (6.36) is invariant under the reflection

$$\kappa_1 : w(x, \cdot) \rightarrow w(-x, \cdot)$$

only and so has Z_2 symmetry.

Stability. In view of the expressions (4.38) and (6.36) the matrix $B(\lambda)$ has the following structure:

$$B(\lambda) = \begin{pmatrix} B_{11}(\lambda) & B_{12}(\lambda) & 0 & 0 & 0 & 0 & 0 \\ B_{21}(\lambda) & B_{22}(\lambda) & 0 & 0 & 0 & 0 & 0 \\ 0 & 0 & B_{33}(\lambda) & 0 & 0 & 0 & 0 \\ 0 & 0 & 0 & B_{33}(\lambda) & 0 & 0 & 0 \\ 0 & 0 & 0 & 0 & B_{55}(\lambda) & 0 & 0 \\ 0 & 0 & 0 & 0 & 0 & B_{33}(\lambda) & 0 \\ 0 & 0 & 0 & 0 & 0 & 0 & B_{33}(\lambda) \end{pmatrix}.$$

The characteristic equation (4.40) therefore decouples into the three independent equations:

$$\det \left[I_4 - \frac{1}{2} \begin{pmatrix} B_{11}(\lambda) & B_{12}(\lambda) \\ B_{21}(\lambda) & B_{22}(\lambda) \end{pmatrix} \right] = 0, \quad (6.39)$$

$$\det \left[I_2 - \frac{1}{2} B_{33}(\lambda) \right] = 0, \quad (6.40)$$

$$\det \left[I_2 - \frac{1}{2} B_{55}(\lambda) \right] = 0. \quad (6.41)$$

The stability region of classical chimera states in the $1D$ case was computed in [79]. It is bounded by curves of fold (solid) and Hopf (dashed) bifurcations, see Figure 22. Note that the pair of complex conjugate eigenvalues responsible for the Hopf instability is determined by Eq. (6.39). The eigenvalues emerge from the essential spectrum for values of A greater than one, i.e. for a sign-changing coupling function.

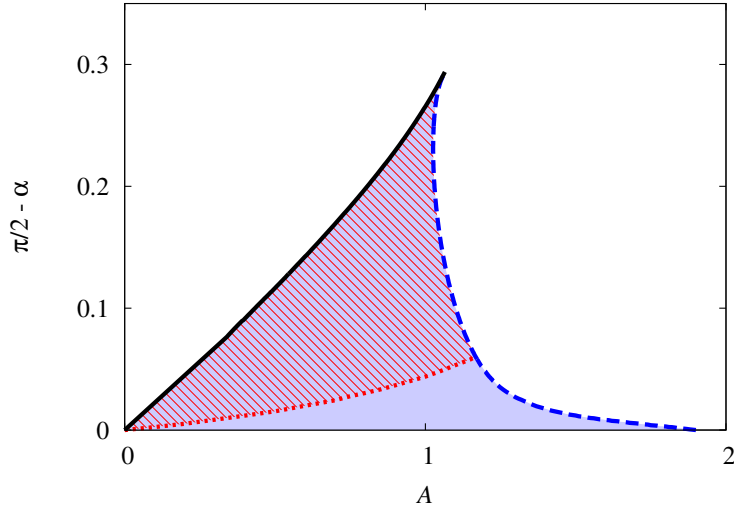


Figure 22: Stability regions of classical chimera states in $1D$ (shaded) and of coherent plane chimera states in $3D$ (hatched). The coherent stripe chimera in the $2D$ case has the same stability region as the coherent plane chimera state. Solid, dashed and dotted lines indicate fold, Hopf and symmetry-breaking bifurcations, respectively.

The stability regions of coherent plane chimeras ($3D$) and of coherent stripe chimeras ($2D$) are identical. They are smaller than the stability region of classical chimeras ($1D$), because Eq. (6.40) has a real unstable eigenvalue for values of α close to $\pi/2$. This eigenvalue is responsible for a symmetry-breaking bifurcation (dotted curve). Note that $\lambda = 0$ turns out to be a simple root of both Eq. (6.39) and Eq. (6.41).

6.6 Coherent spot (2D) and coherent tube (3D)

Self-consistency equation. The coherent tube chimera, Figs. 23(a)–(c), corresponds to a solution of the self-consistency equation (4.2) given by the expression

$$w(x, y, z) = \hat{w}_0 + p(\cos x + \cos y), \quad \text{where } \hat{w}_0 \in \mathbb{C} \quad \text{and} \quad p \in (0, \infty). \quad (6.42)$$

This state has a 2D counterpart, namely the coherent spot chimera, but no 1D counterpart. Substituting ansatz (6.42) into (6.14) shows that this system reduces to the simpler set

$$\hat{w}_0 = \frac{p \langle 1, H(|\hat{w}_0 + p(\cos x + \cos y)|^2)(\hat{w}_0 + p(\cos x + \cos y)) \rangle}{A \langle \cos x, H(|\hat{w}_0 + p(\cos x + \cos y)|^2)(\hat{w}_0 + p(\cos x + \cos y)) \rangle}, \quad (6.43)$$

$$\mu = \frac{A}{p} \langle \cos x, H(|\hat{w}_0 + p(\cos x + \cos y)|^2)(\hat{w}_0 + p(\cos x + \cos y)) \rangle. \quad (6.44)$$

To solve this system, we first solve Eq. (6.43) for \hat{w}_0 as a function of p and then use the result to compute the complex quantity μ from Eq. (6.44), thereby yielding the corresponding values of Ω and α , see Table 2. As for the coherent plane chimeras, the global order parameter of a coherent tube chimera is always strictly positive, see Figure 21.

Symmetries. The coherence-incoherence boundary of a coherent tube chimera is determined by the equation $|w(x, y, z)| = 1$. According to (6.42) this yields a cylindrical surface in z with a four-sided squashed circle in the (x, y) -section. It is easy to see that the function (6.42) has all the discrete symmetries of a square inscribed in the above squashed circle. Hence, all coherent tube chimeras have the symmetry of the dihedral group D_4 .

Stability. In view of expressions (4.38) and (6.42) the matrix $B(\lambda)$ has the following structure:

$$B(\lambda) = \begin{pmatrix} B_{11}(\lambda) & B_{12}(\lambda) & B_{12}(\lambda) & 0 & 0 & 0 & 0 \\ B_{21}(\lambda) & B_{22}(\lambda) & B_{23}(\lambda) & 0 & 0 & 0 & 0 \\ B_{21}(\lambda) & B_{23}(\lambda) & B_{22}(\lambda) & 0 & 0 & 0 & 0 \\ 0 & 0 & 0 & B_{44}(\lambda) & 0 & 0 & 0 \\ 0 & 0 & 0 & 0 & B_{55}(\lambda) & 0 & 0 \\ 0 & 0 & 0 & 0 & 0 & B_{55}(\lambda) & 0 \\ 0 & 0 & 0 & 0 & 0 & 0 & B_{44}(\lambda) \end{pmatrix}.$$

The characteristic equation (4.40) therefore decouples into the three independent equations:

$$\det \left[I_6 - \frac{1}{2} \begin{pmatrix} B_{11}(\lambda) & B_{12}(\lambda) & B_{12}(\lambda) \\ B_{21}(\lambda) & B_{22}(\lambda) & B_{23}(\lambda) \\ B_{21}(\lambda) & B_{23}(\lambda) & B_{22}(\lambda) \end{pmatrix} \right] = 0, \quad (6.45)$$

$$\det \left[I_2 - \frac{1}{2} B_{44}(\lambda) \right] = 0, \quad (6.46)$$

$$\det \left[I_2 - \frac{1}{2} B_{55}(\lambda) \right] = 0. \quad (6.47)$$

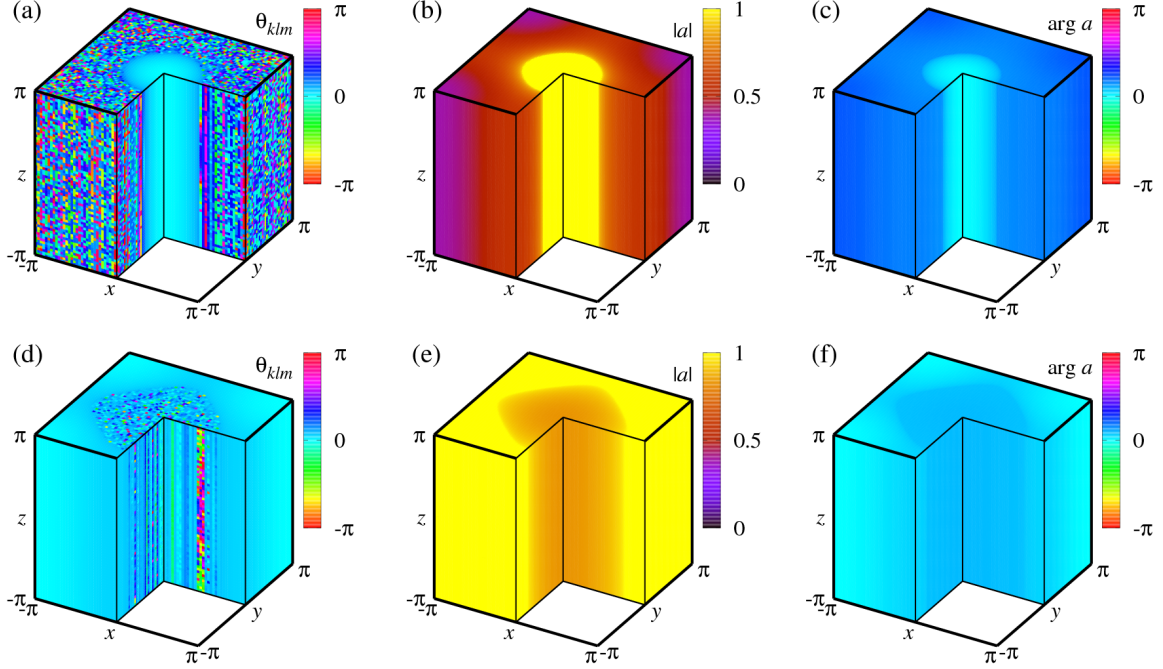


Figure 23: Coherent tube (a)–(c) and incoherent tube (d)–(f) chimera states. (a), (d) Phase snapshots from Eqs. (6.5)–(6.6) observed for $(A, \alpha) = (0.9, 1.5)$ and $(A, \alpha) = (0.4, 1.489)$, respectively. (b), (e) Moduli $|a(x, y, z)|$ and (c), (f) arguments $\arg a(x, y, z)$ of the corresponding relative equilibria (4.1).

Equations (6.45) and (6.47) have simple zeros for all values of the parameters A and α . Moreover, solving Eq. (6.45) numerically we found a real positive eigenvalue for small A and a pair of unstable complex conjugate eigenvalues for large A . Remarkably, for $A \leq 0.8$ the positive real eigenvalue can be found only in a proper subinterval of $\alpha \in (\alpha_{\text{fold}}, \pi/2)$, the existence interval for this type of chimera, because at the ends of this subinterval the eigenvalue is absorbed by the essential spectrum. As a result, the stability region of tube chimeras consists of two disconnected parts, see Figure 24. In one parameter region the chimera states resemble coherent tubes, Figure 23(a)–(c), while in the other region they resemble incoherent tubes, Figure 23(d)–(f). Note that in the latter case we can use $w(x, y, z) = \hat{w}_0 + p(\cos(x + \pi/2) + \cos(y + \pi/2))$ instead of (6.42) in order to bring the incoherent tube into the center of the cube

$[-\pi, \pi]^3$. The stability region of incoherent tubes lies close to the fold bifurcation curve and is extremely narrow. In contrast, the stability region of coherent tubes lies close to the line $\alpha = \pi/2$ and is relatively wide. Notice that all symmetry-breaking bifurcations described by Eq. (6.45) are analogous to those known for the coherent spot chimeras in the $2D$ case [90]. It follows that along with the symmetric coherent plane branch and symmetric coherent tube branch the self-consistency equation (4.2) also has two additional unstable solution branches corresponding to asymmetric chimera patterns, connecting the symmetry-breaking bifurcation points on the coherent plane branch and the coherent tube branch.

We now turn to Eq. (6.46). This equation determines a real positive eigenvalue responsible for another curve of symmetry-breaking bifurcations lying close to the line $\alpha = \pi/2$, see Figure 24. As a consequence the stability region of coherent tubes in $3D$ is smaller than the stability region of $2D$ coherent spots. Since Eq. (6.46) has no other unstable roots, the stability regions of $3D$ incoherent tubes and of $2D$ incoherent spots are identical.

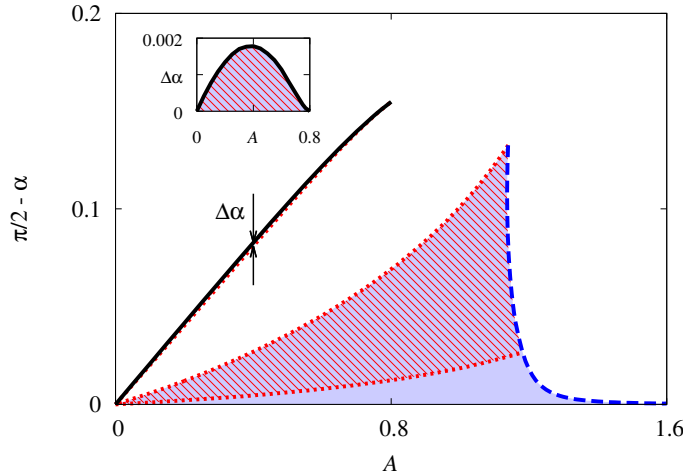


Figure 24: Stability regions of coherent spot chimera states in $2D$ (shaded) and of coherent tube chimera states in $3D$ (hatched). Dashed and dotted lines indicate Hopf and symmetry-breaking bifurcations, respectively. Insert panel shows the width $\Delta\alpha$ of the narrow stability region bounded by fold (solid) and symmetry-breaking (dotted) bifurcation curves.

6.7 Coherent ball ($3D$)

Self-consistency equation. The coherent ball chimera, Figure 25, corresponds to a solution of the self-consistency equation (4.2) given by the expression

$$w(x, y, z) = \hat{w}_0 + p(\cos x + \cos y + \cos z), \quad \text{where } \hat{w}_0 \in \mathbb{C} \quad \text{and} \quad p \in (0, \infty). \quad (6.48)$$

This chimera state is a purely 3D phenomenon and therefore has neither 2D nor 1D counterparts. Substituting ansatz (6.48) into (6.14) shows that this system reduces to the simpler set

$$\hat{w}_0 = \frac{p \langle 1, H(|\hat{w}_0 + p(\cos x + \cos y + \cos z)|^2)(\hat{w}_0 + p(\cos x + \cos y + \cos z)) \rangle}{A \langle \cos x, H(|\hat{w}_0 + p(\cos x + \cos y + \cos z)|^2)(\hat{w}_0 + p(\cos x + \cos y + \cos z)) \rangle}, \quad (6.49)$$

$$\mu = \frac{A}{p} \langle \cos x, H(|\hat{w}_0 + p(\cos x + \cos y + \cos z)|^2)(\hat{w}_0 + p(\cos x + \cos y + \cos z)) \rangle. \quad (6.50)$$

To solve this system, we first solve Eq. (6.49) for \hat{w}_0 as a function of p and then compute the complex quantity μ from Eq. (6.50), yielding the corresponding values of Ω and α , see Table 2. As for the coherent plane chimeras, the global order parameter of a coherent ball chimera is always strictly positive, see Figure 21.

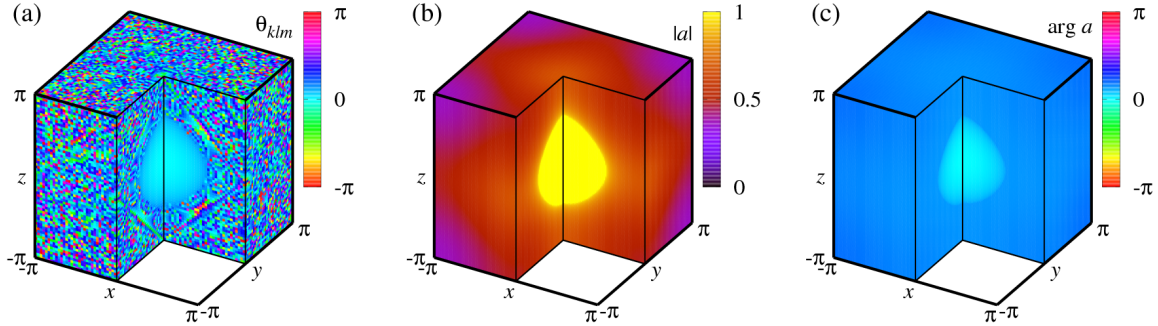


Figure 25: Coherent ball chimera state. (a) Phase snapshot from Eqs. (6.5)–(6.6) for $A = 0.9$ and $\alpha = 1.54$. (b) Modulus $|a(x, y, z)|$ and (c) argument $\arg a(x, y, z)$ of the corresponding relative equilibrium (4.1).

Symmetries. The coherence-incoherence boundary of a coherent ball chimera is determined by the equation $|w(x, y, z)| = 1$. According to (6.48) this yields a six-sided squashed sphere. It is easy to see that the function (6.48) has all the discrete symmetries of a cube inscribed in the above squashed sphere. Hence, all coherent ball chimeras have the symmetry of the octahedral group O_h .

Stability. In view of expressions (4.38) and (6.48) the matrix $B(\lambda)$ has the following struc-

ture:

$$B(\lambda) = \begin{pmatrix} B_{11}(\lambda) & B_{12}(\lambda) & B_{12}(\lambda) & B_{12}(\lambda) & 0 & 0 & 0 \\ B_{21}(\lambda) & B_{22}(\lambda) & B_{23}(\lambda) & B_{23}(\lambda) & 0 & 0 & 0 \\ B_{21}(\lambda) & B_{23}(\lambda) & B_{22}(\lambda) & B_{23}(\lambda) & 0 & 0 & 0 \\ B_{21}(\lambda) & B_{23}(\lambda) & B_{23}(\lambda) & B_{22}(\lambda) & 0 & 0 & 0 \\ 0 & 0 & 0 & 0 & B_{55}(\lambda) & 0 & 0 \\ 0 & 0 & 0 & 0 & 0 & B_{55}(\lambda) & 0 \\ 0 & 0 & 0 & 0 & 0 & 0 & B_{55}(\lambda) \end{pmatrix}.$$

The characteristic equation (4.40) therefore decouples into the two independent equations

$$\det \left[I_8 - \frac{1}{2} \begin{pmatrix} B_{11}(\lambda) & B_{12}(\lambda) & B_{12}(\lambda) & B_{12}(\lambda) \\ B_{21}(\lambda) & B_{22}(\lambda) & B_{23}(\lambda) & B_{23}(\lambda) \\ B_{21}(\lambda) & B_{23}(\lambda) & B_{22}(\lambda) & B_{23}(\lambda) \\ B_{21}(\lambda) & B_{23}(\lambda) & B_{23}(\lambda) & B_{22}(\lambda) \end{pmatrix} \right] = 0, \quad (6.51)$$

and

$$\det \left[I_2 - \frac{1}{2} B_{55}(\lambda) \right] = 0. \quad (6.52)$$

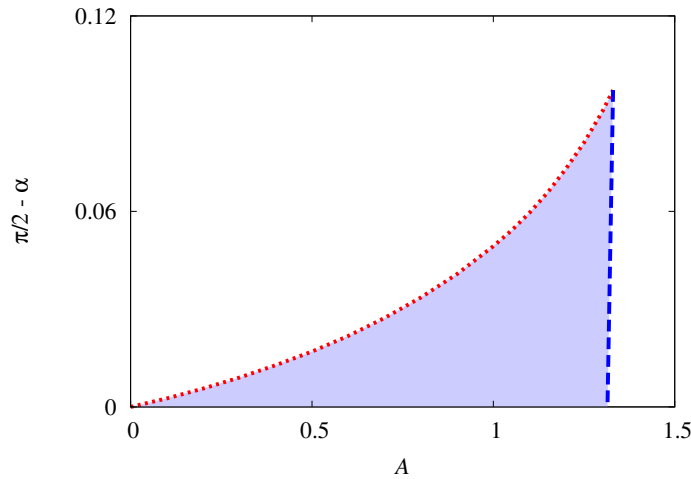


Figure 26: Stability region of coherent ball chimera states (shaded). Dashed and dotted lines indicate Hopf and symmetry-breaking bifurcations, respectively.

Both equations (6.51) and (6.52) have simple zeros for all values of the parameters A and α . Moreover, Eq. (6.51) has a double real positive eigenvalue for small A and a double pair of unstable complex conjugate eigenvalues for large A . Thus the stability region of coherent ball chimeras is bounded by Hopf and symmetry-breaking bifurcation curves as shown in Figure 26.

Note that using Eqs. (6.49)–(6.50) we can follow the branch of coherent ball chimeras beyond the symmetry-breaking bifurcation. This reveals that the coherent ball chimera transforms continuously into a labyrinthine chimera state, see Figure 27. However, the latter coherence-incoherence pattern is unstable and cannot be observed in numerical simulations of Eq. (6.5)–(6.6). On the other hand, such patterns were found in numerical simulations with other coupling functions $G(x, y, z)$, see [67].

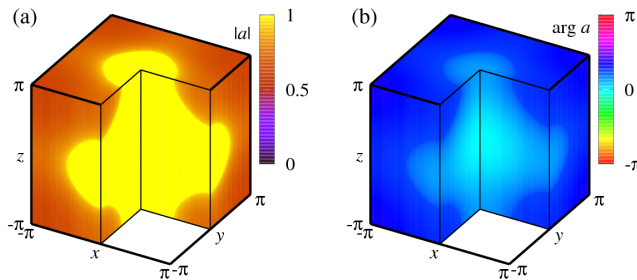


Figure 27: (a) Modulus $|a(x, y, z)|$ and (b) argument $\arg a(x, y, z)$ of the relative equilibrium (4.1) corresponding to an unstable labyrinthine chimera state.

6.8 Other coupling functions

Multi-harmonic coupling functions. All of the above results for 3D chimera states can be easily generalized for coupling functions of the form

$$G(x, y, z) = \frac{1}{(2\pi)^3} \left(1 + A \cos(nx) + A \cos(ny) + A \cos(nz) \right), \quad (6.53)$$

where $n \geq 2$ is an integer and $A \in \mathbb{R}$. Indeed, suppose that $(\mu, w(x, y, z))$ is a solution to the self-consistency equation (4.2) with the coupling function (6.6). Then $(\mu, w(nx, ny, nz))$ is a solution to the self-consistency equation (4.2) with the coupling function (6.53) and $n \geq 2$. Moreover, comparing expressions (4.38) written for the solution $(\mu, w(x, y, z))$ and the coupling function (6.6) with their analogs written for the solution $(\mu, w(nx, ny, nz))$ and coupling function (6.53) we find that the resulting stability matrices $B(\lambda)$ are identical. This leads to the general conclusion: If for some parameters A and α in the model (6.5)–(6.6) we observe a chimera state corresponding to a relative equilibrium of the form (4.1) (for example, one of

those shown in Tables 3 and 4), then for the same parameters we will find a stable multiple analog of this chimera state in the model (6.5) with the coupling function (6.53) and $n \geq 2$, see Figure 28. Note that the sequence of multiple chimera states for multi-harmonic coupling functions was already observed in 1D and 2D models of coupled phase oscillators [128, 136, 137]. Here we have shown that there is a fundamental reason for these observations, which we call the *chimera multiplication principle*.

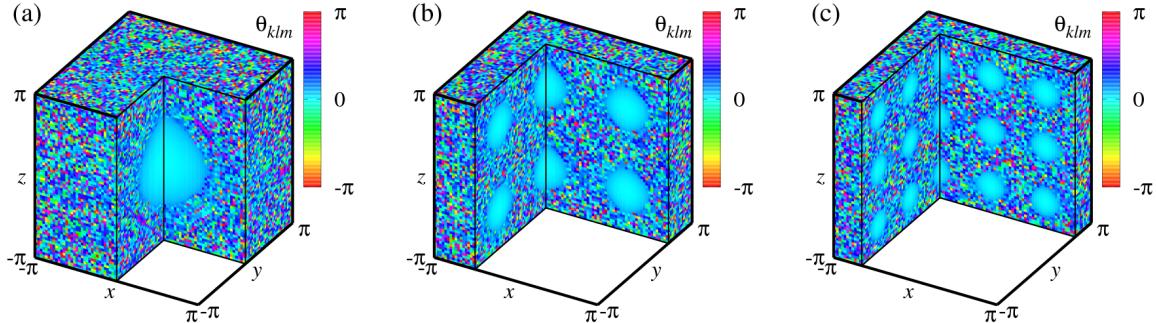


Figure 28: Multiple chimera states in the model (6.5) with the multi-harmonic coupling function (6.53). (a) Coherent ball chimera for $n = 1$. (b) Eight coherent balls chimera for $n = 2$. (c) 27 coherent balls chimera for $n = 3$. Other parameters: $A = 0.9$, $\alpha = 1.54$ and $N = 64$.

Mixed harmonic coupling functions. The Ott-Antonsen equation method described in Section 6.1 can also be used to study chimera states in models (6.1), (6.3) and (6.5) with coupling functions differing from those considered above. For example, the model (6.1) with the balanced mixed harmonic coupling function

$$G(x) = \cos(nx) + \cos((n+1)x), \quad n \in \mathbb{N}, \quad (6.54)$$

was considered in [136]. For this model, several new multiple chimera states were found. In terms of the self-consistency equation (4.2) these correspond to solutions of the form

$$w(x) = p(e^{i(n+1)x} + e^{-inx}), \quad \text{where } p \in (0, \infty),$$

and

$$w(x) = \hat{w}_1 \sin x + \hat{w}_2 \sin 2x, \quad \text{where } \hat{w}_1, \hat{w}_2 \in \mathbb{C}.$$

Note that the two-dimensional analogs of these multiple chimeras were also observed [137] in model (6.3) with the two-dimensional counterpart of the balanced mixed harmonic coupling function (6.54). Therefore according to the chimera inheritance principle we may expect to find three-dimensional analogs of these chimeras too.

Top hat coupling functions. A large number of numerical results [67, 68], including sketches of stability diagrams, were obtained for model (6.5) with the so-called piecewise constant, or top-hat coupling function

$$G(x, y, z) = \begin{cases} (4\pi^4\sigma^3/3)^{-1} & \text{for } x^2 + y^2 + z^2 \leq |\pi\sigma|, \\ 0 & \text{for } x^2 + y^2 + z^2 > |\pi\sigma|, \end{cases} \quad (6.55)$$

where $\sigma \in (0, 1)$ is the coupling radius. Along with the chimera patterns from Tables 3 and 4 and their multiple analogs, remarkable new states, called knotted and linked chimeras, were found in this model [62, 68]. Note, however, that the top-hat coupling function has a Fourier series with infinitely many terms, so that the analysis of the corresponding self-consistency equation (4.2) and especially of the corresponding eigenvalue problem (4.37) requires a significant computational effort that is beyond the scope of the present work.

Importantly, the fact that the top-hat coupling function has a Fourier series with infinitely many terms has also another consequence. Similar to the multi-harmonic coupling functions, every chimera solution $(\mu, w(x, y, z))$ to the self-consistency equation (4.2) with the coupling function (6.55) and $\sigma \in (0, 1)$ can be transformed into a multiple chimera solution $(\mu, w(nx, ny, nz))$ with $n \geq 2$ corresponding to the scaled coupling radius σ/n . However, the stability properties of the new multiple chimera pattern and of the original chimera pattern may be different, because the eigenvalue problem (4.35) cannot be reduced to a finite-dimensional equation of the form (4.40). Hence, the chimera multiplication principle for top-hat coupling functions works only partially [67, 68].

6.9 Open problems

In this chapter, we have given a systematic (albeit incomplete) overview of three-dimensional chimera states in the model (6.5)–(6.6) and their relation to the chimera states in lower-dimensional models. We revealed two important principles, the chimera inheritance principle and the chimera multiplication principle, underlying their appearance. These principles can be easily generalized for higher-dimensional situations allowing one to predict the existence and stability of hyper-dimensional chimera states. Note that the results reported here are far from exhaustive and do not cover all the chimera states that can be found in the model (6.5)–(6.6).

First, the self-consistency equation (4.2) has many symmetric solutions not mentioned in Tables 3 and 4. For example, one can use the ansatz

$$w(x, y, z) = p(\cos x + \cos y + \cos z), \quad p \in (0, \infty), \quad (6.56)$$

$$\text{or } w(x, y, z) = p(e^{ix} + e^{iy} + e^{iz}), \quad p \in (0, \infty) \quad (6.57)$$

to construct new interesting relative equilibria as shown in Figure 29. However, numerical

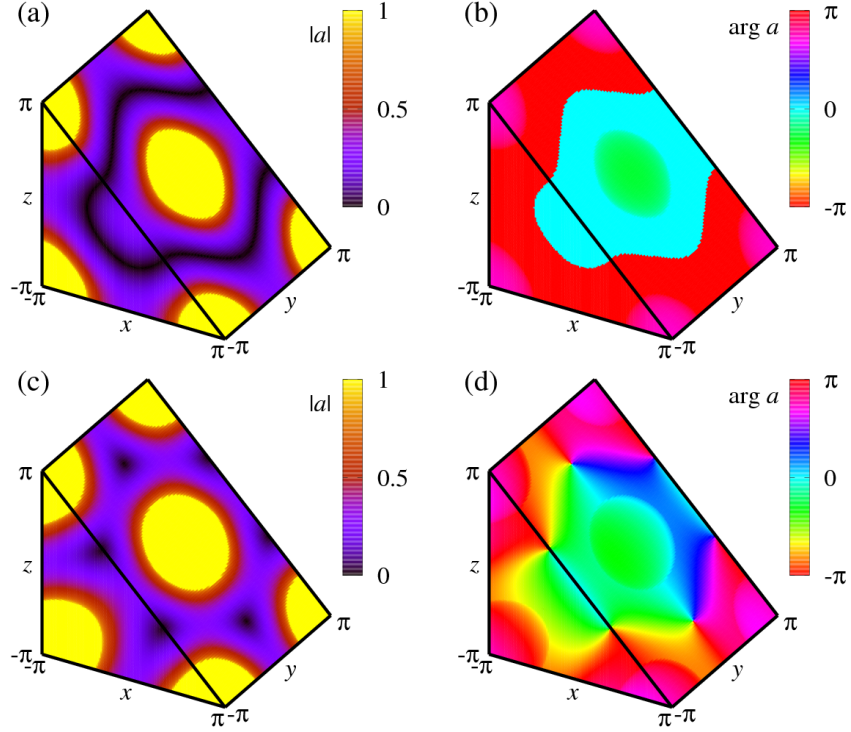


Figure 29: (a), (c) Modulus $|a(x, y, z)|$ and (b), (d) argument $\arg a(x, y, z)$ of two unstable relative equilibria (4.1) corresponding to solutions of the self-consistency equation (4.2) given by expressions (6.56) and (6.57) with $p = 0.5$.

simulations of the model (6.5)–(6.6) do not reveal any chimera states relevant to these equilibria, therefore they are likely to be unstable (although this has not been proved rigorously).

Second, the numerous symmetry-breaking bifurcations in the above stability diagrams indicate that the model (6.5)–(6.6) has solutions with less symmetry than those included in Tables 3 and 4. This hypothesis is further supported by the observation of asymmetric spot chimeras [90] and asymmetric spiral chimeras [82] in the two-dimensional model (6.3)–(6.4) as well as by the observation of two pairs of orthogonal spiral rolls in model (6.5) with the top-hat coupling function, see [67]. These states are the result of spontaneous symmetry breaking and must be distinguished from chimera states arising from forced symmetry breaking such as those present in systems with the coupling function

$$G(x, y, z) = \frac{1}{(2\pi)^3} \left(1 + A_x \cos x + A_y \cos y + A_z \cos z + B_x \sin x + B_y \sin y + B_z \sin z \right) \quad (6.58)$$

with distinct A_x, A_y, A_z, B_x, B_y and B_z . Such forced symmetry breaking destroys the highly

symmetric chimera states described above replacing them with states of lower symmetry. Moreover, for nonvanishing coefficients B_x , B_y and B_z these states typically drift [83, 85]. The lower symmetry of these states makes the corresponding stability calculations more involved, since the linear stability problem may no longer block-diagonalize.

Third, the solution of the characteristic equation (4.40) allows one to determine the stability boundaries of different chimera states but provides no information about the nature of the bifurcations that occur at these boundaries, i.e. whether the reported symmetry-breaking and Hopf bifurcations are subcritical or supercritical and the scaling of the amplitude of the new states generated by these instabilities with the distance from the bifurcation point. Potentially, these questions can be answered via a weakly nonlinear analysis of the Ott-Antonsen equation (2.19). However, in this case one needs to carry out a non-standard center manifold reduction in a situation where point spectrum eigenvalues emerge from an essential spectrum on the imaginary axis, a situation that leads to significant complications already in the case of globally (all-to-all) coupled oscillators [20, 21, 17, 24].

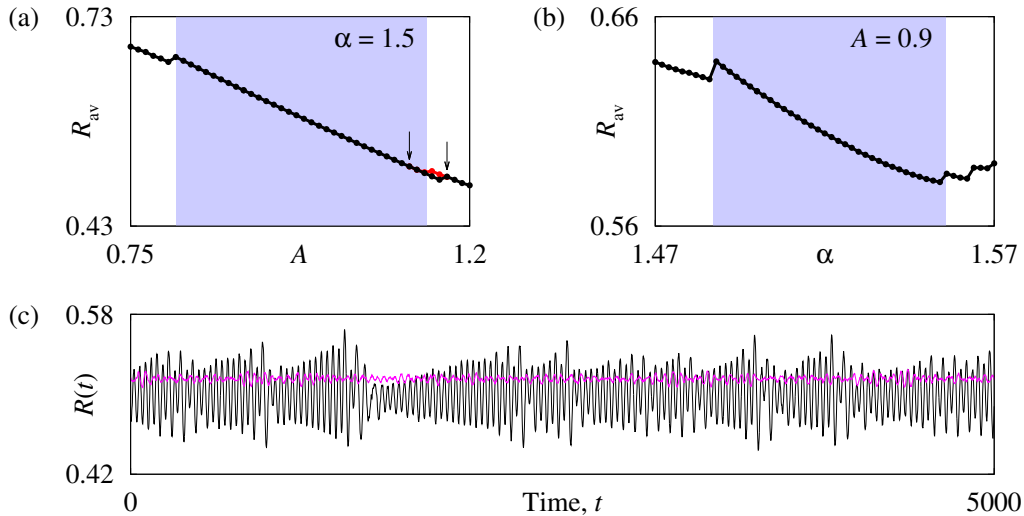


Figure 30: (a), (b) Time-averaged order parameter R_{av} of different chimera patterns obtained via continuation of the coherent tube chimera state for $(A, \alpha) = (0.9, 1.5)$. For each point (A, α) (black dots) the model (6.5)–(6.6) was integrated over 10^4 time units and the last 5000 time units were used to compute R_{av} . The red/bright dots in panel (a) correspond to an additional backward scan where parameter A was decreased from $A = 1.17$ to $A = 1.12$. Shaded boxes show stability regions of the coherent tube chimera. (c) Order parameter $R(t)$ for the two chimera states at the values of A indicated by arrows in panel (a): $A = 1.12$ (purple/bright curve) and $A = 1.17$ (black curve).

At present all stability boundaries in Figures 15(a), 17, 19, 22, 24 and 26 were analyzed only

numerically [84]. For each chimera pattern shown in Tables 3 and 4 a dynamical continuation in four possible directions (increasing or decreasing parameters A and α) was carried out. For every direction the time-averaged order parameter R_{av} was recorded as a function of A or α , see Fig. 30(a),(b). It turned out that in all cases the behaviour of the order parameter R_{av} showed abrupt jumps after the crossing of the corresponding stability boundary. This observation suggests that all the bifurcations reported in Figures 15(a), 17, 19, 22, 24 and 26 are in fact subcritical. More precisely, it was found that crossing a symmetry-breaking stability boundary may lead to a collapse of the corresponding chimera state to either a completely coherent state, or to a splay state or another chimera state, which is stable for the new system parameters. In contrast, crossing Hopf instability boundaries generally resulted in abrupt transitions to more complicated time-intermittent regimes, see Fig. 30(c), suggesting that some of the Hopf bifurcations may be responsible for Type-II intermittent transitions to chaos as described by Pomeau and Manneville in [99]. Note that with non-cosine coupling functions the bifurcations may be supercritical. In particular, supercritical Hopf bifurcations were reported for mixed harmonic [136, 137, 82], exponential [11] and top-hat [120] coupling functions, i.e. for coupling functions containing more than one non-constant Fourier harmonic.

7 Breathing chimera states

In this chapter we consider solutions of the Ott-Antonsen equation (2.19) representing breathing chimera states.¹ These are relative periodic orbits of the form

$$z = a(x, t)e^{i\Omega t}, \quad (7.1)$$

where $a(x, t)$ is a function T -periodic with respect to t for some $T > 0$. Similar to Section 1.4, the frequencies Ω and $\omega = 2\pi/T$ will be referred to as *the primary frequency* and *the secondary frequency*, respectively. For the sake of simplicity throughout the chapter we assume that the spatial coordinate x is one-dimensional and the integral operator \mathcal{G} is of the convolution type, see (5.1), with a one dimensional coupling function $G(x)$.

Remark 7.1 *Note that the product ansatz (7.1) with a T -periodic function $a(x, t)$, in general, is not uniquely determined. Indeed, for every nonzero integer m we can rewrite it in the equivalent form*

$$z = a_m(x, t)e^{i\Omega_m t} \quad \text{with} \quad a_m(x, t) = a(x, t)e^{im\omega t} \quad \text{and} \quad \Omega_m = \Omega - m\omega.$$

To avoid this ambiguity, throughout this chapter we assume that the function $a(x, t)$ and the constant Ω in (7.1) are chosen so that

$$\lim_{\tau \rightarrow \infty} \frac{1}{\tau} \int_0^\tau d \arg Y(t) = 0 \quad \text{where} \quad Y(t) = \frac{1}{2\pi} \int_{-\pi}^\pi a(x, t) dx.$$

¹The results presented in this chapter are adapted from [87].

Roughly speaking, we request that the variation of the complex argument of $Y(t)$ remains bounded for all $t \geq 0$.

Importantly, this calibration condition is well-defined only if $Y(t) \neq 0$ for all $t \geq 0$, therefore we checked carefully that this requirement is satisfied for all examples of breathing chimera states shown below.

The chapter is organized as follows. In Section 7.1 we consider a complex Riccati equation

$$\frac{du}{dt} = W(t) - isu(t) - \overline{W}(t)u^2(t),$$

where s is a real coefficient and $W(t)$ is a continuous complex-valued function. We show that this equation has a unique stable periodic solution satisfying the inequality $|u(t)| \leq 1$. The corresponding solution operator is denoted by

$$\mathcal{U} : (W, s) \in C_{\text{per}}([0, 2\pi]; \mathbb{C}) \times \mathbb{R} \mapsto u \in C_{\text{per}}^1([0, 2\pi]; \mathbb{C}).$$

Its properties are discussed in Sections 7.2 and 7.3. Although the operator \mathcal{U} is defined implicitly, it turns out that its value can be computed by solving only three initial value problems for the complex Riccati equation. In Section 7.4 we show that if Eq. (2.19) has a stable solution of the form (7.1) then its amplitude $a(x, t)$ and its primary and secondary frequencies Ω and ω satisfy a self-consistency equation

$$2\omega e^{i\alpha} w(x, t) - \mathcal{G}\mathcal{U}(w(x, t), s) = 0, \quad (7.2)$$

where

$$\omega = \frac{2\pi}{T}, \quad s = \frac{\Omega}{\omega}, \quad w(x, t) = \frac{e^{-i\alpha}}{2\omega} \mathcal{G}a\left(x, \frac{t}{\omega}\right). \quad (7.3)$$

A modified version of Eq. (7.2) is obtained in Section 7.5. Then in Section 7.6 we suggest a continuation algorithm allowing to compute the solution branches of Eq. (7.2) and thus to predict the properties of breathing chimera states. In Section 7.7 we carry out linear stability analysis of a general relative periodic orbit (7.1) in Eq. (2.19). The analysis relies on the consideration of a monodromy operator describing time evolution of small perturbations in the system. We show that the stability of a relative periodic orbit is determined by the spectrum of the monodromy operator. The spectrum consists of two parts: essential and discrete spectra. The former part is known explicitly and has no influence on the stability of a breathing chimera state, while the latter part is crucial for its stability but can be computed only numerically as explained in Section 7.8. In Section 7.9 we illustrate the performance of the developed methods considering a specific example of breathing chimera state in system (6.1)–(6.2).

Notations. Throughout this chapter we use the following notations. We let $C_{\text{per}}([-\pi, \pi]; \mathbb{C})$ denote the space of all 2π -periodic continuous complex-valued functions. A similar notation $C_{\text{per}}([-\pi, \pi] \times [0, 2\pi]; \mathbb{C})$ will be used to denote the space of all continuous double-periodic functions on the square domain $[-\pi, \pi] \times [0, 2\pi]$. Moreover, the capital calligraphic letters such as \mathcal{G} or \mathcal{U} are used to denote operators on appropriate Banach spaces.

7.1 Periodic complex Riccati equation

Let us consider a complex Riccati equation of the form

$$\frac{du}{dt} = W(t) - isu(t) - \overline{W}(t)u^2(t), \quad (7.4)$$

where $s \in \mathbb{R}$ and $W(t)$ is a continuous complex-valued function. Recall that the symbol \mathbb{D} denotes the open unit disc of the complex plane and $\overline{\mathbb{D}} = \mathbb{D} \cup \partial\mathbb{D}$ is its closure. We are going to show that for every $(W(t), s) \in C_{\text{per}}([0, 2\pi]; \mathbb{C}) \times \mathbb{R}$ such that $|s| + \max_{t \in [0, 2\pi]} |W(t)| \neq 0$, in general, there exists a unique stable solution to Eq. (7.4) lying entirely in the unit disc $\overline{\mathbb{D}}$. The nonlinear operator yielding this solution will be denoted by $\mathcal{U}(W(t), s)$.

Proposition 7.2 *For every $s \in \mathbb{R}$, $W \in C(\mathbb{R}; \mathbb{C})$ and $u_0 \in \overline{\mathbb{D}}$ there exists a unique global solution to equation (7.4) starting from the initial condition $u(0) = u_0$. Moreover, if $|u_0| = 1$ or $|u_0| < 1$, then $|u(t)| = 1$ or $|u(t)| < 1$ for all $t \in \mathbb{R}$, respectively.*

Proof: Suppose that $u(t)$ is a solution to equation (7.4), then

$$\begin{aligned} \frac{d|u|^2}{dt} &= u(t) \frac{d\bar{u}}{dt} + \bar{u}(t) \frac{du}{dt} = u(t)\overline{W}(t) + is|u(t)|^2 - W(t)|u(t)|^2\bar{u}(t) \\ &+ \bar{u}(t)W(t) - is|u(t)|^2 - \overline{W}(t)|u(t)|^2u(t) = 2\text{Re}(u(t)\overline{W}(t))(1 - |u(t)|^2). \end{aligned} \quad (7.5)$$

According to Eq. (7.5), if $|u(0)| = 1$ then $|u(t)| = 1$ for all other $t \neq 0$, therefore the solution $u(t)$ cannot blow up in finite time and hence it can be extended for all $t \in \mathbb{R}$. On the other hand, Eq. (7.5) implies that every solution $u(t)$ satisfying $|u(0)| < 1$ remains trapped inside the disc \mathbb{D} , therefore it also can be extended for all $t \in \mathbb{R}$. \blacksquare

Remark 7.3 *Every solution $u(t)$ to Eq. (7.4) satisfying the identity $|u(t)| = 1$ can be written in the form $u(t) = e^{i\psi(t)}$ where $\psi(t)$ is a solution to the equation*

$$\frac{d\psi}{dt} = -s + 2\text{Im}(W(t)e^{-i\psi}).$$

Now we consider Eq. (7.4) with a 2π -periodic coefficient $W(t)$. It is well-known [16, 131] that the Poincaré map of such equation coincides with the Möbius transformation. Because of Proposition 7.2 this Möbius transformation maps unit disc $\overline{\mathbb{D}}$ onto itself, therefore it can be written in the form

$$\mathcal{M}(u) = \frac{e^{i\theta}(u + b)}{\bar{b}u + 1} \quad \text{where } \theta \in \mathbb{R} \quad \text{and } b \in \mathbb{C}. \quad (7.6)$$

Remark 7.4 *The fact that the Poincaré map of the periodic complex Riccati equation (7.4) coincides with the Möbius transformation (7.6) can also be justified in a different way using a known result from Lie theory, see [72, Sec. III].*

The next proposition shows that the parameters θ and b in formula (7.6) can be uniquely determined using two solutions to Eq. (7.4) starting from the initial conditions $u = 0$ and $u = 1$.

Proposition 7.5 *Suppose $s \in \mathbb{R}$ and $W \in C_{\text{per}}([0, 2\pi]; \mathbb{C})$. Let $U(t)$ and $\Psi(t)$ be solutions of the initial value problems*

$$\frac{dU}{dt} = W(t) - isU(t) - \overline{W}(t)U^2(t), \quad U(0) = 0, \quad (7.7)$$

$$\frac{d\Psi}{dt} = -s + 2\text{Im}(W(t)e^{-i\Psi}), \quad \Psi(0) = 0, \quad (7.8)$$

and let $\zeta = U(-2\pi)$ and $\chi = \Psi(2\pi)$, then the Poincaré map of Eq. (7.4) is determined by the formula (7.6) with

$$b = -\zeta \quad \text{and} \quad e^{i\theta} = \frac{\overline{\zeta} - 1}{\zeta - 1} e^{i\chi}. \quad (7.9)$$

Moreover $|b| < 1$.

Proof: The definition of the Poincaré map and Remark 7.3 imply

$$\frac{e^{i\theta}(\zeta + b)}{\overline{b}\zeta + 1} = 0 \quad \text{and} \quad \frac{e^{i\theta}(1 + b)}{\overline{b} + 1} = e^{i\chi}.$$

The former equation yields $b = -\zeta$. Inserting this into the latter equation we obtain a formula for $e^{i\theta}$. Notice that because of Proposition 7.2 we always have $|\zeta| < 1$, and hence $|b| < 1$ too. ■

Every 2π -periodic solution to Eq. (7.4) corresponds to a fixed point of the Poincaré map, or equivalently to a solution to the equation

$$\mathcal{M}(u) = \frac{e^{i\theta}(u + b)}{\overline{b}u + 1} = u. \quad (7.10)$$

The periodic solution is *stable* or *unstable*, if the corresponding fixed point u_* is stable or unstable with respect to the map $\mathcal{M}(u)$, and the latter condition can be easily verified by estimating the derivative $\mathcal{M}'(u_*)$. Indeed, if $|\mathcal{M}'(u_*)| < 1$, then the fixed point u_* is stable. On the other hand, if $|\mathcal{M}'(u_*)| > 1$, then u_* is unstable. Moreover, the special properties of the map $\mathcal{M}(u)$, see Remark 7.7, allow us to conclude that a fixed point u_* with $|\mathcal{M}'(u_*)| = 1$ is also stable provided it is non-degenerate.

In the next proposition, we show that every Poincaré map (7.6) with $0 < |b| < 1$ has either a unique stable fixed point in the closed unit disc $\overline{\mathbb{D}}$, or a unique fixed point at all (in this case, the fixed point is degenerate and lies on the unit disc boundary $\partial\mathbb{D}$).

Proposition 7.6 *Suppose $\theta \in (-\pi, \pi]$ and $0 < |b| < 1$, then Eq. (7.10) has a unique solution $u_0 \in \mathbb{D}$ such that $|\mathcal{M}'(u_0)| \leq 1$. This solution is given by the formulas*

$$u_0 = \frac{i \sin(\theta/2) + \sqrt{|b|^2 - \sin^2(\theta/2)}}{|b|^2} b e^{i\theta/2} \quad \text{for} \quad |b| > |\sin(\theta/2)|, \quad (7.11)$$

$$u_0 = \frac{i \sin(\theta/2) - i \sqrt{\sin^2(\theta/2) - |b|^2}}{|b|^2} b e^{i\theta/2} \quad \text{for} \quad |b| \leq \sin(\theta/2),$$

$$u_0 = \frac{i \sin(\theta/2) + i \sqrt{\sin^2(\theta/2) - |b|^2}}{|b|^2} b e^{i\theta/2} \quad \text{for} \quad |b| \leq -\sin(\theta/2).$$

Moreover, $|u_0| = 1$ for $|b| \geq |\sin(\theta/2)|$, while $|u_0| < 1$ for $|b| < |\sin(\theta/2)|$. Furthermore, $|\mathcal{M}'(u_0)| < 1$ for $|b| > |\sin(\theta/2)|$, $|\mathcal{M}'(u_0)| = 1$ for $|b| < |\sin(\theta/2)|$, and $\mathcal{M}'(u_0) = 1$ for $|b| = |\sin(\theta/2)|$.

Proof: For every $|b| < 1$ and $u \in \mathbb{D}$ equation (7.10) can be rewritten in the form

$$e^{-i\theta/2} \bar{b} u^2 - 2i \sin(\theta/2) u - e^{i\theta/2} b = 0. \quad (7.12)$$

Since $b \neq 0$ this is a quadratic equation which generically has two complex roots. We are going to check which of these roots lie in the unit disc \mathbb{D} and what are their stability properties. To address the latter question we compute the derivative of the Möbius transformation (7.6)

$$\mathcal{M}'(u) = \frac{e^{i\theta}(1 - |b|^2)}{(\bar{b}u + 1)^2} \quad (7.13)$$

and evaluate its modulus (keeping in mind that $|b| < 1$)

$$|\mathcal{M}'(u)| = \frac{1 - |b|^2}{|\bar{b}u + 1|^2}. \quad (7.14)$$

Depending on the sign of the difference $|b|^2 - \sin^2(\theta/2)$ we distinguish two cases.

Case 1. Suppose $|b| > |\sin(\theta/2)|$, then two solutions to Eq. (7.12) read

$$u_{\pm} = \frac{i \sin(\theta/2) \pm \sqrt{|b|^2 - \sin^2(\theta/2)}}{\bar{b} e^{-i\theta/2}}.$$

It is easy to verify that in this case $|u_+| = |u_-| = 1$. Moreover, we also obtain

$$\begin{aligned} 1 - |b|^2 - |\bar{b}u_{\pm} + 1|^2 &= 1 - |b|^2 - \left(\cos(\theta/2) \pm \sqrt{|b|^2 - \sin^2(\theta/2)} \right)^2 \\ &= -2\sqrt{|b|^2 - \sin^2(\theta/2)} \left(\sqrt{|b|^2 - \sin^2(\theta/2)} \pm \cos(\theta/2) \right). \end{aligned}$$

Obviously, for every $\theta \in (-\pi, \pi]$ and $|\sin(\theta/2)| < |b| < 1$ we have

$$\cos(\theta/2) = \sqrt{1 - \sin^2(\theta/2)} > \sqrt{|b|^2 - \sin^2(\theta/2)},$$

therefore

$$1 - |b|^2 - |\bar{b}u_+ + 1|^2 < 0 \quad \text{and} \quad 1 - |b|^2 - |\bar{b}u_- + 1|^2 > 0, \quad (7.15)$$

and hence

$$|\mathcal{M}'(u_+)| < 1 \quad \text{and} \quad |\mathcal{M}'(u_-)| > 1.$$

Case 2. The other case is determined by the inequality $|b| \leq |\sin(\theta/2)|$. If $|b| < |\sin(\theta/2)|$, then Eq. (7.12) has two solutions

$$u_{\pm} = \frac{i \sin(\theta/2) \pm i \sqrt{\sin^2(\theta/2) - |b|^2}}{\bar{b}e^{-i\theta/2}}, \quad (7.16)$$

while for $|b| = |\sin(\theta/2)|$ the values u_+ and u_- given by (7.16) coincide. To estimate the moduli $|u_+|$ and $|u_-|$ we compute the difference

$$\left(\sin(\theta/2) \pm \sqrt{\sin^2(\theta/2) - |b|^2} \right)^2 - |b|^2 = 2\sqrt{\sin^2(\theta/2) - |b|^2} \left(\sqrt{\sin^2(\theta/2) - |b|^2} \pm \sin(\theta/2) \right).$$

Then for $\sin(\theta/2) > 0$ we obtain

$$\left(\sin(\theta/2) + \sqrt{\sin^2(\theta/2) - |b|^2} \right)^2 - |b|^2 > 0, \quad \left(\sin(\theta/2) - \sqrt{\sin^2(\theta/2) - |b|^2} \right)^2 - |b|^2 < 0,$$

and hence $|u_+| > 1$ and $|u_-| < 1$. Similarly, for $\sin(\theta/2) < 0$ we obtain $|u_+| < 1$ and $|u_-| > 1$.

Finally, we compute a difference relevant to formula (7.14)

$$1 - |b|^2 - |\bar{b}u_{\pm} + 1|^2 = 1 - |b|^2 - \left| \cos(\theta/2) \pm i \sqrt{\sin^2(\theta/2) - |b|^2} \right|^2 = 0,$$

which implies $|\mathcal{M}'(u_+)| = |\mathcal{M}'(u_-)| = 1$.

On the other hand, in the limiting case $|b| = |\sin(\theta/2)|$, formulas (7.13) and (7.16) yield $|u_+| = |u_-| = 1$ and $\mathcal{M}'(u_+) = \mathcal{M}'(u_-) = 1$. ■

Remark 7.7 Let us consider the formula (7.6) with $0 < |b| < |\sin(\theta/2)|$ in more detail. In this case, $\mathcal{M}(u)$ determines an elliptic Möbius transformation, see [75, Ch. 3.VII]. This means that it has two distinct fixed points that are neither attractive nor repulsive but indifferent. (Recall the equation $|\mathcal{M}'(u_{\pm})| = 1$ from the Case 2 in the proof of Proposition 7.6.) Moreover, the transformation moves all other points of the complex plane in circles around the two fixed points. Therefore, according to the Lyapunov stability classification, both fixed points are stable, but not asymptotically stable.

Similarly one can verify that the other two cases $|\sin(\theta/2)| < |b| < 1$ and $|b| = |\sin(\theta/2)| \neq 0$ considered in Proposition 7.6 correspond to the Möbius transformations $\mathcal{M}(u)$ of hyperbolic and parabolic types, respectively. This is in accordance with the fact that $\mathcal{M}(u)$ has a pair of attracting and repulsive fixed points in the former case and a degenerate fixed point in the latter case. Note that the degenerate fixed point of a parabolic Möbius transformation is always unstable in the sense of Lyapunov [75, Ch. 3.VII].

Remark 7.8 If $b = 0$, then Eq. (7.10) degenerates into the linear equation $e^{i\theta}u = u$. For $e^{i\theta} \neq 1$ this equation has only single solution $u = 0$, while for $e^{i\theta} = 1$ it becomes trivial identity $u = u$ and hence has infinitely many solutions $u \in \overline{\mathbb{D}}$. In both cases all the solutions are stable, because $\mathcal{M}(u)$ is linear and $|\mathcal{M}'(u)| = 1$. Moreover, the case $b = 0$ and $e^{i\theta} = 1$ corresponds to the equation (7.4) with $w(t) = 0$ and $s = 0$.

Remark 7.9 If u_0 is determined by formula (7.11), then $\mathcal{M}'(u_0)$ is real and $\mathcal{M}'(u_0) \in (0, 1)$. Indeed, formula (7.11) implies

$$\bar{b}u_0 = \left(i \sin(\theta/2) + \sqrt{|b|^2 - \sin^2(\theta/2)} \right) e^{i\theta/2},$$

therefore

$$\bar{b}u_0 + 1 = \left(\cos(\theta/2) + \sqrt{|b|^2 - \sin^2(\theta/2)} \right) e^{i\theta/2}.$$

Hence the assertion follows from formula (7.13) and from the first of two inequalities (7.15).

7.2 Solution operator \mathcal{U} for periodic complex Riccati equation

In the previous section we showed that for every $W \in C_{\text{per}}([0, 2\pi]; \mathbb{C})$ and $s \in \mathbb{R}$ the complex Riccati equation (7.4) has a uniquely determined 2π -periodic solution $u(t) \in \overline{\mathbb{D}}$ that is stable in the sense of Lyapunov (or at least linearly stable in the degenerate case). Let us denote the corresponding solution operator

$$\mathcal{U} : C_{\text{per}}([0, 2\pi]; \mathbb{C}) \times \mathbb{R} \rightarrow C_{\text{per}}^1([0, 2\pi]; \mathbb{C}).$$

The definition of \mathcal{U} is constructive and relies on the following steps:

1) Given $W(t)$ and s one solves two initial value problems (7.7) and (7.8) and obtains coefficients b and θ of the Möbius transformation (7.6), see Proposition 7.5.

2) Using Proposition 7.6 one computes the initial value u_0 of the periodic solution $u(t)$ that lies entirely in the unit disc $\overline{\mathbb{D}}$ and, moreover, is stable provided $|b| \neq |\sin(\theta/2)|$. In the case $b = 0$, one assumes $u_0 = 0$, see Remark 7.8.

3) One integrates Eq. (7.4) with the initial condition $u(0) = u_0$ and obtains 2π -periodic solution $u(t)$.

Importantly, Propositions 7.5 and 7.6 ensure that the steps 1–3 can always be realized. Therefore, the mapping $\mathcal{U} : (W(t), s) \mapsto u(t)$ is well-defined.

Remark 7.10 *Note that the minimal period of the function $u(t) = \mathcal{U}(W(t), s)$ does not have to be 2π . In general, it can assume any value $2\pi/k$ with $k \in \mathbb{N}$. Moreover, for certain values of the arguments $(W(t), s)$ the operator \mathcal{U} can also return a constant function $u(t)$.*

Due to the definition of \mathcal{U} we have $|u(t)| \leq 1$ for all $t \in [0, 2\pi]$, therefore \mathcal{U} is a bounded operator. Moreover, the operator \mathcal{U} has a specific dichotomy property:

Proposition 7.11 *Let $W_* \in C_{\text{per}}([0, 2\pi]; \mathbb{C})$, $s_* \in \mathbb{R}$ and $u_* = \mathcal{U}(W_*, s_*)$. Moreover, let*

$$M_* = \exp \left(- \int_0^{2\pi} (is_* + 2\overline{W}_*(t)u_*(t))dt \right). \quad (7.17)$$

Then either $|u_(t)| = 1$ for all $t \in [0, 2\pi]$ and M_* is a real number such that $M_* \in (0, 1]$, or $|u_*(t)| < 1$ for all $t \in [0, 2\pi]$ and $|M_*| = 1$.*

Proof: We need only to show that $M_* = \mathcal{M}'(u_0)$ where $u_0 = u_*(0)$. Then the assertion follows from Propositions 7.2 and 7.6 and from Remarks 7.8 and 7.9.

Let us consider Eq. (7.4) for $W(t) = W_*(t)$ and $s = s_*$. Inserting there ansatz $u(t) = u_*(t) + v(t)$ and linearizing the resulting equation with respect to small perturbations $v(t)$ we obtain

$$\frac{dv}{dt} = -(is_* + 2\overline{W}_*(t)u_*(t))v. \quad (7.18)$$

Obviously, formula (7.17) determines the Floquet multiplier of the scalar linear equation (7.18). By definition its value coincides with the derivative of the Poincaré map of the original nonlinear equation (7.4), hence $M_* = \mathcal{M}'(u_0)$ where $u_0 = u_*(0)$. ■

Remark 7.12 *Proposition 7.6 and Remark 7.8 imply that $u_0 = u_*(0)$ is a simple fixed point of Eq. (7.10), if and only if $M_* \neq 1$. Therefore, the equation $M_* = 1$ can be considered as a degeneracy or bifurcation condition.*

7.3 Derivatives of the solution operator \mathcal{U}

In this section we show how to compute partial derivatives of the operator \mathcal{U} .

Proposition 7.13 *Let $W_* \in C_{\text{per}}([0, 2\pi]; \mathbb{C})$, $s_* \in \mathbb{R}$ and $u_* = \mathcal{U}(W_*, s_*)$. Suppose*

$$\Phi_*(2\pi) \neq 1 \quad \text{where} \quad \Phi_*(t) = \exp\left(-\int_0^t (is_* + 2\overline{W}_*(\tau)u_*(\tau))d\tau\right),$$

then there exists a bounded linear operator $\mathcal{J} : C_{\text{per}}([0, 2\pi]; \mathbb{C}) \rightarrow C_{\text{per}}^1([0, 2\pi]; \mathbb{C})$ such that $v(t) = (\mathcal{J}f)(t)$ is a 2π -periodic solution of the equation

$$\frac{dv}{dt} + (is_* + 2\overline{W}_*(t)u_*(t))v(t) = f(t).$$

Moreover

$$(\mathcal{J}f)(t) = \int_0^{2\pi} \frac{\Phi_*(2\pi) + (1 - \Phi_*(2\pi))\Theta(t - \tau)}{1 - \Phi_*(2\pi)} \Phi_*(t)\Phi_*^{-1}(\tau)f(\tau)d\tau$$

where $\Theta(t)$ is the Heaviside step function such that $\Theta(t) = 0$ for $t < 0$ and $\Theta(t) = 1$ for $t \geq 0$.

Proof: This assertion has been proved in [83, Proposition A.1]. ■

Proposition 7.14 *Let the assumptions of Proposition 7.13 be fulfilled. Then for every $W \in C_{\text{per}}([0, 2\pi]; \mathbb{C})$ we have*

$$\partial_\varepsilon \mathcal{U}(W_* + \varepsilon W, s_*)|_{\varepsilon=0} = \mathcal{J}(W - u_*^2 \overline{W}), \quad (7.19)$$

$$\partial_s \mathcal{U}(W_*, s_*) = \mathcal{J}(-iu_*). \quad (7.20)$$

Proof: For every $\varepsilon \in \mathbb{R}$ function $v(t, \varepsilon, s) = \mathcal{U}(W_*(t) + \varepsilon W(t), s)$ satisfies

$$\frac{dv(t, \varepsilon, s)}{dt} = W_*(t) + \varepsilon W(t) - isv(t, \varepsilon, s) - (\overline{W}_*(t) + \varepsilon \overline{W}(t))v^2(t, \varepsilon, s). \quad (7.21)$$

Differentiating this identity with respect to ε and inserting $\varepsilon = 0$ and $s = s_*$, we obtain

$$\frac{dv_\varepsilon(t, 0, s_*)}{dt} = W(t) - (is_* + 2\overline{W}_*(t)u_*(t))v_\varepsilon(t, 0, s_*) - \overline{W}(t)u_*^2(t). \quad (7.22)$$

Now, using Proposition 7.13 we solve Eq. (7.22) with respect to $v_\varepsilon(t, 0, s_*)$ and obtain formula (7.19).

Formula (7.20) is justified similarly. We differentiate (7.21) with respect to s and solve the resulting equation using Proposition 7.13. ■

7.4 Self-consistency equation

Suppose that Eq. (2.19) has a solution of the form (7.1) where $a(x, t + T) = a(x, t)$ for some $T > 0$. Let us define

$$\omega = \frac{2\pi}{T} \quad \text{and} \quad u(x, t) = a\left(x, \frac{t}{\omega}\right), \quad (7.23)$$

then the new function $u(x, t)$ is 2π -periodic with respect to t and satisfies

$$\omega \frac{du}{dt} = -i\Omega u + \frac{1}{2}e^{-i\alpha}\mathcal{G}u - \frac{1}{2}e^{i\alpha}u^2\mathcal{G}\bar{u}. \quad (7.24)$$

Dividing Eq. (7.24) by ω and introducing the notations

$$s = \frac{\Omega}{\omega} \quad \text{and} \quad w(x, t) = \frac{e^{-i\alpha}}{2\omega}\mathcal{G}u, \quad (7.25)$$

we rewrite Eq. (7.24) in the form

$$\frac{dw}{dt} = w(x, t) - isu - \bar{w}(x, t)u^2. \quad (7.26)$$

In Section 7.1 we showed that every stable solution to Eq. (7.26) that lies entirely in the unit disc $\bar{\mathbb{D}}$ is given by the formula $u(x, t) = \mathcal{U}(w(x, t), s)$. Inserting this result into the definition of $w(x, t)$ we arrive at a self-consistency equation

$$w(x, t) = \frac{e^{-i\alpha}}{2\omega}\mathcal{G}\mathcal{U}(w(x, t), s),$$

which can be written in the equivalent form (7.2).

Eq. (7.24) has several continuous symmetries. More precisely, the set of its solutions is invariant with respect to the following transformations:

- 1) spatial translations $u(x, t) \mapsto u(x + c, t)$ for $c \in \mathbb{R}$,
- 2) complex phase shifts $u(x, t) \mapsto u(x, t)e^{i\phi}$ for $\phi \in \mathbb{R}$,
- 3) time shifts $u(x, t) \mapsto u(x, t + \tau)$ for $\tau \in \mathbb{R}$.

All these symmetries are inherited by the self-consistency equation (7.2), therefore to select its unique solution $w(x, t)$ we need to provide three pinning conditions. In practice, this number can be reduced by one if we restrict Eq. (7.2) to the space of even functions

$$X_e = \left\{ w \in C_{\text{per}}([- \pi, \pi] \times [0, 2\pi]; \mathbb{C}) : w(-x, t) = w(x, t) \quad \text{for all} \quad (x, t) \in [- \pi, \pi] \times [0, 2\pi] \right\}.$$

Indeed, for symmetric coupling functions $G(x)$ equation (7.2) is reflection symmetric with respect to x , therefore we can look for solutions $w(x, t)$ satisfying $w(-x, t) = w(x, t)$ only.

In this case the spatial translation symmetry is eliminated automatically. Then two pinning conditions relevant to the complex phase shift and the time shift can be chosen in the form

$$\operatorname{Im} \left(\int_{-\pi}^{\pi} dx \int_0^{2\pi} w(x, t) dt \right) = 0, \quad (7.27)$$

$$\operatorname{Im} \left(\int_{-\pi}^{\pi} dx \int_0^{2\pi} w(x, t) e^{it} dt \right) = 0. \quad (7.28)$$

In the next sections we will show that the augmented system consisting of Eqs. (7.2), (7.27) and (7.28) is well-defined. This means that for fixed phase lag α and kernel $G(x)$ it correctly determines the unknown even function $w(x, t)$ and two scalar parameters ω and s .

Proposition 7.15 *Let the triple $(w(x, t), \omega, s)$ be a solution to the self-consistency equation (7.2) and let $u(x, t) = \mathcal{U}(w(x, t), s)$ and $a(x, t) = u(x, \omega t)$. Then the continuum limit analog of the global order parameter can be computed by*

$$|Z(t)| = \frac{1}{2\pi} \left| \int_{-\pi}^{\pi} a(x, t) dx \right| = \frac{1}{2\pi} \left| \int_{-\pi}^{\pi} u(x, \omega t) dx \right|,$$

while the effective frequency profile is given by

$$\Omega_{\text{eff}}(x) = -\operatorname{Im} \left(\frac{1}{T} \int_0^T e^{i\alpha} a(x, t) (\mathcal{G}\bar{a})(x, t) dt \right) = -2\omega \operatorname{Im} \left(\frac{1}{2\pi} \int_0^{2\pi} u(x, t) \bar{w}(x, t) dt \right).$$

Proof: The first formula for $|Z(t)|$ follows directly from (2.20). In order to obtain the second formula for $\Omega_{\text{eff}}(x)$ we insert the ansatz $z = a(x, t)e^{i\Omega t}$ into (2.21) and use (7.23) and (7.25). ■

7.5 Modified self-consistency equation

In this section we show that the phase shift symmetry can also be eliminated from Eq. (7.2). Then we decrease the number of equations and unknowns in the augmented system described above.

Let us define a linear operator

$$\mathcal{P} : C_{\text{per}}([-\pi, \pi] \times [0, 2\pi]; \mathbb{C}) \rightarrow \mathbb{C}, \quad \mathcal{P}w = \frac{1}{(2\pi)^2} \int_{-\pi}^{\pi} dx \int_0^{2\pi} w(x, t) dt,$$

which gives a constant part of the function $w(x, t)$. Using this operator and the identity operator \mathcal{I} , we rewrite Eq. (7.2) in the equivalent form

$$\begin{aligned} 2\omega e^{i\alpha} \mathcal{P}w &= \mathcal{P}\mathcal{G}\mathcal{U}(w, s), \\ 2\omega e^{i\alpha} (\mathcal{I} - \mathcal{P})w &= (\mathcal{I} - \mathcal{P})\mathcal{G}\mathcal{U}(w, s). \end{aligned} \quad (7.29)$$

Dividing the latter equation by the former one (which is a scalar equation!) we obtain

$$\frac{(\mathcal{I} - \mathcal{P})w}{\mathcal{P}w} = \frac{(\mathcal{I} - \mathcal{P})\mathcal{G}\mathcal{U}(w, s)}{\mathcal{P}\mathcal{G}\mathcal{U}(w, s)},$$

or equivalently

$$(\mathcal{P}\mathcal{G}\mathcal{U}(w, s))(\mathcal{I} - \mathcal{P})w = (\mathcal{P}w)(\mathcal{I} - \mathcal{P})\mathcal{G}\mathcal{U}(w, s). \quad (7.30)$$

If we assume

$$w(x, t) = p + v(x, t), \quad \text{where } p \in (0, \infty) \quad \text{and} \quad v(x, t) \in \{u \in X_e : \mathcal{P}u = 0\}, \quad (7.31)$$

then pinning condition (7.27) is fulfilled automatically and can be discarded. Moreover, inserting the ansatz (7.31) into Eq. (7.30) and pinning condition (7.28) we obtain

$$(\mathcal{P}\mathcal{G}\mathcal{U}(p + v, s))v = p(\mathcal{I} - \mathcal{P})\mathcal{G}\mathcal{U}(p + v, s), \quad (7.32)$$

and

$$\text{Im} \left(\int_{-\pi}^{\pi} dx \int_0^{2\pi} v(x, t) e^{it} dt \right) = 0. \quad (7.33)$$

Now instead of solving the system of equations (7.2), (7.27) and (7.28), we can look for solutions of the system comprising Eqs. (7.32) and (7.33). In this case $p > 0$ must be given, then the system of equations (7.32) and (7.33) has to be solved with respect to two unknowns: scalar parameter s and even function $v(x, t)$ satisfying $\mathcal{P}v = 0$. As soon as such solution is found, one can compute the corresponding values of ω and α from Eq. (7.29) written in the form

$$2\omega e^{i\alpha} = \frac{1}{p} \mathcal{P}\mathcal{G}\mathcal{U}(p + v, s).$$

7.6 Modified self-consistency equation for cosine coupling function

In this section we consider a specific example of integral operator \mathcal{G} and show how system (7.32), (7.33) can be solved approximately using Galerkin's method. For this we assume that $G(x)$ is the cosine coupling function (6.2).

Given a positive integer F let us define a set of $8F + 2$ functions $\psi_k(x, t)$

$$\begin{aligned} & \sqrt{2} \cos x, \quad i\sqrt{2} \cos x, \\ & e^{imt}, \quad ie^{imt}, \quad e^{imt}\sqrt{2} \cos x, \quad ie^{imt}\sqrt{2} \cos x, \quad m = -F, \dots, -1, 1, \dots, F. \end{aligned}$$

Note that $m \neq 0$, therefore constant functions $\sqrt{2}$ and $i\sqrt{2}$ are not included in the set. The order of $\psi_k(x, t)$ is irrelevant apart from the only place below where we will assume $\psi_8(x, t) = ie^{-it}$.

It is easy to verify that $\psi_k(x, t)$ satisfy the orthonormality condition $\langle \psi_k, \psi_n \rangle = \delta_{kn}$ with respect to the scalar product

$$\langle u, v \rangle = \text{Re} \left(\frac{1}{(2\pi)^2} \int_{-\pi}^{\pi} dx \int_0^{2\pi} \bar{u}(x, t) v(x, t) dt \right),$$

where δ_{kn} is the Kronecker delta. Hence functions $\psi_k(x, t)$ span a finite-dimensional subspace of $\{u \in X_e : \mathcal{P}u = 0\}$. We look for approximate solution to Eq. (7.32) in the form

$$v(x, t) = \sum_{k=1}^{8F+2} c_k \psi_k(x, t) \quad (7.34)$$

where $c_k \in \mathbb{R}$ are unknown coefficients. Inserting (7.34) into Eq. (7.32) we write $8F + 2$ orthogonality conditions

$$\langle \psi_n, (\mathcal{P}\mathcal{G}\mathcal{U}(p + v, s))v \rangle = p \langle \psi_n, (\mathcal{I} - \mathcal{P})\mathcal{G}\mathcal{U}(p + v, s) \rangle, \quad n = 1, \dots, 8F + 2.$$

Since for the cosine coupling function $G(x)$ it holds $\mathcal{P}\mathcal{G} = \mathcal{P}$, the above system can be written as follows

$$\sum_{k=1}^{8F+2} \left\langle \psi_n, \psi_k \mathcal{P}\mathcal{U} \left(p + \sum_{m=1}^{8F+2} c_m \psi_m, s \right) \right\rangle c_k = p \left\langle \psi_n, (\mathcal{I} - \mathcal{P})\mathcal{G}\mathcal{U} \left(p + \sum_{m=1}^{8F+2} c_m \psi_m, s \right) \right\rangle. \quad (7.35)$$

To account for the pinning condition (7.33) we assume $\psi_8(x, t) = ie^{-it}$, then

$$\text{Im} \left(\int_{-\pi}^{\pi} dx \int_0^{2\pi} v(x, t) e^{it} dt \right) = \text{Re} \left(\int_{-\pi}^{\pi} dx \int_0^{2\pi} v(x, t) (-i) e^{it} dt \right) = (2\pi)^2 \langle \psi_8, v \rangle.$$

This means $c_8 = 0$. Inserting this identity into Eq. (7.35) we end up with a system of $8F + 2$ nonlinear equations with respect to $8F + 2$ real unknowns (these are $8F + 1$ coefficients c_k with $k \neq 8$ and the parameter s). The system (7.35) can be solved by Newton's method, using a semi-analytic Jacobian expression involving the derivative representations obtained in Section 7.3. Note that breathing chimera states typically have a very fine spatial structure, therefore to approximate the integrals in (7.35) with the same accuracy, one needs to use either a nonuniform grid with a moderate number of nodes in the x -direction, or a uniform grid with a much larger number of nodes. For example, all numerical results reported in Section 7.9 were obtained using a nonuniform grid with ca. 10^3 discretization points in the x -direction (the distribution of points, in this case, was 10 to 100 times denser in the vicinity of the coherence-incoherence boundaries than in the other regions of the chimera state). On a uniform grid, the same accuracy would be achieved only with at least 10^5 discretization points, what would lead to extremely large computational times.

7.7 Stability analysis of relative periodic orbits

Suppose that Eq. (2.19) has a solution of the form

$$z = a(x, t)e^{i\Omega t}, \quad (7.36)$$

where $a(x, t)$ is T -periodic with respect to its second argument. To analyze the stability of this solution we insert the ansatz

$$z = (a(x, t) + v(x, t))e^{i\Omega t}$$

into Eq. (2.19) and linearize it with respect to the small perturbation $v(x, t)$. In the result we obtain a linear equation with T -periodic coefficients

$$\frac{dv}{dt} = -\eta(x, t)v + \frac{1}{2}e^{-i\alpha}\mathcal{G}v - \frac{1}{2}e^{i\alpha}a^2(x, t)\mathcal{G}\bar{v}, \quad (7.37)$$

where

$$\eta(x, t) = i\Omega + e^{i\alpha}a(x, t)\mathcal{G}\bar{a}. \quad (7.38)$$

Along with Eq. (7.37) it is convenient to consider its complex-conjugate version

$$\frac{d\bar{v}}{dt} = -\bar{\eta}(x, t)\bar{v} + \frac{1}{2}e^{i\alpha}\mathcal{G}\bar{v} - \frac{1}{2}e^{-i\alpha}\bar{a}^2(x, t)\mathcal{G}v.$$

These two equations can be written in the operator form

$$\frac{dV}{dt} = \mathcal{A}(t)V + \mathcal{B}(t)V, \quad (7.39)$$

where $V(t) = (v_1(t), v_2(t))^T$ is a function with values in $C_{\text{per}}([-\pi, \pi]; \mathbb{C}^2)$, and

$$\mathcal{A}(t)V = \begin{pmatrix} -\eta(\cdot, t) & 0 \\ 0 & -\bar{\eta}(\cdot, t) \end{pmatrix} \begin{pmatrix} v_1 \\ v_2 \end{pmatrix},$$

and

$$\mathcal{B}(t)V = \frac{1}{2} \begin{pmatrix} e^{-i\alpha} & -e^{i\alpha}a^2(\cdot, t) \\ -e^{-i\alpha}\bar{a}^2(\cdot, t) & e^{i\alpha} \end{pmatrix} \begin{pmatrix} \mathcal{G}v_1 \\ \mathcal{G}v_2 \end{pmatrix}.$$

For every fixed t the operators $\mathcal{A}(t)$ and $\mathcal{B}(t)$ are linear operators from $C_{\text{per}}([-\pi, \pi]; \mathbb{C}^2)$ into itself. Moreover, they both depend continuously on t and thus their norms are uniformly bounded for all $t \in [0, T]$.

Our further consideration is concerned with the stability of the zero solution to Eq. (7.39). Therefore, we are dealing only with the linear stability of the solution (7.36). We apply the

methods of qualitative analysis of differential equations in Banach spaces [22]. Since $\mathcal{A}(t)$ and $\mathcal{B}(t)$ are uniformly bounded operators, we can define an operator exponent

$$\mathcal{E}(t) = \exp \left(\int_0^t (\mathcal{A}(t') + \mathcal{B}(t')) dt' \right).$$

Then the solution of Eq. (7.39) with the initial condition $V(0) = V_0$ is given by the formula $V(t) = \mathcal{E}(t)V_0$. Recalling that $\mathcal{A}(t)$ and $\mathcal{B}(t)$ are T -periodic, we conclude [22, Chapter V] that the stability of the zero solution to Eq. (7.39) is determined by the spectrum of the *monodromy operator* $\mathcal{E}(T)$. Roughly speaking, the necessary condition for the stability of the zero solution to Eq. (7.39) is that the spectrum of the operator $\mathcal{E}(T)$ lies entirely in the unit circle on the complex plane. Otherwise, this solution is unstable.

The main problem in the application of the above stability criterion is concerned with the fact that the monodromy operator $\mathcal{E}(T)$ acts in an infinite-dimensional functional space. Therefore, its spectrum consists of infinitely many points, which can be arbitrarily distributed in the complex plane. Below we use the explicit form of the operators $\mathcal{A}(t)$ and $\mathcal{B}(t)$ and show the following properties of the monodromy operator $\mathcal{E}(T)$:

(i) The spectrum of the operator $\mathcal{E}(T)$ is bounded and symmetric with respect to the real axis of the complex plane. It consists of two qualitatively different parts: essential spectrum Σ_{ess} and discrete spectrum Σ_{disc} .

(ii) The essential spectrum Σ_{ess} is given by

$$\Sigma_{\text{ess}} = \left\{ \exp \left(- \int_0^T \eta(x, t) dt \right) : x \in [-\pi, \pi] \right\} \cup \{\text{c.c.}\}. \quad (7.40)$$

(iii) The discrete spectrum Σ_{disc} comprises finitely many isolated eigenvalues μ , which can be found using the formula $\mu = e^{\lambda T}$ where λ are roots of a characteristic equation specified below.

Proposition 7.16 *The monodromy operator $\mathcal{E}(T)$ can be written as a sum*

$$\mathcal{E}(T) = \mathcal{E}_0(T) + \mathcal{K}, \quad (7.41)$$

where $\mathcal{E}_0(T)$ is a multiplication operator of the form

$$\mathcal{E}_0(T) = \exp \left(\int_0^T \mathcal{A}(t) dt \right),$$

and \mathcal{K} is a compact operator from $C_{\text{per}}([-\pi, \pi]; \mathbb{C}^2)$ into itself.

Proof: Every function $V(t)$ satisfying Eq. (7.39) and the initial condition $V(0) = V_0$ solves also integral equation

$$V(t) = \mathcal{E}_0(t)V_0 + \int_0^t \mathcal{E}_0(t)\mathcal{E}_0^{-1}(t')\mathcal{B}(t')V(t')dt', \quad (7.42)$$

where

$$\mathcal{E}_0(t) = \exp\left(\int_0^t \mathcal{A}(t')dt'\right).$$

On the other hand, every solution to Eq. (7.42) can be decomposed into a sum

$$V(t) = \mathcal{E}_0(t)V_0 + W(t), \quad (7.43)$$

where $W(t)$ is a solution to integral equation

$$W(t) = \int_0^t \mathcal{E}_0(t)\mathcal{E}_0^{-1}(t')\mathcal{B}(t')\mathcal{E}_0(t')V_0dt' + \int_0^t \mathcal{E}_0(t)\mathcal{E}_0^{-1}(t')\mathcal{B}(t')W(t')dt'. \quad (7.44)$$

The Volterra integral equation (7.44) has unique solution $W(t)$ that continuously depends on the initial value V_0 . Moreover, the mapping $V_0 \mapsto W(T)$ is a compact operator from $C_{\text{per}}([-\pi, \pi]; \mathbb{C}^2)$ into itself (recall the compactness of the operator \mathcal{G} involved in the definition of the operator $\mathcal{B}(t)$). This fact along with the formula (7.43) implies that the monodromy operator $\mathcal{E}(T)$ is the sum of the multiplication operator $\mathcal{E}_0(T)$ and a compact operator abbreviated by $W(T)$. \blacksquare

The spectrum of monodromy operator $\mathcal{E}(T)$ consists of all numbers $\mu \in \mathbb{C}$ such that the difference operator $\mathcal{E}(T) - \mu\mathcal{I}$ is not invertible. Because of the definition of $\mathcal{A}(t)$ and $\mathcal{B}(t)$ this spectrum is symmetric with respect to the real axis. Moreover, since $\mathcal{A}(t)$ and $\mathcal{B}(t)$ are uniformly bounded for $t \in [0, T]$, the monodromy operator $\mathcal{E}(T)$ is bounded too, and hence its spectrum lies in a circle of finite radius of the complex plane. Other spectral properties of $\mathcal{E}(T)$ follow from the decomposition formula (7.41).

Indeed, formula (7.41) implies [46] that the essential spectrum of monodromy operator $\mathcal{E}(T)$ coincides with the spectrum of multiplication operator $\mathcal{E}_0(T)$. Using the definition of $\mathcal{A}(t)$ we obtain

$$\mathcal{E}_0(t) = \begin{pmatrix} \Phi(x, t) & 0 \\ 0 & \bar{\Phi}(x, t) \end{pmatrix},$$

where

$$\Phi(x, t) = \exp\left(-\int_0^t \eta(x, t')dt'\right).$$

This allows us to calculate the spectrum of $\mathcal{E}_0(T)$ explicitly and obtain formula (7.40) for Σ_{ess} .

Remark 7.17 Suppose that we consider a relative periodic orbit (7.36) with the amplitude $a(x, t)$, primary frequency Ω and secondary frequency ω satisfying the self-consistency equation (7.2) where $w(x, t)$ and s are defined by (7.3). Then inserting (7.23) and (7.25) into (7.38) we obtain

$$\exp\left(-\int_0^T \eta(x, t) dt\right) = \exp\left(-\int_0^{2\pi} (is + 2\bar{w}(x, t)u(x, t)) dt\right)$$

and therefore formula (7.40) and Proposition 7.11 imply that every $\mu \in \Sigma_{\text{ess}}$ lies either on the boundary of the unit circle $|\mu| = 1$ or on the interval $(0, 1)$ of the real axis. Hence the essential spectrum Σ_{ess} cannot be relevant to any instability of the solution (7.36) obtained from the self-consistency equation (7.2). Note that, in general, Eq. (2.19) may have solutions of the form (7.36) with an unstable essential spectrum, but such solutions don't satisfy the self-consistency equation (7.2).

Formula (7.41) also implies

$$\mathcal{E}(T) - \mu\mathcal{I} = (\mathcal{E}_0(T) - \mu\mathcal{I}) + \mathcal{K}.$$

For every $\mu \notin \Sigma_{\text{ess}}$ the right-hand side of this formula reads as a sum of the invertible operator $\mathcal{E}_0(T) - \mu\mathcal{I}$ and the compact operator \mathcal{K} , hence it defines a Fredholm operator of index zero. This means that apart from the essential spectrum Σ_{ess} the monodromy operator $\mathcal{E}(T)$ can have a discrete spectrum Σ_{disc} consisting of eigenvalues of finite multiplicity. Since the entire spectrum $\Sigma_{\text{ess}} \cup \Sigma_{\text{disc}}$ is confined in a bounded region of the complex plane, there can be at most finitely many such eigenvalues. These eigenvalues can be computed only numerically and in the following we outline the way how this can be done.

Proposition 7.18 Let λ be a complex number such that the equation

$$\frac{dV}{dt} = \mathcal{A}(t)V + \mathcal{B}(t)V - \lambda V \tag{7.45}$$

has a nontrivial T -periodic solution, then the number $\mu = e^{\lambda T}$ is an eigenvalue of the monodromy operator $\mathcal{E}(T)$. Conversely, for every nonzero $\mu \in \Sigma_{\text{disc}}$ there exists a number $\lambda \in \mathbb{C}$ such that Eq. (7.45) has a nontrivial T -periodic solution and $\mu = e^{\lambda T}$.

Proof: Eq. (7.45) has a nontrivial T -periodic solution if and only if

$$\exp\left(\int_0^T (\mathcal{A}(t') + \mathcal{B}(t') - \lambda\mathcal{I}) dt'\right) = \exp\left(\int_0^T (\mathcal{A}(t') + \mathcal{B}(t')) dt'\right) e^{-\lambda T} = \mathcal{I}.$$

This is equivalent to the identity $\mathcal{E}(T) = e^{\lambda T}\mathcal{I}$ that ends the proof. ■

Remark 7.19 Notice that formula $\mu = e^{\lambda T}$ isn't a one-to-one relation between λ and μ . For every $\lambda \in \mathbb{C}$ it yields one value μ . In contrast, given a nonzero μ one obtains infinitely many corresponding values λ , namely $\lambda = (\log \mu + 2\pi ki)/T$ with $k \in \mathbb{Z}$.

Proposition 7.20 Let λ be a complex number such that $e^{\lambda T} \notin \Sigma_{\text{ess}}$, then for every continuous T -periodic function $F(t)$ there exists a unique T -periodic solution of equation

$$\frac{dV}{dt} = (\mathcal{A}(t) - \lambda \mathcal{I})V + F(t),$$

which is given by

$$V(t) = \int_0^T \mathcal{D}_\lambda(t, t') F(t') dt'$$

where

$$\mathcal{D}_\lambda(t, t') = (\mathcal{I} - \mathcal{E}_\lambda(T))^{-1} (\mathcal{E}_\lambda(T) + \Theta(t - t') (\mathcal{I} - \mathcal{E}_\lambda(T))) \mathcal{E}_\lambda(t) \mathcal{E}_\lambda^{-1}(t')$$

and

$$\mathcal{E}_\lambda(t) = \exp \left(\int_0^t (\mathcal{A}(t') - \lambda \mathcal{I}) dt' \right) = \mathcal{E}_0(t) e^{-\lambda t}.$$

Proof: This assertion can be proved by analogy with [83, Proposition A.1]. ■

Proposition 7.20 implies that for every $\lambda \in \mathbb{C}$ such that $e^{\lambda T} \notin \Sigma_{\text{ess}}$ all T -periodic solutions $V(t)$ of Eq. (7.45) satisfy also the integral equation

$$V(t) = \int_0^T \mathcal{D}_\lambda(t, t') \mathcal{B}(t') V(t') dt'. \tag{7.46}$$

This fact can be used to compute the discrete spectrum Σ_{disc} numerically. To this end let us choose $C > 0$ and consider Eq. (7.46) in the rectangular region

$$\Pi = \{\lambda \in \mathbb{C} : |\operatorname{Re} \lambda| \leq C, |\operatorname{Im} \lambda| \leq \pi/T\}.$$

If we find all $\lambda \in \Pi$ such that Eq. (7.46) has a bounded nontrivial solution $V(t)$, then according to Proposition 7.18 and Remark 7.19 we also find all eigenvalues $\mu = e^{\lambda T}$ of the monodromy operator $\mathcal{E}(T)$ lying in the circular region $e^{-CT} \leq |\mu| \leq e^{CT}$. Since the spectrum of the monodromy operator $\mathcal{E}(T)$ is bounded, this ensures that for sufficiently large C we determine all eigenvalues $\mu \in \Sigma_{\text{disc}}$ relevant to the stability of the solution (7.36). Indeed, considering Eq. (7.46) for $\lambda \in \Pi$ we may overlook eigenvalues μ in the circle $|\mu| \leq e^{-CT}$. However, all these eigenvalues satisfy $|\mu| < 1$ and therefore have no impact on the stability of the solution (7.36).

7.8 Computation of the discrete spectrum

Recalling the definitions of $\mathcal{B}(t)$ and $\mathcal{D}_\lambda(t, t')$ it is easy to see that Eq. (7.46) is a homogeneous Fredholm integral equation. In general, it cannot be solved explicitly, but its solutions can be found approximately using Galerkin's method. For this one needs to choose a set of linearly independent functions $\varphi_k(x, t)$, $k = 1, \dots, K$, which are 2π -periodic with respect to x and T -periodic with respect to t . Without loss of generality it can be assumed that these functions are orthonormalized with respect to the scalar product

$$\langle\langle v_1, v_2 \rangle\rangle = \frac{1}{2\pi T} \int_0^T dt \int_{-\pi}^{\pi} \bar{v}_1(x, t) v_2(x, t) dx$$

such that $\langle\langle \varphi_j, \varphi_k \rangle\rangle = \delta_{jk}$. Then one looks for an approximate solution to Eq. (7.46) in the form

$$V(t) = \sum_{k=1}^K V_k \varphi_k(\cdot, t), \quad \text{where } V_k \in \mathbb{C}^2.$$

Inserting this ansatz into Eq. (7.46) and writing the projected problem yield

$$V_n = \sum_{k=1}^K \left\langle\left\langle \varphi_n, \int_0^T \mathcal{D}_\lambda(t, t') \mathcal{B}(t') \varphi_k(\cdot, t') dt' \right\rangle\right\rangle V_k, \quad n = 1, \dots, K.$$

This is a system of linear algebraic equations for the K two-dimensional coefficients V_k . Obviously, it has a nontrivial solution if and only if λ satisfies the characteristic equation

$$\det(\mathbf{M}_{2K}(\lambda) - \mathbf{I}_{2K}) = 0, \quad (7.47)$$

where

$$\mathbf{M}_{2K}(\lambda) = \begin{pmatrix} \mathbf{B}_{11}(\lambda) & \dots & \mathbf{B}_{1K}(\lambda) \\ \vdots & \ddots & \vdots \\ \mathbf{B}_{K1}(\lambda) & \dots & \mathbf{B}_{KK}(\lambda) \end{pmatrix}$$

is a block matrix with the (2×2) -matrix entries

$$\mathbf{B}_{nk}(\lambda) = \left\langle\left\langle \varphi_n, \int_0^T \mathcal{D}_\lambda(t, t') \mathcal{B}(t') \varphi_k(\cdot, t') dt' \right\rangle\right\rangle. \quad (7.48)$$

Solving Eq. (7.47) one obtains approximate eigenvalues λ of Eq. (7.46) and hence the corresponding approximate eigenvalues $\mu = e^{\lambda T}$ of the monodromy operator $\mathcal{E}(T)$.

Taking into account that functions $\varphi_k(x, t)$ appearing in the definition of matrix $\mathbf{M}_{2K}(\lambda)$ must be 2π -periodic with respect to x and T -periodic with respect to t it is convenient to

choose them in the form of spatiotemporal Fourier modes. More precisely, let K_x and K_t be two positive integers, then we assume

$$\varphi_{nm}(x, t) = e^{inx+2\pi imt/T}, \quad n = -K_x, \dots, K_x, \quad m = -K_t, \dots, K_t.$$

Thus we obtain a set of $K = (2K_x + 1)(2K_t + 1)$ functions such that $\langle\langle \varphi_{nm}, \varphi_{n'm'} \rangle\rangle = \delta_{nn'} \delta_{mm'}$.

Notice that functions $\varphi_{nm}(x, t)$ have an important property. If coupling function $G(x)$ has a Fourier series representation

$$G(x) = g_0 + \sum_{k=1}^{\infty} 2g_k \cos(kx), \quad \text{where} \quad g_k = \frac{1}{2\pi} \int_{-\pi}^{\pi} G(x) e^{-ikx} dx = \frac{1}{2\pi} \int_{-\pi}^{\pi} G(x) \cos(kx) dx,$$

then for all integer indices n and m it holds

$$\mathcal{G}\varphi_{nm} = 2\pi g_n \varphi_{nm}.$$

This implies

$$\mathcal{B}(t)\varphi_{nm} = 2\pi g_n \mathcal{B}_0(t)\varphi_{nm}, \quad \text{where} \quad \mathcal{B}_0(t) = \frac{1}{2} \begin{pmatrix} e^{-i\alpha} & -e^{i\alpha} a^2(\cdot, t) \\ -e^{-i\alpha} \bar{a}^2(\cdot, t) & e^{i\alpha} \end{pmatrix},$$

therefore in the case of functions $\varphi_{nm}(x, t)$ formula (7.48) can be written

$$\mathbf{B}_{nmm'n'}(\lambda) = \frac{g_{n'}}{2\pi T} \int_{-\pi}^{\pi} dx \int_0^T dt \int_0^T \bar{\varphi}_{nm}(x, t) \mathcal{D}_\lambda(t, t') \mathcal{B}_0(t') \varphi_{n'm'}(x, t') dt'. \quad (7.49)$$

The main advantage of the latter expression is that it doesn't contain any operators, but only explicitly known functions. More precisely, the term $\mathcal{D}_\lambda(t, t')$ is a (2×2) -matrix with entries depending on x, t, t' and λ , while $\mathcal{B}_0(t')$ is a (2×2) -matrix with entries depending on x and t' . Importantly, the triple integration in (7.49) must be carried out for each entry of the resulting product matrix separately. As soon as all matrices $\mathbf{B}_{nmm'n'}(\lambda)$ are determined they must be combined into the block matrix $\mathbf{M}_{2K}(\lambda)$ and then the left-hand side of the characteristic equation (7.47) can be computed.

Remark 7.21 *In Section 7.4 we mentioned that Eq. (7.24) has three continuous symmetries. This implies that the monodromy operator $\mathcal{E}(T)$ has three linearly independent eigenfunctions corresponding to the unit eigenvalue $\mu = 1$. Respectively the characteristic equation (7.47) has the triple root $\lambda = 0$, which is embedded in the essential spectrum.*

7.9 Example of a breathing chimera state

Let us illustrate the performance of the methods developed in Section 7.4–7.8. For this we consider a breathing chimera state observed in the system (6.1)–(6.2) for $A = 1.05$ and $\alpha = \pi/2 - 0.16$. In Section 1.4 we showed that the primary frequency Ω and the secondary frequency ω of this state can be extracted from the time trajectory of the global order parameter $Z_N(t)$. As soon as the primary frequency Ω is known we can find the approximate values of the amplitude $a(x, t)$ in the ansatz (7.1)

$$a(x_k, t) = \frac{1}{2M + 1} \sum_{j=k-M}^{k+M} e^{i(\theta_j(t) - \Omega t)}, \quad (7.50)$$

where the indices j are taken modulo N , $x_k = -\pi + 2\pi k/N$ is the scaled position of the k th oscillator and $M = \lfloor \sqrt{N}/2 \rfloor$ is the largest integer that does not exceed $\sqrt{N}/2$. Note that formula (7.50) resembles the definition of local order parameter (1.21) but differs from it by the additional exponential factor $e^{-\Omega t}$. Inserting the approximate values of Ω , ω and $a(x, t)$ into formulas (7.23) and (7.25) we obtain approximate values of the parameter s and function $w(x, t)$. Finally using continuous symmetries of Eq. (7.24) we ensure that $w(x, t)$ is even with respect to x and satisfies the pinning conditions (7.27) and (7.28). The obtained function $w(x, t)$ can be represented as a Fourier series

$$w(x, t) = \sum_{k=-\infty}^{\infty} (\hat{w}_{0,k} + \hat{w}_{1,k} \cos x) e^{ikt}.$$

Then the leading coefficients $\hat{w}_{0,k}$, $\hat{w}_{1,k}$ with indices $k = -10, \dots, 10$ can be used as an initial guess in the Galerkin's system (7.35) with $F = 10$. The latter system was solved using Newton's method up to the accuracy 10^{-9} . The obtained set of coefficients c_k was transformed into function $w(x, t)$ using formulas (7.31) and (7.34). Then the corresponding solution $u(x, t)$ to Eq. (7.24) was computed using the operator \mathcal{U} defined in Section 7.2.

Figure 31(a),(b) shows an approximate amplitude $a(x, t)$ of the breathing chimera state in the system (6.1)–(6.2) with $N = 8192$ oscillators for $A = 1.05$ and $\alpha = \pi/2 - 0.16$. The amplitude was computed using formula (7.50). On the other hand, using Galerkin's system (7.35) we solved the corresponding self-consistency equation (7.2) and found a time-periodic solution $u(x, t)$ to Eq. (7.24), see Figure 31(c),(d). As expected, the graphs of $a(x, t)$ and $u(x, t)$ agree with each other on a large scale, but have some fine structure differences which can be attributed to finite size effects. The assertion is confirmed by simulations of system (6.1) with more oscillators (not shown). In particular, several darker filaments protruding into the coherent region (yellow/bright) in Fig. 31(a) become thinner for growing system size and disappear in the limit $N \rightarrow \infty$, see Fig. 31(c), in accordance with the coherence/incoherence invariance property described in Proposition 7.2.

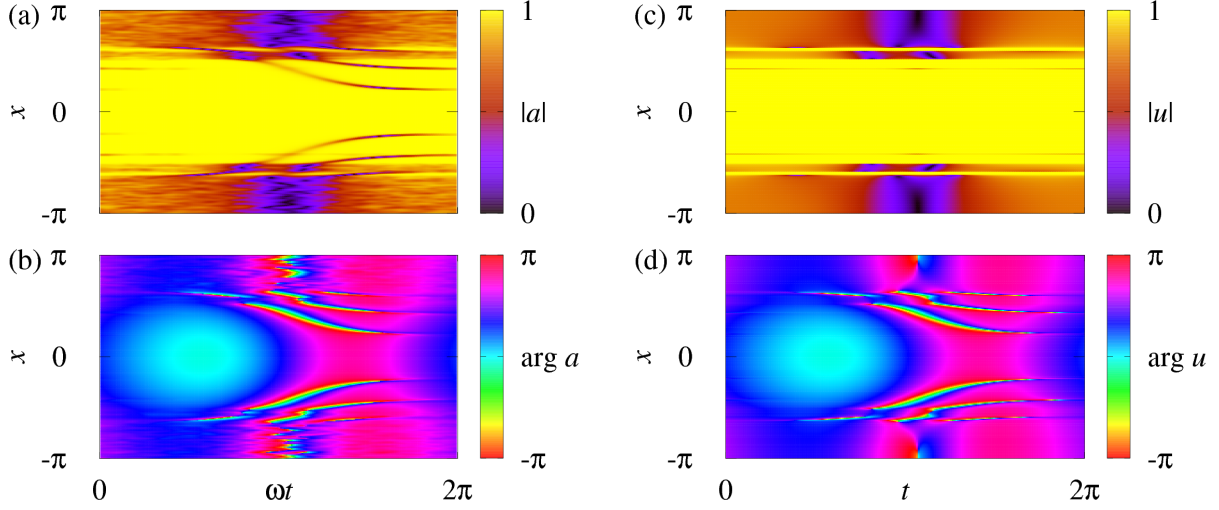


Figure 31: (a), (b) Approximate complex amplitude $a(x, t)$ of the relative periodic orbit (7.1) corresponding to a breathing chimera state in the system (6.1)–(6.2) with $N = 8192$ oscillators for $A = 1.05$ and $\alpha = \pi/2 - 0.16$. (c), (d) The corresponding solution $u(x, t)$ to Eq. (7.24) obtained from the Galerkin’s system (7.35) with $F = 10$.

The self-consistency equation (7.2) allows us to predict almost perfectly the graphs of the global order parameter $Z_N(t)$, see (1.19), and of the effective frequencies $\Omega_{\text{eff},k}$, see (1.18). In Figure 32 these quantities, computed for a chimera state in the system (6.1)–(6.2), are

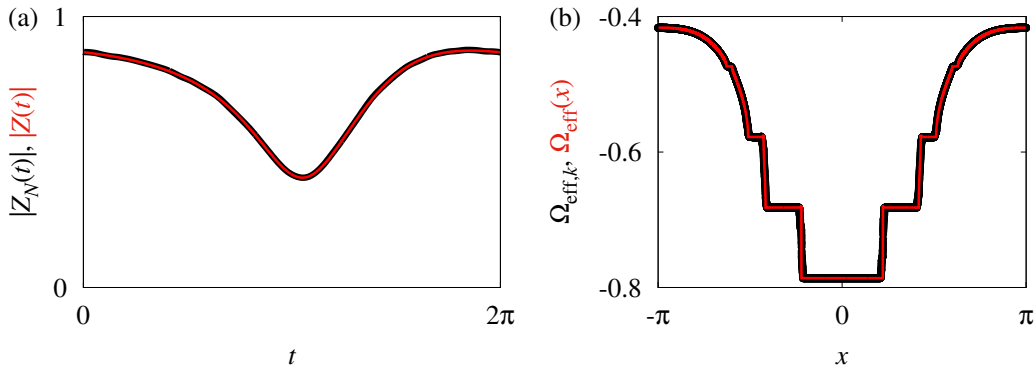


Figure 32: (a) Global order parameter $Z_N(t)$ and (b) effective frequencies $\Omega_{\text{eff},k}$ computed for the chimera state in Fig. 31 and the corresponding theoretical predictions $Z(t)$ and $\Omega_{\text{eff}}(x)$ obtained using Proposition 7.15.

compared with their continuum limit counterparts $Z(t)$ and $\Omega_{\text{eff}}(x)$ computed by the formulas from Proposition 7.15 where we inserted the functions $w(x, t)$ and $u(x, t)$ obtained from the Galerkin's system (7.35).

Figure 33 illustrates another application of the self-consistency equation (7.2). We used it for computation of a branch of breathing chimera states in Eq. (2.19). The theoretically predicted primary and secondary frequencies are compared with the corresponding values of Ω and ω observed in breathing chimera states in the coupled oscillator system (6.1) with $N = 8192$. Again, the agreement between the theoretical curve and the numerical points is very good. A slightly recognizable mismatch can be attributed to finite size effects or to the small number of Fourier modes ($F = 10$) in the Galerkin's approximation. Note that the curves in Figure 33 fold for $\alpha \approx \pi/2 - 0.145$. This fact explains a sudden collapse of breathing chimera states to the completely synchronous state, which we observed in system (6.1) for $\alpha > \pi/2 - 0.145$.

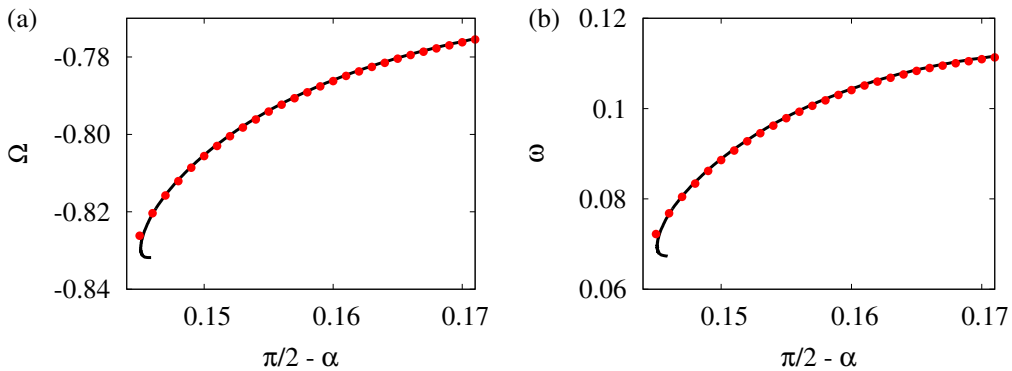


Figure 33: (a) Primary frequency Ω and (b) secondary frequency ω of breathing chimera states in the system (6.1)–(6.2) for $A = 1.05$. The solid curve shows theoretical predictions made using the Galerkin's system (7.35) with $F = 10$. The points show frequencies extracted from the breathing chimera states observed in the system (6.1)–(6.2) with $N = 8192$ oscillators.

For all breathing chimera states on the solution branch in Figure 33 we also computed the corresponding essential spectra Σ_{ess} . These spectra look identically, see Figure 34(a), and have the maximal possible size, see Remark 7.17 for more detail. The computation of the discrete spectra Σ_{disc} turned out to be a time demanding task, therefore at present it was not carried out. However, because of Remark 7.21 we assert that Σ_{disc} includes a triple eigenvalue $\mu = 1$ embedded into the essential spectrum. Since for every breathing chimera state the unit circle $|\mu| = 1$ is a subset of its essential spectrum Σ_{ess} , the destabilization of such chimera state cannot occur via a classical bifurcation of finite codimension. Indeed, any unstable eigenvalue can emerge only from the essential spectrum and therefore this eigenvalue cannot be isolated at the bifurcation point. By analogy with other dynamical systems we may expect that breathing

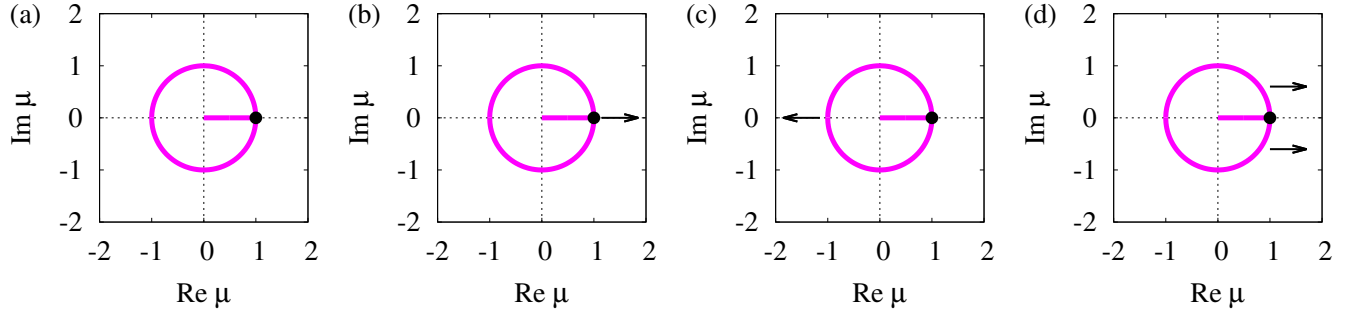


Figure 34: All breathing chimera states on the solution branch in Fig. 33 have identical essential spectra shown in panel (a). The point indicates a multiple eigenvalue embedded into the essential spectrum. Other panels show hypothetical bifurcation scenarios for breathing chimera states: (b) Fold and symmetry-breaking bifurcations, (c) period-doubling bifurcation, (d) torus bifurcation. The arrows indicate directions in which one or two eigenvalues can appear from the essential spectrum.

chimera states in general can lose their stability via a fold, symmetry breaking, period-doubling or torus bifurcation, which are associated with the appearance of one or two unstable eigenvalues μ from the essential spectrum on the unit circle as shown in Figure 34(b)-(d). Note that proper consideration of such bifurcations requires the use of generalized spectral methods [17, 24, 18], which, however, must be adapted to a situation where the reference solution is a relative periodic orbit rather than a simple equilibrium.

In summary, we emphasize that the consideration scheme described in this chapter can be applied to systems (6.1) with arbitrary coupling functions $G(x)$, including exponential [11] and top-hat [120, 121] coupling. In particular, using the self-consistency equation (7.2) one can carry out a more rigorous asymptotic analysis of breathing chimera states reminiscent of that in [121]. Moreover, all above methods can be extended to the study of breathing spiral chimera states in two-dimensional lattices of phase oscillators [137, 82]. Furthermore, our results can also be applied to explore the appearance of pulsing and alternating coherence-incoherence patterns [86] and modulated travelling chimera states [85] in systems of heterogeneous nonlocally coupled phase oscillators, though in this case one needs to modify the definition of the solution operator \mathcal{U} .

8 Nonstationary coherence-incoherence patterns

In Chapters 4–7 we considered different types of coherence-incoherence patterns observed in systems of identical oscillators. However, identical interacting agents almost never occur in real

world, therefore it is natural to ask how robust are these patterns with respect to the oscillator heterogeneities? The simplest way to address this question is to consider the system (1.14) with natural frequencies ω_k chosen from a Lorentzian distribution (1.17) with a width $\gamma > 0$. In Section 2.3 we showed that in this case the continuum limit dynamics of the system is represented by the local order parameter $z(x, t)$ evolving according to Eq. (2.17). Note that the only difference between the Ott-Antonsen equation (2.19) for identical oscillators and the Ott-Antonsen equation (2.17) for heterogeneous oscillators is the additional term $-\gamma z$.

It turns out that for small widths γ all stationary chimera states observed in the system (1.14) with Lorentzian distributed natural frequencies ω_k have similar macroscopic dynamics as their counterparts for identical natural frequencies, compare Fig. 2(a)-(d) and Fig. 5. This fact was rigorously justified by Laing first for chimera states on a ring [57] and later for chimera states in two-dimensional domains [61]. However, analogous assertion does not hold for breathing chimera states, which can change their properties already for relatively small Lorentzian widths $\gamma \sim 10^{-2}$, see [86]. In particular, their stability region in the system parameters space can grow significantly. Moreover, breathing chimera states can turn into nonstationary coherence-incoherence patterns (CIPs) which behave as periodically disappearing and re-appearing chimera states (see pulsing and alternating chimera states in Fig. 6). To give a better understanding of these phenomena, in Section 8.2 we show several bifurcation diagrams computed for Eq. (2.17) using the Poincaré section method described in Section 8.1.

8.1 Poincaré section method

One of the main advantages of Eq. (2.17) is that all its stable solutions can be studied by direct numerical simulations. For this one discretizes Eq. (2.17) on a uniform grid and integrate the resulting ODE system with some solver. In the following we apply this approach to nonstationary CIPs in a one-dimensional version of Eq. (2.17). More precisely, we assume that the spatial coordinate x of the local order parameter $z(x, t)$ varies in the interval $[-\pi, \pi]$ and the integral operator \mathcal{G} is given by (6.7). Then using the global order parameter

$$Z(t) = \frac{1}{2\pi} \int_{-\pi}^{\pi} z(x, t) dx$$

we make the following definition: A coherence-incoherence pattern is called nonstationary if the corresponding modulus $|Z(t)|$ is time-dependent.

Obviously, for non-constant $|Z(t)|$ the minimal and maximal values

$$R_{\min} = \min_t |Z(t)|, \quad R_{\max} = \max_t |Z(t)|$$

are well-defined and differ from each other, therefore a Poincaré section for $|Z(t)|$ can be chosen at the mean level $R_{\text{mean}} = (R_{\min} + R_{\max})/2$. Then every time moment t_k where $|Z(t)|$ crosses the value R_{mean} from above is called the intersection with the Poincaré section, or briefly *event*.

Given a nonstationary CIP it is useful to find all event moments t_k , calculate the inter-event intervals $\Delta t_k = t_k - t_{k-1}$ and plot them on the same graph. If $|Z(t)|$ is a periodic function of time, then the sequence of intervals Δt_k contains at most a finite number of different values. On the other hand, if $|Z(t)|$ varies irregularly, then one obtains infinitely many different values of Δt_k .

8.2 Stability diagram of nonstationary coherence-incoherence patterns

The top panel of Fig. 35 shows a bifurcation diagram of nonstationary CIPs in the Eq. (2.17) with the cosine coupling (6.2). The parameters $\gamma = 0.01$ and $\alpha = \pi/2 - 0.15$ are fixed, while the parameter A of the coupling function (6.2) varies. For every fixed A we plot ca. 100 inter-event intervals Δt_k obtained using the Poincaré section technique. All these intervals either coincide or assume only two different values within the numerical precision. This indicates that the observed CIPs are relative periodic orbits of Eq. (2.17). Note that outside the stability interval $A \in (1.098, 1.323)$ we found only stationary CIPs, therefore this part of the diagram remains empty.

We distinguish six qualitatively different zones in the bifurcation diagram of nonstationary CIPs. The zones are separated by five critical values of A : three values correspond to the infinite growth of Δt , and two other values correspond to a symmetry breaking (a single curve in the diagram splits into two curves or two curves merge together into a single one). In the small panels of Fig. 35 we show typical CIPs for each of the zones I–VI. The CIPs are represented by the solutions $z(x, t)$ of Eq. (2.17) and by the corresponding complex global order parameters $Z(t)$.

(I) The CIPs for $A \in (1.098, 1.123)$ are pulsing chimera states, see Fig. 6(a)-(d). Their profiles are reflection symmetric, i.e. $|z(-x, t)| = |z(x, t)|$. The minimal period T_I of every such CIP coincides with the period of the corresponding $|Z(t)|$ -graph. It is likely that in the phase space of the Ott-Antonsen equation (2.17) there exists a homoclinic orbit underlying the existence of pulsing chimera states. This orbit apparently is approached for $A \approx 1.123$ when Δt grows to infinity. Importantly, pulsing chimera states cannot appear in systems of identical oscillators, because in this case the coherent and incoherent regions cannot change their size [79, Lemma 2].

(II) The CIPs for $A \in (1.124, 1.157)$ are not only reflection symmetric but also have a space-time symmetry. Their profiles $|z(x, t)|$ are invariant with respect to the spatial shift by π combined with the time-shift by half-period, what means $|z(x + \pi, t + T_{II}/2)| = |z(x, t)|$ where T_{II} is the minimal period of the CIP. Note that T_{II} equals to the doubled period of the corresponding $|Z(t)|$ -graph.

The coherent and incoherent regions of type-II CIPs exchange their positions periodically, therefore these patterns correspond to alternating chimera states, see Fig. 6(e)-(h). Similar

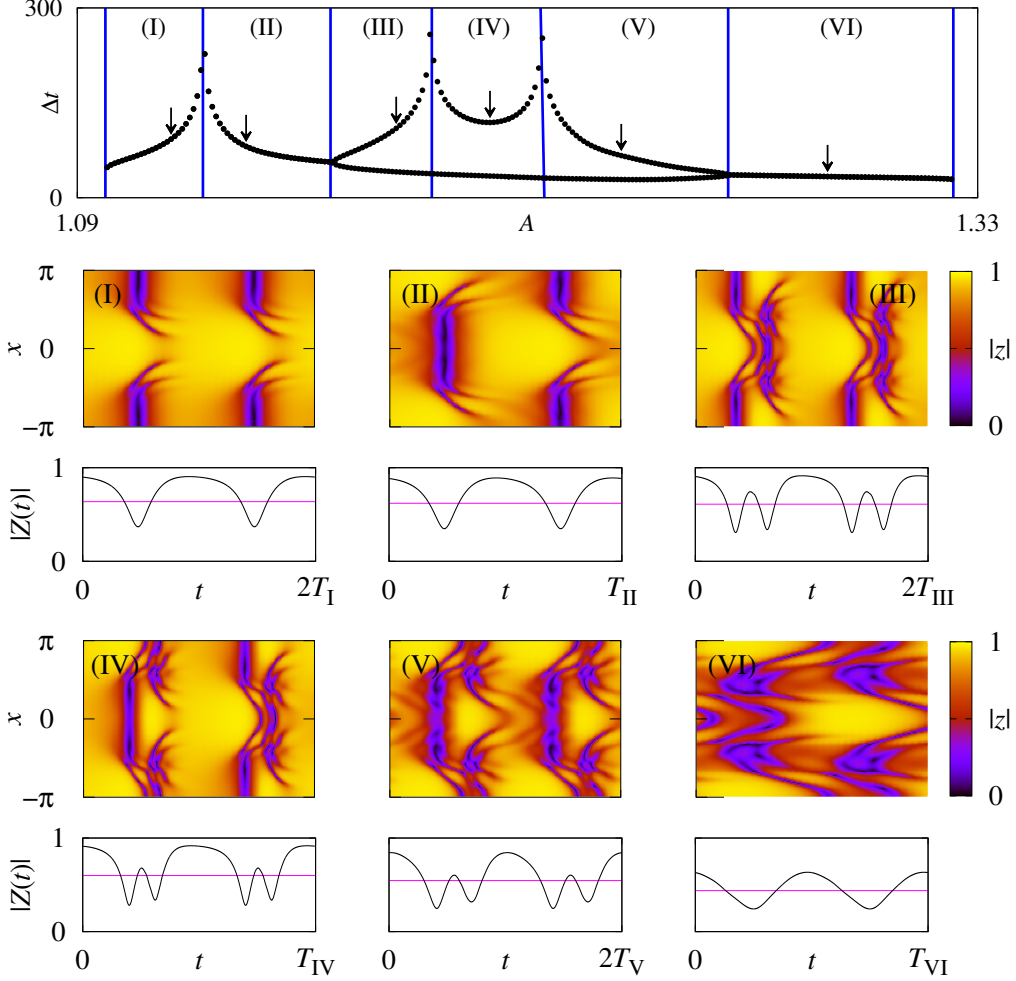


Figure 35: Inter-event intervals Δt versus A for nonstationary coherence-incoherence patterns in Eq. (2.17). Other parameters: $\gamma = 0.01$ and $\alpha = \pi/2 - 0.15$. Vertical lines separate six zones I–VI with different types of solutions exemplified in the small panels below. These panels show the moduli of the solutions $z(x, t)$ of Eq. (2.17) at $A = 1.115, 1.135, 1.175, 1.2, 1.235, 1.29$ (see arrows in the main panel) and the corresponding moduli of the global order parameter $Z(t)$. The purple (gray) lines in the $|Z(t)|$ -graphs indicate the mean level R_{mean} (see text).

alternating dynamics was reported for two subpopulations models [66, 59], for spatially modulated systems of non-locally coupled phase oscillators [138] as well as for more complicated oscillatory media [36]. We conjecture that alternating chimera states appear due to a heteroclinic switching mechanism [8]. Moreover, in the presence of noise they can also be found in systems of nonlocally coupled excitable units (e.g. coherence-resonance chimeras [112]) or in a two populations system with two metastable states (e.g. switching chimera [140]).

(III) The CIPs for $A \in (1.158, 1.184)$ differ from the type-II CIPs by broken space-time symmetry (the reflection symmetry is preserved). The shape of such pattern at the moment when its incoherent region is centered around $x = 0$ looks differently than the shape of the pattern at the moment when its incoherent region is centered around $x = \pi$. On the other hand, for the incoherent region it takes longer to switch from the position $x = 0$ to the position $x = \pi$ than to switch in the opposite direction. Because of this, the corresponding $|Z(t)|$ -graph has two non-equidistant peaks with different heights, and the bifurcation diagram in Fig. 35 comprises two points Δt for each A from the zone III. Note, while one of the inter-event intervals Δt remains bounded for all $A \in (1.158, 1.184)$, the other interval grows to infinity as A approaches the right endpoint 1.184. Finally, the minimal period T_{III} of a type-III CIP coincides with the period of the corresponding $|Z(t)|$ -graph.

(IV) This zone extends over the interval $A \in (1.185, 1.213)$. In general, the transition from the type-III CIPs to the type-IV CIPs resembles the transition from pulsing to alternating chimera states at the boundary between zones I and II. In the bifurcation diagram the inter-event intervals Δt grow to infinity at the left endpoint of zone IV. The minimal period T_{IV} equals to the doubled period of the $|Z(t)|$ -graph. Moreover, all type-IV CIPs have the same space-time symmetry and hence similar alternating dynamics as the type-II CIPs.

(V), (VI) These two zones extend over the intervals $A \in (1.214, 1.263)$ and $A \in (1.264, 1.323)$, respectively. The symmetries of the type-V/VI CIPs are identical to those of the type-III/II CIPs. However, the $|z(x, t)|$ -plots of the former patterns are more homogeneous in time and lose their pulsing behavior. Simultaneously, they get more structured in the x -direction such that now we see four horizontal stripes in these plots: the two stripes are more coherent (brighter), while the other two are less coherent (darker).

Bifurcation diagrams similar to that in Fig. 35(top panel) can be also computed for other nonvanishing values γ . We did this for 20 different values γ varying from 0.001 to 0.02 with the step $\Delta\gamma = 0.001$. Two of these diagrams are shown in Fig. 36. For each γ we identified the endpoints of the stability interval and found all critical values A corresponding to infinite period singularities or symmetry breaking events. This allowed us to draw a $2D$ -stability region of nonstationary CIPs in the (A, γ) -plane, see Fig. 37. We found that the bifurcation diagrams look qualitatively similar for all $\gamma \in [0.008, 0.02]$ and comprise the same six zones as Fig. 35. In contrast, for smaller values γ these diagrams change dramatically. The two rightmost infinite period critical values A coalesce together and disappear for some $\gamma \in (0.007, 0.008)$, therefore

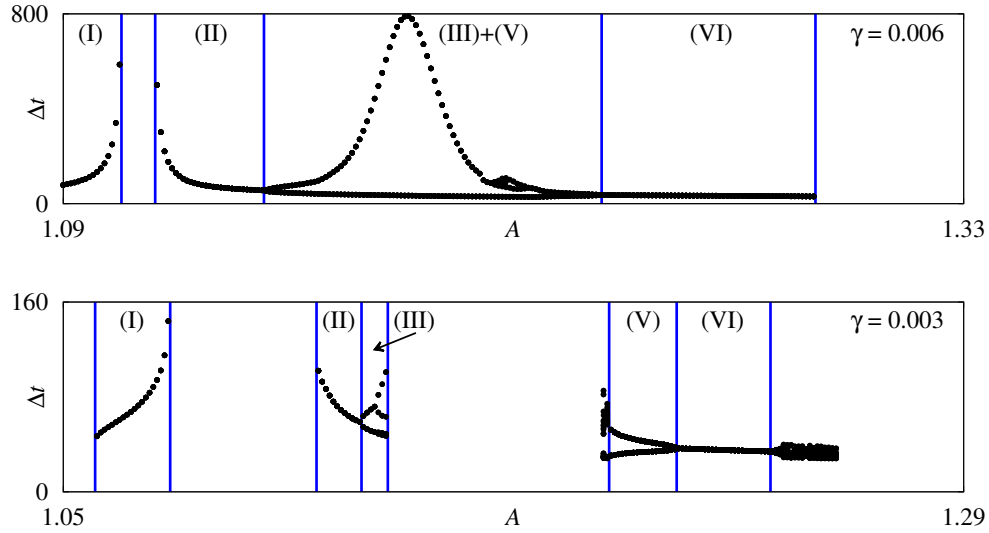


Figure 36: Inter-event intervals Δt versus A for nonstationary coherence-incoherence patterns in Eq. (2.17) with $\gamma = 0.006$ (top panel) and $\gamma = 0.003$ (bottom panel). Parameters: $\alpha = \pi/2 - 0.15$. Vertical lines separate zones I–VI with different types of solutions (see Fig. 35 for more detail).

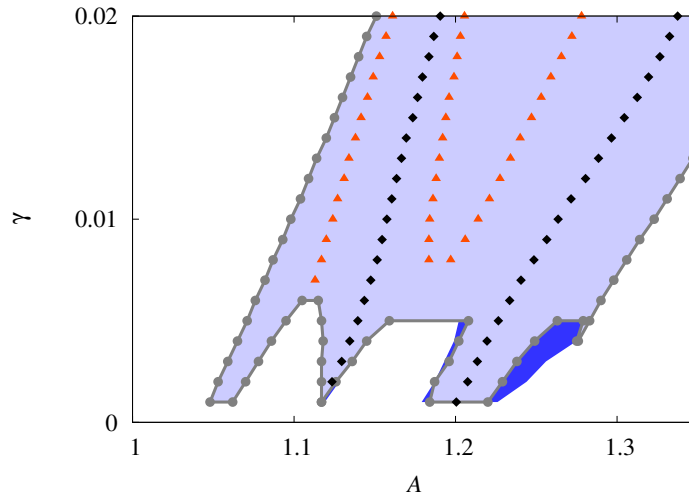


Figure 37: Stability region (light shaded) of the nonstationary coherence-incoherence patterns in Eq. (2.17) for $\alpha = \pi/2 - 0.15$. (Note that the extension of the stability region for $\gamma < 0.001$ is not shown.) Triangles and squares mark symmetry breaking and infinite period critical values, respectively. Dark shaded region corresponds to irregular nonstationary coherence-incoherence patterns.

for $\gamma \leq 0.007$ we don't find any type-IV CIPs. However, the diagrams still preserve ghost peaks close to their former location, see Fig. 36 (top panel). At $\gamma = 0.006$ the stability interval of nonstationary CIPs breaks into two pieces, and at $\gamma = 0.005$ it becomes a union of four disjoint subintervals. Each of these subintervals shrinks for decreasing γ . Moreover one of them completely vanishes for $\gamma < 0.004$, see Fig. 36 (bottom panel). It is likely that one of the remaining three subintervals also vanishes for $\gamma < 0.001$ and only the other two constitute the stability region of breathing chimera states for $\gamma \rightarrow 0$. This conjecture is confirmed by the fact that the corresponding system (1.14) with identical natural frequencies does support two breathing chimera states for $A \approx 1.05$ and $A \approx 1.19$, see Fig. 3(a)-(d) and Fig. 3(e)-(h), respectively.

Note that for $\gamma \leq 0.005$ all bifurcation diagrams contain small ranges of parameter A with irregular nonstationary CIPs. In this case for a fixed A we obtain dozens of different values Δt_k (not a few as it was for larger γ). These points appear as a vertical dotted line in the bifurcation diagram, see Fig. 36 (bottom panel). All occurrences of irregular nonstationary CIPs are marked by the dark shaded regions in Fig. 37.

8.3 Remarks

In this chapter we revealed a constructive role of natural frequency heterogeneity for the emergence of nonstationary CIPs in spatially extended oscillator systems. We showed that a narrow (but non-degenerate) frequency distribution facilitates their emergence and increases their variety. Though counterintuitive these results are not completely unexpected, because they have analogies in the behaviour of other coupled oscillator networks where diversity facilitates collective order [113] or even is required for symmetric pattern formation [76].

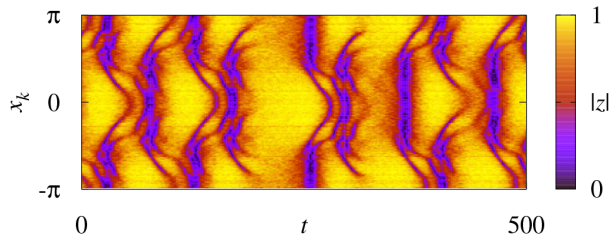


Figure 38: Irregular nonstationary coherence-incoherence pattern in the system (1.14) with Lorentzian distributed natural frequencies ($\gamma = 0.01$) and cosine coupling (6.2). Space-time plot of the local order parameter $|z(x, t)|$ defined by (1.21). Parameters: $N = 16384$, $A = 1.175$ and $\alpha = \pi/2 - 0.15$.

In Section 8.1 we described the Poincaré section technique for the Ott-Antonsen equation (2.17) and used it to explore a complex bifurcation scenario underlying the transformation

of nonstationary CIPs into each other. We emphasize that this analysis is based on the continuum limit assumption, therefore nonstationary CIPs observed in the system (1.14) with small N may differ qualitatively from the solutions of Eq. (2.17). For example, all CIPs shown in the small panels of Fig. 35 indeed are reproduced in detail in the numerical simulations of the system (1.14) with $N \geq 2^{15}$. However, for smaller system sizes the correspondence becomes less pronounced, compare Fig. 35(III) with Fig. 38.

9 Travelling chimera states

This chapter is concerned with the mathematical description of travelling chimera states. We focus on their prototype example observed in the system (1.14) with Lorentzian distributed natural frequencies ω_k and an asymmetric coupling function (1.16), see Fig. 8. In the continuum limit such chimera states are represented by travelling waves in Eq. (2.17). These are solutions of the form

$$z = a(x - st)e^{i\Omega t}, \quad (9.1)$$

where $a(x)$ is a smooth 2π -periodic complex-valued function, $\Omega \in \mathbb{R}$ and $s \in \mathbb{R}$. Here and throughout this chapter we assume that the coordinate x in Eq. (2.17) is one-dimensional and the integral operator \mathcal{G} is given by the formula (6.7).

Eq. (2.17) can be discretized in space on a uniform grid and solved numerically. For example, using the parameters from Figs. 5 and 8 we obtain solutions shown in Fig. 39. The first two solutions agree with the ansatz (9.1). In particular, the solution in panel (a) is a *stationary wave* with $s = 0$, while the solution in panel (b) is a *travelling wave* with $s \neq 0$. The remaining solution in panel (c) has a more complicated dynamics, which is not described by the ansatz (9.1). This is a modulated travelling wave, see Table 1.

In contrast to Chapter 8, where we used numerical simulations of Eq. (2.17) to reveal the bifurcation diagram of nonstationary coherence-incoherence patterns, here we cannot rely on this approach, because travelling chimera states show a more complicated dependence on the system parameters, see Fig. 9. Therefore we analyze these states differently.

Inserting ansatz (9.1) into Eq. (2.17) we obtain an integro-differential equation

$$-s \frac{da}{dx} = -(\gamma + i\Omega)a + \frac{1}{2}e^{-i\alpha}\mathcal{G}a - \frac{1}{2}e^{i\alpha}a^2\mathcal{G}\bar{a}. \quad (9.2)$$

This equation needs to be solved with respect to the unknown 2π -periodic function $a(x)$ and the unknown scalars Ω and s . The coupling function $G(x)$ and the other system parameters γ and α are supposed to be given. In Section 9.1 we show that the periodic boundary value problem formulated in this way is well-posed. We use the fact that Eq. (9.2) has two continuous symmetries and apply the Lyapunov-Schmidt reduction. This allows us to formulate a numerical method for the continuation of travelling waves.

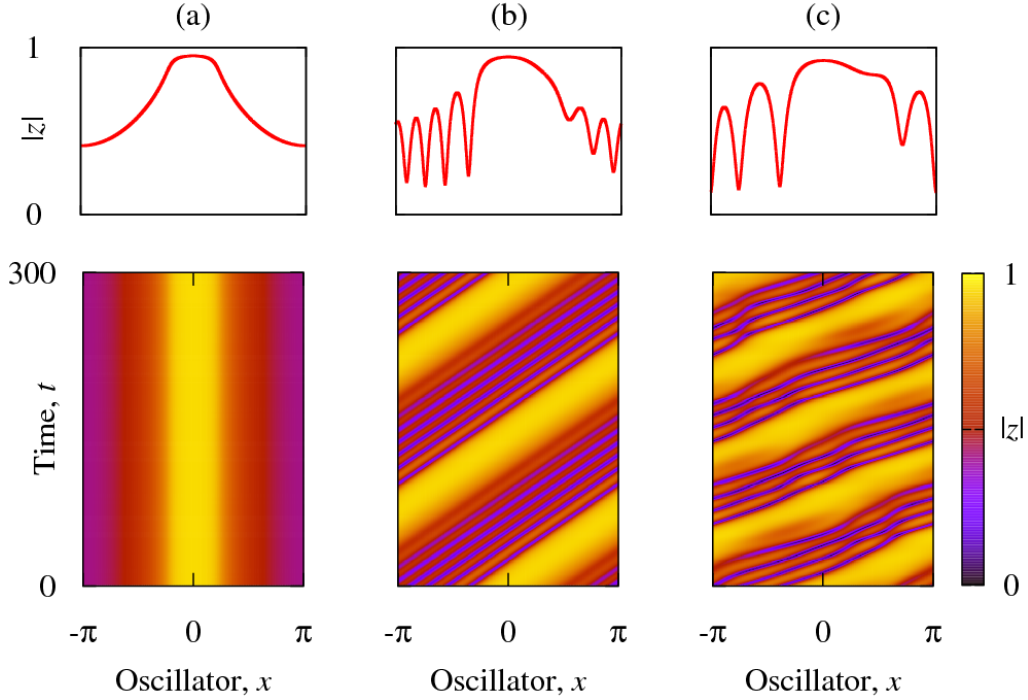


Figure 39: Solutions of Eq. (2.17) with trigonometric coupling function (1.16) for (a) $B = 0$, (b) $B = 0.09$ and (c) $B = 0.13$. Top panels show initial snapshots $|z(x, 0)|$. Bottom panels show dynamics of $|z(x, t)|$. Other parameters: $A = 0.9$, $\gamma = 0.01$ and $\alpha = \pi/2 - 0.1$.

In Section 9.2 we carry out stability analysis of travelling waves in Eq. (2.17). We apply standard techniques from the PDE theory [44, 108] adapted to the case of integro-differential equations. More precisely, we linearize Eq. (2.17) around a travelling wave (9.1) and consider the corresponding differential operator on the space of periodic functions. We derive a characteristic equation describing the operator's spectrum and prove the following assertions:

(i) The spectrum of any travelling wave (9.1) is purely discrete. In general, it consists of infinitely many isolated eigenvalues λ_k of finite multiplicity. For $|\lambda_k| \rightarrow \infty$ the eigenvalues condensate along the line $\lambda = -\text{Re } \eta_m$ where

$$\eta_m = \left(\frac{1}{2\pi} \int_{-\pi}^{\pi} (\gamma + i\Omega + e^{i\alpha} a(x) \mathcal{G}\bar{a}) dx \right).$$

Therefore a practical test for the stability of a travelling wave (9.1) includes two conditions. First, the inequality $\text{Re } \eta_m > 0$ must be satisfied. Second, all eigenvalues λ_k in a sufficiently large neighbourhood of zero must satisfy $\text{Re } \lambda_k \leq 0$. If any of these two conditions is not fulfilled, the travelling wave is unstable.

(ii) Consider a stable travelling wave (9.1). If the inequality $\text{Re } \eta_m > 0$ persists for varying system parameters, then the travelling wave in general can become unstable through a fold, symmetry breaking or Hopf bifurcation.

The continuation method and the stability analysis scheme presented in Sections 9.1 and 9.2 were used in [85] to compute a bifurcation diagram of travelling waves in the equation (2.17) with the trigonometric coupling function (1.16). The diagram is shown in Figure 40. Note that the coupling function (1.16) depends on two parameters A and B . In Figure 40 the former parameter is fixed at $A = 0.9$ and the latter one varies from 0 to 0.13. Thus the impact of the coupling function asymmetry on the properties of travelling waves is demonstrated.

For small values of the asymmetry parameter B , i.e. $|B| \ll \min(1, |A|)$, the collective frequency Ω remains nearly constant, while the lateral speed s increases proportionally to B . This observation agrees with the asymptotic formulas obtained in [83]. In contrast, for large values B the dependence Ω vs. B as well as the dependence s vs. B become non-monotone. The corresponding graphs develop loops. Moreover, moving along the branch of travelling waves we see that some of these waves are unstable because a single real eigenvalue (blue curves) or a pair of complex-conjugate eigenvalues (red curves) lie in the unstable complex half-plane $\text{Re } \lambda > 0$. Importantly, the bifurcation diagram in Fig. 40(b) explains qualitatively and quantitatively most of the numerical results presented in Fig. 9 for $B \leq 0.09$. (The absence of the pinning region for $B \approx 0$ is concerned with its finite size nature.) However, Fig. 9 contains also several data points for $B > 0.09$ where, according to Fig. 40(b), one doesn't expect any stable travelling waves of the form (9.1). These points correspond to modulated travelling waves, see Fig. 39(c). Though we didn't study the modulated travelling waves here it is likely that they appear in the result of supercritical Hopf bifurcations at the points separating black and red parts of the solution branch in Fig. 40.

The non-monotone increase of the lateral speed s for growing asymmetry B is accompanied by a complicated transformation of the spatial profiles of travelling waves, see Fig. 41. For small asymmetries B the profiles of travelling waves resemble very much the profile of the stationary wave for $B = 0$. However, for $B > 0.02$ all $z(x, t)$ -graphs become spatially modulated. When the asymmetry B increases from 0.02 to 0.06 the amplitude of the spatial modulation increases too, while its wavelength decreases. But for $B > 0.06$ the modulation amplitude stabilizes and the modulation wavelength starts to increase. Fig. 41 shows three coexisting travelling waves for each of the values $B = 0.085$ and $B = 0.097$. In the former case two waves are stable and one unstable, while in the latter case only one wave is stable and two other unstable. The spectra of the travelling waves for $B = 0.097$ are shown in the insert panels.

Another remarkable transformation of travelling waves occurs for $B > 0.11$, see Fig. 42. To explain it let us notice that in all panels of Fig. 41 the modulus $|z(x, t)|$ is separated from zero and the total variation of the argument of $z(x, t)$ for x varying from $-\pi$ to π equals zero. On the other hand, moving along the solution branch in Fig. 40 we encounter several distinct points where the modulus $|z(x, t)|$ touches zero. Beyond each of these points the argument of $z(x, t)$

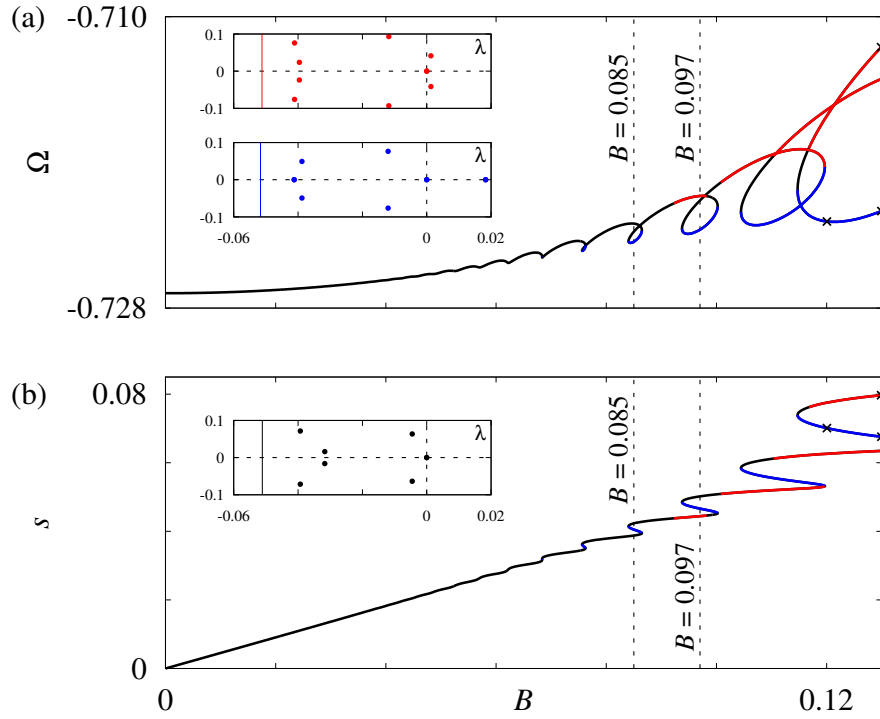


Figure 40: (a) Collective frequency Ω and (b) lateral speed s of travelling waves (9.1) satisfying Eq. (2.17) with a trigonometric coupling function (1.16). All points for $B < 0.03$ were obtained by direct numerical simulations of Eq. (2.17). For $B \geq 0.03$ the continuation algorithm from Section 9.1 was employed. The stability of travelling waves was checked using the method from Section 9.2. It reveals stable (black), one-real-eigenvalue unstable (blue) and Hopf unstable (red) waves. Insert panels show the spectra of three travelling waves coexisting for $B = 0.097$. Each spectrum condensates around the thin solid line for $\text{Im } \lambda \rightarrow \pm\infty$. Parameters: $A = 0.9$, $\alpha = \pi/2 - 0.1$ and $\gamma = 0.01$.

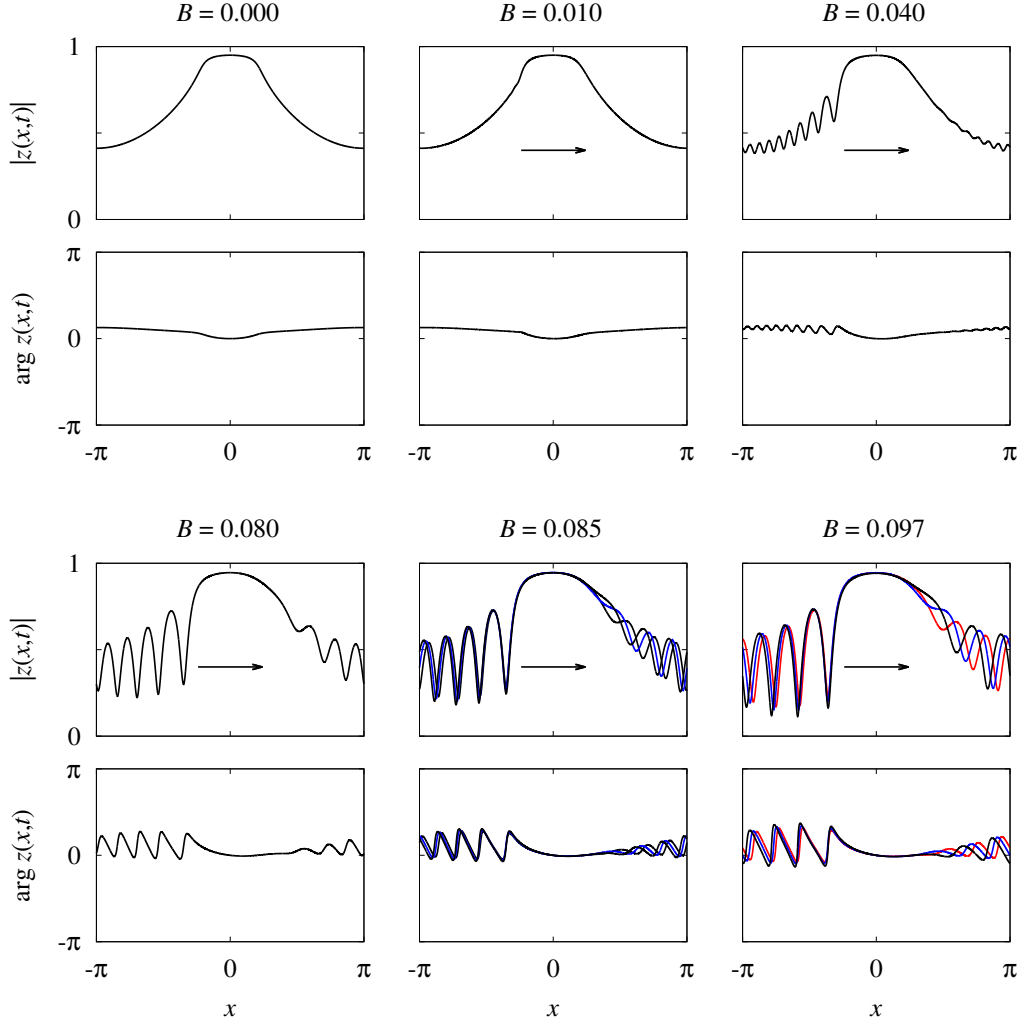


Figure 41: Travelling wave solutions of Eq. (2.17) for trigonometric coupling function (1.16) with different asymmetry parameters B . Black, blue and red colours denote stable, one-real-eigenvalue unstable and Hopf unstable solutions, respectively. Arrows show the direction of the wave's lateral motion for $B \neq 0$. Parameters: $A = 0.9$, $\alpha = \pi/2 - 0.1$ and $\gamma = 0.01$.

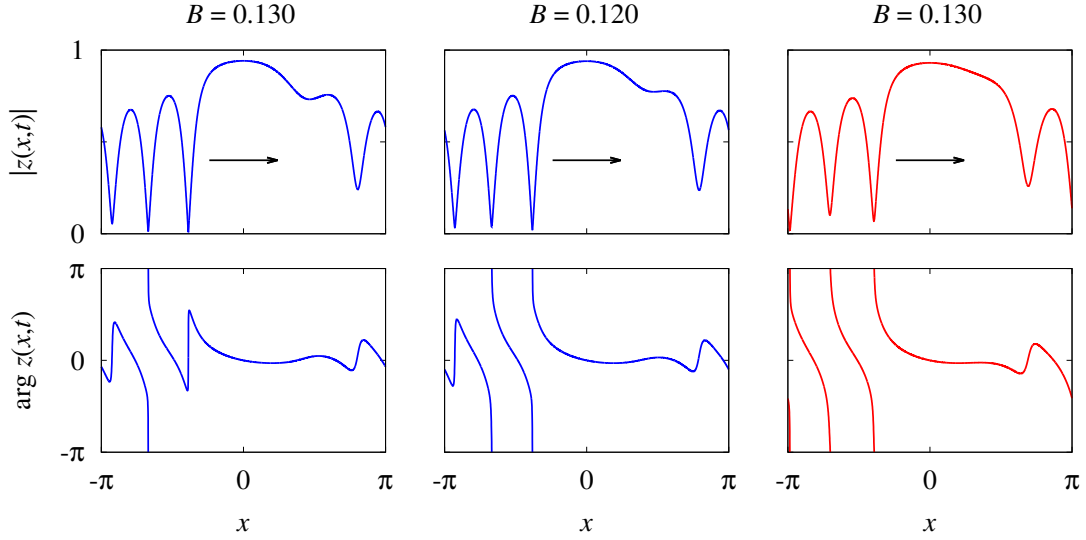


Figure 42: Development of phase twists in travelling wave solutions of Eq. (2.17). The snapshots correspond to three crosses in Fig. 40.

becomes more twisted than it was before. Respectively, its total variation jumps first from zero to -2π , Fig. 42(a), then from -2π to -4π , Fig. 42(b), and finally from -4π to -6π , Fig. 42(c). This fact explains the "twisted" profile of travelling chimera state shown in Fig. 8(e).

9.1 Continuation algorithm for travelling chimera states

Let us consider Eq. (9.2) with an integral operator \mathcal{G} given by the formula (6.7) and assume that the operator kernel $G(x, B)$ depends two real arguments x and B . Then Eq. (9.2) is equivalent to the operator equation

$$\mathcal{F}(a, \Omega, s, B) = s \frac{da}{dx} - (\gamma + i\Omega)a + \frac{1}{2}e^{-i\alpha}\mathcal{G}a - \frac{1}{2}e^{i\alpha}a^2\mathcal{G}\bar{a} = 0 \quad (9.3)$$

where

$$\mathcal{F} : C_{\text{per}}^1([-\pi, \pi]; \mathbb{C}) \times \mathbb{R}^3 \rightarrow C_{\text{per}}([-\pi, \pi]; \mathbb{C}).$$

In the following we assume that the system parameters γ and α are fixed. Then our aim is to solve the following local problem:

Given a triplet (a_0, Ω_0, s_0) satisfying the equation (9.3) with $B = B_0$ find all other solutions of equation (9.3) for $B \approx B_0$.

If we know how to solve this local problem, we can formulate a general continuation algorithm for travelling waves in Eq. (9.3).

There is an important fact about Eq. (9.3) which we have keep in mind. This equation has two symmetries: the complex phase shift symmetry and the translation symmetry. This means, if any triplet $(a(x), \Omega, s)$ solves Eq. (9.3) then every other triplet $(a(x+c)e^{i\phi}, \Omega, s)$ with $\phi \in \mathbb{R}$ and $c \in \mathbb{R}$ solves the same equation too. The symmetries of Eq. (9.3) lead to a specific property of the derivative operator $\mathcal{L} = \partial_a \mathcal{F}(a_0, \Omega_0, s_0, B_0)$. Indeed, using the explicit expression

$$\mathcal{L}a = s_0 \frac{da}{dx} - \eta_0 a + \frac{1}{2} e^{-i\alpha} \mathcal{G}a - \frac{1}{2} e^{i\alpha} a_0^2 \mathcal{G}\bar{a}$$

with

$$\eta_0(x) = \gamma + i\Omega_0 + e^{i\alpha} a_0(x) \mathcal{G}\bar{a}_0,$$

it is easy to verify that the homogeneous equation $\mathcal{L}a = 0$ has two non-trivial solutions $a = ia_0$ and $a = \partial_x a_0$, and hence the operator \mathcal{L} is not invertible. This implies that Eq. (9.3) cannot be solved with respect to a by means of the Implicit Function Theorem. On the other hand, if the equation $\mathcal{L}a = 0$ has no other linearly independent solutions and the operator \mathcal{L} is a Fredholm operator of index zero, then we can perform the Lyapunov-Schmidt reduction of Eq. (9.3) and obtain a modified equation or system suitable for applying the Implicit Function Theorem. In order to describe this method preciser, we make two assumptions:

(A₁) Suppose that ia_0 and $\partial_x a_0$ are linearly independent functions and that the equation $\mathcal{L}a = 0$ has no other linearly independent solutions apart from ia_0 and $\partial_x a_0$.

(A₂) Suppose

$$\Phi_0(\pi) \neq 1, \quad \text{where} \quad \Phi_0(x) = \exp\left(\frac{1}{s_0} \int_{-\pi}^x \eta_0(y) dy\right). \quad (9.4)$$

In the following we also will use the next two definitions:

(D₁) For every pair $w_1, w_2 \in C_{\text{per}}([-\pi, \pi]; \mathbb{C})$ we define their inner product by the formula

$$\langle w_1, w_2 \rangle = \text{Re} \int_{-\pi}^{\pi} w_1(x) \overline{w_2(x)} dx.$$

(D₂) Given a bounded linear operator \mathcal{A} acting on $C_{\text{per}}([-\pi, \pi]; \mathbb{C})$ we call its adjoint operator the linear operator \mathcal{A}^\dagger satisfying

$$\langle w_1, \mathcal{A}w_2 \rangle = \langle \mathcal{A}^\dagger w_1, w_2 \rangle \quad \text{for all} \quad w_1, w_2 \in C_{\text{per}}([-\pi, \pi]; \mathbb{C}).$$

Remark 9.1 (about the role of assumption (A_1)) Assumption (A_1) implies that the kernel of operator \mathcal{L} is two-dimensional. Moreover, applying the Gram-Schmidt process to the functions ia_0 and $\partial_x a_0$ we can construct two other functions u_1 and u_2 such that

$$\ker \mathcal{L} = \text{span}(u_1, u_2) \quad \text{and} \quad \langle u_j, u_k \rangle = \delta_{jk}$$

where δ_{jk} is the Kronecker delta.

Remark 9.2 (about the linear independence of ia_0 and $\partial_x a_0$) According to the geometric interpretation of the inner product $\langle \cdot, \cdot \rangle$ the functions ia_0 and $\partial_x a_0$ are linearly independent if and only if

$$\frac{|\langle ia_0, \partial_x a_0 \rangle|^2}{\langle ia_0, ia_0 \rangle \langle \partial_x a_0, \partial_x a_0 \rangle} < 1.$$

Remark 9.3 (about the role of assumption (A_2)) Assumption (A_2) ensures the existence of the inverse operator

$$\mathcal{K}_0 = (-s_0 \partial_x + \eta_0)^{-1} : C_{\text{per}}([- \pi, \pi]; \mathbb{C}) \rightarrow C_{\text{per}}^1([- \pi, \pi]; \mathbb{C}).$$

This is an integral operator of the form

$$(\mathcal{K}_0 u)(x) = - \int_{-\pi}^{\pi} \frac{\Phi_0(\pi) + (1 - \Phi_0(\pi))\Theta(x - y)}{s_0(1 - \Phi_0(\pi))} \Phi_0(x)\Phi_0^{-1}(y)u(y)dy \quad (9.5)$$

where $\Phi_0(x)$ is defined by (9.4) and $\Theta(x)$ denotes the Heaviside step function such that $\Theta(x) = 0$ for $x < 0$ and $\Theta(x) = 1$ for $x \geq 0$.

Let us consider the product operator

$$\mathcal{K}_0 \mathcal{L} a = -a + \frac{1}{2} \mathcal{K}_0 (e^{-i\alpha} \mathcal{G} a - e^{i\alpha} a_0^2 \mathcal{G} \bar{a}). \quad (9.6)$$

Obviously, we have $\ker \mathcal{K}_0 \mathcal{L} = \ker \mathcal{L}$. Moreover, because of the compact embedding

$$C_{\text{per}}^1([- \pi, \pi]; \mathbb{C}) \hookrightarrow C_{\text{per}}([- \pi, \pi]; \mathbb{C})$$

the operator $\mathcal{K}_0 \mathcal{L}$ is a Fredholm operator of index zero on $C_{\text{per}}([- \pi, \pi]; \mathbb{C})$. According to the Fredholm alternative, the cokernel of the operator $\mathcal{K}_0 \mathcal{L}$ coincides with the kernel of the adjoint operator $(\mathcal{K}_0 \mathcal{L})^\dagger$. Moreover, the dimension of $\ker (\mathcal{K}_0 \mathcal{L})^\dagger$ is equal to the dimension of $\ker \mathcal{K}_0 \mathcal{L}$. Consequently, there exist two functions v_1 and v_2 such that

$$\ker (\mathcal{K}_0 \mathcal{L})^\dagger = \text{span}(v_1, v_2) \quad \text{and} \quad \langle v_j, v_k \rangle = \delta_{jk}.$$

These functions can be written explicitly if one finds two linearly independent solutions of the adjoint equation $(\mathcal{K}_0 \mathcal{L})^\dagger v = 0$ and apply to them the Gram-Schmidt orthonormalization.

Proposition 9.4 *The adjoint of the operator $\mathcal{K}_0\mathcal{L}$ reads*

$$(\mathcal{K}_0\mathcal{L})^\dagger v = -v + \frac{1}{2}e^{i\alpha}\mathcal{G}^\dagger \left(\mathcal{K}_0^\dagger v - a_0^2 \overline{\mathcal{K}_0^\dagger v} \right), \quad (9.7)$$

where the operators \mathcal{G}^\dagger and \mathcal{K}_0^\dagger are defined by

$$(\mathcal{G}^\dagger u)(x) = \int_{-\pi}^{\pi} G(y-x)u(x)dy \quad (9.8)$$

and

$$(\mathcal{K}_0^\dagger u)(x) = \int_{-\pi}^{\pi} \frac{\overline{\Phi_0^{-1}(\pi)} + (1 - \overline{\Phi_0^{-1}(\pi)})\Theta(x-y)}{s_0(1 - \overline{\Phi_0^{-1}(\pi)})} \overline{\Phi_0^{-1}(x)\Phi_0(y)} u(y)dy. \quad (9.9)$$

Proof: Formulas (9.8) and (9.9) can be justified using the definition (D_2) . Then it follows from (9.6) that for every $u, v \in C_{\text{per}}([-\pi, \pi]; \mathbb{C})$ we have

$$\begin{aligned} \langle v, \mathcal{K}_0\mathcal{L}u \rangle &= \langle v, -u \rangle + \frac{1}{2}\langle v, \mathcal{K}_0(e^{-i\alpha}\mathcal{G}u - e^{i\alpha}a_0^2\overline{\mathcal{G}u}) \rangle \\ &= \langle -v, u \rangle + \frac{1}{2}\langle \mathcal{K}_0^\dagger v, e^{-i\alpha}\mathcal{G}u \rangle - \frac{1}{2}\langle \mathcal{K}_0^\dagger v, e^{i\alpha}a_0^2\overline{\mathcal{G}u} \rangle \\ &= \langle -v, u \rangle + \frac{1}{2}\langle e^{i\alpha}\mathcal{K}_0^\dagger v, \mathcal{G}u \rangle - \frac{1}{2}\langle e^{i\alpha}a_0^2\overline{\mathcal{K}_0^\dagger v}, \mathcal{G}u \rangle. \end{aligned}$$

Now formula (9.7) follows from the above identity. ■

Remark 9.5 *It can be shown that formula (9.9) yields the integral representation of the inverse operator $(s_0\partial_x + \overline{\eta}_0)^{-1}$.*

Above we explained how to find the functions u_1, u_2, v_1 and v_2 which span the kernel and cokernel of the operator $\mathcal{K}_0\mathcal{L}$. Using them we construct a modified operator

$$\mathcal{K}_0\mathcal{L} + \langle u_1, \cdot \rangle v_1 + \langle u_2, \cdot \rangle v_2$$

which is a rank-2 perturbation of $\mathcal{K}_0\mathcal{L}$. According to the Lyapunov-Schmidt method this operator is an isomorphism from $C_{\text{per}}([-\pi, \pi]; \mathbb{C})$ onto itself. In other words, it is invertible on the space of 2π -periodic continuous functions. This immediately implies that the composite operator

$$\mathcal{M} = \mathcal{K}_0^{-1}(\mathcal{K}_0\mathcal{L} + \langle u_1, \cdot \rangle v_1 + \langle u_2, \cdot \rangle v_2) = \mathcal{L} + \langle u_1, \cdot \rangle \mathcal{K}_0^{-1}v_1 + \langle u_2, \cdot \rangle \mathcal{K}_0^{-1}v_2 \quad (9.10)$$

is an isomorphism from $C_{\text{per}}([-\pi, \pi]; \mathbb{C})$ onto $C_{\text{per}}^1([-\pi, \pi]; \mathbb{C})$. Using this observation we define

$$\mathcal{H}(a, \Omega, s, B) = \mathcal{F}(a, \Omega, s, B) + \langle u_1, a \rangle \mathcal{K}_0^{-1} v_1 + \langle u_2, a \rangle \mathcal{K}_0^{-1} v_2 \quad (9.11)$$

and consider a system

$$\begin{cases} \mathcal{H}(a, \Omega, s, B) = 0, \\ \langle u_1, a \rangle = 0, \\ \langle u_2, a \rangle = 0. \end{cases} \quad (9.12)$$

Obviously, every solution of system (9.12) yields a solution of Eq. (9.3). Moreover, because of the identities $\langle ia_0, a_0 \rangle = \langle \partial_x a_0, a_0 \rangle = 0$ the triplet (a_0, Ω_0, s_0) is a solution of the system (9.12) with $B = B_0$. On the other hand, system (9.12) is much easier to solve than Eq. (9.3). Indeed, above we have showed that the derivative operator $\mathcal{M} = \partial_a \mathcal{H}(a_0, \Omega_0, s_0, B_0)$ is invertible. Therefore Implicit Function Theorem implies that the equation $\mathcal{H}(a, \Omega, s, B) = 0$ determines a function $a = \tilde{a}(\Omega, s, B)$ such that $\tilde{a}(\Omega_0, s_0, B_0) = a_0$. Inserting this function into the second and the third equations of the system (9.12) we obtain

$$\begin{cases} \langle u_1, \tilde{a}(\Omega, s, B) \rangle = 0, \\ \langle u_2, \tilde{a}(\Omega, s, B) \rangle = 0. \end{cases} \quad (9.13)$$

System (9.13) can be solved with respect to the variables Ω and B if its Jacobian matrix

$$\mathbf{D} = \begin{pmatrix} \langle u_1, \partial_\Omega \tilde{a}(\Omega_0, s_0, B_0) \rangle & \langle u_1, \partial_B \tilde{a}(\Omega_0, s_0, B_0) \rangle \\ \langle u_2, \partial_\Omega \tilde{a}(\Omega_0, s_0, B_0) \rangle & \langle u_2, \partial_B \tilde{a}(\Omega_0, s_0, B_0) \rangle \end{pmatrix} \quad (9.14)$$

is non-singular. Then it yields two functions $\Omega = \tilde{\Omega}(s)$ and $B = \tilde{B}(s)$ such that $\tilde{\Omega}(s_0) = \Omega_0$ and $\tilde{B}(s_0) = B_0$. Inserting these functions into the formula $a = \tilde{a}(\tilde{\Omega}(s), s, \tilde{B}(s))$ we obtain an s -parameterized solution branch of Eq. (9.3).

Remark 9.6 (about the calculation of matrix \mathbf{D}) *Using formulas (9.3) and (9.11) we calculate the derivatives*

$$\begin{aligned} \partial_\Omega \mathcal{H}(a_0, \Omega_0, s_0, B_0) &= -ia_0, \\ \partial_s \mathcal{H}(a_0, \Omega_0, s_0, B_0) &= \partial_x a_0, \\ \partial_B \mathcal{H}(a_0, \Omega_0, s_0, B_0) &= \frac{1}{2} e^{-i\alpha} \tilde{\mathcal{G}} a_0 - \frac{1}{2} e^{i\alpha} a_0^2 \tilde{\mathcal{G}} \bar{a}_0 \end{aligned}$$

where

$$(\tilde{\mathcal{G}} a_0)(x) = \int_{-\pi}^{\pi} \partial_B G(x - y, B_0) a_0(y) dy. \quad (9.15)$$

Thus we obtain

$$\partial_{\Omega}\tilde{a}(\Omega_0, s_0, B_0) = -\mathcal{M}^{-1}\partial_{\Omega}\mathcal{H}(a_0, \Omega_0, s_0, B_0) = -\mathcal{M}^{-1}(-ia_0), \quad (9.16)$$

$$\partial_s\tilde{a}(\Omega_0, s_0, B_0) = -\mathcal{M}^{-1}\partial_s\mathcal{H}(a_0, \Omega_0, s_0, B_0) = -\mathcal{M}^{-1}\partial_x a_0, \quad (9.17)$$

$$\begin{aligned} \partial_B\tilde{a}(\Omega_0, s_0, B_0) &= -\mathcal{M}^{-1}\partial_B\mathcal{H}(a_0, \Omega_0, s_0, B_0) \\ &= -\frac{1}{2}\mathcal{M}^{-1}\left(e^{-i\alpha}\tilde{\mathcal{G}}a_0 - e^{i\alpha}a_0^2\tilde{\mathcal{G}}\bar{a}_0\right). \end{aligned} \quad (9.18)$$

Consequently, all elements of the matrix \mathbf{D} are given by explicit expressions.

Let us summarize the sufficient conditions for the local solvability of system (9.12). We assume that the triple (a_0, Ω_0, B_0) is a solution of the system (9.12) with $s = s_0$ and choose the lateral speed s to be a free parameter. Consequently, we need to solve system (9.12) with respect to the triplet $(a, \Omega, B) \in C_{\text{per}}([-\pi, \pi]; \mathbb{C}) \times \mathbb{R}^2$. According to Implicit Function Theorem this can be done if the corresponding linear system

$$\begin{cases} \mathcal{M}a_1 + \partial_{\Omega}\mathcal{H}(a_0, \Omega_0, s_0, B_0)\Omega_1 + \partial_B\mathcal{H}(a_0, \Omega_0, s_0, B_0)B_1 = f_0, \\ \langle u_1, a_1 \rangle = f_1, \\ \langle u_2, a_1 \rangle = f_2 \end{cases} \quad (9.19)$$

has a unique solution for every $(f_0, f_1, f_2) \in C_{\text{per}}([-\pi, \pi]; \mathbb{C}) \times \mathbb{R}^2$. This question is addressed in the following proposition.

Proposition 9.7 *Suppose that the operator \mathcal{M} is invertible and the matrix \mathbf{D} is non-singular, then for every $(f_0, f_1, f_2) \in C_{\text{per}}([-\pi, \pi]; \mathbb{C}) \times \mathbb{R}^2$ there exists a unique solution $(a_1, \Omega_1, B_1) \in C_{\text{per}}^1([-\pi, \pi]; \mathbb{C}) \times \mathbb{R}^2$ of the system (9.19), which is given by the formulas*

$$\begin{pmatrix} \Omega_1 \\ B_1 \end{pmatrix} = \mathbf{D}^{-1} \begin{pmatrix} f_1 - \langle u_1, \mathcal{M}^{-1}f_0 \rangle \\ f_2 - \langle u_2, \mathcal{M}^{-1}f_0 \rangle \end{pmatrix} \quad (9.20)$$

and

$$a_1 = \mathcal{M}^{-1}f_0 + \partial_{\Omega}\tilde{a}(\Omega_0, s_0, B_0)\Omega_1 + \partial_B\tilde{a}(\Omega_0, s_0, B_0)B_1. \quad (9.21)$$

Proof: If the operator \mathcal{M} is invertible then the first equation of the system (9.19) can be written as follows

$$\begin{aligned} a_1 &= \mathcal{M}^{-1}f_0 - \mathcal{M}^{-1}\partial_{\Omega}\mathcal{H}(a_0, \Omega_0, s_0, B_0)\Omega_1 - \mathcal{M}^{-1}\partial_B\mathcal{H}(a_0, \Omega_0, s_0, B_0)B_1 \\ &= \mathcal{M}^{-1}f_0 + \partial_{\Omega}\tilde{a}(\Omega_0, s_0, B_0)\Omega_1 + \partial_B\tilde{a}(\Omega_0, s_0, B_0)B_1, \end{aligned} \quad (9.22)$$

see formulas (9.16)–(9.18). Inserting this expression into the second and the third equations of the system (9.19) we obtain a two-dimensional system of the form

$$\langle u_k, \partial_\Omega \tilde{a}(\Omega_0, s_0, B_0) \rangle \Omega_1 + \langle u_k, \partial_B \tilde{a}(\Omega_0, s_0, B_0) \rangle B_1 = f_k - \langle u_k, \mathcal{M}^{-1} f_0 \rangle, \quad k = 1, 2.$$

For non-singular matrix \mathbf{D} this system is solved by the formula (9.20). Inserting the found values of Ω_1 and B_1 into (9.22) we obtain (9.21). \blacksquare

If all conditions of Proposition 9.7 are fulfilled, system (9.12) can be solved using the Newton's iterations. Then for every $s \approx s_0$ we obtain a triplet $(a(s), \Omega(s), B(s))$ which in turn yields a solution of Eq. (9.3). For the sake of clarity we repeat again the technical steps which one needs to carry out in order to compute the solution of Eq. (9.3).

Step 1. Using Remark 9.2 check if the functions ia_0 and $\partial_x a_0$ are linearly independent. Then compute the basis functions u_1 and u_2 using the Gram-Schmidt formulas.

Step 2. Check that the inequality (9.4) is satisfied. If so, find the cobasis functions v_1 and v_2 .

Step 3. Constructe the inverse operator \mathcal{M}^{-1} . Then using formulas (9.15)–(9.18) compute the derivatives $\partial_\Omega \tilde{a}(\Omega_0, s_0, B_0)$, $\partial_s \tilde{a}(\Omega_0, s_0, B_0)$ and $\partial_B \tilde{a}(\Omega_0, s_0, B_0)$.

Step 4. Check if the Jacobian matrix \mathbf{D} given by the formula (9.14) is nonsingular.

Step 5. Use the triplet (a_0, Ω_0, B_0) as an initial condition in the Newton's iteration scheme

$$\begin{aligned} \begin{pmatrix} \Omega_{n+1} \\ B_{n+1} \end{pmatrix} &= \begin{pmatrix} \Omega_n \\ B_n \end{pmatrix} - \mathbf{D}^{-1} \begin{pmatrix} \langle u_1, a_n - b_n \rangle \\ \langle u_2, a_n - b_n \rangle \end{pmatrix}, \\ a_{n+1} &= a_n - b_n - \begin{pmatrix} \partial_\Omega \tilde{a}(\Omega_0, s_0, B_0) \\ \partial_B \tilde{a}(\Omega_0, s_0, B_0) \end{pmatrix}^T \mathbf{D}^{-1} \begin{pmatrix} \langle u_1, a_n - b_n \rangle \\ \langle u_2, a_n - b_n \rangle \end{pmatrix}, \end{aligned}$$

where $b_n = \mathcal{M}^{-1} \mathcal{H}(a_n, \Omega_n, s, B_n)$. If the new value s is close enough to s_0 , then the Banach fixed point theorem guarantees that these iterations are convergent. In practice, one can stop them when the desired precision ε is achieved, i.e. when $\|a_{n+1} - a_n\|_\infty \leq \varepsilon$, $|\Omega_{n+1} - \Omega_n| \leq \varepsilon$ and $|B_{n+1} - B_n| \leq \varepsilon$.

Remark 9.8 *If the matrix \mathbf{D} in Step 4 is singular, this can be the indication of a fold bifurcation. Then the above algorithm needs to be modified. For example, if the matrix*

$$\tilde{\mathbf{D}} = \begin{pmatrix} \langle u_1, \partial_\Omega \tilde{a}(\Omega_0, s_0, B_0) \rangle & \langle u_1, \partial_s \tilde{a}(\Omega_0, s_0, B_0) \rangle \\ \langle u_2, \partial_\Omega \tilde{a}(\Omega_0, s_0, B_0) \rangle & \langle u_2, \partial_s \tilde{a}(\Omega_0, s_0, B_0) \rangle \end{pmatrix}$$

is non-singular, then system (9.13) can be solved with respect to the variables Ω and s . In this case we seek the solution of Eq. (9.3) in the form $(a(B), \Omega(B), s(B))$ where B is the new

independent variable. Respectively, the Newton's iteration formula from Step 5 must be replaced with

$$\begin{aligned} \begin{pmatrix} \Omega_{n+1} \\ s_{n+1} \end{pmatrix} &= \begin{pmatrix} \Omega_n \\ s_n \end{pmatrix} - \tilde{\mathbf{D}}^{-1} \begin{pmatrix} \langle u_1, a_n - b_n \rangle \\ \langle u_2, a_n - b_n \rangle \end{pmatrix}, \\ a_{n+1} &= a_n - b_n - \begin{pmatrix} \partial_{\Omega} \tilde{a}(\Omega_0, s_0, B_0) \\ \partial_s \tilde{a}(\Omega_0, s_0, B_0) \end{pmatrix}^{\mathbf{T}} \tilde{\mathbf{D}}^{-1} \begin{pmatrix} \langle u_1, a_n - b_n \rangle \\ \langle u_2, a_n - b_n \rangle \end{pmatrix}, \end{aligned}$$

where $b_n = \mathcal{M}^{-1} \mathcal{H}(a_n, \Omega_n, s_n, B)$.

Remark 9.9 *In the case of the trigonometric coupling function (1.16) the operator \mathcal{G} is a degenerate rank-6 integral operator. More precisely, for every $v \in C_{\text{per}}([-\pi, \pi]; \mathbb{C})$ it holds*

$$\begin{aligned} \mathcal{G}v &= \frac{1}{2\pi} \langle \psi_1, v \rangle \psi_1 + \frac{1}{2\pi} \langle \psi_2, v \rangle \psi_2 + \frac{A}{2\pi} \sum_{k=3}^6 \langle \psi_k, v \rangle \psi_k \\ &\quad + \frac{B}{2\pi} \left(\langle \psi_3, v \rangle \psi_5 + \langle \psi_4, v \rangle \psi_6 - \langle \psi_5, v \rangle \psi_3 - \langle \psi_6, v \rangle \psi_4 \right), \\ \mathcal{G}\bar{v} &= \frac{1}{2\pi} \langle \psi_1, v \rangle \psi_1 - \frac{1}{2\pi} \langle \psi_2, v \rangle \psi_2 + \frac{A}{2\pi} \sum_{k=3}^6 (-1)^{k+1} \langle \psi_k, v \rangle \psi_k \\ &\quad + \frac{B}{2\pi} \left(\langle \psi_3, v \rangle \psi_5 - \langle \psi_4, v \rangle \psi_6 - \langle \psi_5, v \rangle \psi_3 + \langle \psi_6, v \rangle \psi_4 \right), \end{aligned}$$

where

$$(\psi_1(x), \dots, \psi_6(x))^{\mathbf{T}} = (1, i, \cos x, i \cos x, \sin x, i \sin x)^{\mathbf{T}}.$$

Because of this fact, the adjoint equation $(\mathcal{K}_0 \mathcal{L})^\dagger v = 0$ can be reduced to a homogeneous six-dimensional linear system, see [85, Sec. 3.3]. Similarly, it can be shown that the calculation of the inverse operator \mathcal{M}^{-1} is equivalent to solving an eight-dimensional linear system, see [85, Sec. 3.4].

Remark 9.10 (about the singularly perturbed Eq. (9.3)) *The continuation algorithm described above relies strongly on the inequality $s_0 \neq 0$. Roughly speaking, we take a travelling wave observed for some parameter values and extend it to other parameter values. If $s_0 = 0$, we encounter a qualitatively different situation. In this case we take a standing wave and look how it transforms into a travelling wave for arbitrarily small parameter changes. The corresponding periodic boundary value problem for Eq. (9.3) becomes singularly perturbed. This problem was considered in [83].*

9.2 Stability of travelling chimera states

Suppose that we know a travelling wave solution of Eq. (2.17) written in the form (9.1). To analyze its stability we insert the ansatz

$$z(x, t) = \left(a(x - st) + v(x - st, t) \right) e^{i\Omega t}$$

into Eq. (2.17). Linearizing the resulting equation with respect to the small perturbation v we obtain

$$-s\partial_\xi v + \partial_t v = -\eta(\xi)v + \frac{1}{2}e^{-i\alpha}\mathcal{G}v - \frac{1}{2}e^{i\alpha}a^2(\xi)\mathcal{G}\bar{v}, \quad (9.23)$$

where $\xi = x - st$ is the wave variable and $\eta(\xi) = \gamma + i\Omega + e^{i\alpha}a(\xi)\mathcal{G}\bar{a}$. Note that the function v is smooth with respect to its both arguments and 2π -periodic with respect to the variable ξ .

Next, we analyze the stability of the zero solution of Eq. (9.23). For this we consider perturbations of the form

$$v(\xi, t) = v_+(\xi)e^{\lambda t} + \bar{v}_-(\xi)e^{\bar{\lambda}t}.$$

Inserting this ansatz into Eq. (9.23) and equating the terms proportional to $e^{\lambda t}$ and $e^{\bar{\lambda}t}$ separately, we obtain

$$\lambda \begin{pmatrix} v_+ \\ v_- \end{pmatrix} = \begin{pmatrix} s\partial_\xi v_+ - \eta v_+ + \frac{1}{2}e^{-i\alpha}\mathcal{G}v_+ - \frac{1}{2}e^{i\alpha}a^2\mathcal{G}v_- \\ s\partial_\xi v_- - \bar{\eta}v_- + \frac{1}{2}e^{i\alpha}\mathcal{G}v_- - \frac{1}{2}e^{-i\alpha}\bar{a}^2\mathcal{G}v_+ \end{pmatrix}. \quad (9.24)$$

Using the notation $\mathbf{v} = (v_+, v_-)^T$ system (9.24) can be written in the operator form

$$(\mathcal{D} - \lambda\mathcal{I} + \mathcal{N})\mathbf{v} = 0, \quad (9.25)$$

where

$$\mathcal{D}\mathbf{v} = \begin{pmatrix} s\partial_\xi v_+ - \eta v_+ \\ s\partial_\xi v_- - \bar{\eta}v_- \end{pmatrix}$$

is a two-component differential operator in $C_{\text{per}}^1([-\pi, \pi]; \mathbb{C}^2)$,

$$\mathcal{N}\mathbf{v} = \begin{pmatrix} \mathcal{N}_+\mathbf{v} \\ \mathcal{N}_-\mathbf{v} \end{pmatrix} = \frac{1}{2} \begin{pmatrix} e^{-i\alpha}\mathcal{G}v_+ - e^{i\alpha}a^2\mathcal{G}v_- \\ -e^{-i\alpha}\bar{a}^2\mathcal{G}v_+ + e^{i\alpha}\mathcal{G}v_- \end{pmatrix}$$

is a two-component integral operator in $C_{\text{per}}([-\pi, \pi]; \mathbb{C}^2)$, and \mathcal{I} is the identity-operator.

We are going to prove the following statements regarding Eq. (9.24).

(i) In Proposition 9.11 we will show that for every $\lambda \in \mathbb{C}$ the operator $\mathcal{D} - \lambda\mathcal{I} + \mathcal{N}$ is a Fredholm operator of index zero from $C_{\text{per}}^1([-\pi, \pi]; \mathbb{C}^2)$ into $C_{\text{per}}([-\pi, \pi]; \mathbb{C}^2)$, therefore all

nontrivial solutions of the spectral problem (9.24) correspond to isolated eigenvalues λ of finite multiplicity.

(ii) In Proposition 9.13 we will show that all eigenvalues of the problem (9.24) lie in a specific region of the complex plane.

(iii) Finally, in Proposition 9.15 we will show that in the case of the trigonometric coupling function (1.16) all eigenvalues of the problem (9.24) can be found solving an explicitly known characteristic equation.

Note that in Propositions 9.11 and 9.13 we formulate explicitly the minimal regularity conditions for the operator \mathcal{G} and for the functions a and η needed to prove these assertions. These conditions are usually satisfied for all operators \mathcal{G} with smooth kernels $G(x)$ and for all travelling wave solutions of Eq. (2.17). We also note that in some proofs below we refer to propositions and remarks from Appendix. Their numbers start with the letter A.

Proposition 9.11 *Suppose that \mathcal{G} is a bounded linear operator in $C_{\text{per}}([-\pi, \pi]; \mathbb{C})$ and $a, \eta \in C_{\text{per}}([-\pi, \pi]; \mathbb{C})$, then for every $\lambda \in \mathbb{C}$ the operator $\mathcal{D} - \lambda\mathcal{I} + \mathcal{N}$ is Fredholm of index zero from $C_{\text{per}}^1([-\pi, \pi]; \mathbb{C}^2)$ into $C_{\text{per}}([-\pi, \pi]; \mathbb{C}^2)$.*

Proof: Because of Remark A3, there exists $\lambda_0 \in \mathbb{C}$ such that $\mathcal{D} - \lambda_0\mathcal{I}$ is an isomorphism from $C_{\text{per}}^1([-\pi, \pi]; \mathbb{C}^2)$ onto $C_{\text{per}}([-\pi, \pi]; \mathbb{C}^2)$. Choosing this λ_0 we obtain

$$\mathcal{D} - \lambda\mathcal{I} + \mathcal{N} = \mathcal{D} - \lambda_0\mathcal{I} + (\lambda_0 - \lambda)\mathcal{I} + \mathcal{N}.$$

The both operators $(\lambda_0 - \lambda)\mathcal{I}$ and \mathcal{N} are compact because of the compact embedding of the space of smooth functions $C_{\text{per}}^1([-\pi, \pi]; \mathbb{C}^2)$ into the space of continuous functions $C_{\text{per}}([-\pi, \pi]; \mathbb{C}^2)$. Hence, the operator $\mathcal{D} - \lambda\mathcal{I} + \mathcal{N}$ can be decomposed into the sum of an invertible operator and a compact operator. This ends the proof. \blacksquare

Remark 9.12 *Proposition 9.11 implies that the spectrum of the operator $\mathcal{D} + \mathcal{N}$ is purely discrete. In other words, it comprises only distinct eigenvalues of finite multiplicity. Hence it follows that in every bounded region of the complex plane we can find at most finitely many eigenvalues of the operator $\mathcal{D} + \mathcal{N}$.*

In order to prove the next proposition we need to require that the functions a and η are not only continuous but also smooth. An additional smoothening requirement is also imposed on the operator \mathcal{G} .

Proposition 9.13 *Suppose that \mathcal{G} is a bounded linear operator from $C_{\text{per}}([-\pi, \pi]; \mathbb{C})$ into $C_{\text{per}}^1([-\pi, \pi]; \mathbb{C})$ and $a, \eta \in C_{\text{per}}^1([-\pi, \pi]; \mathbb{C})$, then there exist constants $c_*, c_{**} > 0$ such that all eigenvalues of the problem (9.24) lie in the region*

$$\left\{ \lambda \in \mathbb{C} : |\operatorname{Re}(\lambda + \eta_m)| \leq \min(c_*, c_{**}/|\lambda|) \right\},$$

where

$$\eta_m = \frac{1}{2\pi} \int_{-\pi}^{\pi} \eta(\xi) d\xi. \quad (9.26)$$

Proof: Remark A3 implies that the operators $\partial_\xi - \eta - \lambda$ and $\partial_\xi - \bar{\eta} - \lambda$ are isomorphisms from $C_{\text{per}}^1([-\pi, \pi]; \mathbb{C}^2)$ onto $C_{\text{per}}([-\pi, \pi]; \mathbb{C}^2)$ for all $\lambda \in \mathbb{C}$ such that $\text{Re}(\lambda + \eta_m) \neq 0$. Moreover,

$$\|(\partial_\xi - \eta - \lambda)^{-1}\| + \|(\partial_\xi - \bar{\eta} - \lambda)^{-1}\| \leq \frac{c_1}{\text{Re}(\lambda + \eta_m)},$$

where $c_1 > 0$ is independent of λ , since in the formula (A.8) the constant c_0 depends on the difference $\nu - \nu_0$ only.

Let us assume that the norm of $\mathbf{v} = (v_+, v_-)^T \in C_{\text{per}}([-\pi, \pi]; \mathbb{C}^2)$ is defined by the expression

$$\|\mathbf{v}\|_\infty = \|(v_+^2 + v_-^2)^{1/2}\|_\infty.$$

Then for $\text{Re}(\lambda + \eta_m) \neq 0$ the operator $\mathcal{D} - \lambda\mathcal{I}$ is invertible, and

$$\|(\mathcal{D} - \lambda\mathcal{I})^{-1}\| \leq \frac{c_2}{\text{Re}(\lambda + \eta_m)},$$

where the constant $c_2 > 0$ may differ from the constant c_1 , but still it does not depend on λ . Because of the assumptions made about a , η and \mathcal{G} the operator \mathcal{N} is a bounded linear operator on $C_{\text{per}}([-\pi, \pi]; \mathbb{C}^2)$, therefore there exists a constant $c_3 > 0$ such that

$$\|\mathcal{N}\| \|(\mathcal{D} - \lambda\mathcal{I})^{-1}\| < 1$$

for all $\lambda \in \mathbb{C}$ satisfying $|\text{Re}(\lambda + \eta_m)| > c_3$. In this case, due to [46, Theorem IV.1.16], the operator $\mathcal{D} - \lambda\mathcal{I} + \mathcal{N}$ is invertible and hence the equation (9.25) has no non-trivial solutions.

Let us consider the first equation of the two-component system (9.25) written in the form

$$\partial_\xi v_+ - \frac{\eta + \lambda}{s} v_+ = -\frac{1}{s} \mathcal{N}_+ \mathbf{v}. \quad (9.27)$$

Because of the smoothness assumptions imposed on the functions a and η as well as on the operator \mathcal{G} there exists a constant $c_4 > 0$ such that

$$\|\mathcal{N}_+ \mathbf{v}\|_\infty + \|\partial_\xi \mathcal{N}_+ \mathbf{v}\|_\infty \leq c_4 \|\mathbf{v}\|_\infty.$$

Suppose that $\lambda \in \mathbb{C}$ satisfies two inequalities $|\lambda| > 2\|\eta\|_\infty$ and $\text{Re}(\lambda + \eta_m) \neq 0$, then we can apply Remark A4 to Eq. (9.27) and obtain

$$\begin{aligned} \|v_+\|_\infty &\leq \|(\eta + \lambda)^{-1}\|_\infty \left(\|\mathcal{N}_+ \mathbf{v}\|_\infty + \frac{cs}{|\text{Re}(\lambda + \eta_m)|} (\|\partial_\xi \mathcal{N}_+ \mathbf{v}\|_\infty + s\|(\eta + \lambda)^{-1}\|_\infty \|\mathcal{N}_+ \mathbf{v}\|_\infty) \right) \\ &\leq c_4 \|(\eta + \lambda)^{-1}\|_\infty \left(1 + \frac{cs}{|\text{Re}(\lambda + \eta_m)|} (1 + s\|(\eta + \lambda)^{-1}\|_\infty) \right) \|\mathbf{v}\|_\infty, \end{aligned}$$

where $c > 0$ is the constant from the formula (A.10), which in our case is independent of λ . For every $|\lambda| > 2\|\eta\|_\infty$ we have $\|(\lambda + \eta)^{-1}\|_\infty < 2/|\lambda| < 1/\|\eta\|_\infty$, therefore

$$\|v_+\|_\infty \leq \frac{2c_4}{|\lambda|} \left(1 + \frac{cs(1 + s/\|\eta\|_\infty)}{|\operatorname{Re}(\lambda + \eta_m)|} \right) \|\mathbf{v}\|_\infty.$$

Similarly, we consider the second equation of the system (9.25) and obtain an analogous inequality for $\|v_-\|_\infty$. Altogether this implies that there exist two constants $c_5, c_6 > 0$ independent of λ such that every solution \mathbf{v} to Eq. (9.25) satisfies the inequality

$$\|\mathbf{v}\|_\infty \leq \frac{1}{|\lambda|} \left(c_5 + \frac{c_6}{\operatorname{Re}(\lambda + \eta_m)} \right) \|\mathbf{v}\|_\infty,$$

provided $|\lambda|$ is large enough and $\operatorname{Re}(\lambda + \eta_m) \neq 0$. This means that Eq. (9.25) does not have non-trivial solutions if

$$\frac{1}{|\lambda|} \left(c_5 + \frac{c_6}{|\operatorname{Re}(\lambda + \eta_m)|} \right) < 1, \quad \text{or equivalently} \quad |\operatorname{Re}(\lambda + \eta_m)| > \frac{c_6}{|\lambda| - c_5}.$$

Thus, all eigenvalues of the problem (9.25) lie in the region $|\operatorname{Re}(\lambda + \eta_m)| \leq c_7/|\lambda|$ with some $c_7 > 0$. Assuming $c_* = c_3$ and $c_{**} = c_7$ we obtain the above formulated spectral region estimate. \blacksquare

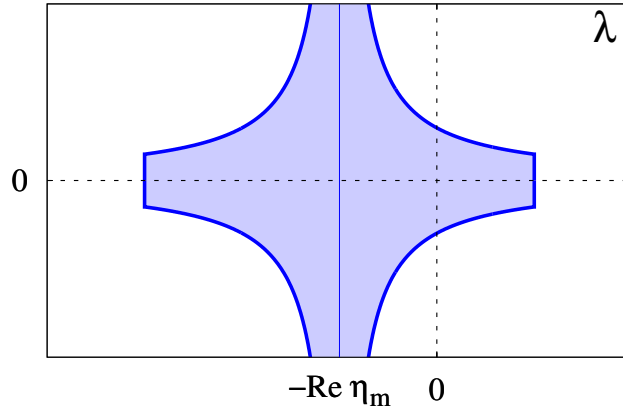


Figure 43: Schematic representation of the region determined by Proposition 9.13.

Remark 9.14 *The region of the complex plane determined by Proposition 9.13 is shown schematically in Fig. 43. Note that for $\operatorname{Im}\lambda \rightarrow \pm\infty$ the left and right borders of the shaded area converge*

asymptotically to the line $\text{Re } \lambda = -\text{Re } \eta_m$. Hence, the eigenvalues of the operator $\mathcal{D} + \mathcal{N}$ condensate along this line for $|\lambda| \rightarrow \infty$. Moreover, if $\text{Re } \eta_m > 0$, then there can be at most finitely many eigenvalues with $\text{Re } \lambda \geq 0$.

In the remaining part of the section we consider the eigenvalue problem (9.24) in the case of the trigonometric coupling function (1.16). We are going to derive a characteristic equation determining its eigenvalues. For this we rewrite Eq. (9.24) in the form

$$\begin{pmatrix} s\partial_\xi v_+ - \eta v_+ - \lambda v_+ \\ s\partial_\xi v_- - \bar{\eta} v_- - \lambda v_- \end{pmatrix} = -\frac{1}{2} \begin{pmatrix} e^{-i\alpha} & -e^{i\alpha} a^2 \\ -e^{-i\alpha} \bar{a}^2 & e^{i\alpha} \end{pmatrix} \begin{pmatrix} \mathcal{G}v_+ \\ \mathcal{G}v_- \end{pmatrix}. \quad (9.28)$$

If $(v_+, v_-)^T$ is a solution of Eq. (9.28), then there exist numbers $\hat{v}_+^k, \hat{v}_-^k \in \mathbb{C}$, $k = 1, 2, 3$, such that

$$(\mathcal{G}v_+)(\xi) = \sum_{k=1}^3 \hat{v}_+^k \varphi_k(\xi) \quad \text{and} \quad (\mathcal{G}v_-)(\xi) = \sum_{k=1}^3 \hat{v}_-^k \varphi_k(\xi), \quad (9.29)$$

where $(\varphi_1(\xi), \varphi_2(\xi), \varphi_3(\xi))^T = (1, \cos \xi, \sin \xi)^T$ are functions spanning the range of the operator \mathcal{G} with the trigonometric coupling function (1.16). Inserting ansatz (9.29) into Eq. (9.28) we obtain

$$\begin{pmatrix} s\partial_\xi v_+ - \eta v_+ - \lambda v_+ \\ s\partial_\xi v_- - \bar{\eta} v_- - \lambda v_- \end{pmatrix} = -\frac{1}{2} \sum_{k=1}^3 \begin{pmatrix} e^{-i\alpha} \varphi_k & -e^{i\alpha} a^2 \varphi_k \\ -e^{-i\alpha} \bar{a}^2 \varphi_k & e^{i\alpha} \varphi_k \end{pmatrix} \begin{pmatrix} \hat{v}_+^k \\ \hat{v}_-^k \end{pmatrix}. \quad (9.30)$$

Let us define two functions

$$\Phi_+(\xi, \lambda) = \exp\left(\frac{1}{s} \int_{-\pi}^{\xi} (\eta(y) + \lambda) dy\right) \quad (9.31)$$

and

$$\Phi_-(\xi, \lambda) = \exp\left(\frac{1}{s} \int_{-\pi}^{\xi} (\bar{\eta}(y) + \lambda) dy\right), \quad (9.32)$$

and two integral operators

$$(\mathcal{K}_\pm(\lambda)u)(\xi) = \frac{1}{s} \int_{-\pi}^{\xi} \Phi_\pm(\xi, \lambda) \Phi_\pm^{-1}(y, \lambda) u(y) dy.$$

Considering Eq. (9.30) as a two-dimensional ODE system with an initial condition $v_\pm(-\pi) = \hat{v}_\pm^0$ we write its general solution in the form

$$\begin{pmatrix} v_+ \\ v_- \end{pmatrix} = \begin{pmatrix} \Phi_+(\xi, \lambda) & 0 \\ 0 & \Phi_-(\xi, \lambda) \end{pmatrix} \begin{pmatrix} \hat{v}_+^0 \\ \hat{v}_-^0 \end{pmatrix} - \frac{1}{2} \sum_{k=1}^3 \begin{pmatrix} e^{-i\alpha} \mathcal{K}_+(\lambda) \varphi_k & -e^{i\alpha} \mathcal{K}_+(\lambda) (a^2 \varphi_k) \\ -e^{-i\alpha} \mathcal{K}_-(\lambda) (\bar{a}^2 \varphi_k) & e^{i\alpha} \mathcal{K}_-(\lambda) \varphi_k \end{pmatrix} \begin{pmatrix} \hat{v}_+^k \\ \hat{v}_-^k \end{pmatrix}. \quad (9.33)$$

This formula yields a 2π -periodic function if and only if

$$\begin{pmatrix} \hat{v}_+^0 \\ \hat{v}_-^0 \end{pmatrix} = \sum_{k=0}^3 \mathbf{J}_{0\mathbf{k}}(\lambda) \begin{pmatrix} \hat{v}_+^k \\ \hat{v}_-^k \end{pmatrix}, \quad (9.34)$$

where

$$\mathbf{J}_{00}(\lambda) = \begin{pmatrix} \Phi_+(\pi, \lambda) & 0 \\ 0 & \Phi_-(\pi, \lambda) \end{pmatrix}$$

and

$$\mathbf{J}_{0\mathbf{k}}(\lambda) = -\frac{1}{2} \begin{pmatrix} e^{-i\alpha} \mathcal{K}_+(\lambda) \varphi_k & -e^{i\alpha} \mathcal{K}_+(\lambda) (a^2 \varphi_k) \\ -e^{-i\alpha} \mathcal{K}_-(\lambda) (\bar{a}^2 \varphi_k) & e^{i\alpha} \mathcal{K}_-(\lambda) \varphi_k \end{pmatrix} \Big|_{\xi=\pi}$$

for $k = 1, 2, 3$.

Along with Eq. (9.34) the coefficients \hat{v}_\pm^k in formulas (9.29) should also satisfy some self-consistency relations following from the definition of the operator \mathcal{G} . Indeed, for every $v \in C_{\text{per}}([-\pi, \pi]; \mathbb{C})$ the coupling function formula (1.16) yields

$$\begin{aligned} (\mathcal{G}v)(\xi) &= \frac{1}{2\pi} \int_{-\pi}^{\pi} \left(\varphi_1(\xi) \varphi_1(y) + A \varphi_2(\xi) \varphi_2(y) + A \varphi_3(\xi) \varphi_3(y) \right. \\ &\quad \left. + B \varphi_3(\xi) \varphi_2(y) - B \varphi_2(\xi) \varphi_3(y) \right) v(y) dy. \end{aligned}$$

Comparing this identity with ansatz (9.29) we find

$$\begin{aligned} \hat{v}_\pm^1 &= \frac{1}{2\pi} \int_{-\pi}^{\pi} \varphi_1(y) v_\pm(y) dy, \\ \hat{v}_\pm^2 &= \frac{1}{2\pi} \int_{-\pi}^{\pi} (A \varphi_2(y) - B \varphi_3(y)) v_\pm(y) dy, \\ \hat{v}_\pm^3 &= \frac{1}{2\pi} \int_{-\pi}^{\pi} (A \varphi_3(y) + B \varphi_2(y)) v_\pm(y) dy. \end{aligned}$$

Inserting here v_+ and v_- from formula (9.33) we obtain

$$\begin{pmatrix} \hat{v}_+^1 \\ \hat{v}_-^1 \end{pmatrix} = \sum_{k=0}^3 \mathbf{J}_{1\mathbf{k}}(\lambda) \begin{pmatrix} \hat{v}_+^k \\ \hat{v}_-^k \end{pmatrix}, \quad (9.35)$$

$$\begin{pmatrix} \hat{v}_+^2 \\ \hat{v}_-^2 \end{pmatrix} = \sum_{k=0}^3 (A \mathbf{J}_{2\mathbf{k}}(\lambda) - B \mathbf{J}_{3\mathbf{k}}(\lambda)) \begin{pmatrix} \hat{v}_+^k \\ \hat{v}_-^k \end{pmatrix}, \quad (9.36)$$

$$\begin{pmatrix} \hat{v}_+^3 \\ \hat{v}_-^3 \end{pmatrix} = \sum_{k=0}^3 (A \mathbf{J}_{3\mathbf{k}}(\lambda) + B \mathbf{J}_{2\mathbf{k}}(\lambda)) \begin{pmatrix} \hat{v}_+^k \\ \hat{v}_-^k \end{pmatrix}, \quad (9.37)$$

where for every $j, k = 1, 2, 3$ we denote

$$\mathbf{J}_{j0}(\lambda) = \begin{pmatrix} \frac{1}{2\pi} \int_{-\pi}^{\pi} \varphi_j \Phi_+(\cdot, \lambda) d\xi & 0 \\ 0 & \frac{1}{2\pi} \int_{-\pi}^{\pi} \varphi_j \Phi_-(\cdot, \lambda) d\xi \end{pmatrix}$$

and

$$\mathbf{J}_{jk}(\lambda) = -\frac{1}{2} \begin{pmatrix} \frac{e^{-i\alpha}}{2\pi} \int_{-\pi}^{\pi} \varphi_j \mathcal{K}_+(\lambda) \varphi_k d\xi & -\frac{e^{i\alpha}}{2\pi} \int_{-\pi}^{\pi} \varphi_j \mathcal{K}_+(\lambda) (a^2 \varphi_k) d\xi \\ -\frac{e^{-i\alpha}}{2\pi} \int_{-\pi}^{\pi} \varphi_j \mathcal{K}_-(\lambda) (\bar{a}^2 \varphi_k) d\xi & \frac{e^{i\alpha}}{2\pi} \int_{-\pi}^{\pi} \varphi_j \mathcal{K}_-(\lambda) \varphi_k d\xi \end{pmatrix}.$$

Four equations (9.34) and (9.35)–(9.37) correspond to the eight-dimensional system

$$(\hat{v}_+^0, \hat{v}_-^0, \hat{v}_+^1, \hat{v}_-^1, \hat{v}_+^2, \hat{v}_-^2, \hat{v}_+^3, \hat{v}_-^3)^T = \mathbf{J}(\lambda) (\hat{v}_+^0, \hat{v}_-^0, \hat{v}_+^1, \hat{v}_-^1, \hat{v}_+^2, \hat{v}_-^2, \hat{v}_+^3, \hat{v}_-^3)^T, \quad (9.38)$$

where

$$\mathbf{J}(\lambda) = \begin{pmatrix} \mathbf{J}_{00} & \mathbf{J}_{01} & \mathbf{J}_{02} & \mathbf{J}_{03} \\ \mathbf{J}_{10} & \mathbf{J}_{11} & \mathbf{J}_{12} & \mathbf{J}_{13} \\ A\mathbf{J}_{20} - B\mathbf{J}_{30} & A\mathbf{J}_{21} - B\mathbf{J}_{31} & A\mathbf{J}_{22} - B\mathbf{J}_{32} & A\mathbf{J}_{23} - B\mathbf{J}_{33} \\ A\mathbf{J}_{30} + B\mathbf{J}_{20} & A\mathbf{J}_{31} + B\mathbf{J}_{21} & A\mathbf{J}_{32} + B\mathbf{J}_{22} & A\mathbf{J}_{33} + B\mathbf{J}_{23} \end{pmatrix}.$$

Obviously, this system has non-trivial solutions if and only if $\lambda \in \mathbb{C}$ satisfies the characteristic equation

$$\det(\mathbf{I}_8 - \mathbf{J}(\lambda)) = 0. \quad (9.39)$$

Taking into account the constructive way of the derivation of Eq. (9.39), we obtain the following proposition.

Proposition 9.15 *In the case of the trigonometric coupling function (1.16) every eigenvalue of the spectral problem (9.24) corresponds to a zero of Eq. (9.39) and vice versa.*

Remark 9.16 *Because of the complex phase-shift symmetry and translation symmetry of the Ott-Antonsen equation (2.17), the characteristic equation (9.39) has always a double zero at $\lambda = 0$. Hence, if Eq. (9.39) has no other solutions $\lambda \neq 0$ in the right half-plane $\text{Re } \lambda \geq 0$, then the corresponding travelling wave (9.1) is stable. In contrast, if Eq. (9.39) has at least one solution λ with $\text{Re } \lambda > 0$, then the corresponding travelling wave (9.1) is unstable.*

Note that Proposition 9.13 indicates that the operator $\mathcal{D} + \mathcal{N}$ is of hyperbolic type and it is known that the linear stability principle may fail for such operators [103]. However, the spectral problem (9.24) is one dimensional in space ($\xi \in \mathbb{R}$), therefore the relation between the stability of travelling wave (9.1) and the position of the rightmost roots of Eq. (9.39) follows from [64].

According to the definitions (9.31) and (9.32) the functions $\Phi_+(\xi, \lambda)$ and $\Phi_-(\xi, \lambda)$ are analytic with respect to λ in the whole complex plane, therefore the determinant $\det(\mathbf{I}_8 - \mathbf{J}(\lambda))$ is also analytic for all $\lambda \in \mathbb{C}$. This implies that the characteristic equation (9.39) has only isolated zeros of finite multiplicity. Moreover, if $\text{Re } \eta_m > 0$, then only finite number of them can be found in the unstable half-plane $\text{Re } \lambda \geq 0$, see Remark 9.14.

10 Conclusion and outlook

In this work, we gave a comprehensive overview of different synchrony patterns emerging in spatially extended networks of coupled phase oscillators. We focused mainly on the networks of the form (1.14) and their two- and three-dimensional generalizations. The choice of the sinusoidal phase coupling function allowed us to exploit the full potential of the Ott-Antonsen method [88]. Thus, we could completely solve the existence and stability problem for stationary, periodically breathing and travelling coherence-incoherence patterns. Importantly, we have not only obtained many theoretical results, but also demonstrated their application on specific examples.

Note that our approach to relative equilibria and relative periodic orbits of the Ott-Antonsen equation (2.19) is not limited to periodic boundary conditions in space. With a suitable definition of the integral operator \mathcal{G} , it can be easily extended to the case of arrays with open boundary conditions and even to the case of unbounded arrays (see [70, 58] for examples of phase models with such boundary conditions). In a more general context, the mathematical methods developed in this work can be adapted to other phase models concerned with the application of the Ott-Antonsen ansatz. These are, for example, networks of pulse-coupled Winfree oscillators [94], networks of theta neurons [65, 60, 15], and networks of quadratic integrate-and-fire neurons [74, 28]. Further potential applications include also random networks [3] and systems of coupled oscillators with distributed parameters [104, 40]. Moreover, beyond the Ott-Antonsen theory, many of our theoretical constructions and formulas can be used as a starting point to describe the dynamical behaviour of spatially extended phase oscillator models with noise and non-sinusoidal phase coupling functions. All these facts indicate the relevance of the reported results and their importance for future research at the intersection of synchronization and pattern formation theories.

Appendix

Let us consider a linear differential equation

$$\frac{du}{dx} - \nu(x)u(x) = f(x), \quad x \in [-\pi, \pi], \quad (\text{A.1})$$

with a continuous 2π -periodic coefficient ν and a continuous 2π -periodic inhomogeneity f . Below we formulate sufficient conditions for the solvability of Eq. (A.1) in the space of smooth 2π -periodic functions and provide an explicit solution formula.

Proposition A1 *Suppose that $\nu \in C_{\text{per}}([-\pi, \pi]; \mathbb{C})$ and*

$$\Phi(\pi) \neq 1 \quad \text{where} \quad \Phi(x) := \exp\left(\int_{-\pi}^x \nu(y)dy\right). \quad (\text{A.2})$$

Then for every $f \in C_{\text{per}}([-\pi, \pi]; \mathbb{C})$ there exists a unique solution $u \in C_{\text{per}}^1([-\pi, \pi]; \mathbb{C})$ to Eq. (A.1) given by the formula

$$u(x) = \int_{-\pi}^{\pi} K(x, y)f(y)dy, \quad (\text{A.3})$$

where

$$K(x, y) = \frac{\Phi(\pi) + (1 - \Phi(\pi))\Theta(x - y)}{1 - \Phi(\pi)} \Phi(x)\Phi^{-1}(y).$$

Proof: The general solution to Eq. (A.1) is given by the formula

$$\begin{aligned} u(x) &= u_* \exp\left(\int_{-\pi}^x \nu(y)dy\right) + \int_{-\pi}^x f(y) \exp\left(\int_y^x \nu(\xi)d\xi\right) dy \\ &= u_* \Phi(x) + \int_{-\pi}^x \Phi(x)\Phi^{-1}(y)f(y)dy \end{aligned} \quad (\text{A.4})$$

where $u_* \in \mathbb{C}$ denotes the initial condition $u(-\pi) = u_*$. This solution is 2π -periodic if and only if $u(\pi) = u(-\pi)$, e.g.

$$u_*(1 - \Phi(\pi)) = \int_{-\pi}^{\pi} \Phi(\pi)\Phi^{-1}(y)f(y)dy.$$

Because of (A.2) the latter equation can be solved with respect to u_* . Inserting the result into formula (A.4) and performing straightforward transformations we obtain (A.3). \blacksquare

Remark A2 Let $\mathcal{K} : C_{\text{per}}([-\pi, \pi]; \mathbb{C}) \rightarrow C_{\text{per}}^1([-\pi, \pi]; \mathbb{C})$ be the solution operator to Eq. (A.1) defined by formula (A.3). If $\min_{x \in [-\pi, \pi]} |\nu_r(x)| > 0$ where $\nu_r(x) = \text{Re } \nu(x)$, then

$$\|\mathcal{K}f\|_{\infty} \leq \left\| \frac{f}{\nu_r} \right\|_{\infty}. \quad (\text{A.5})$$

Proof: Formula (A.3) implies

$$|(\mathcal{K}f)(x)| \leq \left\| \frac{f}{\nu_r} \right\|_{\infty} \int_{-\pi}^{\pi} |K(x, y)| |\nu_r| dy. \quad (\text{A.6})$$

Then, using the inequality $|\sinh \Lambda| \geq |\sinh \Lambda_r|$ where $\Lambda_r = \text{Re } \Lambda$, we obtain

$$|K(x, y)| \leq \frac{1}{2|\sinh \Lambda_r|} \exp \left(\int_y^x \nu_r(\xi) d\xi + \Lambda_r \text{sign}(x - y) \right).$$

According to Proposition A1, the formula

$$u_0(x) = \int_{-\pi}^{\pi} \frac{1}{2|\sinh \Lambda_r|} \exp \left(\int_y^x \nu_r(\xi) d\xi + \Lambda_r \text{sign}(x - y) \right) |\nu_r(y)| dy$$

gives the 2π -periodic solution to the equation

$$\frac{du}{dx} - \nu_r(x)u(x) = -\nu_r(x),$$

hence $u_0(x) = 1$. Taking into account that the integral in the right-hand side of the inequality (A.6) is bounded by $u_0(x)$, we obtain (A.5). \blacksquare

Remark A3 Suppose that $\text{Re } \nu_0 \neq 0$ where

$$\nu_0 = \frac{1}{2\pi} \int_{-\pi}^{\pi} \nu(\xi) d\xi, \quad (\text{A.7})$$

then there exists a constant $c_0 > 0$ depending on the difference $\nu(x) - \nu_0$ only such that

$$\|\mathcal{K}f\|_{\infty} \leq \frac{c_0}{|\text{Re } \nu_0|} \|f\|_{\infty}, \quad (\text{A.8})$$

where \mathcal{K} is the solution operator to Eq. (A.1) defined by formula (A.3).

Proof: Because of the definition (A.7), the function

$$u_1(x) = \exp\left(\int_{-\pi}^x (\nu(\xi) - \nu_0) d\xi\right)$$

is 2π -periodic function, therefore via the transformation $u(x) = \tilde{u}(x)u_1(x)$ every 2π -periodic solution to Eq. (A.1) corresponds to a 2π -periodic solution of the equation

$$\frac{d\tilde{u}}{dx} - \nu_0\tilde{u}(x) = \frac{f(x)}{u_1(x)}, \quad x \in [-\pi, \pi], \quad (\text{A.9})$$

and vice versa. Applying formula (A.5) from Remark A2 we find that every solution \tilde{u} to Eq. (A.9) satisfies the inequality

$$\|\tilde{u}\|_\infty \leq \frac{1}{|\operatorname{Re} \nu_0|} \left\| \frac{f}{u_1} \right\|_\infty.$$

Therefore because of the relation $u = \tilde{u}u_1$ connecting the solution u of Eq. (A.1) with the solution \tilde{u} of Eq. (A.9) we obtain

$$\|\mathcal{K}f\|_\infty \leq \|\tilde{u}\|_\infty \|u_1\|_\infty \leq \frac{1}{|\operatorname{Re} \nu_0|} \|u_1\|_\infty \|u_1^{-1}\|_\infty \|f\|_\infty.$$

Recall that the function u_1 is expressed via the difference $\nu - \nu_0$ only, thus formula (A.8) is completely justified. ■

Remark A4 Let $\mathcal{K} : C_{\text{per}}([-\pi, \pi]; \mathbb{C}) \rightarrow C_{\text{per}}^1([-\pi, \pi]; \mathbb{C})$ be the solution operator to Eq. (A.1) defined by formula (A.3) and let the following assumptions are satisfied:

- 1) $\nu \in C_{\text{per}}^1([-\pi, \pi]; \mathbb{C})$,
- 2) $|\nu(x)| \neq 0$ for all $x \in [-\pi, \pi]$,
- 3) $\operatorname{Re} \nu_0 \neq 0$, where ν_0 is defined by formula (A.7).

Then there exists a constant $c > 0$ depending on the difference $\nu(x) - \nu_0$ only such that for every $f \in C_{\text{per}}^1([-\pi, \pi]; \mathbb{C})$ we have

$$\|\mathcal{K}f\|_\infty \leq \|\nu^{-1}\|_\infty \left(\|f\|_\infty + \frac{c}{|\operatorname{Re} \nu_0|} (\|\partial_x f\|_\infty + \|\nu^{-1}\|_\infty \|f\|_\infty) \right). \quad (\text{A.10})$$

Proof: Integrating by parts the right-hand side of formula (A.3) and using the periodicity of functions ν and f we obtain

$$(\mathcal{K}f)(x) = -\frac{f(x)}{\nu(x)} + \int_{-\pi}^{\pi} K(x, y) \frac{d}{dy} \left(\frac{f(y)}{\nu(y)} \right) dy.$$

Now, the triangle inequality for the norm $\|\cdot\|_\infty$ and the Remark A3 yield

$$\|\mathcal{K}f\|_\infty \leq \|\nu^{-1}\|_\infty \|f\|_\infty + \frac{c_0}{|\operatorname{Re} \nu_0|} \left\| \frac{d}{dx} \left(\frac{f}{\nu} \right) \right\|_\infty,$$

where $c_0 > 0$ depends on the difference $\nu - \nu_0$ only. On the other hand, because of the quotient rule we get

$$\left\| \frac{d}{dx} \left(\frac{f}{\nu} \right) \right\|_\infty = \left\| \frac{\partial_x f}{\nu} - \frac{f \partial_x \nu}{\nu^2} \right\|_\infty \leq \|\nu^{-1}\|_\infty (\|\partial_x f\|_\infty + \|\partial_x \nu\|_\infty \|\nu^{-1}\|_\infty \|f\|_\infty),$$

therefore

$$\|\mathcal{K}f\|_\infty \leq \|\nu^{-1}\|_\infty \left(\|f\|_\infty + \frac{c_0}{|\operatorname{Re} \nu_0|} (\|\partial_x f\|_\infty + \|\partial_x \nu\|_\infty \|\nu^{-1}\|_\infty \|f\|_\infty) \right).$$

Taking into account that $\|\partial_x \nu\|_\infty = \|\partial_x(\nu - \nu_0)\|_\infty$ we justify the formula (A.10). ■

Acknowledgements

I would like to thank the many people who have helped me to undertake this research and encouraged me to summarize it in the form of this Habilitation thesis.

First and foremost I am extremely grateful to Prof. Arkady Pikovsky for the opportunity to work in his research group at the University of Potsdam. Most of the above results were obtained thanks to this creative and rich in new ideas scientific environment. Moreover, his advice and support were very important to me at every stage of the Habilitation process.

I would also like to acknowledge the Deutsche Forschungsgemeinschaft for the funding that made my research in Potsdam possible.

Returning to the origins, I would like to thank Prof. Yuri Maistrenko and Prof. Peter Tass, who introduced me to the world of nonlinear dynamics, phase oscillators and their applications, and with whom I published my first paper on chimera states.

Furthermore, my sincere thanks are dedicated to all my coauthors and project partners. It has been a pleasure to work with them. In particular, I would like to acknowledge Dr. Matthias Wolfrum, Prof. Eckehard Schöll, Prof. Edgar Knobloch and Prof. Carlo Laing for fruitful cooperation and many inspiring scientific discussions. Special thanks go to Edgar, who encouraged me to write a review paper “The mathematics behind chimera states”, which was the first step in the direction of this thesis.

Finally, I would like to thank my parents, my wife and my daughter. Without their tremendous understanding and encouragement in the past few years, it would be impossible for me to complete this work. In particular, I am pleased that Iryna and Julia were the first readers of the thesis (at least some parts of it) and that their valuable comments helped me many times.

References

- [1] D.M. Abrams and S.H. Strogatz, “Chimera states for coupled oscillators”, *Phys. Rev. Lett.* **93**, 174102 (2004)
- [2] J. A. Acebrón, L. L. Bonilla, C. J. P. Vicente, F. Ritort, and R. Spigler, “The Kuramoto model: A simple paradigm for synchronization phenomena”, *Rev. Mod. Phys.* **77**, 137–185 (2005)
- [3] A. Arenas, A. Diaz-Guilera, J. Kurths, Y. Moreno, and C. Zhou, “Synchronization in complex networks”, *Phys. Rep.* **469**, 93–153 (2008)
- [4] P. Ashwin, S. Coombes, and R. Nicks, “Mathematical frameworks for oscillatory network dynamics in neuroscience”, *J. Math. Neurosci.* **6**, 2 (2016)
- [5] P. Ashwin and A. Rodrigues, Hopf normal form with SN symmetry and reduction to systems of nonlinearly coupled phase oscillators, *Physica D* **325**, 14–24 (2016)
- [6] C. Beta and K. Kruse, “Intracellular oscillations and waves”, *Annu. Rev. Condens. Matter Phys.* **8**, 239–264 (2017)
- [7] C. Bick and E. A. Martens, “Controlling chimeras”, *New J. Phys.* **17**, 033030 (2015)
- [8] C. Bick, “Heteroclinic switching between chimeras”, *Phys. Rev. E* **97**, 050201 (2018)
- [9] C. Bick, M. Goodfellow, C. R. Laing, and E. A. Martens, “Understanding the dynamics of biological and neural oscillator networks through mean-field reductions: a review”, *J. Math. Neurosci.* **10**, 9 (2020)
- [10] S. Boccaletti, V. Latora, Y. Moreno, M. Chavez, and D. U. Hwang, “Complex networks: Structure and dynamics”, *Phys. Rep.* **424**, 175–308 (2006)
- [11] M. Bolotov, L. Smirnov, G. Osipov, and A. Pikovsky, “Simple and complex chimera states in a nonlinearly coupled oscillatory medium”, *Chaos* **28**, 045101 (2018)
- [12] L. L. Bonilla, “Stable nonequilibrium probability densities and phase transitions for mean-field models in the thermodynamic limit”, *J. Stat. Phys.* **46**, 659–678 (1987)
- [13] A. E. Botha. “Characteristic distribution of finitetime Lyapunov exponents for chimera states”, *Sci. Rep.* **6**, 29213 (2016)
- [14] J. Buck and E. Buck, “Mechanism of rhythmic synchronous flashing of fireflies”, *Science* **159**, 1319–1327 (1968)

- [15] A. Byrne, D. Avitabile, and S. Coombes, “Next-generation neural field model: The evolution of synchrony within patterns and waves”, *Phys. Rev. E* **99**, 012313 (2019)
- [16] J. Campos, “Möbius transformations and periodic solutions of complex Riccati equations”, *Bull. London Math. Soc.* **29**, 205–215 (1997)
- [17] H. Chiba and I. Nishikawa, “Center manifold reduction for large populations of globally coupled phase oscillators”, *Chaos* **21**, 043103 (2011)
- [18] H. Chiba and G. S. Medvedev, “The mean field analysis of the Kuramoto model on graphs II. Asymptotic stability of the incoherent state, center manifold reduction, and bifurcations”, *Discrete Contin. Dyn. Syst.* **39**, 3897–3921 (2019)
- [19] M. G. Clerc, S. Coulibaly, M. A. Ferré, and R. G. Rojas, “Chimera states in a Duffing oscillators chain coupled to nearest neighbors”, *Chaos* **28**, 083126 (2018)
- [20] J. D. Crawford and K. T. R. Davies, “Synchronization of globally coupled phase oscillators: singularities and scaling for general couplings”, *Physica D* **125**, 1–46 (1999)
- [21] H. Daido, “Onset of cooperative entrainment in limit-cycle oscillators with uniform all-to-all interactions: bifurcation of the order function”, *Physica D* **91**, 24–66 (1996)
- [22] Ju. L. Daleckii and M. G. Krein, *Stability of Solutions of Differential Equations in Banach Spaces*, AMS, Providence, 1974
- [23] S. De Monte, F. d’Ovidio, S. Danø, and P. G. Sørensen, “Dynamical quorum sensing: Population density encoded in cellular dynamics”, *Proc. Natl. Acad. Sci. USA* **104**, 18377–18381 (2008)
- [24] H. Dietert, “Stability and bifurcation for the Kuramoto model”, *J. Math. Pures Appl.* **105**, 451–489 (2016)
- [25] F. Dörfler and F. Bullo, “Synchronization in complex networks of phase oscillators: A survey”, *Automatica* **50**, 1539–1564 (2014)
- [26] B. Ermentrout, “Neural networks as spatio-temporal pattern-forming systems”, *Rep. Prog. Phys.* **61**, 353–430 (1998)
- [27] G. B. Ermentrout and D. H. Terman, *Mathematical Foundations of Neuroscience*, Springer, Berlin, 2010
- [28] J. M. Esnaola-Acebes, A. Roxin, D. Avitabile, and E. Montbrió, “Synchrony-induced modes of oscillation of a neural field model”, *Phys. Rev. E* **96**, 052407 (2017)

- [29] W. Gilpin and M. S. Bull and M. Prakash, “The multiscale physics of cilia and flagella”, *Nat. Rev. Phys.* **2**, 74–88 (2020)
- [30] T. Girnyk, M. Hasler, and Y. Maistrenko, “Multistability of twisted states in non-locally coupled Kuramoto-type models”, *Chaos* **22**, 013114 (2012)
- [31] L. Glass, “Synchronization and rhythmic processes in physiology”, *Nature* **410**, 277–284 (2001)
- [32] R. E. Goldstein, “Fluid dynamics at the scale of the cell”, *J. Fluid Mech.* **807**, 1–39 (2016)
- [33] R. Gopal, V. K. Chandrasekar, A. Venkatesan, and M. Lakshmanan, “Observation and characterization of chimera states in coupled dynamical systems with nonlocal coupling”, *Phys. Rev. E* **89**, 052914 (2014)
- [34] J. Guckenheimer, “Isochrons and phaseless sets”, *J. Math. Biol.* **1**, 259–273 (1975)
- [35] A. M. Hagerstrom, T. E. Murphy, R. Roy, P. Hövel, I. Omelchenko, and E. Schöll, “Experimental observation of chimeras in coupled-map lattices”, *Nature Phys.* **8**, 658–661 (2012)
- [36] S. W. Haugland, L. Schmidt, and K. Krischer, “Self-organized alternating chimera states in oscillatory media”, *Sci. Rep.* **5**, 9883 (2015)
- [37] S. Heitmann and G. B. Ermentrout, “Synchrony, waves and ripple in spatially coupled Kuramoto oscillators with Mexican hat connectivity”, *Biological Cybernetics* **109**, 1–15 (2015)
- [38] M. E. Henderson and H. B. Keller, “Complex bifurcation from real paths”, *SIAM J. Appl. Math.* **50**, 460–482 (1990)
- [39] F. C. Hoppensteadt and E. M. Izhikevich, *Weakly Connected Neural Networks*, Springer, Berlin, 1997
- [40] D. Iatsenko, P. V. E. McClintock, and A. Stefanovska, “Glassy states and super-relaxation in populations of coupled phase oscillators”, *Nat. Commun.* **5**, 4118 (2014)
- [41] A. Jenkins, “Self-oscillation”, *Phys. Rep.* **525**, 167–222 (2013)
- [42] T. Kapitaniak, P. Kuzma, J. Wojewoda, K. Czolczynski, and Y. Maistrenko, “Imperfect chimera states for coupled pendula”, *Sci. Rep.* **4**, 6379 (2014)

- [43] T. Kapitula and B. Sandstede, “Edge bifurcations for near integrable systems via Evans function techniques”, *SIAM J. Math. Anal.* **33**, 1117–1143 (2002)
- [44] T. Kapitula, N. Kutz, and B. Sandstede, “The Evans function for nonlocal equations”, *Indiana Univ. Math. J.* **53**, 1095–1126 (2004)
- [45] T. Kasimatis, J. Hizanidis, and A. Provata, “Three-dimensional chimera patterns in networks of spiking neuron oscillators”, *Phys. Rev. E* **97**, 052213 (2018)
- [46] T. Kato, *Perturbation Theory for Linear Operators*, Springer, Berlin, 1966
- [47] F. P. Kemeth, S. W. Haugland, L. Schmidt, I. G. Kevrekidis, and K. Krischer, A classification scheme for chimera states, *Chaos* **26**, 094814 (2016)
- [48] I. Z. Kiss, Y. Zhai, and J. L. Hudson, “Emerging coherence in a population of chemical oscillators”, *Science* **296**, 1676–1678 (2002)
- [49] N. Kopell and G. B. Ermentrout, “Symmetry and phaselocking in chains of weakly coupled oscillators”, *Comm. Pure Appl. Math.* **39**, 623–660 (1986)
- [50] N. Kopell and G. B. Ermentrout, “Phase transitions and other phenomena in chains of coupled oscillators”, *SIAM J. Appl. Math.* **50**, 1014–1052 (1990)
- [51] N. Kopell, W. Zhang, and G. B. Ermentrout, “Multiple coupling in chains of oscillators”, *SIAM J. Math. Anal.* **21**, 935–953 (1990)
- [52] S. Kundu, B. K. Bera, D. Ghosh, and M. Lakshmanan, “Chimera patterns in three-dimensional locally coupled systems”, *Phys. Rev. E* **99**, 022204 (2019)
- [53] Y. Kuramoto, *Chemical Oscillations, Waves, and Turbulence*, Springer, Berlin, 1984
- [54] Y. Kuramoto, “Scaling behavior of turbulent oscillators with non-local interaction”, *Prog. Theor. Phys.* **94**, 321–330 (1995)
- [55] Y. Kuramoto and D. Battogtokh, “Coexistence of coherence and incoherence in nonlocally coupled phase oscillators”, *Nonlinear Phenom. Complex Syst.* **5**, 380–385 (2002)
- [56] Y. Kuramoto and H. Nakao, “On the concept of dynamical reduction: the case of coupled oscillators”, *Phil. Trans. R. Soc. A* **377**, 20190041 (2019)
- [57] C. R. Laing, “The dynamics of chimera states in heterogeneous Kuramoto networks”, *Physica D* **238**, 1569–1588 (2009)

- [58] C. R. Laing, “Fronts and bumps in spatially extended Kuramoto networks”, *Physica D* **240**, 1960–1971 (2011)
- [59] C. R. Laing, “Disorder-induced dynamics in a pair of coupled heterogeneous phase oscillator networks”, *Chaos* **22**, 043104 (2012)
- [60] C. R. Laing, “Derivation of a neural field model from a network of theta neurons”, *Phys. Rev. E* **90**, 010901 (2014)
- [61] C. R. Laing, “Chimeras in two-dimensional domains: heterogeneity and the continuum limit”, *SIAM J. Appl. Dyn. Syst.* **16**, 974–1014 (2017)
- [62] H. W. Lau and J. Davidsen, “Linked and knotted chimera filaments in oscillatory systems”, *Phys. Rev. E* **94**, 010204 (2016)
- [63] K. Lehnertz, S. Bialonski, M. T. Horstmann, D. Krug, A. Rothkegel, M. Staniek, and T. Wagner, “Synchronization phenomena in human epileptic brain networks”, *J. Neurosci. Methods* **183**, 42–48 (2009)
- [64] M. Lichtner, “Spectral mapping theorem for linear hyperbolic systems”, *Proc. Amer. Math. Soc.* **136**, 2091–2101 (2008)
- [65] T. B. Luke, E. Barreto and P. So, “Complete classification of the macroscopic behavior of a heterogeneous network of theta neurons”, *Neural Comput.* **25**, 3207–3234 (2013)
- [66] R. Ma, J. Wang, and Z. Liu, “Robust features of chimera states and the implementation of alternating chimera states”, *Europhys. Lett.* **91**, 40006 (2010)
- [67] Y. Maistrenko, O. Sudakov, O. Osiv, and V. Maistrenko, “Chimera states in three dimensions”, *New J. Phys.* **17**, 073037 (2015)
- [68] V. Maistrenko, O. Sudakov, O. Osiv, and Y. Maistrenko, “Multiple scroll wave chimera states”, *Eur. Phys. J. Spec. Top.* **226**, pp. 1867–1881 (2017)
- [69] S. Majhi, B. K. Bera, D. Ghosh, and M. Perc, “Chimera states in neuronal networks: A review”, *Physics of Life Reviews* **28**, 100–121 (2019)
- [70] E. A. Martens, C. R. Laing, and S. H. Strogatz, “Solvable model of spiral wave chimeras”, *Phys. Rev. Lett.* **104**, 044101 (2010)
- [71] E. A. Martens, S. Thutupalli, A. Fourriere, and O. Hallatschek, “Chimera states in mechanical oscillator networks”, *Proc. Natl Acad. Sci. USA* **110**, 10563–10567 (2013)

- [72] S. A. Marvel, R. E. Mirollo, and S. H. Strogatz, “Identical phase oscillators with global sinusoidal coupling evolve by Möbius group action”, *Chaos* **19**, 043104 (2009)
- [73] T. J. Mitchison and H. M. Mitchison, “How cilia beat”, *Nature* **463**, 308–309 (2010)
- [74] E. Montbrió, D. Pazó, and A. Roxin, “Macroscopic Description for Networks of Spiking Neurons”, *Phys. Rev. X*, **5**, 021028 (2015)
- [75] T. Needham, *Visual Complex Analysis*, Oxford University Press, Oxford, 2009
- [76] T. Nishikawa and A. E. Motter, “Symmetric states requiring system asymmetry”, *Phys. Rev. Lett.* **117**, 114101 (2016)
- [77] O. E. Omel’chenko, M. Wolfrum, and Y. L. Maistrenko, “Chimera states as chaotic spatiotemporal patterns”, *Phys. Rev. E* **81**, 065201 (2010)
- [78] O. E. Omel’chenko, M. Wolfrum, S. Yanchuk, Y. L. Maistrenko, and O. Sudakov. “Stationary patterns of coherence and incoherence in two-dimensional arrays of non-locally coupled phase oscillators”, *Phys. Rev. E* **85**, 036210 (2012)
- [79] O. Omel’chenko, “Coherence-incoherence patterns in a ring of non-locally coupled phase oscillators”, *Nonlinearity* **26**, 2469–2498 (2013)
- [80] O. E. Omel’chenko, M. Wolfrum, and C. R. Laing, “Partially coherent twisted states in arrays of coupled phase oscillators”, *Chaos* **24**, 023102 (2014)
- [81] O. E. Omel’chenko, “The mathematics behind chimera states”, *Nonlinearity* **31**, R121–R164 (2018)
- [82] O. E. Omel’chenko, M. Wolfrum, and E. Knobloch, “Stability of spiral chimera states on a torus”, *SIAM J. Appl. Dyn. Syst.* **17**, 97–127 (2018)
- [83] O. E. Omel’chenko, “Traveling chimera states”, *J. Phys. A: Math. Theor.* **52**, 104001 (2019)
- [84] O. E. Omel’chenko and E. Knobloch, “Chimerapedia: coherence-incoherence patterns in one, two and three dimensions”, *New J. Phys.* **21**, 093034 (2019)
- [85] O. Omel’chenko, “Travelling chimera states in systems of phase oscillators with asymmetric nonlocal coupling”, *Nonlinearity* **33**, 611–642 (2020)
- [86] O. E. Omel’chenko, “Nonstationary coherence-incoherence patterns in nonlocally coupled heterogeneous phase oscillators”, *Chaos* **30**, 043103 (2020)

- [87] O. Omel’chenko, “Mathematical framework for breathing chimera states”, *J. Nonlinear Sci.* **32**, 22 (2022)
- [88] E. Ott and T. M. Antonsen, “Low dimensional behavior of large systems of globally coupled oscillators”, *Chaos* **18**, 037113 (2008)
- [89] E. Ott and T. M. Antonsen. “Long time evolution of phase oscillator systems”, *Chaos* **19**, 023117 (2009)
- [90] M. J. Panaggio and D. M. Abrams, “Chimera states on a flat torus”, *Phys. Rev. Lett.* **110**, 094102 (2013).
- [91] M. J. Panaggio and D. M. Abrams, “Chimera states: coexistence of coherence and incoherence in networks of coupled oscillators”, *Nonlinearity* **28**, R67–R87 (2015)
- [92] F. Parastesh, S. Jafari, H. Azarnoush, Z. Shahriari, Z. Wang, S. Boccaletti, and M. Perc, “Chimeras”, *Phys. Rep.* **898**, 1–114 (2021)
- [93] J. E. Paultet and G. B. Ermentrout, “Stable rotating waves in two-dimensional discrete active media”, *SIAM J. Appl. Math.* **54**, 1720–1744 (1994)
- [94] D. Pazó and E. Montbrió, “Low-dimensional dynamics of populations of pulse-coupled oscillators”, *Phys. Rev. X*, **4**, 011009 (2014)
- [95] B. Pietras and A. Daffertshofer, Network dynamics of coupled oscillators and phase reduction techniques, *Phys. Rep.* **819**, 1–105 (2019)
- [96] A. Pikovsky, M. Rosenblum, and J. Kurths, *Synchronization, a Universal Concept in Nonlinear Sciences*, Cambridge University Press, Cambridge, 2001
- [97] A. Pikovsky and A. Politi, *Lyapunov Exponents, a Tool to Explore Complex Dynamics*, Cambridge University Press, Cambridge, 2016
- [98] A. Pikovsky and M. Rosenblum, “Dynamics of globally coupled oscillators: Progress and perspectives”, *Chaos* **25**, 097616 (2015)
- [99] Y. Pomeau and P. Manneville, “Intermittent transition toturbulence in dissipative dynamical systems”, *Commun. Math. Phys.* **74**, 189–197 (1980)
- [100] O. V. Popovych, Y. L. Maistrenko, and P. A. Tass, “Phase chaos in coupled oscillators”, *Phys. Rev. E* **71**, 065201((2005)
- [101] L. Ren and G. B. Ermentrout, “Monotonicity of phaselocked solutions in chains and arrays of nearest-neighbor coupled oscillators”, *SIAM J. Math. Anal.* **29**, 208–234 (1998)

- [102] L. Ren and G. B. Ermentrout, “Phase locking in chains of multiple-coupled oscillators”, *Physica D* **143**, 56–73 (2000)
- [103] M. Renardy, “On the linear stability of hyperbolic PDEs and viscoelastic flows”, *Z. Angew. Math. Phys.* **45**, 854–865 (1994)
- [104] J. G. Restrepo and E. Ott, “Mean-field theory of assortative networks of phase oscillators”, *Europhys. Lett.* **107**, 60006 (2014)
- [105] F. A. Rodriguez, T. K. D. M. Peron, P. Ji, and J. Kurths, “The Kuramoto model in complex networks”, *Phys. Rep.* **610**, 1–98 (2016)
- [106] D. P. Rosin, D. Rontani, N. D. Haynes, E. Schöll, and D. J. Gauthier, “Transient scaling and resurgence of chimera states in networks of Boolean phase oscillators”, *Phys. Rev. E* **90**, 030902 (2014)
- [107] H. Sakaguchi and Y. Kuramoto, “A soluble active rotator model showing phase transitions via mutual entertainment”, *Prog. Theor. Phys.* **76**, 576–581 (1986)
- [108] B. Sandstede, “Stability of traveling waves”, in *Handbook of Dynamical Systems*, Vol. 2, ed. B. Fiedler (Amsterdam, North-Holland), 983–1055 (2002)
- [109] L. Schmidt, K. Schönleber, K. Krischer, and V. García-Morales, “Coexistence of synchrony and incoherence in oscillatory media under nonlinear global coupling”, *Chaos* **24**, 013102 (2014)
- [110] H. Schmidt and D. Avitabile, “Bumps and oscillons in networks of spiking neurons”, *Chaos* **30**, 033133 (2020)
- [111] E. Schöll, “Synchronization patterns and chimera states in complex networks: interplay of topology and dynamics”, *Eur. Phys. J. Spec. Top.* **225**, 891–919 (2016)
- [112] N. Semenova, A. Zakharova, V. Anishchenko, and E. Schöll, “Coherence-resonance chimeras in a network of excitable elements”, *Phys. Rev. Lett.* **117**, 014102 (2016)
- [113] T. Shibata and K. Kaneko, “Heterogeneity-induced order in globally coupled chaotic systems”, *Europhys. Lett.* **38**, 417 (1997)
- [114] S. Shima and Y. Kuramoto, “Rotating spiral waves with phase-randomized core in non-locally coupled oscillators”, *Phys. Rev. E* **69**, 036213 (2004)
- [115] J. Sieber, O. E. Omel’chenko, and M. Wolfrum. “Controlling unstable chaos: Stabilizing chimera states by feedback”, *Phys. Rev. Lett.* **112**, 054102 (2014)

- [116] B. Sonnenschein and L. Schimansky-Geier, “Approximate solution to the stochastic Kuramoto model”, *Phys. Rev. E* **88**, 052111 (2013)
- [117] S. H. Strogatz, *Nonlinear Dynamics and Chaos*, Addison-Wesley, Readings, MA, 1984
- [118] S. H. Strogatz, “From Kuramoto to Crawford: exploring the onset of synchronization in populations of coupled oscillators”, *Physica D* **143**, 1–20 (2000)
- [119] Y. Suda and K. Okuda, “Persistent chimera states in nonlocally coupled phase oscillators”, *Phys. Rev. E* **92**, 060901 (2015)
- [120] Y. Suda and K. Okuda, “Breathing multichimera states in nonlocally coupled phase oscillators”, *Phys. Rev. E* **97**, 042212 (2018)
- [121] Y. Suda and K. Okuda, “Emergence of second coherent regions for breathing chimera states”, *Phys. Rev. E* **101**, 062203 (2020)
- [122] A. M. Tayar, E. Karzbrun, V. Noireaux, and R. H. Bar-Ziv, “Synchrony and pattern formation of coupled genetic oscillators on a chip of artificial cells”, *Proc. Natl Acad. Sci. USA* **114**, 11609–11614 (2017)
- [123] A. F. Taylor, M. R. Tinsley, F. Wang, Z. Huang, and K. Showalter, “Dynamical quorum sensing and synchronization in large populations of chemical oscillators”, *Science* **323**, 614–616 (2009)
- [124] M. R. Tinsley, S. Nkomo, and K. Showalter, “Chimera and phase-cluster states in populations of coupled chemical oscillators”, *Nature Phys.* **8**, 662–665 (2012)
- [125] J. F. Tetz, J. Rode, M. R. Tinsley, K. Showalter, and H. Engel, “Spiral wave chimera states in large populations of coupled chemical oscillators”, *Nature Phys.* **14**, 282–285 (2018)
- [126] N. Uchida and R. Golestanian, “Synchronization and collective dynamics in a carpet of microfluidic rotors”, *Phys. Rev. Lett.* **104**, 178103 (2010)
- [127] P. J. Uhlhaas and W. Singer, “Neural synchrony in brain disorders: relevance for cognitive dysfunctions and pathophysiology”, *Neuron* **52**, 155–168 (2006)
- [128] S. R. Ujjwal and R. Ramaswamy, “Chimeras with multiple coherent regions”, *Phys. Rev. E* **88**, 032902 (2013)
- [129] M. Wickramasinghe and I. Z. Kiss, “Spatially organized dynamical states in chemical oscillator networks: synchronization, dynamical differentiation, and chimera patterns”, *PLoS ONE* **8**, e80586 (2013)

- [130] K. Wiesenfeld, P. Colet, and S. H. Strogatz, “Synchronization transitions in a disordered Josephson series array”, *Phys. Rev. Lett.* **76**, 404–407 (1996)
- [131] P. Wilczyński, “Planar nonautonomous polynomial equations: The Riccati equation”, *J. Differential Equations* **244**, 1304–1328 (2008)
- [132] D. A. Wiley, S. H. Strogatz, and M. Girvan, “The size of the sync basin”, *Chaos* **16**, 015103 (2006)
- [133] A. T. Winfree, *The Geometry of Biological Time*, Springer, Berlin, 1980
- [134] M. Wolfrum, O. E. Omel’chenko, S. Yanchuk, and Y. L. Maistrenko, “Spectral properties of chimera states”, *Chaos* **21**, 013112 (2011)
- [135] M. Wolfrum and O. E. Omel’chenko, “Chimera states are chaotic transients”, *Phys. Rev. E* **84** 015201 (2011)
- [136] J. Xie, E. Knobloch, and H.-C. Kao, “Multicluster and traveling chimera states in nonlocal phase-coupled oscillators”, *Phys. Rev. E* **90**, 022919 (2014)
- [137] J. Xie, E. Knobloch, and H.-C. Kao, “Twisted chimera states and multicore spiral chimera states on a two-dimensional torus”, *Phys. Rev. E* **92**, 042921 (2015)
- [138] J. Xie, H.-C. Kao, and E. Knobloch, “Chimera states in systems of nonlocal nonidentical phase-coupled oscillators”, *Phys. Rev. E* **91**, 032918 (2015)
- [139] S. Yamaguchi, H. Isejima, T. Matsuo, R. Okura, K. Yagita, M. Kobayashi, and H. Okamura, “Synchronization of cellular clocks in the suprachiasmatic nucleus”, *Science* **302**, 1408–1412 (2003)
- [140] Y. Zhang, Z. G. Nicolaou, J. D. Hart, R. Roy, and A. E. Motter, “Critical switching in globally attractive chimeras”, *Phys. Rev. X* **10**, 011044 (2020)